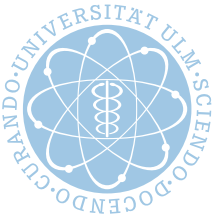
Integrated Electromagnets and Radiofrequency Spectroscopy in a Planar Paul Trap



ulm university universität ulm

DISSERTATION

zur Erlangung des Doktorgrades
Dr. rer. nat. an der naturwissenschaftlichen Fakultät
der Universität Ulm

vorgelegt von

Amado Bautista-Salvador

aus San Ildefonso Villa Alta

2015

Declaration

Amtierender Dekan:	Prof. Dr. Joachim Ankerhold
Erstgutachter:	Prof. Dr. Ferdinand Schmidt-Kaler
Zweitgutachter:	Prof. Dr. Fedor Jelezko
Tag der Promotion:	24. Juli, 2015

Hiermit erkläre ich, Amado Bautista-Salvador, dass ich die vorliegende Dissertation selbstständig angefertigt und keine anderen als die angegebenen Quellen und Hilfs mittel benutzt sowie die wörtlich und inhaltlich übernommenen Stellen als solche kenntlich gemacht und die Satzung der Universität Ulm zur Sicherung guter wissenschaftlicher Praxis beachtet habe.

A. Bautista-Salvador
Gustavsburg, 17. Januar, 2015

The work described in this thesis was accomplished by the author at the

Universität Ulm
Institut für Quanteninformationsverarbeitung
Albert-Einstein-Allee 11
D-89069 Ulm

Johannes Gutenberg-Universität Mainz
Institut für Physik, QUANTUM
Staudingerweg 7
D-55128 Mainz

Dedication

A la memoria de mi amada madre,

Flavia Salvador López

Contents

Abstract xi

Zusammenfassung xiii

Introduction xix

1 Basic Tools in Planar Traps 1
- 1.1 $^{40}Ca^{+}$ Ion as Qubit . . . 1
  - 1.1.1 Optical Qubit . . . 1
  - 1.1.2 Spin Qubit . . . 2
- 1.2 Ion Confinement in Paul Traps . . . 2
  - 1.2.1 Adiabatic Approximation . . . 5
- 1.3 Simulation Tools of Planar Traps . . . 6
  - 1.3.1 House Model . . . 6
  - 1.3.2 Numerical Simulations . . . 10
- 1.4 Basic Laser-Ion Interactions . . . 14
  - 1.4.1 Doppler Laser Cooling . . . 14
  - 1.4.2 Optical Qubit Coherent Dynamics . . . 15
  - 1.4.3 Resolved Sideband Cooling . . . 15
- 1.5 Quantum Simulations in Planar Traps . . . 17
  - 1.5.1 One-dimensional ion chains . . . 17

2 Planar Trap Designs 21
- 2.1 Trap I and Trap II: Planar Trap with Integrated Electromagnets . 21
  - 2.1.1 Design Parameters . . . 21
  - 2.1.2 Electric Fields . . . 23
  - 2.1.3 Magnetic Field Gradients . . . 31
  - 2.1.4 Induced Electric Field While Supplying Currents . . . 33
- 2.2 Trap III: Thick-film Technology and Glass Micromachining . . . 40
  - 2.2.1 Ion Chip with High Aspect Ratio Structures . . . 41
  - 2.2.2 High-density Current-Carrying Wires . . . 42
- 2.3 Trap IV: Tapered RF rails . . . 45

2.3.1 Design for measuring ion-to-surface dependence for ion heating rates . . . 46

3 Trap Microfabrication **51**
3.1 Optical Lithography . . . 51
3.1.1 Wafer Preparation . . . 53
3.1.2 Patterning . . . 57
3.2 Metal Depostion . . . 60
3.2.1 Thermal Evaporation . . . 61
3.2.2 Lift-off . . . 63
3.2.3 Electroplating . . . 63
3.3 Resist Stripping . . . 65
3.4 Etching . . . 65
3.4.1 Gold Etching . . . 66
3.4.2 Chromium Etching . . . 67
3.5 Fabrication Layouts . . . 68
3.5.1 Trap I: Evaporated Gold Electrodes . . . 68
3.5.2 Trap II: Electroplated Electrodes . . . 68
3.5.3 Trap III: Laser-micromachining and thick film technology 72

4 Chip Assembly and Apparatus **77**
4.1 Vacuum Vessel . . . 77
4.1.1 Chip Assembly of Trap I . . . 78
4.1.2 Trap Montage of Trap I . . . 82
4.1.3 Bake Test of SMD Elements . . . 83
4.1.4 Chamber Bake Out . . . 85
4.1.5 Trap Assembly and Setup Uptade for Trap III . . . 87
4.2 Voltage and Current Supply . . . 88
4.2.1 Radiofrequency Power Supply . . . 88
4.2.2 Control Voltages . . . 90
4.3 Laser Systems . . . 91
4.3.1 Fluorescence excitation, Doppler cooling and optical pumping . . . 91
4.3.2 Two-Step Photoionization . . . 93
4.3.3 Repumping and Quenching . . . 93
4.3.4 Electron Shelving . . . 95
4.3.5 Beams Alignment and Guiding . . . 96

4.4 Imaging and Detection System . . . 98
4.4.1 State Readout . . . 99
4.5 Experiment Control . . . 100

5 Trap Characterization 103
5.1 Current Failure Tests . . . 103
5.1.1 Single pulse . . . 103
5.1.2 Pulse Train . . . 105
5.2 Ion Trapping . . . 107
5.2.1 Doppler beam positioning . . . 107
5.2.2 Neutral atom fluorescence . . . 107
5.3 Ion Loading and Compensation . . . 108
5.3.1 Loading Ions . . . 108
5.3.2 Trapping Frequencies . . . 111
5.4 Laser Spectroscopy . . . 113
5.4.1 Pulse Sequence . . . 113
5.4.2 Resolved Sideband Cooling . . . 115
5.4.3 Optical Qubit Coherent Dynamics . . . 117
5.4.4 Sideband Cooling . . . 118
5.4.5 Ion Heating Rate . . . 119
5.5 Radiofrequency Spectroscopy . . . 121
5.5.1 Spin Qubit Preparation and Manipulation . . . 122
5.5.2 Spin Qubit Resonance . . . 123
5.6 Ion as Magnetic Field Probe . . . 126
5.6.1 Measuring the Magnetic Field Strength via Laser Spectroscopy . . . 127
5.6.2 Measuring the Magnetic Field Strength via Radiofrequency Spectroscopy . . . 128
5.7 Ion Instability under Non-linear Fields and Pulsed Static Currents 132
5.7.1 Experimental Sequence . . . 132

Conclusions 135

A Surface Quality Characterization 139

B Fabrication Processes for Planar Traps **143**
B.1 In-plane Electrodes 143
B.2 Very Large Scale Integration 144
B.3 Buried Multilayered Electrodes 145

C Calculation of the Hesse Matrix **147**

D Publications **149**
D.1 Related to this work 149
D.2 Previous work 149
D.3 Posters 149

Acknowledgements **151**

Abstract

In modern ion quantum technology the fields of quantum information and microfabrication are being merged to build devices in which ions are confined near trap electrodes at the micrometer scale –with novel functionality where ion qubits enabling quantum devices. A long term goal in this field is to build a trapped-ion based quantum computer. Today's quest, however, requires a progressive ion trap development in which materials selection, trap's design and fabrication methods play a fundamental role. Here, we report on two fabrication methods for planar traps. We present the characterization of a planar trap with integrated electromagnets which is designed to coherently manipulate $^{40}Ca^{+}$ ions' internal states via magnetic field gradients and long-wavelength radiation. By implementing radiofrequency spectroscopy, in the presence of static magnetic fields, and by moving a single $^{40}Ca^{+}$ ion about 600 µm along the trap axis we measured the total static magnetic field which yields a gradient of $1.11 \pm 0.18\,\mathrm{T\,m^{-1}\,A^{-1}}$ in this direction. We anticipate in this trap magnetic gradients of $10\,\mathrm{T\,m^{-1}\,A^{-1}}$ perpendicular to the trap axis. A second generation of this trap, a novel hybrid planar trap, is built by combining the capabilities of thick film technology and laser-induced glass micromachining to structure independent current-carrying wires beneath an ion trap. Into the vacuum chamber, we also incorporate surface cleaning tools such as ion-beam bombardment to diminish possible adsorbed contaminants which may reflect in excessive ion heating rates. Based on numerical simulations, we predict that the wires underneath the ion trap, although far from trap center, will be capable of producing high magnetic field gradients of about $3\,\mathrm{T\,m^{-1}\,A^{-1}}$. Already such robust fields will allow to investigate strong (ν_{ss} =30 kHz) spin-spin interactions in $^{40}Ca^{+}$ ion crystals in planar traps. Those interactions are useful to employ linear ion crystals for quantum simulation of spin-spin interactions to mimic solid state Hamiltonians.

Zusammenfassung

In der modernen Ionen-Quantentechnologie vereinen sich die Felder der Quanteninformation und Mikrofabrikation, um Fallen zu entwickeln, in denen Ionen in der Nähe von Fallenelektroden auf einer Skala von wenigen Dutzend Mikrometern gefangen werden – und mit neuartiger Funktionalität mit der Ionen-Qubits gezielt manipuliert werden können. Ein langfristiges Ziel in diesem Bereich ist der Aufbau eines Ionenfallen-basierten Quantenrechner. Die heutigen Herausforderungen erfordern jedoch eine progressive Ionenfallen-Entwicklung, in der die Auswahl der Materialien, das Fallen-Design und das Herstellungsverfahren eine fundamentale Rolle spielen. Hier berichten wir über zwei Fertigungsprozessen zusammen mit dem Betrieb und Charakterisierung einer planaren Falle mit integrierten Elektromagneten. Die Falle ist so konzipiert, dass $^{40}Ca^{+}$ Ionen kohärent über einen Magnetfeld-Gradienten manipuliert werden können. Wir demonstrieren Radiofrequenz-Spektroskopie an einem einzigen $^{40}Ca^{+}$ Ion in Gegenwart von statischen Magnetfeldern. Zusätzlich wurde das statische Magnetfeld durch Transport eines Ions über 600 µm entlang der Fallenachse gemessen, so dass wir ein Gradient der absoluten Magnetfeld von $1.11 \pm 0.18\,\mathrm{T\,m^{-1}\,A^{-1}}$ in diese Richtung entnehmen konnten. In obiger Falle erwarten wir magnetischen Gradienten von $10\,\mathrm{T\,m^{-1}\,A^{-1}}$ senkrecht zur Fallenachse. Eine zweite Generation der Falle wurde mit Dickschicht-Technologie und Laser-induzierter Glasmikrobearbeitung fabriziert. In die Vakuumkammer wurde zusästlich eine Vorrichtung zum Beschuss der Fallenoberfläche durch einen Ionenstrahl integriert um eine in situ Reinigung der Fallenoberfläche von Verunreinigungen zu ermöglichen. Basierend auf numerischen Simulationen erwarten wir, dass die drei unabhängigen Leitungen unterhalb der Falle am Fangort hohe Magnetfeld-Gradienten von etwa $3\,\mathrm{T\,m^{-1}\,A^{-1}}$ erzeugen werden. Schon Gradienten dieser Großenordnung können verwendet um starke (ν_{ss} =30 kHz) Spin-Spin-Wechselwirkungen in $^{40}Ca^{+}$ Ionen Kristalle zu induzieren. Lineare Ionenkristalle sind daher nützlich um mittels solcher hohen Magnet-Gradienten Modelle von Quantenmagnetismus in einem Festkörper zu simulieren.

List of Figures

1 Laser and laser-less qubit manipulation schemes xxi
2 From linear to planar Paul traps xxiii

1.1 Relevant energy levels and transitions in the $^{40}Ca^{+}$ ion 2
1.2 Ideal geometry in the House model 7
1.3 Quantized ladder scheme for sideband cooling 16
1.4 Calculation of axial spin-spin coupling in a ten ion crystal 18
1.5 Calculation of radial spin-spin coupling in a ten ion crystal . . . 20

2.1 Planar trap design with on-chip current-carrying wires 23
2.2 Idealized trap geometry with two integrated electromagnets . . . 24
2.3 Trapping parameters of planar traps 25
2.4 Analytical determination of static voltage configuration 26
2.5 Meshing prior application of the boundary element method . . . 27
2.6 Numerical determination of the pseudo potential 28
2.7 Numerical calculation of the axial potential 30
2.8 Magnetic field gradients of electromagnets 32
2.9 Model of N-rectangular electrodes to simulate current-carrying wires 34
2.10 Voltage distribution over the surface of an electromagnet 36
2.11 Contour plots of stray potential after sending static currents . . 38
2.12 Trapping potentials on Mainz-Translume trap 42
2.13 Ion-trap chip on thick film wires 45
2.14 Design layout of Trap IV with tapered RF geometry 47
2.15 Axial potentials of planar trap with tapered RF rails 48
2.16 Radial confinement of trap with tapered RF rails 49

3.1 Photomask of microfabricated traps 54
3.2 Chemical-mechanical wafer cleaning 55
3.3 Thermal evaporation 62
3.4 Electroplating deposition 64
3.5 Isotropic and anisotropic etching 66
3.6 Fabrication layout including thermal evaporation and lift-off . . 69

3.7 Fabrication layout including electroplating . . . 70
3.8 Fabrication output from electroplated and evaporated Traps. . . 71
3.9 Glass-micromachining and thick film technology . . . 73
3.10 Micromachined ion chip and thick printed wires . . . 75

4.1 Vacuum system setup . . . 78
4.2 Packaging and RF filtering of Trap I . . . 79
4.3 Trap montage into the vacuum vessel . . . 82
4.4 Heating test of SMD elements . . . 84
4.5 Mass spectrometry during chamber bakeout . . . 86
4.6 Vacuum chamber scheme to include Ar^+ cleaning and water cooling systems . . . 87
4.7 Radiofrequency power supply . . . 89
4.8 Laser system at 397 nm . . . 92
4.9 Laser systems at 854 nm and 866 nm . . . 94
4.10 Laser system at 729 nm . . . 95
4.11 Simplified picture of laser alignment and beam guiding. . . . 96
4.12 Imaging optics for Ion fluorescence detection . . . 98
4.13 Ion flourescence histogram of a single ion . . . 100
4.14 Functional diagram block of experiment control . . . 101

5.1 Current failure test for static currents sent through micro wires . 104
5.2 Resistance increase while applying static pulsed currents to inner wires . . . 106
5.3 Fluorescence signal of trapped $^{40}Ca^+$ ion crystals . . . 109
5.4 Fluorescence detection of an ion chain for thirty eight $^{40}Ca^+$ ions 111
5.5 Electronic excitation of the secular modes of a single trapped $^{40}Ca^+$ ions . . . 112
5.6 Pulsed laser spectroscopy scheme . . . 114
5.7 Resolved sideband cooling experiments . . . 116
5.8 Rabi oscillations from the ground state $S_{1/2}$ to the $D_{5/2}$ state . . . 117
5.9 Phonon number state after sideband cooling protocol . . . 118
5.10 Heating rate of planar trap with integrated electromagnets . . . 119
5.11 Spin qubit implementation on the Zeeman sublevels . . . 121
5.12 Radiofrequency spectroscopy sequence . . . 122
5.13 Spin qubit coherent excitation pulse . . . 123
5.14 Carrier transition on the Zeeman sublevels . . . 125

5.15 Schemes for measuring the magnetic field of current-carrying wires 126
5.16 Magnetic field of wire W_1: current dependence 127
5.17 Radiofrequency resonance of the Zeeman sub levels 129
5.18 Magnetic field of wire W_1: ion position dependence 130
5.19 Stability diagram and non linear terms of a single $^{40}Ca^{+}$ ion . . . 133

5.20 Buried Interconnects based on Damascene process 136

A.1 Optical micrographs of different planar traps 140
A.2 Scanning Electron Micrographs of Grain Size in Trap I 141
A.3 Atomic Force Micrographs of Trap I 142

B.1 Fabrication Processes and Geometry of Current Planar Traps . . 145

Introduction

In the early 19th century, at the heart of the industrial revolution, a typical flag of progress would carry a lemma –*the larger the better*–. In modern times, in contrast, at the heart of the miniaturization revolution it may say –*the smaller the more efficient*–. This visionary idea was already exposed by Feynman in his famous talk given at Caltech in 1959[1]. He succinctly described the importance of manipulating minute objects to store an unprecedented amount of data.

Since the advent of the first microprocessor[2], in 1971, microfabrication has been consolidated as the most powerful tool to enhance computational power of current computing devices by increasing, twice every two years, the number of transistors per unit area in modern processors[2]. Although, modern transistors have already achieved the nanometer scale, there are no roadblocks in sight for their further miniaturization. Even more, it is expected that by the year 2020 miniaturized devices will already meet the single atom regime[2]. At the atomic scale, classical information processing will be substituted by quantum information processing or simply quantum technologies –information processing by well-controlled quantum systems.

Aim of research is to investigate information processing in this regime, and among the most promising quantum systems to host future quantum technologies stand trapped ions. In this system, additional well-established technologies such as laser cooling and laser spectroscopy permit a high degree of control of the ion's energy levels. Aside, in the quest of building quantum devices whit entanglement-enabled and nanoscale spatial resolution emerge superconducting quantum interference devices (SQUID) and nitrogen-vacancy (N-V) centers as magnetic field sensors[3].

Quantum Computing and Quantum Simulation.– Since their first conception in 1980, quantum technologies have been the central subject of extensive theoretical and experimental investigation. Their major goal, is the practical realization of quantum computers[4] and quantum simulators[5] in which intractable physical problems can be tackled more efficient than in their classical analogues. For solving intractable problems an exponential amount of computational resources are demanded, whereas solving tractable problems requires

polynomial amounts of resources[6]. In general, as remarked by Feynman in 1982, the task of simulating a large quantum system using a classical computer is an intractable problem[5]. He conjectured correctly as demonstrated by Lloyd, that there is a type of universal quantum computer able to simulate an arbitrary quantum system whose dynamics is governed by local interactions[6]. Quantum computers not only offer the possibility of simulating other quantum systems but also to solving other classically intractable problems such as factoring large numbers[7]. In contrast to a classical computer, where information is collected on either charged or uncharged capacitors, information in a quantum computer is stored in a basic unit of quantum information, a quantum bit or simply called qubit. It can be implemented with a two-level system, such as a ground state $|g\rangle$ and an excited state $|e\rangle$ of an atom. Moreover, possible quantum systems that may host qubits are: atomic ion (energy levels), electrons (spins), photons (polarization) and Josephson junctions (phase, charge or flux).

Trapped-Ion Quantum Computer.– Among the most promising candidates for implementing quantum technologies are cold strings of atomic ions confined in radiofrequency (Paul) traps[8,9]. In a trapped-ion quantum computer, as proposed by Cirac and Zoller[10] in 1995, information is stored in two internal energy levels of atomic ions. Qubit manipulation is performed by laser fields and a collective vibrational mode serves as a bus for information transfer mediated to internal degrees of freedom by lasers and the Coulomb interaction (Figure 1a). Most of the requirements for quantum computation[11] have been established in this system, such as efficient quantum state preparation[12–14], qubit manipulation[14–17] and read-out[14,18,19]. In a large ions' string, however, qubit manipulation is limited by the repulsive action of the Coulomb interaction which reduces the inter-ion spacing as the number of trapped ions increases. One way to surpass this challenge suggests the use of a scalable (addressing) architecture, where ions are held on individual microtraps[20] or on traps with independent zones to split (merge) crystal ions within storing (processing) regions by segmented control electrodes[21]. Another alternative approach relies on adding an inhomogeneous magnetic field to lift the degeneracy of hyperfine or Zeeman ground states. Then each qubit may be individually resolved by radiofrequency[22] or microwaves[23] radiation instead of laser light. This scheme has the advantage of using well-developed NMR techniques.

Trapped-Ion Quantum Simulator for Many-Body Physics.– Trapped-ion systems are also an excellent platform to host quantum simulations of many-body physics[24–27]. As first proposed by Porras and Cirac[24] they constitute an ideal system to investigate effective spin systems. In their original approach, laser mediated optical dipole forces induced spin dependent forces generating effective spin-spin interactions. In 2008, a proof of principle experiment demonstrated the adiabatic evolution from a paramagnetic into a ferromagnetic order of a two spin system was demonstrated[28]. The extension into nearest- and next-nearest-neighbors interactions for three spins[29] and up to nine spins[30] permit to study magnetic ordering and spin frustration phenomena. Recently, experiments investigating frustrated anti-ferromagnetic interactions with up to N=16 spins[31] and the quantum dynamics[32,33] of entanglement in a many-body system place trapped-ions as benchmark platform for large-scale quantum simulations. Another possibility to design spin-spin interactions, as proposed by Wunderlich[34], consists in applying a strong static magnetic gradient to couple qubit internal states and long-wavelength radiation[35].

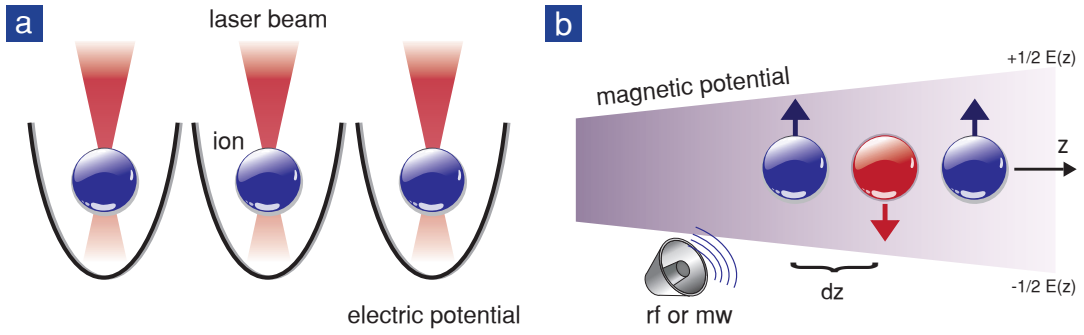


Figure 1 Schemes for qubit manipulation. a) Cirac and Zoller[10,20] proposal for optical qubit manipulation: each ion confined by electric potentials in an individual trap or an array of microtraps is addressed by a tightly focused laser beam[36] to couple its internal degrees of freedom to a collective vibrational mode. b) Wunderlich and Mintert[35] laser-less qubit manipulation: individual qubit addressing is subjected to strong magnetic field gradients ($10–100\,\mathrm{T\,m^{-1}}$) along the ion chain direction (z) which generates a differential Zeeman or Hyperfine energy shifts such that each qubit can be resolved in frequency space by either radiofrequency or microwave radiation.

In an inhomogeneous magnetic field, ions via their magnetic dipole moment experience Stern-Gerlach forces such that the ions are displaced from

their equilibrium positions in the ion crystal, thus, leading to a mutual effective spin-spin interaction. Single ion addressing using this scheme (Figure 1b) with static[22,37,38] and oscillating[23,39] magnetic fields have been recently demonstrated. First experiments of a magnetically J-type coupling of a three-spin pseudomolecule[40] and spin-spin interactions and entanglement of ion-duet trapped in a double well potential[41] also performed by entangling operations which are entirely tuned by laser-less qubit manipulation approach[42] have been demonstrated. As the interactions are generated without laser light fields, but only by magnetic gradients, scaling of the simulation to more particles might be facilitated[43].

Quantum Computing and Quantum Simulation in Planar Traps.– Extending entanglement to lager systems ($N > 30$) impose new challenges for both optical and microwave qubit manipulation approaches. As the number of ions (N) in a Paul trap increases the distance between l_z ions scales as $\omega_z^{-2/3} N^{-0.56}$ for a given ω_z axial frequency[44]. Thus to keep qubit optical addressing sufficiently efficient in a long chain it will require either the use of anharmonic potentials[45] to keep a constant ion-spacing or to transport the qubit in a fast-controllable[46,47] way within different processing and storing zones. In contrast, microwave addressing will demand strong magnetic field gradients of about $10\,\mathrm{T\,m^{-1}}$ to $100\,\mathrm{T\,m^{-1}}$ at the ion's position. Such demanding gradients are under reach in current modern Paul traps or simply planar traps. In such miniature traps, trapped ions are placed in close proximity to electric and magnetic field sources.

Microfabricated ion traps[53], with a characteristic length ($d \sim 100\,\mu\mathrm{m}$) two orders of magnitude smaller than micro-machined traps ($d \sim 1\,\mathrm{mm}$), create more robust electric and magnetic fields at the ion's position. In particular, these planar traps (Figure 2c) open a novel route towards quantum technologies based on trapped ions. Their architecture can not only be scaled down but also include on-chip elements compatible to lithographic processes. The integration of micro-optics elements enhancing ion fluorescence detection[54,55], in-substrate capacitors filtering pick-up driving rf-fields[56] or ''X'' and ''Y'' junctions[57] serving as reliable joints for computing network architectures are among proved applications. What is more, development of planar traps including integrated radiofrequency or microwave circuitry is a vivid –and rapidly evolving– field with tremendous implications in quantum technologies[37–39,56,58,59].

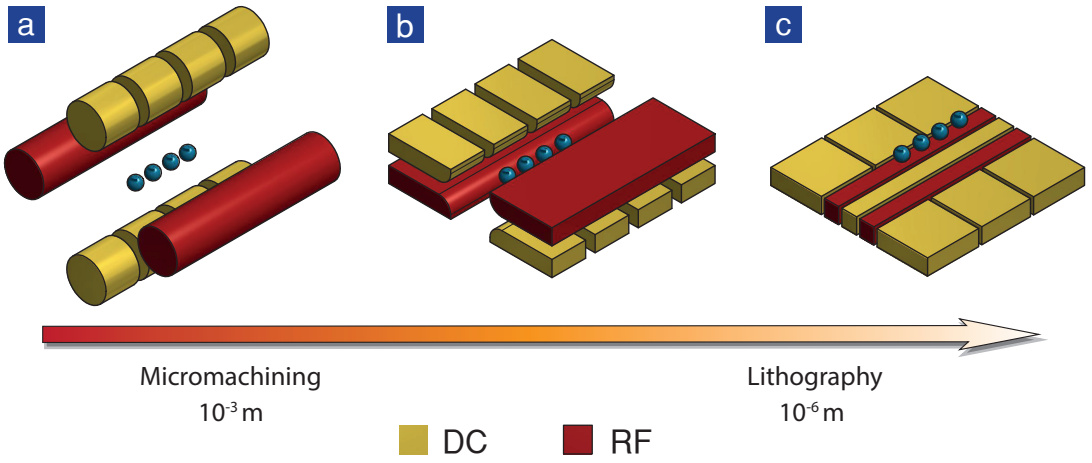


Figure 2 From linear to planar Paul traps. A modification from linear (a) into planar (c) geometry reduces the characteristic trap size (d) from 10^{-3} m to 10^{-6} m. Ions are confined axially (along trap axis) and radially (perperdicular to trap axis) by static (DC) and oscillating radiofrequency (RF) potentials respectively. a) micromachined linear trap with segmented control electrodes[48]. b) microstructured linear ion trap with segmented control electrodes. It can be fabricated by laser micromachining[49,50] or by semiconductor microprocessing[51]. c) planar configuration with all confining electrodes lying on a single plane[52] can provide short ion-to-surface distance d~30 µm[39].

Ion confining in Paul traps is achieved by means of quadrupole fields[8], or at least assumed to be so. This condition may be no longer valid for the case of planar traps where due to the flat electrode configuration the electric field lines are forced to bend on a single outermost ground plane leading to higher order multipoles of the trapping potential the farther from the trap center[60]. As far as a trapped ion remains at the very center of the trap it will interact minimally or not at all with such high order multipoles. In contrast, a perturbed or uncompensated trapped ion will sense higher order contributions of the potentials when its excursion becomes comparable to the trap size leading to mode frequency shifts and ion instabilities.

Another side effect, when placing trapped ions in close vicinity to current-carrying elements and/or near trap electrodes results in an increase in motional ion heating rates. This mean phonon number gained after certain time depends strongly on the trap characteristic length (d^{-4})[61,62] but its main source remains still unclear[63]. Important to underline is the recent demonstration of the reduction of ion heating rates by two orders of magnitude at cryogenic temperatures[64,65] or after in-situ surface cleaning treatments (Ar^+)[66,67]. In

the latter experiments, the ion is used as an extremely sensitive noise sensor of the fast oscillating stray electric field produced by impurities adsorbed on the metal surfaces prior and after surface cleaning. At those low levels of ion heating motion near to thermal Johnson noise limit, which increases as the square power of the characteristic trap size (d^{-2}), similarly as the magnetic field gradient, one will be able to apply quantum error corrections.

Thesis Outline.– In this thesis I report on the development and characterization of planar ion traps towards performing quantum simulations and reducing ion heating rates. Planar traps with integrated electromagnets (Trap I and Trap II), a hybrid trap (Trap III) and a tapered trap (Trap IV) are described. Trap I is loaded with ions and characterized towards performing quantum simulations of spin-spin interactions. This design includes on-chip current carrying wires to generate static magnetic field gradients[34] together with a scalable architecture[21]. Fabrication of a Trap IV, is accomplished by combining the capabilities of thick film and laser induced glass-etching. High current-density wires are positioned as closed as (200 µm) to ion's position. Trap's vacuum setup is upgraded to include an (Ar^+) ion bombardment cleaning to reduce ion heating rates. Excessive Joule heating produced by operating the printed wires at a maximal current (20 A) will be dissipated by an in-vacuum water cooling system. In this setup, strong magnetic field gradients ($3\,\mathrm{T\,m^{-1}\,A^{-1}}$) will allow the investigation of spin-spin interactions of about 30 kHz. Finally, a trap design (Trap IV) which will allow the systematic study of heating rates as a function of the trap characteristic size (d) from 165–40 µm is presented.

This thesis is organized as follows. In **Chapter 1** the fundamentals of ion trapping, laser-ion interactions and quantum simulations are briefly described. In **Chapter 2**, analytical and numerical methods are detailed for designing the traps presented here. The discussion particularly focuses on Trap I with integrated electromagnets, followed shortly for describing the characteristics of Trap III and Trap IV. In **Chapter 3** microfabrication processes developed for building the traps given in this work are detailed. Microfabrication techniques required for this work are mainly divided in three categories: evaporation, electroplating and etching. The trap apparatus such as vacuum, electronics and laser systems for successful ion trapping and state manipulation of $^{40}Ca^+$ ions are described in **Chapter 4**. The implementation of laser spectroscopy, sideband cooling and radiofrequency spectroscopy tools necessary for ion trap characterization: ion heating rates, laser-less qubit manip-

ulation and magnetic field gradient measurements on a single $^{40}Ca^{+}$ ion are detailed in **Chapter 5**. Finally, I propose a new fabrication layout to build multi-layer planar traps based on a Damascene process. Such traps including vias and interconnects, within realm of state-of-the-art fabrication processing, will reduce stray (induced electric and magnetic) fields which currently limit the state fidelity of multi-ion gates in planar traps assisted by magnetic field gradients.

1 Basic Tools in Planar Traps

Today's backbone of trapped-ion based quantum computation and quantum simulation is a Paul trap. In such a device, ion confinement arises from the combination of oscillatory and static electric fields. Modern Paul traps or planar traps – whereby all trapping electrodes lay on a single plane – promise the possibility to scale current quantum technologies to a larger number of qubits. In addition, including on-chip elements such as microstructured wires opens the possibility for the creation of stronger magnetic and electric fields.

In this chapter, I first describe two types of qubits implemented on $^{40}Ca^{+}$ ions. Then I move on reviewing the confinement of charged particles on conventional and planar Paul traps. The fundamental laser-ion interactions such as Doppler and sideband cooling are covered in a following section. In a last part I will discuss the potential investigation of quantum simulations of strong spin-spin interactions in planar traps with our approach.

. . . . . .

1.1 $^{40}Ca^{+}$ Ion as Qubit

With a single valence electron, $^{40}Ca^{+}$ ion belongs to the family of alkaline metals. Manipulation of its internal electronic states have shown their potential to effectively implement quantum computation [68] or quantum simulation [25] tasks. The lowest five energy levels of $^{40}Ca^{+}$ are shown in Figure 1.1. The electromagnetic radiation required to manipulate its main optical transitions is provided by diode laser light as explained in Sec. 4.3. In addition the Zeeman sublevels can be manipulated by oscillating (radiofrequency) magnetic fields as it will be explained in Sec. 5.5.

1.1.1 Optical Qubit

Two optical transitions defined between a ground state $S_{1/2}$ or $|0\rangle$ and a metastable state $D_{5/2}$ or $|1\rangle$ are used to implement an *optical qubit*. The quadrupole transition at 729 nm is used for shelving the population from the Zemman levels $S_{1/2}$ and the metastable states from $D_{5/2}$.

1.1.2 Spin Qubit

A second qubit, termed *spin qubit*, may be implemented between two Zeeman sublevels of the ground state $S_{1/2}$ named $|m = -1/2\rangle$ or $|\downarrow\rangle$ and $|m = +1/2\rangle$ or $|\uparrow\rangle$. Its two possible states are split by 2.82 MHz/G and may be coherently manipulated by radiofrequency (RF) radiation produced by an oscillating current supplied through an inner wire W_2.

Both optical and spin qubits may be initialized by either right (σ^+) or left (σ^-) circularly polarized light.

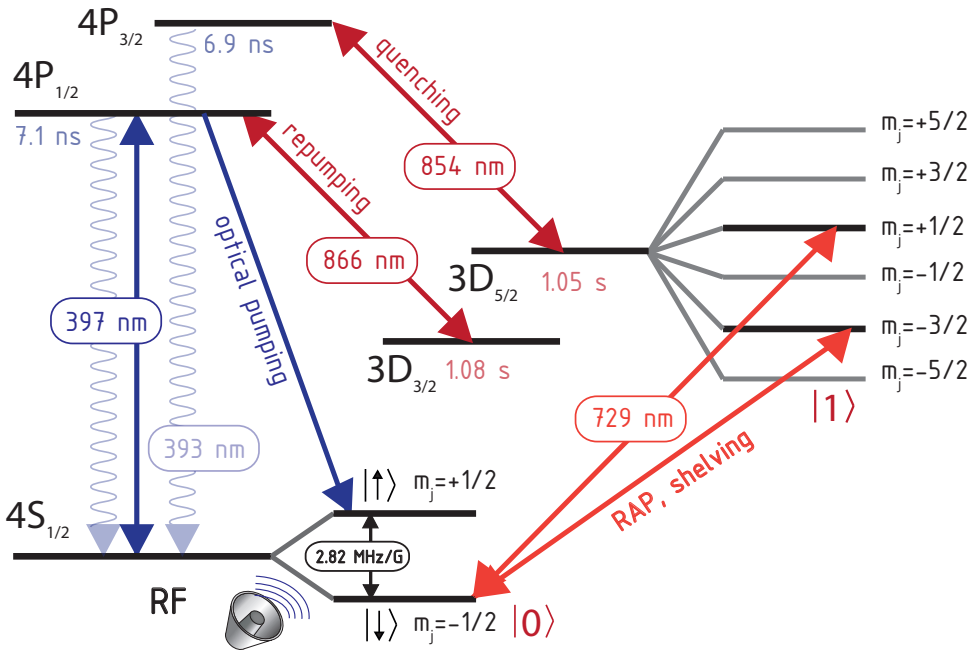


Figure 1.1 energy diagram of $^{40}Ca^+$ ion. The dipole transition from the $S_{1/2}$ to $P_{1/2}$ serves for optical pumping, Doppler cooling and ion flourescence detection. The electron at $P_{1/2}$ rapidly decaying into the metastable level $D_{3/2}$ is repumped at 866 nm to keep efficient Doppler cooling. A quenching pulse at 854 nm recycles the population from the metastable state $D_{5/2}$ after electron shelving to the ground state $S_{1/2}$. The quadrupole transition at 729 nm is used for shelving the population from the Zeeman sublevels into the metastable state $D_{5/2}$. The ground Zeeman states $S_{1/2}$ are lifted 2.82 MHz/G and coherently manipulated by radiofrequency (rf) magnetic fields.

. . . . . .

1.2 Ion Confinement in Paul Traps

In general, the confinement of charged particles by only static electric potentials is not allow by the laws of physics[69]. Therefore in Paul traps (term

coined after its inventor[a]) the combination of both static and dynamic potentials permits to trap charged atoms or ions[70]. The typical oscillatory frequencies used are in the range of 1 to 200 MHz and the static potentials are in the range of 1 to 1000 V. Depending on the electrode size, ion mass specie and the magnitude of both static and oscillatory potentials the ion trapping stability is achieved.

In a Pault trap an ion held by an oscillatory potential undergoes a restoring force towards the minimum of the potential and is proportional to the electric field. The total potential for an ion with mass m and charge e is described by

$$\Phi(r,z,t) = \Phi_{dc}(r,z) + \Phi_{rf}(r,z,t) \tag{1.1}$$

where $\Phi_{dc}(r,z)$ and $\Phi_{rf}(r,z,t)$ are the static and dynamic potentials, respectively. Given the Laplace condition $\nabla^2\Phi = 0$ we can obtain the type of geometry for a the trap. However, the solution of the Laplace equation is not a sufficient condition to guarantee stable ion trapping as we will see below.

We expand Eq. 1.1 to second order around the equilibrium position. Additionally, by rewriting it in terms of classical ion motion with charge e and mass m it leads to

$$m\frac{d^2u_i}{dt^2} + e\sum_j \left[\left(\frac{\partial^2\Phi_{\mathrm{dc}}}{\partial u_i \partial u_j}\right) + \left(\frac{\partial^2\Phi_{\mathrm{rf}}}{\partial u_i \partial u_j}\right)\cos(\Omega t)\right] u_j = 0, \tag{1.2}$$

where Ω is the angular drive frequency of the rf potential and $u_1 = x$, $u_2 = y$ and $u_3 = z$ are the directions of the coordinate system. By rearranging Eq. 1.2 into its canonical form and rewriting terms we obtain the generalized multidimensional Mathieu equation of the ion motion as[71]

$$\frac{d^2\mathbf{u}}{d\tau^2} + [A + 2Q\cos(2\tau)]\,\mathbf{u} = 0, \tag{1.3}$$

here $\tau = \Omega t/2$, A the stiffness matrix and Q the excitation matrix with entries,

$$A_{ij} = \frac{4e}{m\Omega^2}\left(\frac{\partial^2\Phi_{dc}}{\partial u_i \partial u_j}\right), \quad Q_{ij} = \frac{2e}{m\Omega^2}\left(\frac{\partial^2\Phi_{rf}}{\partial u_i \partial u_j}\right), \tag{1.4}$$

determine the stability of an ion held in a Paul trap. The stability parameters from Eq. 1.4 are the multidimensional versions of the stability parameters a

[a] Wolfgang Paul, 1989 Nobel Prize

and q used commonly in ion trap literature[8,72]. In general if $[AQ-QA]=0$ the matrices are diagonal and the mode of ion motion are decoupled. However, if the modes of ion motion are not independent of each other the directions of the modes are not necessary aligned to the coordinate system. Additionally the micromotion terms may not necessarily be aligned to the modes of oscillation. We will come back to an uncoupled system later in Section 1.3.1. For the moment let us just make the common assumption the matrices A and Q commute and all mode directions can be treated independent of each other.

In this case we rewrite Eq. 1.3 along the x-axis and it is reduced to

$$\frac{d^2x}{d\tau^2}+[a_x+2q_x\cos(2\tau)]x=0 \tag{1.5}$$

where $\tau=\frac{\Omega t}{2}$ and $a_x=A_{xx}$ and $q_x=Q_{xx}$ are the stability parameters along x-direction. The stable solutions of Eq. 1.5 can generally be expressed in the form of a Fourier series[72]

$$x(\tau)=C_x e^{i\beta_x\tau}\sum_{n=-\infty}^{+\infty}c_{2n}e^{i2n\tau}+D_x e^{-i\beta_x\tau}\sum_{n=-\infty}^{+\infty}c_{2n}e^{-i2n\tau}, \tag{1.6}$$

where C_x and D_x are constants depending on the initial conditions and β_x and the coefficients c_{2n} are functions of (a_x,q_x). By substituting Eq. 1.6 into Eq. 1.5 and rearranging terms we obtain a recursion relation that connects the coefficients c_{2n} to the stability parameters a_x and q_x as

$$\begin{aligned} &c_{2n+2}-\alpha_{2n}c_{2n}+c_{2n-2}=0,\\ &\alpha_{2n}=\left[a_x-(2n+\beta_x)^2\right]/q_x, \end{aligned} \tag{1.7}$$

the recursive use of Eq. 1.7 yields to fraction expressions for the coefficients c_{2n}

$$\frac{c_{2n,x}}{c_{2n\mp2,x}}=-\frac{q_x}{(2n+\beta_x)^2-a_x-\frac{q_x^2}{(2n\pm2+\beta_x)^2-a_x-\ldots}} \tag{1.8}$$

which constitute the amplitudes of the Fourier components of the ion motion. The term β^2 can be also expressed in term of a_x and q_x by[8]

$$\beta_x^2=a_x-q_x\left(\frac{1}{\alpha_0-\frac{1}{\alpha_2-\frac{1}{\ldots}}}+\frac{1}{\alpha_0-\frac{1}{\alpha_{-2}-\frac{1}{\ldots}}}\right) \tag{1.9}$$

A map of β_i on the plane (a_i,q_i) give the regions of stability for the ion motion. The typical ion traps operate in the lowest order, say $0<\beta_i<1$ where $a_i,q_i\approx0$ and $i\in x,y,z$.

1.2.1 Adiabatic Approximation

In ion trapping a useful condition to described the ion motion as an harmonic oscillator is the adiabatic approximation by considering a time-averaged pseudopotential energy. This condition is called the adiabatic approximation, since the total kinetic energy remains constant as the particle moves through the high frequency electric field[72]. Moreover the time-varying field over the extension of the ion motion is considered as nearly constant since the the ion is confined under the action of an inhomogeneous electric field with high frequency, i. e. $\omega_j \ll \Omega$. By imposing this condition we can describe the time-averaged ion motion by an effective potential energy or pseudopotential

$$\Psi(x,y,z) = \frac{e^2}{4m\Omega^2}|\nabla\Phi_{rf}|^2 \tag{1.10}$$

Furthermore, Eq.1.10 is nothing else than the mean average kinetic energy under the action of the high frequency electric field. It is typical called the trap depth since it represents the maximal energy at which an ion can be contained in the trap.

Taken the lowest order in the stability plane of (a_i, q_i) the adiabatic condition is satisfied. In this case the ion trajectory $x(t)$ can be approximated if $|a_i|, q_i^2 \ll 1$ by also assuming $c_{\pm 4,i} \approx 0$ and $C_i = D_i$. Both the the stability parameter β_i from Eq. 1.9 and the ion trajectory in all directions can be approximated to[8]

$$\beta_i \approx \sqrt{a_i + \frac{q_i^2}{2}} \tag{1.11}$$

and

$$x_i(t) \approx \alpha_{0,i} C_i \cos\left(\beta_i \frac{\Omega}{2} t\right)\left[1 - \frac{q_i}{2}\cos(\Omega t)\right] \tag{1.12}$$

where $i = x, y, z$ for each oscillation direction. This condition permits to treat the ion motion as close as an harmonic oscillator which is of relevance when high precision measurements are performed. The adiabatic condition is only satisfied for $q_i < 0.45$. As we have seen the parameter q_i is a function of both oscillatory potential and trap dimensions and will be exemplified for different trap geometries and trapping conditions in Sec. 2.1.2.

For the traps and operating conditions used in this thesis, $a_i \approx 0, q_{x,y} = 0.1 - 0.2$, lead to ion stability inside the adiabatic condition as we will see in the next sections. The typical dynamics of a trapped ion in a planar trap is illustrated in section 2.1.2, where different sizes for a five-wire configuration are compared with typical operating parameters of our system.

. . . . . .

1.3 Simulation Tools of Planar Traps

The methods used to simulate the designs developed for this work are here described. The first step is to optimize a desired trap geometry. At first, an analytical model considering only rectangular electrodes, described in Sec. 1.3.1, provide the initial geometry. After microfabrication and during trap operation, powerful numerical simulations based on the boundary element method (BEM), as given in Sec. 2.1.2, permit to calculate the electric field contribution of the whole chip covering an 1 cm^2 area.

1.3.1 House Model

Analytical approximations are useful tools to spare considerable time during trap design. Already important trap characteristics such as trap depth, ion's position and ion motion may be extracted assuming the trap electrodes are describe by rectangular electrodes. For optimization purposes we approximate our design following the House model[71], in which the potential field produced by rectangular electrodes can be analytically described. Other powerful analytical approaches based on the Biot-Savart-like method[73–75], not treated here, may be also employed to design planar traps of arbitrary 2D geometry. Both House and Biot-Savart-like methods are equivalent to the each other when the trap electrodes have a rectangular shape. When both methods are compared to numerical simulations based on the boundary element methods their result lay within 97 % of accuracy.

In what follows the House model is detailed going along the lines of Ref. 71. Later we shall describe the electric field of the full chip geometry given by the boundary element method from Ref. 76. For the analytical model, the inner part of a planar trap design is composed of ideal rectangular electrodes as shown in Figure 1.2. All upper electrode surfaces are assumed to lay entirely on a zero plane ($y = 0$), and their extensions to go along the x and z directions.

In this case the trap axis goes along the z direction and the ion is trapped a distance y_0.

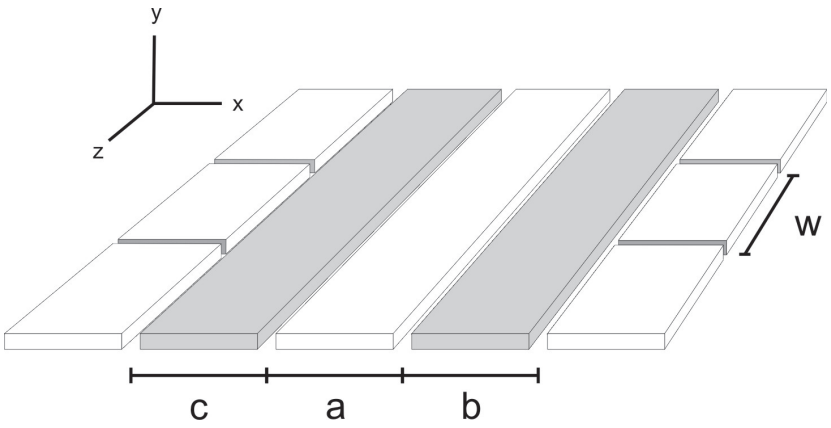


Figure 1.2 Ideal geometry of a planar trap assumed in the House model. Radiofrequency (RF) potentials applied on two electrodes (gray) of width b and c confine the ion at a distance y_0. An inner electrode of width a and a set of control electrodes (white) of width w and infinite length in the x axis place the trapped ion in a controlled way along the trap axis z. Electrode dimensions are considered from the center of each gap.

The inter-electrode spacing or electrode gap is supposed to be infinitely small and the voltages (V_i) applied to each individual electrode are defined by the potential $\Phi(x,0,z)$. Above the zero plane ($y > 0$) the potential Φ can be found by applying appropriate Dirichlet boundary conditions[77]. In addition to the condition that Φ must satisfied the Laplace equation ($\nabla^2\Phi$) it is required to be equal to the voltages applied to the electrodes on the zero plane ($y = 0$). Additionally, it must vanish far along the normal direction of the trap surface ($y \to \infty$) and it must also be finite parallel to the surface electrodes ($x \to \pm\infty$ and $z \to \pm\infty$).

For the case of a single electrode with opposite corners $(x_1, 0, z_1)$ and $(x_2, 0, z_2)$ set at the voltage V surrounded by a ground plane in $y = 0$

$$\Phi(x,0,z) = \begin{cases} V, & x_1 < x < x_2 \wedge z_1 < z < z_2, \\ 0, & \text{otherwise}, \end{cases} \tag{1.13}$$

the following solution can be obtained[a],

$$\begin{aligned}\Phi(x,y,z) = \frac{V}{\pi}\Bigg\{ &\arctan\left[\frac{(x_2-x)(z_2-z)}{y\sqrt{y^2+(x_2-x)^2+(z_2-z)^2}}\right] \\ &-\arctan\left[\frac{(x_1-x)(z_2-z)}{y\sqrt{y^2+(x_1-x)^2+(z_2-z)^2}}\right] \\ &-\arctan\left[\frac{(x_2-x)(z_1-z)}{y\sqrt{y^2+(x_2-x)^2+(z_1-z)^2}}\right] \\ &+\arctan\left[\frac{(x_1-x)(z_1-z)}{y\sqrt{y^2+(x_1-x)^2+(z_1-z)^2}}\right]\Bigg\}\end{aligned} \tag{1.14}$$

Equation 1.14 is general and can be applied to obtain the potential field produced by either RF or DC rectangular electrodes. Thus now the total potential field can be derived by first calculating the individual contribution of each single electrode and then summing up all together.

Analytical Potential Field in the Radial Plane.– A useful approximation can be made by assuming that the RF electrodes are infinitely long ($z_1 \to -\infty$ and $z_2 \to \infty$) directions. In this case Eq. 1.14 is reduced to

$$\Phi(x,y) = \frac{V}{\pi}\left[\arctan\left(\frac{x_2-x}{y}\right) - \arctan\left(\frac{x_1-x}{y}\right)\right] \tag{1.15}$$

this approximation is completely valid since the typical length of the RF electrodes is at least one order of magnitude longer than its width. If we now define the two RF electrodes (gray) shown in Figure 1.2 as one having edges at $x = -c$ and $x = 0$, whereas the second one having edges at $x = a$ and $x = a + b$ then the potential is set as

$$\Phi(x,0,t) = \begin{cases} V_{RF}\cos(\Omega t), & -c < x < 0, \\ V_{RF}\cos(\Omega t), & a < x < a+b, \\ 0, & \text{otherwise.} \end{cases} \tag{1.16}$$

[a] see reference for derivation [71]

where V_{RF} is the amplitude or peak voltage driven by the RF angular frequency Ω. The RF potential can be approximately described by

$$\Phi(x,y,t) = \frac{V_{RF}}{\pi}\left[\arctan\left(\frac{a+b-x}{y}\right) - \arctan\left(\frac{a-x}{y}\right)\right]\cos(\Omega t) \tag{1.17}$$

In general to find the ion position in the plane xy we have to obtain from Eq. 1.17 the local minimum of the absolute value of the electric field above the zero plane ($y = 0$). In our particular case, and from the symmetric electrode configuration shown in Figure 1.2, at this point (x_0, y_0) the ion is held above the surface trap and is given by

$$x_0 = \frac{a}{2};\;\; y_0 = \frac{\sqrt{2ab + a^2}}{2} \tag{1.18}$$

In general, for a non-symmetric configuration trap depth can be found as upper limit by evaluating numerically for the region above the ion's position at which the gradient of the pseudopotential vanishes. For the case of a symmetric configuration (Figure 1.2) the scape point (x_d, y_d) at which the ion leaves the trap can be analytically determined by

$$x_d = \frac{a}{2};\;\; y_d = \frac{\sqrt{2ab + a^2 + 2(a+b)\sqrt{2ab + a^2}}}{2} \tag{1.19}$$

at this point the pseudopotential (Eq. 1.10) is evaluated and the following expression for the trap depth is obtained

$$\psi_d = \frac{q^2 V_{RF}^2}{\pi^2 m \Omega^2}\left[\frac{b}{(a+b)^2 + (a+b)\sqrt{2ab + a^2}}\right]^2 \tag{1.20}$$

Analytical Determination of the Applied Static Voltages.– In the z direction the ion's position is control by segmented electrode pairs. For ion confining along the trap axis it is desirable to set the right combination of DC potentials such that a desired axial trap strength (A_{zz}) can be achieved. Ion stability dependents on the entries of the stability matrices (A, Q). In addition the absolute value of the electric field produced by the DC potentials at the ion's position (x_0, y_0, z_0) has to vanish otherwise an undesirable micromotion is observed. Therefore to find the right combination of DC potentials we have at least four constraints. Which can be summarized as three physical constrains (no force putting the ion outwards the trap center) and a user constraint (a

desired harmonic oscillator potential). To obtain the voltages to be applied in a set of DC electrodes we start by minimizing the sum of the squares of the set of voltages.

$$\text{minimize} \sum_i {V_i}^2 \tag{1.21}$$

We set three physical constraints for having no external electric force exerted at the ion's position,

$$\text{subject to} \quad \sum_i V_i \nabla \Phi_i = 0 \tag{1.22}$$

and a final user constraint requiring the desired harmonic oscillator frequency along the z direction,

$$\sum_i V_i \frac{\partial^2 \Phi_i}{\partial z^2} = \frac{m\Omega^2}{4q} A_{zz} \tag{1.23}$$

here V_i are the applied voltages and Φ_i the potential field of a unitary voltage. At least four independent DC electrodes are required to fullfil the constraints imposed above, but a larger set of electrodes produce a more robust potential. Finally, the method of Lagrangian multipliers can be applied to solve the system of linear equations to determine the unknowns (V_i).

The House model also probed to be useful for calculating induced electric fields while supplying current through inner integrated electromagnets W_1 and W_2 as it will be explained in Sec. 2.1.4.

1.3.2 Numerical Simulations

Numerical simulations are powerful tools to describe the electromagnetic field generated by the whole set of electrodes on a chip. Methods such as the finite element method (FEM), boundary element method (BEM) and the integral boundary method (IBM) are extensively used in this work. The use of each method is determined by the type of physical phenomena to be solved.

Finite Element Method.– The finite element method (FEM) is widely extended on various fields of science and technology such as applied physics, engineering, chemistry and biology. This method is a very powerful tool specially when complex geometries and inhomogeneous media sare involved. It

permits to solve complex problems such as mechanical stress, chemical reactions, electrodynamics and heat transfer in inhomogeneous media or even when more of these phenomena are coupled. The typical procedure starts with the discretization of the solution domain into arbitrary subdomains (elements). These elements can be consist of triangular or tetrahedral shapes in either 2D or 3D. The number of elements are defined by the user or by the physical problem to be solved and are the core of the solution. The ordinary differential equations are solved at each element and then interpolated to any arbitrary point on the space. Accurate results, however, are limited by the size of the domain discretization or meshing. For the type of electrostatic problem to be solved in ion traps, where we are typically interested on the fields around the trap center or ion position, the elements size have to be comparable to the average cold ion wavepacket displacement on the nanometer range. Therefore, if we are temp to use FEM to calculate the trapping field of the chip with high accuracy we will end up to setting a locally fine meshing around the trap center. Since we are also interested on the influence of electrodes at the edge of the chip but also limited by the computational power we have to set a coarser meshing outside the trap center. By doing that, note, we have lost information of the fields within the farthest electrode regions. Thus, increasing the meshing locally around the center does not improve the accuracy of our calculation.

Boundary Element Method.– To describe with high accuracy the trapping potentials produced by the entire chip geometry we use numerical simulations. For the accurate calculation of the trapping potentials we employ the boundary element method (BEM). A numerical toolbox (BEMSolver) developed in our group by Singer et. al.[76] reaches 99 % accuracy compared to experimental results of the electric field of a segmented ion trap[78]. The boundary element method (BEM) starts with the discretization of the domain solution into subdomains or elements. Indeed the solution is calculated at each knot of a user-defined cubic grid in space. In contrast to alternative methods, such as finite element (FEM), the boundary element method discretizes electrode surface instead of its whole volume. This has a direct consequence on reducing the problem into 2D dimensions for the case of 3D ion trap geometry. However, an inherent drawback of method is that the error solution scales proportional to the third power. To reduce the power scale and make the error dependence to scale linearly, Singer et. al.[76] have additionally implemented the fast multipole method (FMM) into the BEMSolver.

The application of the method to accurately calculate the fields produced by the whole chip geometry are given in Chapter 2. In what follows the numerical methods to obtain the set of applied voltages on each DC electrode segment is discussed.

Thikonov Regularization and Numerical Determination of Axial Potential.– The potential field generated by a set of control electrodes is calculated using the boundary element method discussed in Sec. 2.1.2. Each electrode pair or control segment is set at a unitary voltage (1 V) and the potential field calculated along a linear path grid of M points along the trap axis or RF minimum in the z-direction.

Then we store the potential of one individual electrode as a column matrix with M entries. Further calculation of the N' electrodes permit to construct the matrix A of N'×M dimensions, where N' is the number of individual electrodes and M the number of points where the potential is calculated. Experimentally we can set both sides of the DC segments at one common voltage. Thus the dimensions of A can be further diminished to N×M, where only N has been redefined as the number of DC electrode segments.

Once obtained the set of individual potentials produced by each segment we are also interested on getting the voltage configuration $\{V_j\}$ for confining the ion along the axial direction with a desired frequency (ω_z). In general this is an inverse ill-conditioned problem and can be tackled by following the methods developed by Huber et. al.[78]. We start (as for the data set depicted in Figure 2.7) with the matrix A calculated at points z_i along a linear grid on the trap axis. Then the total potential ($\Phi(z_i)$) can be defined by the superposition of segments contribution weighted by the appropriate voltage configuration

$$\Phi_i = \sum_{j=1}^{N} A_{ij} V_j, \quad i = 1,...,M \tag{1.24}$$

where N means the number of segments and M the number of grid points taken to calculate the potentials. Then the problem is reduced to obtain the inverse matrix (A^{-1}) and since M is larger than N it is an overdetermined or ill-conditioned problem in case of having singularities on the solution. Using a standard singular value decomposition (SVD) algorithm the matrix A can be decomposed into the product $A = VSW^T$ of unitary matrices $V(N \times N)$ and $W(M \times M)$, and the diagonal $S(N \times M)$ with entries ($s_k \geq 0$). Then we can write

the inverse matrix as $A^{-1} = WS^{-1}V^T$, where the unitary matrices are simply transposed and the entries of S^{-1} are given by $1/s_k$. To avoid singular values for small $s_k \approx 0$ we could simply cut off the diverging inverse values. However, a method which suppress the diverging values consists on a Thikonov regularization. The entries $1/s_k$ are substituted for a more stable expression $s'_k = \frac{s_k}{s_k^2+\alpha^2}$. In this case, for small values of the regularization parameter ($\alpha \ll s_k$) the $1/s_k$ behaviour of the entries of the matrix S is reproduced, whereas the diverging solutions are suppressed for large values ($\alpha \gg s_k$). An approximated solution is then given by[79]

$$\mathbf{u} = WS'V^T\Phi, \tag{1.25}$$

where $\Phi = \{\Phi(z_1),...,\Phi(z_M)\}^T$ and $\mathbf{u} = \{V_1,...,V_N\}^T$ are vectors, and S' being the regularized matrix with entries $s'_k = \frac{s_k}{s_k^2+\alpha^2}$. We are also interested on upgrading the voltage configuration from a previous trapped point z_{t-1} to a succesive transport position z_t along the RF minimum in a smooth manner. This can be achieved by addition of a second term on Eq. 1.25 leading to

$$\mathbf{u}' = WS'V^T\Phi + WDW^T\mathbf{u}_{t-1} \tag{1.26}$$

where $\mathbf{u}_{t-1}$ corresponds to any previous voltage configuration, set at the position z_{t-1} and $D(N\times N)$ being a diagonal matrix with entries $\eta_k = \frac{\alpha^2}{(s_k^2+\alpha^2)}$. In this case, the entries η_k tends towards 1 whereas the Thikonov truncation s'_k goes to vanishing voltages. This algorithm minimizes $\|A\mathbf{u}'-\Phi\|+\alpha\|\mathbf{u}'-\mathbf{u}_{t-1}\|^2$. The last penalty permits to set electrode voltages on the experimental range ($-10\,\mathrm{V} \leq V_i \leq 10\,\mathrm{V}$). That is done by multiplying each column of the matrix A by an appropriate weighting factor on each electrode such that $A'_{ij} = w_j A_{ij}$ for $0 < w_j < 1$. For electrodes having voltages u_j out of range the algorithm iteratively decreases w_j from an initial factor ($w_j = 1$) for all electrodes.

This algorithm is used to generate the potentials to transport the ion during the experiments presented in Sec. 5.6.2. In such potentials a constrained harmonic potential, $\Phi(z) = a(z-z_0)^2$, for $a = 0.3\,\mathrm{V\,mm^{-1}}$ results in a constant axial frequency of $\omega_z = 2\pi\cdot 300\,\mathrm{kHz}$.

. . . . . .

1.4 Basic Laser-Ion Interactions

In ion trap technology laser-matter interactions represents a key tool for state preparation and read-out of electronic states of trapped ions. Light-induced forces are used for cooling atomic objects[80,81] to reach low temperatures 1×10^{-3} K. On a basic picture, assuming a two-level system defined by a ground state $|g\rangle$ and an excited state $|e\rangle$, an atom interacts with a perturbing field $\tilde{V}(t)$. This accounts for the light-atom interaction[82]:

$$\tilde{V}(t) = e\mathbf{r} \cdot \mathbf{E}_0(t) \tag{1.27}$$

corresponding to a energy shift of the atomic dipole in the electric field $\mathbf{E}_0(t)$ of the light. The Hamiltonian operator of the system is given by

$$\tilde{H} = \tilde{H}_0 + \tilde{V}(t) \tag{1.28}$$

where a time-independent part $\tilde{H}_0$ describing the atom in the dark and perturbation term $\tilde{V}$ act on a wave function $\psi = c_g |g\rangle + c_e |e\rangle$ described by the wave function amplitudes c_g and c_e.

Laser beams have been used in this work for cooling and detecting single or multiple $^{40}Ca^{+}$ ions. For temperatures below the Doppler limit and close to ion's internal ground state a resolved sideband routine[83] has been implemented.

1.4.1 Doppler Laser Cooling

A typical routine for storing ions into the trap has to be followed every time the experiment is run. Ions are photoionized in a two step photoionization process at the trap center, see Sec. 4.3.2. Initially the Doppler laser is red detuned about 120 MHz while the other lasers are kept near resonance. Oven currents about 3.5 A guarantee ion loading rates of approximately one $^{40}Ca^{+}$ ion every ~30 s (if other parameters are led constant). Once an ion is loaded, the cooling laser is tuned back close to resonance at the half of the transition line-width, where Doppler cooling works more efficiently. In this case the minimal Doppler temperature T_d is defined as[83],

$$T_d = \frac{\hbar\Gamma}{2\, k_B} \tag{1.29}$$

where k_B is the Boltzmann constant and Γ corresponds to the laser line width. Since an excess of ion micromotion broadens the linewidth, in order to mantain an ion sufficiently cold within the trap energy typically a red detuned laser is required.

After efficient Doppler cooling the ion's internal and motional states are coupled into the Lamb-Dicke regime,

$$\eta^2 \bar{n} < 1, \quad \eta = k\sqrt{\frac{\hbar}{2m\omega}} \tag{1.30}$$

where k is the wavevector of the incident light. For a parallel beam with a wavelength at 729 nm and an oscillator frequency at $\omega_z = 2\pi \cdot 760\,\text{kHz}$ we have $\eta^2 \cdot 18 < 1$ (for $\eta \approx 0.11$), see Sec. 5.4.3.

1.4.2 Optical Qubit Coherent Dynamics

The probability of having the qubit in the excited state, or simply $|e\rangle$, assuming a pure two-level system is determined by[82]

$$|c_e(t)|^2 = \sin^2\left(\frac{\Omega_L t}{2}\right) \tag{1.31}$$

where $\Omega_L = |\frac{\kappa E0}{\hbar}|$ is the frequency at which the qubit oscillates between $|g\rangle$ and $|e\rangle$ proportional to the magnitude of laser electric field. For the analysis we define a pulse area θ equal to $\Omega_L t$ such that qubit manipulation may be done. In this case, inverting its state is achieved by applying a π pulse or a superposition state by $\pi/2$ pulse.

1.4.3 Resolved Sideband Cooling

The situation when the two-level system is coupled to a harmonic potential, and including the phonon thermal distribution, leads to an extension of Eq. 1.31. An scheme of a quantized harmonic ladder is given in Figure 1.3.

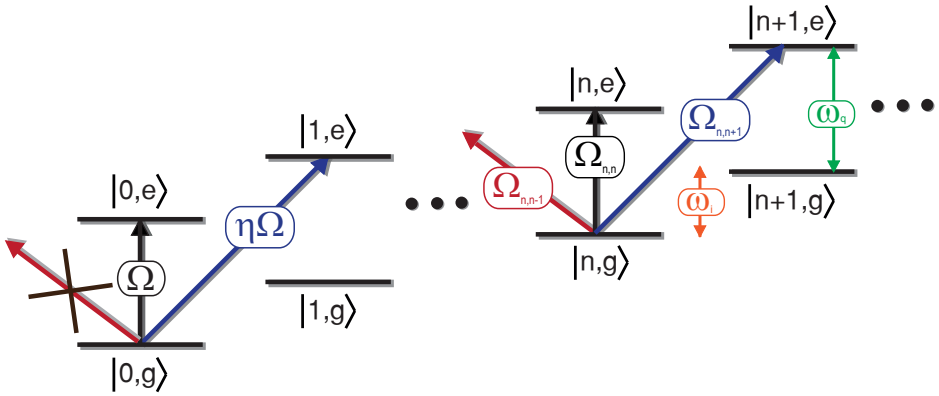


Figure 1.3 Quantized harmonic ladder of the sideband cooling scheme. When the ground state is reached $|0,g\rangle$, with high probability, the red sideband excitation vanishes. Note that at the ground state, the Lamb-Dicke paremeter (η) can be directly measured, by comparing the Rabi frequencies between the first blue sideband ($\eta\Omega$) and the carrier (Ω).

The probability of having the qubit in the $|e\rangle$ or $|D\rangle$ state is described by[83],

$$P_D(t) = |c_{e,n}(t)|^2 = \sum_n^{\infty} p_n \sin^2\left(\frac{\Omega_{n,n}t}{2}\right) \tag{1.32}$$

where the Rabi frequency for an arbitrary state of motion $\Omega_{n,n} = \Omega_0 L_n(\eta^2)$ is proportional to the Laguerre polynomial $L_n(\eta^2) = 1 - \eta^2 n + \frac{1}{4}\eta^4 n(n+1)$ and $p_n = x^n (n+1)^{-1}$.

After preparing the ion into the Lamb-Dicke regime we can manipulate its motional states by repetitively exciting in resonance the lower sideband (red) of its carrier transition until the motional ground state is reached with high probability.

Continuing from Eq. 1.32, writing the Rabi oscillation as an average phonon distribution following ref. 84, we can described the Rabi frequency in terms of the average phonon number $\bar{n}$ as:

$$\begin{aligned} \Omega_{n,n+1} &= \eta\sqrt{n+1}\,\Omega_C \\ \Omega_{n,n-1} &= \eta\sqrt{n}\,\Omega_C \end{aligned} \tag{1.33}$$

The basic diagram of the quantum mechanical representation for a two-level system and different phonon numbers is represented in Figure 1.3. In this case, after the last investigation with the preparation pulse only the blue sideband transitions ($\Omega_{n,n+1}$) should be presented since at ground state $|n,g\rangle$ the red sideband transition ($\Omega_{n,n-1}$) completely vanishes.

. . . . . .

1.5 Quantum Simulations in Planar Traps

In this section we describe how magnetic interactions may be simulated when using one-dimensional (1D) ion crystal chains in a planar ion trap. The topic of this section has been extensively discussed elsewhere[59,85] thus here only outlined. We start briefly reviewing the dynamics of a linear ion chain.

1.5.1 One-dimensional ion chains

First, we consider a linear chain of N cold ions. The position of the n^{th} ion, with equilibrium positions given in Cartesian coordinates i, is denoted by $x_{n,i}$. Then the potential energy of the ion chain is described by[44]:

$$V = m\omega_z^2\left(\sum_{n=1}^{N}\sum_{i=0}^{2}\frac{1}{2\alpha_i}x_{n,i}^2 + \frac{l^3}{2}\sum_{n=1}^{N}\sum_{\substack{m=1\\m\neq n}}^{N}\frac{1}{|\mathbf{x}_n-\mathbf{x}_m|}\right) \tag{1.34}$$

where $l^3 = q^2/4\pi\epsilon_0 m\omega_z^2$ denotes a scaling factor, m the mass of each ion, q the electron charge, ϵ_0 the permitivity of free space, ω trap frequency and $\alpha_i = \omega_z^2/\omega_i^2$ the anisotropy between the axial and radial confinement.

With an additional magnetic field gradient the Hamiltonian in one dimension for a linear string of N ions is given by[34]:

$$H = \frac{\hbar}{2}\sum_{n=1}^{N}\omega_n(\bar{\mathbf{x}}_n)\sigma_{z,n} + 2\pi\hbar\sum_{n=1}^{N}\nu_n a_n^\dagger a_n - \frac{\hbar}{2}\sum_{n<m}J_{n,m}\sigma_{z,n}\sigma_{z,m}. \tag{1.35}$$

The first term on the right hand side represents the sum of internal energies of N two level ions. The electric potential confinement leads to N vibrational eigenmodes with frequency ν_n. The last part describes a pairwise spin-spin coupling between the ions where the coupling constants,

$$J_{n,m} = \frac{\hbar}{2}\frac{\partial\omega_n}{\partial x_{n,i}}\bigg|_{\bar{x}_{n,i}}\frac{\partial\omega_m}{\partial x_{m,i}}\bigg|_{\bar{x}_{m,i}}(M^{-1})_{n,m} \tag{1.36}$$

are determined by the Hessian M of the potential. The reason for such spin dependent forces is that the position of ion m is slightly modified when flipping an ion's spin. Consequently, it leads to changes in the Coulomb repulsion

energy on ion n, and thus also changes its position. Ion m experiences now a different Zeeman energy. Positive values of J result in an energy reduction for parallel spin orientations, whereas negative values lead to reduced energy for anti-parallel spins. Decoherence effects, from magnetic field fluctuations, are expected but they might be reduced by spin echo techniques since low frequency Fourier components typically dominate the noise-spectrum.

Magnetic gradient in the trap axis.– A magnetic field along the trap axis $\vec{B} = (b_0 + z \cdot b)\vec{e_z}$ results in a field b_0, which provides a quantization axis and which splits the $|m = +1/2\rangle$ and the $|m = -1/2\rangle$ spin states by an energy higher than the vibrational quanta energy. The second term $z \cdot b$ results in a position dependent Zeeman shift, leading to forces against the axial vibrational modes only which are determined by the block A in the Hesse matrix M yielding:

$$J^{ax}_{n,m} = \frac{g_J^2 \mu_B^2}{2\hbar} \frac{b^2}{m\omega_z^2} (A^{-1})_{n,m} \tag{1.37}$$

with Bohr magneton μ_B and Landé factor $g_J = 2$. The relative magnitude between different entries of J depends only on the number of ions, whereas the absolute height is proportional to b^2/ω_z^2. Figure 1.4 shows the coupling constants for ten ions, normalized to a unit magnetic field gradient of 1 T/m . All couplings are positive and strongest for nearest neighbors with a strength of $2\pi \cdot 7.4$ Hz for 7 T/m and an axial frequency of $\omega_z = 2\pi \cdot 310$ kHz.

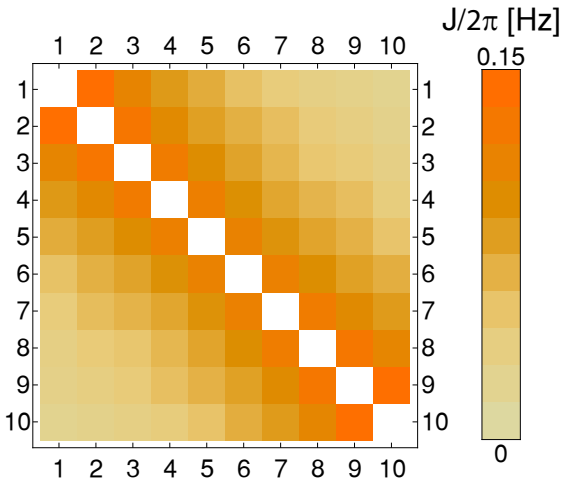


Figure 1.4 Coupling constants $J_{n,m}$ in a ten ion crystal at $\omega_z = 2\pi \cdot 310$ kHz, for a b=1 T/m magnetic field gradient in the z-direction, thus aligned along the ion crystal. A maximum $J_{n,m}$ of $2\pi \cdot 0.15$ Hz/T is achieved.

Magnetic gradient in the radial axis.– If now we consider a gradient aligned along the x-axis and the spin dependent force acting against the transversal

eigenmodes, governed by the anisotropy parameter, the transverse confinement and the lowest radial eigenfrequency can be reduced without modifying the distances between the ions. The Stern-Gerlach force acts by moving the ions transversally away from the trap axis, and the lowest frequency transversal eigenmode, the zig-zag mode governs the interaction. This mode is excited most efficiently with an alternating, anti-ferromagnetic spin alignment.

The transversal magnetic gradient couplings $J_{n,m}$. determined by the matrix B^x (see Appendix C), are plotted in Figure 1.5 for various values of the anisotropic parameterα. When α approaches its critical value, we find coupling strengths of about $2\pi \cdot 158$ kHz, where the zig-zag mode frequency ν_{zz} is at 11 kHz and the transversal field gradient is 23 T/m.

High magnetic field gradients in the radial direction are generated by sending a current to central wire W_1 (see Sec. 2.1.3). An alternative scheme for realizing a transversal magnetic field is presented in Sec. 2.2.2. A second substrate beneath the trap supports three independent high current density wires which create a vertical magnetic field. Working with the same current density as before will give rise to a gradient of about 63 T/m at a height of 200 µm over the upper wires' surface. With the above values a coupling strength of up to $2\pi \cdot 479$ kHz for $\nu_{zz} = 11$ kHz will be within reach.

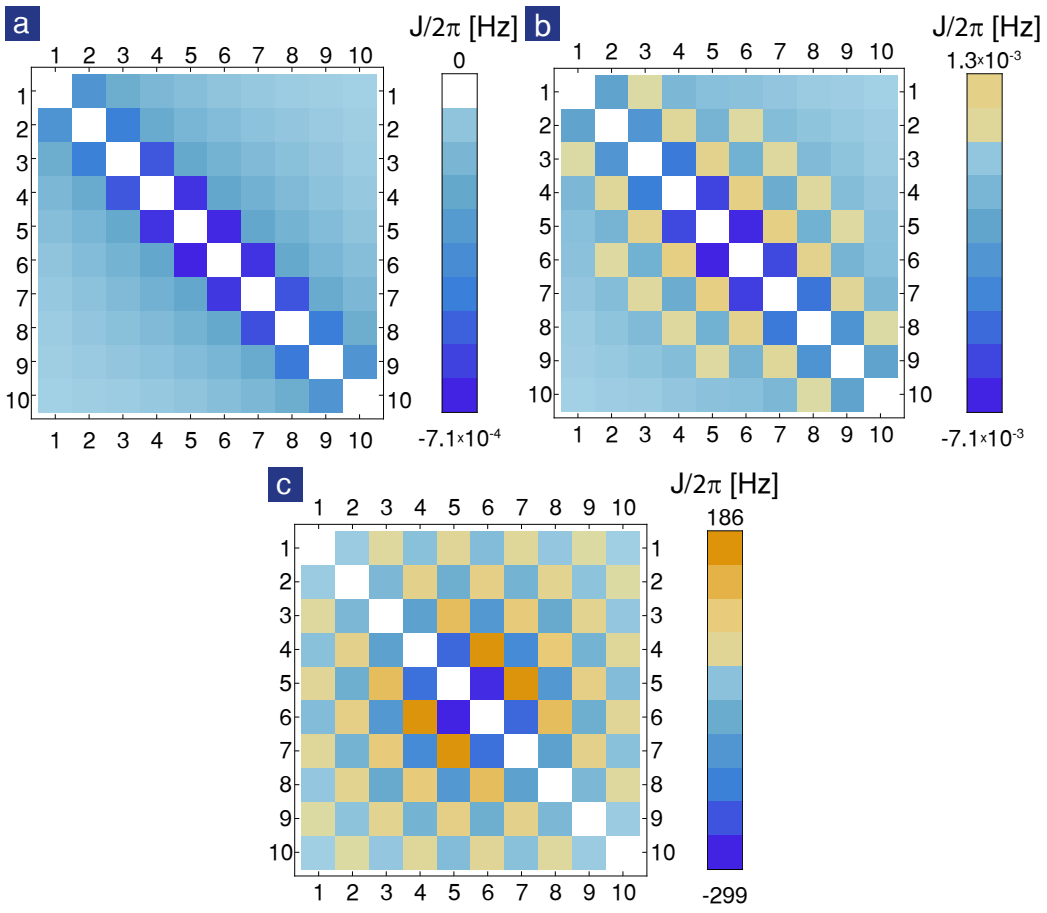


Figure 1.5 Coupling constant of ten ions normalized to b=1 T/m magnetic field gradient in the radial direction when approaching the critical anisotropy for ten ions ($\alpha_{crit} = 0.047348$). The three subplots indicate in color coding the transition into a ferromagnetic coupling with red for positive and blue for negative values of J. a) Choosing a value of $\alpha = 0.0097819$ results in ν_{zz}=2.8 MHz and a maximum $J_{n,m}$ of $2\pi \cdot 7.1\ 10^{-4}$Hz/T. b) For $\alpha = 0.032669$, $\nu_{zz} = 1.7$ MHz and $J_{n,m}$ increases to $2\pi \cdot 7.1\ 10^{-3}$Hz/T. c) With $\alpha = 0.047347$ we find ν_{zz} =10.7 kHz and $J_{n,m}$ = 2π·300 Hz/T.

2 Planar Trap Designs

Planar traps offer a flexible way to place, with high precision, ion crystals in close vicinity to on-chip elements. In this chapter I will describe the design of a planar trap which includes on-chip electromagnets. Its electric and magnetic fields are analytically and numerically calculated. A second trap design in which glass micromachining and thick film technology are combined, results in a ion trap with high aspect ratio structures and thick printed current wires.

At the end of this chapter I will cover the design of a third planar trap which includes a tapering of the trapping electrodes such that the ion-to-surface distance of a single trapped $^{40}Ca^{+}$ ion's may be controlled.

. . . . . .

2.1 Trap I and Trap II: Planar Trap with Integrated Electromagnets

A planar trap design which confines ionic crystals above and in the vicinity of two integrated current-carrying elements is presented. The design layout is used to built two types of trap named Trap I and Trap II. They differ mainly to each other by the type of growth method employed to build the trapping electrodes. Therefore we will make a distinction between both traps in a corresponding chapter given the details for their fabrication (see Chapter 3). In what follows both designs are treated as a common since they main geometry and trap electrodes configuration remained with minor changes.

2.1.1 Design Parameters

In this trap design two current-carrying wires, named W_1 and W_2, are built on top of an insulating substrate as it is illustrated in Figure 2.1. These inner current-carrying wires, arising from the splitting of a central RF ground electrode, allow to apply high current densities for generating strong magnetic field gradients at the ion's position. In addition, two nearby RF electrodes (red) permit to confine ion crystals in radial direction (x, y) at a distance y_0 from trap's surface. The axial confinement along the z-direction is provided by nine segments (S) consisting each of two (DC) electrodes.

Beyond calculating relevant trap characteristics such as its trap depth and resulting ion's position, additional demands have to be also fulfilled for success ion trapping. First, trap electrode configuration should minimize stray light scattered within the electrode gaps. In addition, it is desirable to increase electrode gap distance to reduce trap's capacitance and increase Q-factor for trap-helical resonator system. Large insulator areas exposed to strong focused laser beams may lead to patch potentials which deviate stable ion motion.

After considering these technical limitations three types of gaps were chosen as follows:

- ($g_1 = 10\,\mu m$): between the inner wires W_1 and W_2 in accordance to simulations of the magnetic field gradient as shown in Sec. 2.1.3.
- ($g_2 = 14\,\mu m$): for the separation between RF electrode and nearest neighbors i.e. between inner electrodes W_1 and W_2 (yellow), DC electrodes (orange) and RF electrodes (red) to reduce trap capacitance and increase threshold voltage before electrical breakdown.
- ($g_3 = 3\,\mu m$): as DC electrode spacing to release scattered light from exposed insulator areas. It may seem counterproductive for decreasing total capacitance but trap capacitance depends stronger on the distance between RF and surrounding electrodes than DC electrode spacing.

Another limitation is the anomalous heating with a stronger ion-trap distance ($\sim d^4$) dependence than the magnetic field gradient scaling ($\sim d^2$). To guarantee ion trapping and generate still strong magnetic field gradients a trapping distance of $165\,\mu m$ was chosen. The trap is also equipped with nine pairs of DC electrodes which provide enough freedom for micromotion compensation. They further facilitate ion transport for about 4 mm along the trap axis.

The RF electrodes in a symmetric configuration have a common width of $b = c \approx 210\,\mu m$. The two inner wires W_1 and W_2 have a width of $a_1 \approx 100\,\mu m, a_2 \approx 50\,\mu m$ respectively. The DC electrodes width corresponds to $w \approx 600\,\mu m$. These dimensions are given from the center of the corresponding gaps (g_1, g_2, g_3) described above. The simulation of electric and magnetic fields based on these dimensions will be explained in the following sections. The resulting geometry was also used for designing the masks corresponding to Trap I and Trap II as it will be shown in Sec. 3.1.

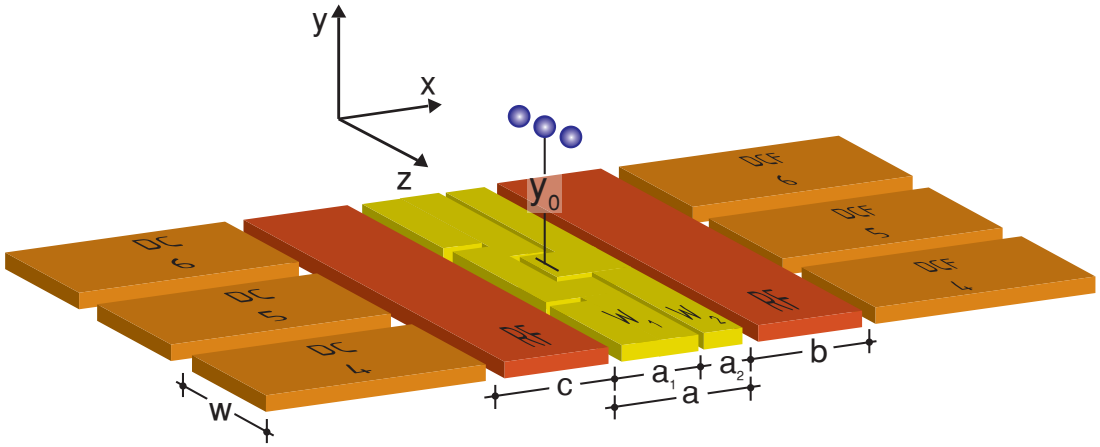


Figure 2.1 Planar trap design with on-chip current-carrying wires. Two radiofrequency (RF) electrodes (red) confine the ion along the plane (x,y) at a distance (y_0) from the trap surface. Nine (DC) electrodes pairs (orange) position the trapped ion along the trap axis z. Two inner wires W_1 and W_2 (yellow) are used either as single RF-ground or as two independent electromagnets. They may be switched on or off by applying static and/or oscillating currents. The trap dimensions (taken from the center of the gaps) are $a_1 \approx 100\,\mu m, a_2 \approx 50\,\mu m, b = c \approx 210\,\mu m, w \approx 600\,\mu m$

2.1.2 Electric Fields

The static and oscillating electric fields provided by the trap electrodes have to be determined with high accuracy. Due to the finite size and complex geometry of trap electrodes the usual way of calculating the electric fields relies on numerical simulations. Commonly the Finite-Element Method (FEM)[86] or the Boundary Element Method (BEM) are extensively applied. These numerical methods, and in particular BEM, are highly accurate though time consuming.

For short computing time, and under certain assumptions, the electric fields can be calculated by analytical methods as explained in Sec. 1.3.1. Therefore for finding the adequate geometry and trapping potentials in our traps we adopt the following strategy. For a fast calculation of the trapping potentials an analytical model (House model) was used. It takes into account an idealized inner trap section. Furthermore, the trapping electrodes are considered rectangular in shape and separated by infinitesimal small gaps. A second, and more refined step, consists on calculating the potentials by a numerical toolbox (BEMSolver)[76] based on the previous analytically calculated geometry. This permits to account the contribution of the whole chip geometry. On

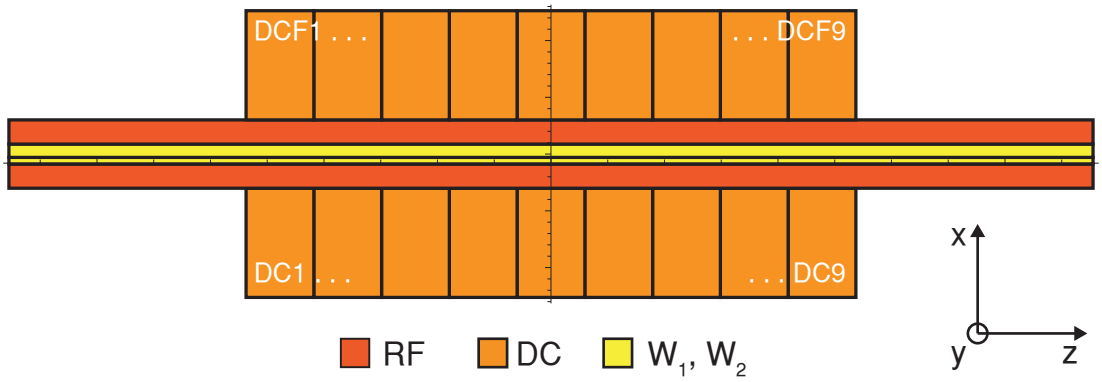


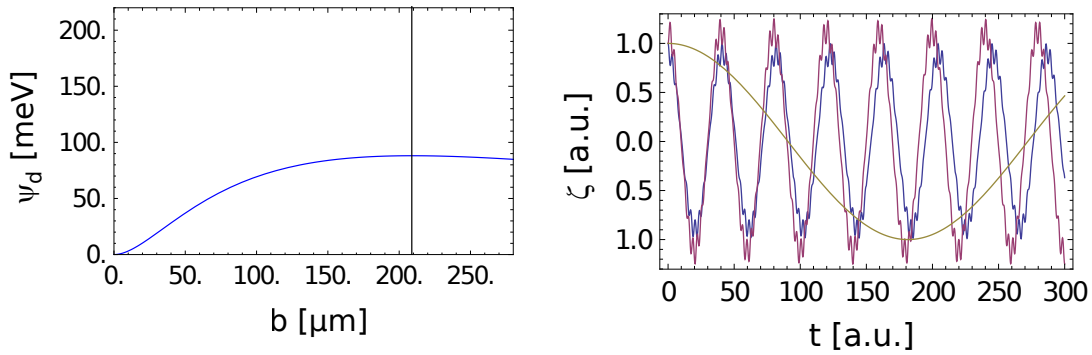
Figure 2.2 Idealized trap geometry with two integrated electromagnets for performing analytical simulations of trapping potentials. The RF electrodes (red) shape, inner current-carrying wires (yellow) and DC electrodes (orange) are considered to have a rectangular shape to fit into the House model.

what follows both analytical and numerical solutions are shown. The outputs given by both methods are compared on the last part of this section.

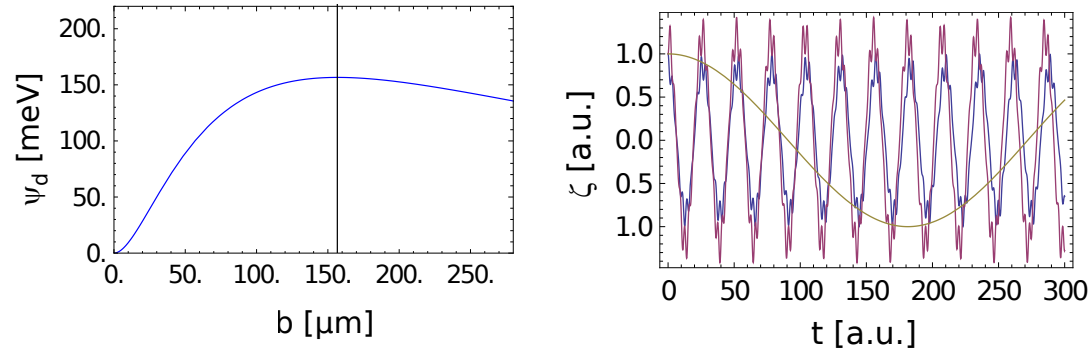
Analytical Calculation of Trapping Parameters for Trap I.– Idealized rectangular electrodes as shown in Figure 2.2, defined the trap geometry to be taken into account into the analytical model (Sec. 1.3.1). All trapping electrodes, are considered to lye in a single plane (xz). The oscillating (RF) voltage is applied to a pair of symmetric electrodes (red) and nine (DC) electrode pairs (orange) control the ion's position (x_0, y_0, z_0) along the trap axis z. Two inner wires W_1 and W_2 can be set at RF-ground or at certain static current. Except for the DC electrode length (here $\frac{5}{3}$w) all electrode dimensions are set according to those given previously in Figure 2.1.

The operating parameters (V_{rf}, Ω) and trap geometry (b/a) strongly influence trap depth (ψ_d) and ion stability as shown in Figure 2.3. Here three trap sizes are compared.

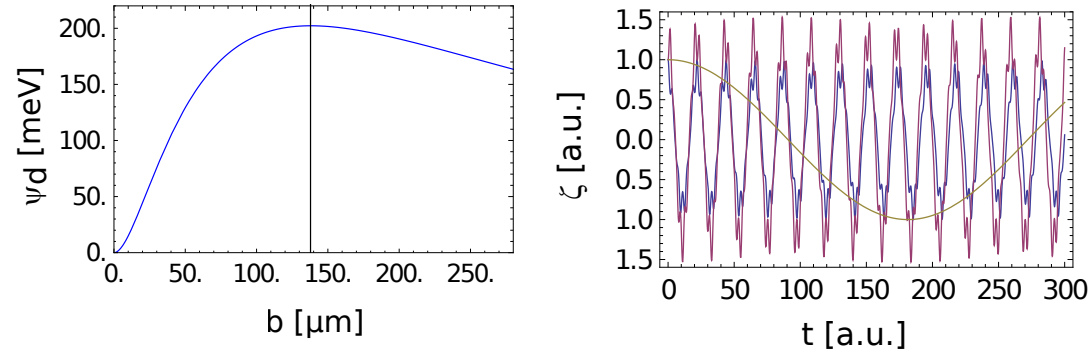
In Figure 2.3 three planar geometries are compared. Reducing the trap size impact on ion's stability and trap depth if trapping parameters are kept constant. By changing the trap size, the trap depth is shallower and ion instability also increases if the operating parameters (Ω, V_{RF}) are also kept constant. Although the the ion's stability can be recovered by increasing V_{RF} proportional to Ω in typical scenarios we are technically limited to low amplitudes of V_{RF}. In these cases, either a given Q-factor of the helical resonator or a voltage threshold before electrical breakdown are the main source.



(a) $a = 175\,\mu m$, $y_0 = 162\,\mu m$, $\psi_d^{max} = 80\,meV$, $q = 0.2$



(b) $a = 131\,\mu m$,$y_0 = 132\,\mu m$, $\psi_d^{max} = 150\,meV$, $q = 0.33$



(c) $a = 115\,\mu m$, $y_0 = 116\,\mu m$, $\psi_d^{max} = 187\,meV$, $q = 0.4$

Figure 2.3 Trap depths and ion trajectories for different trap sizes calculated after applying the House model. From a) to c) the ion's position has been reduced by modifying the width of RF and inner RF-ground electrodes. The ratio a/b= 1.2 and other trap dimensions (c, w) are set different for each trap. By changing the trap size the trap depth is shallower and ion instability also increases if the operating parameters (Ω, V_{RF}) are also kept constant.

For determining the trap depth a application of Eq. 1.14 is required to calculate the potential field contribution of each electrode. In general, to avoid ion heating or ion lost during transport the curvature of the potential (proportional to the matrix entry A_{zz}) should be kept constant along the minimum of the RF potential. The strength of the DC potentials at the ion position dependent of the width of the control electrodes as plotted in Figure 2.4.

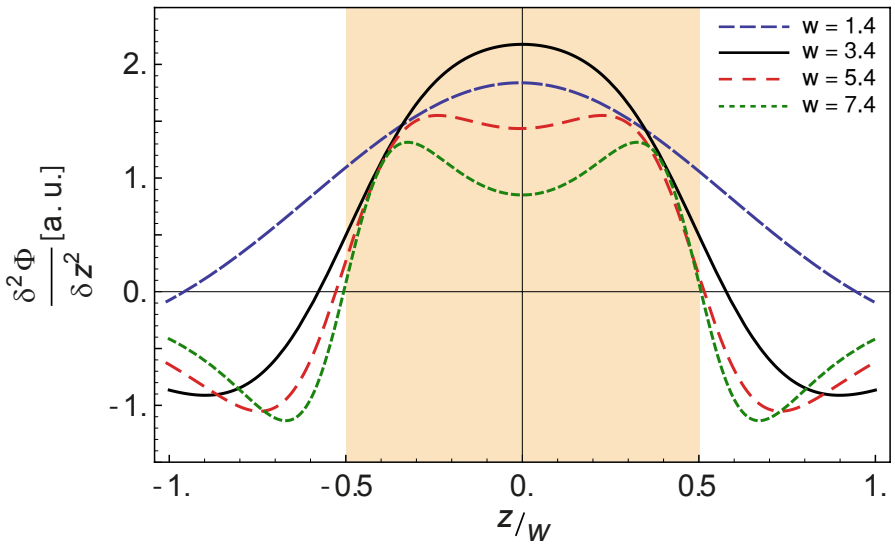


Figure 2.4 Analytical determination of static voltage configuration. Narrow DC electrodes ($w = 1.4a$) flattens the curvature of the potential at the ion position ($z/w = 0$) whereas too wide DC electrode ($w = 7.4a$) compromises ion transport at the boundary of two nearest DC electrodes. An adequate curvature of potential is obtained for a value of ($w = 3.4a$). This is due to the fact that the electrode width should be chosen in such a way that the field it creates has significant curvature everywhere along the path of the ion near the border electrodes.

For narrow widths of the control electrodes ($w = 1.4a$) the potential curvature flattens and high voltages have to be applied in order to achieve the desired curvature. Whereas for wide DC electrodes ($w = 7.4a$) the potential has a null value at the boundary between two nearest electrodes at $w \pm 0.5$ (light orange). This is an inconvenient place since the neighbor electrode will require high voltages to keep the appropriate curvature while transporting the ion from one electrode to the other. For the design here presented we have chosen $w = 3.4a$ which does not compromise ion transport and provides high curvatures while applying low voltages.

The discrepancy of this analytical method ranges about 10 % compared to numerical calculations shown in what follows.

Numerical Calculation of Potentials for Trap I.– Numerical simulations are used to describe with high accuracy the trapping potentials produced by the entire chip geometry. The first step starts by setting a coarse triangular mesh on electrodes surface in the AutoCAD file (Figure2.5). Into BEMSolver the complete chip geometry is imported and a cubic grid defined by the user constitutes the solution domain.

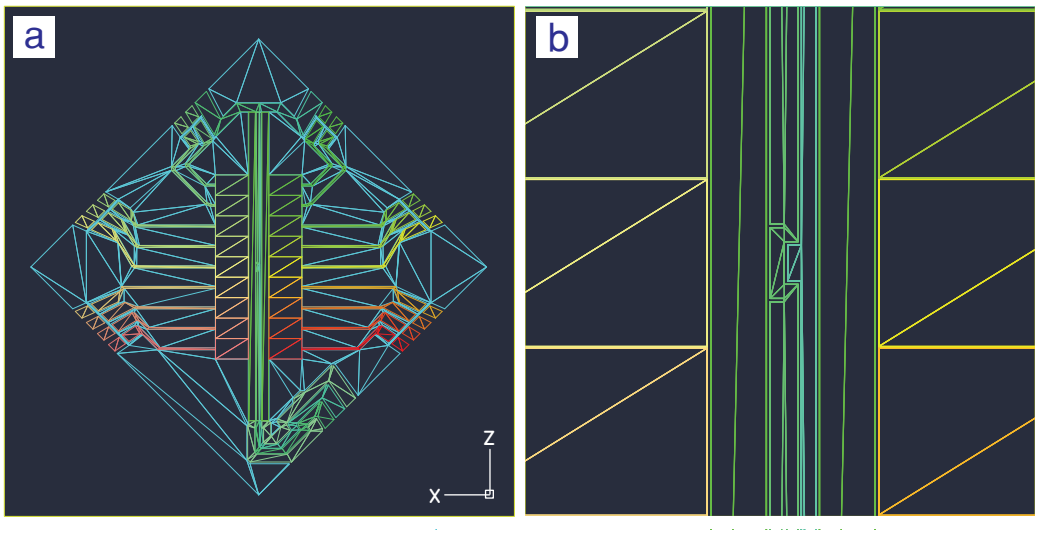


Figure 2.5 Initial Meshing of Trap I prior BEM calculations. a) coarse mesh of chip surface (10×10 mm^2). b) inner part of chip: DC electrodes, RF electrodes and current-carrying wires W_1 and W_2 are partially shown. Observe the RF electrode extension of more than 1 mm to avoid edge effects for the confining fields.

All surface elements contribution are calculated by Coulombs law at each grid knot and the solution stored in a cache file for successive post-processing. Post-processing stage takes place in a C++ environment and an interpolation function in between the knots of the cubic grid smooths the fields.

Then the contribution to the field of each electrode is solved for unit voltages applied and stored in a data file. In this way, the computational task is reduced, and makes the post-processing a fast procedure. Post-processing of the data can take place on the same *C++* and ROOT OpenGL viewer or on a more common mathematical software such as Mathematica or Matlab.

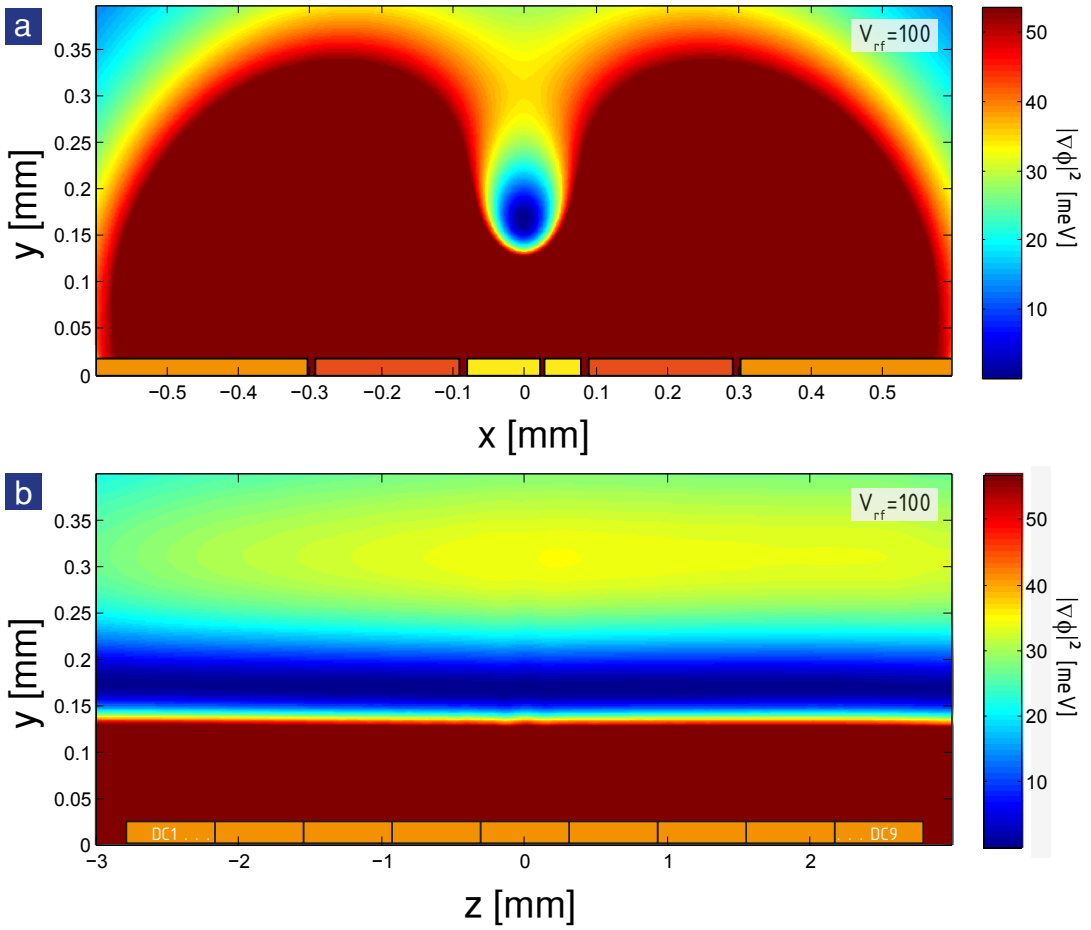


Figure 2.6 Numerical determination of the pseudo potential. a) radial and b) axial cut of the pseudopotential. Electrodes are rescaled for clarity. At an RF voltage amplitude of 100 V a single ion can be confine up to an energy of 35 meV. The driving frequency taken in this case is $\Omega = 2\pi \cdot 30.8\,\mathrm{MHz}$

The potentials generated by RF electrodes permit the radial ion confinement. These time-varying fields have a wavelength much larger than the dimensions of the trap thus we can consider the fields produced by these electrodes as static. The adiabatic aproximation, Sec. 1.2.1, and the notion of a pseudopotential is applied to describe the pseudo energy at which the ion can be contained.

For the numerical simulations explained in the last section we set a unit voltage at each RF electrode and ground otherwise. We solve for the total unitary potential and the pseudopotential. During post-processing we simply

multiply by the applied peak amplitude voltage V_{RF} and the constants given in Eq. 1.10 to the unit pseudopotential.

The pseudopotential contour plot on planes xy and zy, in Figure 2.6, provide information about the ion height and the maximal energy at which the ion can be stored (given in meV). In Figure 2.6a) the radial confinement is cut at the trap center ($z_0 = 0$) and the pseudopotential in the radial directions is plotted. A cross section of trapping electrodes are only rescaled in the x-direction. The ion is trapped at a distance ($y_0 = 167\,\mu m$) and the scape point is placed at a distance ($y_s = 306\,\mu m$) from the electrode surface in the y-direction. Setting the typical parameters used in the experiments given in Chapter 5, at a peak amplitude voltage ($V_{RF} = 100\,V$) and a drive angular frequency ($\Omega = 2\pi \cdot 30.8\,MHz$) an ion with a maximal kinetic energy of 34.6 meV can be contained. Although the trap depth is shallow it still can contain an ion with a temperature of 346 K which is typically way above the temperature of a Doppler cooled ion

The second plot (Figure2.6b) provides information of the RF minimum along the trap axis. We have rescaled the segmented DC electrodes along the z-axis. Note that at the trap center ($z_0 = 0$) the energy confinement is increased for positive z direction. In contrast for negative values of z the trap depth differs about 10% compare to the trap depth $z_0 = 0$. This trap depth asymmetry is produced by the contribution of the RF paths at the end of the chip (bottom part on Figure 2.5). With that we want to point out the accuracy and capabilities of using the boundary element method to describe the potential contribution of the whole chip geometry. This asymmetry however should not compromise trapping but stability, and it indicates the most preferable part to do experiments along the positive side of the z-direction.

As we have mentioned in Sec. 1.3.1, the axial confinement is given by setting axial voltages to DC electrode pairs or here simply called segments. We also use BEM to calculate numerically the potential field generated by these segments at the ion's position.

The potential along the RF minimum in the z-direction of each segment set at 1 V are plotted in Figure 2.7. The segments widths are rescaled for illustration purposes. We do compare the potential contribution of the entire segment geometry (thick) and an ideal rectangular geometry (dashed). We notice that the potential strength deviates minimally from that of the ideal situation unless from that of the last two segments, eight (S8) and nine (Sg9), where it appreciably increases. Recalling the entire chip geometry from Figure 2.5, we can

attribute this effect due to the proximity of the corresponding segment paths (for both Sg8 and S9) to trap axis. This effect can be however experimentally counteracted by appropriate weighting factors on these two electrodes.

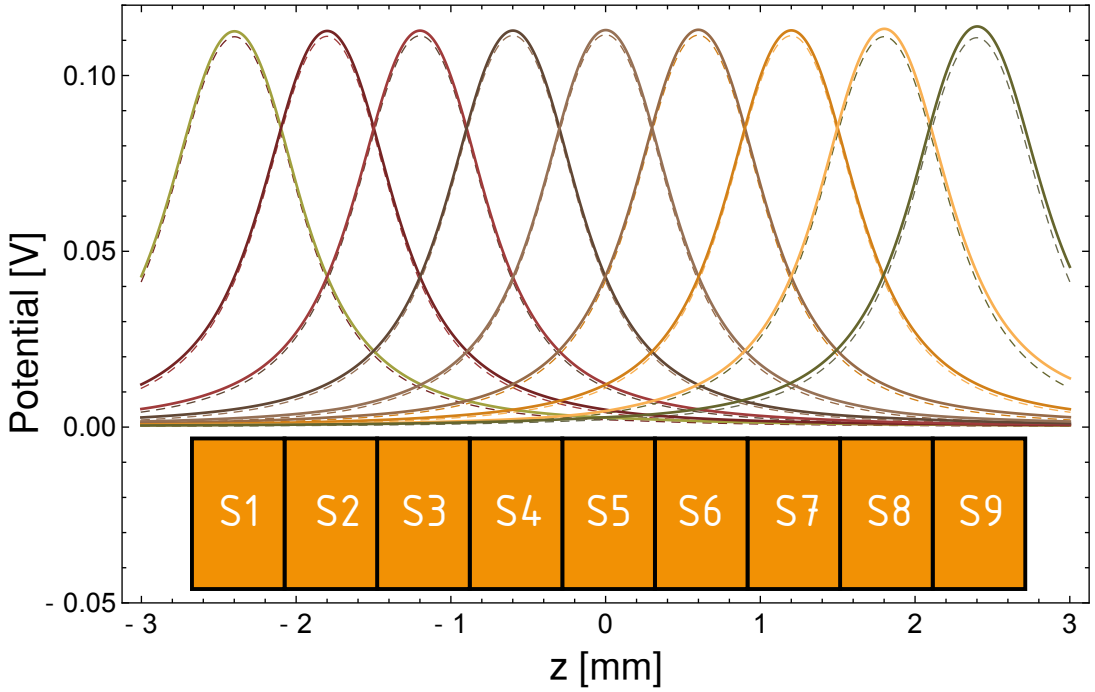


Figure 2.7 Numerical calculation of the axial potential. The DC potentials are obtained after applying a unit voltage to each segments on the chip (lines). Additionally we consider that this unitary voltage is applied only in an ideal rectangular geometry (dashed lines). Each static (DC) segment is rescaled (bottom) in the z direction. A desired axial frequency is determined after appropriate weighting factor to the potential voltage matrix of DC segments of interest.

Comparison of Numerical and Analytical Methods.– Both analytical and numerical solutions are presented in this section. Both methods present a close agreement with the experiment as it will be shown in Sec. 5.5. The disagreement between one of the other are within 10 % as we can see from Table 2.1. It is clear that the analytical model, although its great agreement misses the contributions of the complex shape of the chip. Therefore the experiments were compared within the frame of the numerical results. The capabilities of the numerical methods are only limited for the time consuming calculations when since a more refined meshed is needed. As it is required for the optimization of the geometry, the analytical approach turns to be the best choice. Whereas

for the axial frequencies in both methods agrees within 1 % to each other, in the radial directions it increases to about 7 %.

Table 2.1 Trap frequencies analytically (A.) and numerically (N.) calculated

Sg4 & Sg6 [V]	Sg5 [V]	V_{RF} [V]	$\omega_x/2\pi$ [MHz]	$\omega_y/2\pi$ [MHz]	$\omega_z/2\pi$ [MHz]	Ψ [meV]	d_0 [µm]	
+0.95	-0.88	80	1.03	1.18	0.26	22.2	167	(N.)
			1.18	1.29	0.26	24.6	162	(A.)
+0.95	-0.88	100	1.32	1.46	0.26	34.6	167	(N.)
			1.50	1.59	0.26	38.5	162	(A.)

As an example of the possible differences between both the analytical and numerical model presented in the last section, the Table 2.1 is included with the characterization of the trap as presented in Chapter 5. The static potential are created by a set of three DC segments (Sg4, Sg5 and Sg6) and the radial confinement by a peak amplitude voltage (V_{RF}) driven by an angular frequency ($\Omega = 2\pi \cdot 30.8\,\mathrm{MHz}$). Both methods are within agreement below 1 % for the axial frequency. Larger discrepancies still below 10 % are found for the ion height (d_0), trap depth (Φ) and the radial frequencies (ω_x, ω_y).

2.1.3 Magnetic Field Gradients

For the numerical calculations of the magnetic fields generated by the inner two wires (W_1 and W_2) we have employed the numerical package RADIA[a]. It is based on the boundary integral method (BIM) where volume objects are subdivided into a number of smaller objects. The solution is built by constructing an large (interaction) matrix representing mutual interactions between the objects and stored temporarily in memory. By iteratively multiplication of the interaction matrix the solution on each small element is obtained (relaxation procedure).

[a] ESRF, France. www.esrf.eu

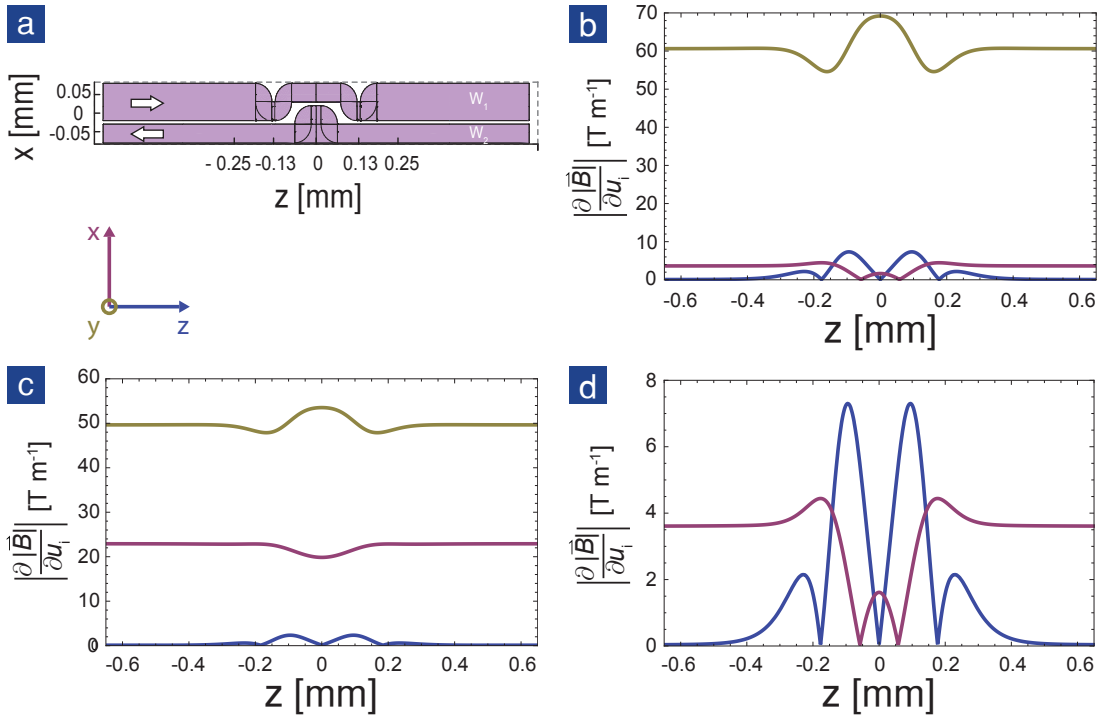


Figure 2.8 Magnetic field gradients of electromagnets. Magnetic gradient $\left|\nabla|\vec{B}|\right|$ in x, y and z direction. a) inner two wires W_1 and W_2 and current flow (arrows). b) The upper limit for the transversal gradient in our trap is reached with $I_{W_1} = 4\,\mathrm{A}$ and $I_{W_2} = -10\,\mathrm{A}$. c) $I_{W_1} = -I_{W_2} = 10\,\mathrm{A}$ results in a higher axial gradient, which is shown d) magnified.

Contrary to FEM the vacuum does not need to be meshed which leads to important advantages. For instance, after relaxation the field integrals can be analytically calculated anywhere in space, at an independent distance from the current-carrying wires. However, a drawback of the integral method is the large amount of memory required when a large number of elements are needed. In this case FEM is more efficient. In our trap the current-carrying wires have a finite rectangular shape and the fields generated near the ion position can be accurately solved by the RADIA package.

The trap design explained in Sec. 2.1 presents a split of the inner electrode into two wires W_1 and W_2 (see Figure 2.1). The small loop in W_1 at the center of the trap, having inner length 150 µm and outer length 250 µm, generates a high magnetic field gradient at a relatively short ion-surface distance ($d_0 = 167\,\mu\mathrm{m}$) where the ion crystal is contained. The results of our numerical simulations using the RADIA package are summarized in Figure 2.8. The

magnetic field gradient components are plotted as a function of z.

For a given width of W_1 (100 µm) the gradient components along z-direction peaks at two locations depend on the inner length of the loop. The transversal components x and z become constant whereas the axial component z vanishes far away from the trap center ($z = 0$). For a current of $I_{W_1} = 4\,\mathrm{A}$ and $I_{W_2} = -10\,\mathrm{A}$ one can achieve a much higher value, up to $23\,\mathrm{T\,m^{-1}}$ at a magnetic field strength about 7.6 mT. The y-component is even higher with more than 50 T m.

In the experiment, the magnetic field gradient is switched on only for a short time such that the resistive heat load is reduced. In Sec. 5.1 we present current tests with the first generation of traps. For a current of 6 A, corresponding to a current density of $4 \times 10^6\,\mathrm{A\,cm^{-2}}$, we are able to apply the load for more than 0.1 s.

While supplying static current through an inner wire (W_1), surface charges on top of the trapping electrodes produce an stray electric field. Such an electric field, if not counteracted, may negatively affect ion stability. The flexibility of the design, where the outer ground electrode is segmented, and as it will be demonstrated in next section, permits to create a counteracting field to nullify this effect, by appropriate choose of DC voltage applied to the segmented electrodes.

2.1.4 Induced Electric Field While Supplying Currents

On a conductor, fulfilling Gauss law, its entirely charge resides on the surface when a potential gradient is applied. In the case of our trap, while sending a current through the inner wires W_1 and W_2 the electric field produced at the ion's position alters the ion stability. It is therefore necessary to know the strength of those fields in order to keep ion motion stability while sending a current pulse. Based on the analytical model shown in Sec. 1.3.1 we can calculate directly the potential field of a current-carrying wires if we assume a voltage drop distributed on the upper wire surface.

In our trap, a DC current is supplied to the inner wires (W_1 and/or W_2) which surface charges leads to an electric field effecting the ion motion in all three directions. The corresponding potential field mainly superimposes to the axial potential generated by the DC segments. Moreover, the total electric field may not necessarily vanish at the ion position. Consequently, if this additional potential field is not counteracted by an appropriate DC configuration,

an undesired ion micromotion and finally ion loss while sending a current pulse may occur.

Current-Carrying Wire Composed of an N-Rectangular Array.– The potential field generated by the charge distributed on the surface of our current-carrying wires can be modeled by N tiny resistors of width w conforming the current-carrying electrode, as shown in Figure 2.9. Then we can consider that each of these tiny electrodes, from now on called elements, have been set at a proportional voltage determined by the voltage drop along the surface of the conductor. Then the potential field produced by each rectangular element can be analytically calculated. The resulting potential field can be superposed to the axial potential generated by the control (DC) electrodes.

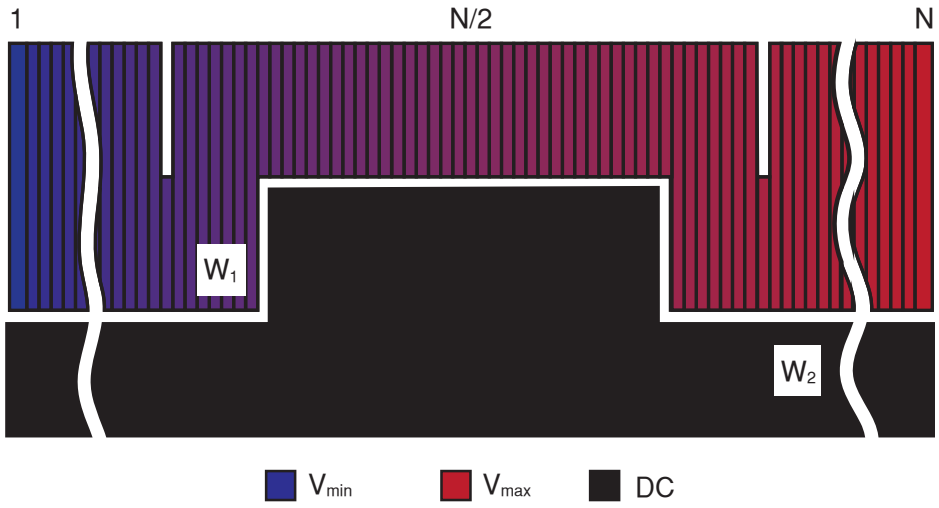


Figure 2.9 Model of N-rectangular electrodes to simulate current-carrying wires. Each current carrying wire can be defined by an array of N-rectangular electrodes. Above we exemplefly this for wire W_1 in which we additionally suppose that each of the N-tiny rectangular electrodes is set at a static voltage V_N. Thus the voltage drop at each individual tiny electrode is determined by applied static current passing through the cumulative resistance. In this case, the second wire (W_2) is set to 0 V.

To compensate the ions motion while sending a static current through an inner wire, the conditions explained in Sec. 1.3.1 can be extended as follows:

- the potential field Φ_w generated by the voltage drop along the inner wire W_2 and the potential field generated by an initial DC configuration (Φ_{DC}) should provide together a desired curvature (A_{zz}) along the trap axis z.

- the resulting electric field from the superimposed potential Φ_t should vanish in all directions at the ion's position

The voltage distribution on the surface of a wire carrying certain DC current can be described as sum of the voltage set to an array of N tiny resistors as shown in Figure 2.9. A planar trap geometry with nine DC segments as discussed in section 2.1, current-carrying wires W_1 and W_2 composed our system. If W_2 is set to 0 V, a current is supplied to W_1 and the rest of the trapping potential field is generated by n DC electrodes, then the total DC potential can be described as:

$$\Phi_{dc}^{T}(x,y,z) = \sum_{i=1}^{n} U_i \Phi_i^{W}(x,y,z) + \sum_{j=1}^{N} V_j \Phi_j^{S}(x,y,z) \tag{2.1}$$

where n is equal to the number of DC electrodes and N equal to the number of rectangular discretization elements of the current-carrying wire and Φ_i and Φ_j their corresponding potential fields when each electrode is set to 1 V. Experimentally, the values of U_i can be arbitrarily set between 0 V to 10 V and the values of V_j are determined by the voltage drop at each element N along the wire W_1.

Adding an opto-isolator[a] to the current pulse generator, an arbitrary voltage value can be set along the circuit at the position N. The shift of the 0 V (ΔV) over the wire surface is depicted in Figure 2.10. If we consider the voltage over the wire surface as been linearly distributed over the wire surface, then the voltage set at the middle of the wire or at the rectangular element $N/2$ is set to a voltage value of ($V_{N/2}$).

Compensation of Potential Field Φ_w.– In order to find out the compensation DC configuration to counteract the potential field generated by a current-carrying wire we require at least three pairs of DC segments. This set of electrodes together with the voltage distribution over the wire generate the trapping DC potential field with a curvature A_{zz} along the z-axis.

Since the potential generated by the wire is asymmetric in all three directions, we require at least three degrees of freedom to fulfill the conditions explained in section 2.1.4. One to set electrodes DC5 and DCF5 independent from each other and from segments DC4 and DC6. Two to set electrodes named DC4 and DC6 equal to their respective counterpart DCF4 and

[a] H11F1

DCF6, but independent from each other. The potential field generated by the wire may have to situations and for the compensation those have to be considered. In the next sections both are discussed and DC potential configuration to counteract their contribution to the trapping potential are shown.

Variable Voltage $V_{N/2}$ along Wire Surface.– As mentioned before, by adding an opto-isolator element to the circuit the ground point may be varied along the current-carrying wire surface. Thus different values of the voltage distribution around the center of the wire named $V_{N/2}$ may be taken into account to counteract their contribution to the overall potential Φ_{DC}^{total}.

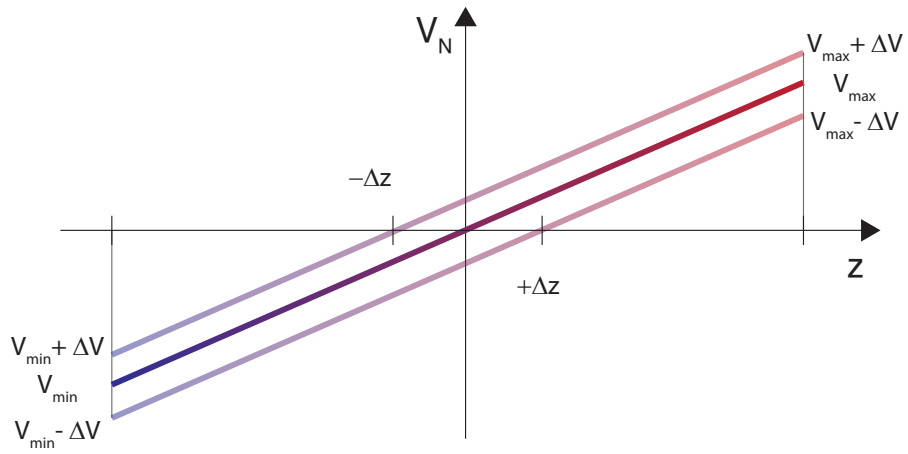


Figure 2.10 Voltage distribution over the surface of an electromagnet. At each element a voltage (V_N) proportional to the applied static current is distributed over its surface in the direction of the trap axis (z-axis)

To illustrate the contribution for different values of $V_{N/2}$ at the center of wire W_1, we plot the potential on the xy- and zy-planes as shown in Figure 2.11. The voltage distribution ($V_{N/2}$) for generating a dc current (I_{W_1}=1 A) is varied around the middle of wire W_1 and its potential field Φ_w added to the potential field Φ_{dc}^{ideal} generated by three segments, case (C_0) shown in Table 2.2. From Figure 2.11 we can see that minimal changes on the value of $V_{N/2}$ around the middle of wire W_1 strongly shift the minimum of the DC potential in all directions. For instance, if $V_{N/2}$ =+100 mV right below the ion at the surface of wire W_1, the minimum of the DC potential moves by $[\delta x, \delta y] = [+6\ \mu m, +30\ \mu m]$ and $[\delta z, \delta y] = [+12\ \mu m, +30\ \mu m]$ apart from the rf minimum position in their respective xy- and zy-planes. The necessary DC

configurations, for values of $V_{N/2}$ from $-0.1\,\mathrm{V}$ to $0.1\,\mathrm{V}$ are additionally given in Table 2.2.

Table 2.2 DC configuration for compensating the potential field generated by wire W_1 while shifting the ground position along the wire surface

Case	DC4 [V]	DC5 [V]	DCF5 [V]	DC6 [V]	W_1 current [A]	$V_{N/2}$ [V]	A_{zz} [a. u.]
C_0	+0.96	-0.90	-0.90	+0.96	0.0	0.0	$3 \cdot 10^{-4}$
$C_{-0.1}$	+1.05	-1.26	-1.15	+1.25	1.0	-0.1	$3 \cdot 10^{-4}$
$C_{0.0}$	+0.86	-0.90	-0.90	+1.06	1.0	0.0	$3 \cdot 10^{-4}$
$C_{+0.1}$	+0.68	-0.55	-0.66	+0.88	1.0	+0.1	$3 \cdot 10^{-4}$

From Table 2.2 we can see that if we initially do not change the value of $V_{N/2}$ while sending a current of 1 A through wire W_1 (case $C_{0.0}$) then only DC4 and DC6 segments are required to compensate a change on the potential slope due to the current. However, if both current of the wire and value of $V_{N/2}$ are changed simultaneously, also the setting for both segments DC4, DC6 and electrodes DC5 and DCF5 have to be changed simultaneously.

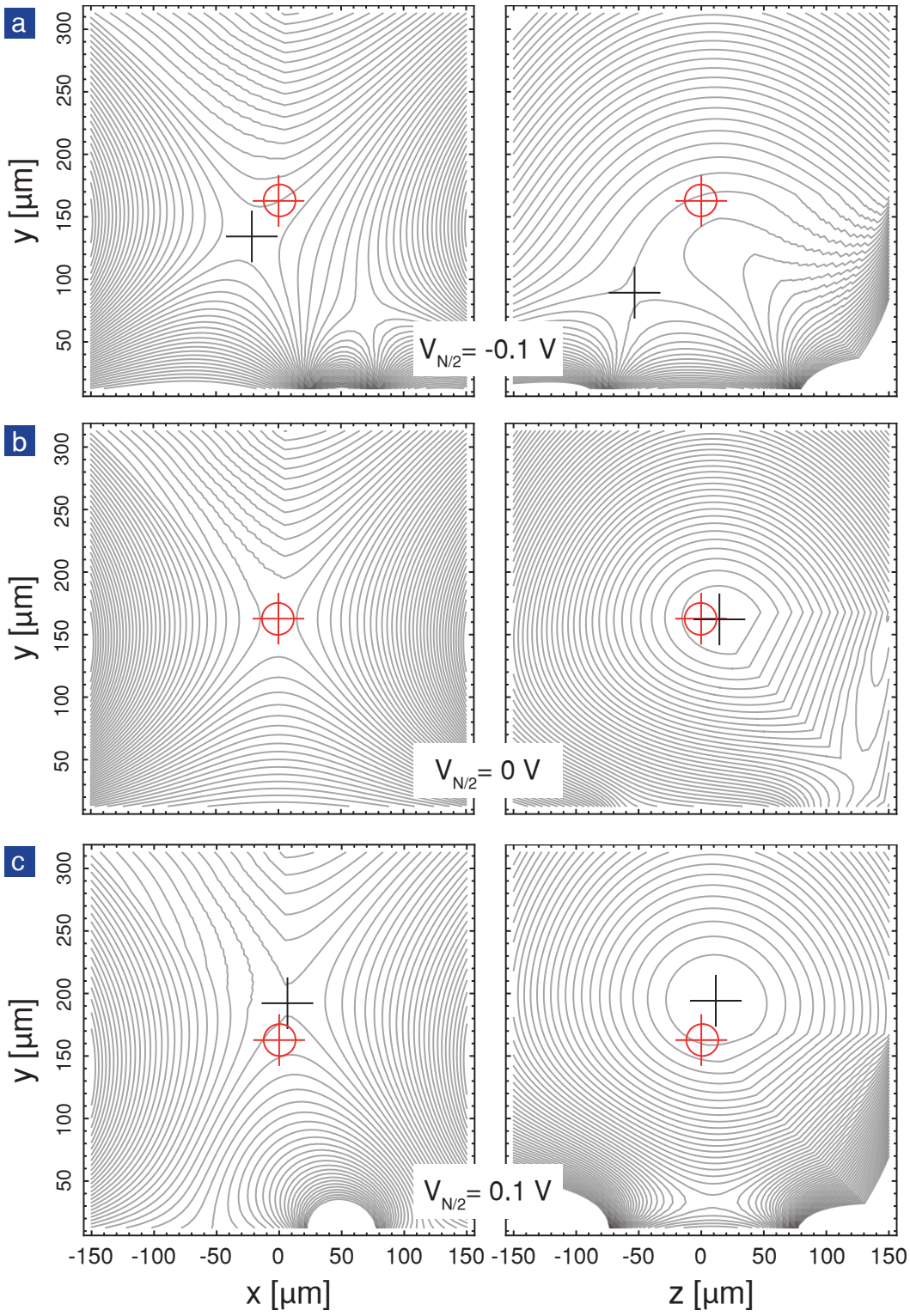


Figure 2.11 Contour plots of DC potential (case C_0) and potential field generated by W_1 (Φ_w) while sending a constant current of 1 A for different values of $V_{N/2}$ a) -0.1 V, b) 0.0 V and c) 0.1 V. The planes xy (left) and zy (right) are considered. In this case, the potential field generated by the DC segments (Φ_{DC}^{ideal}) does not counteract the field generated by the wire.

Variable Current of W_1.– If now we keep the value of $V_{N/2}$ fixed over the wire surface at the nearest position below the ion, and supply additional current values through W_1, we find that no change in segment DC5 is needed while a voltage change pro Ampere (ΔDC) has to be added to segments DC4 and DC6 as shown in Table 2.3.

Table 2.3 dc configuration for compensating the potential field generated while sending a current through wire W_1

Case	ΔDC4 [V/A]	ΔDC5 [V/A]	ΔDCF5 [V/A]	ΔDC6 [V/A]	$V_{N/2}$ [V]	A_{zz} [a. u.]
$\Delta C_{-0.1}$	-0.1	0.0	0.0	+0.1	-0.1	$3 \cdot 10^{-4}$
$\Delta C_{0.0}$	-0.1	0.0	0.0	+0.1	0.0	$3 \cdot 10^{-4}$
$\Delta C_{+0.1}$	-0.1	0.0	0.0	+0.1	+0.1	$3 \cdot 10^{-4}$

Since finding the optimal voltage configuration for the compensation of the potential field generated by the current-carrying represents an optimization problem, we have to change only one variable whereas the rest have to be kept constant.

Firstly, a way to experimentally investigate the adequate compensation configuration will require to set the zero voltage at the nearest position from the ion. As it can be seen in Figure 2.11b and in Table 2.2 for the case $C_{0.0}$, as far as the zero voltage value at the wire surface is placed nearest to the ion, we do not need any voltage change for inner segment (DC5) but a compensation of the potential field slope by the nearest adjacent segments (DC4 and DC6). To determine the ion position along the voltage distribution, we might have to run ion detection (flourescence) sequences and to determine the asymmetry of the system when setting a current going in either directions.

Once the zero voltage at the wire surface is set nearest to the ion, the compensation of the potential field has to be done by the adjacent segments in a linear manner and proportional to the current setting such that for each additional ampere we have to add a voltage compensation to segments DC4 and DC6 of −0.1 V and 0.1 V respectively.

Although challenging, due to the time-dependence nature of the stray fields, the compensation method here discussed needs at least three pairs of electrodes. They should synchronized to the applied voltage while sending a current through a (certain) wire. As example, a pair of DC electrodes (compen-

sating the voltage distribution $V_{N/2}$) around the wire center[a] and two adjacent segments (compensating the voltage drop) are proposed.

Moreover, if the trap geometry is extended vertically i.e. adding multi-layered processes, an intermediate metallic layer may serve to shield the stray electric field produced by the voltage drop along the current-carrying wires. Even more, placing a single layer planar trap on top of printed thick wires suffices on reduced those stray fields as we will see in Section 2.2.

. . . . . .

2.2 Trap III: Thick-film Technology and Glass Micromachining

The design of a planar trap fabricated by combining the capabilities of thick-film technology and glass micromachining is here described. From one hand, thick film technology leads to high current density thick metal films (Ag/Pt) printed on a high thermal conductive substrate (AlN). On the other hand, laser induced glass etching micromachining shapes high-aspect ratio structures on fused silica (SiO_2). This novel hybrid planar trap design includes three independent thick wires, underneath the ion trap, capable of nulling the magnetic field and maximizing the magnetic field gradient at ion's position.

The fabrication of high density currents is not only a vivid research field in high-frequency microelectronics but also recently in the field of laser-less ion quantum computing. Different approaches have been so far developed in order to create high aspect ratio structures which could carry high density currents. Thick film technology remains as a promising candidate with relatively low cost and high performance. Our approach relies on the latter but substitutes the typical Al_2O_3 substrate ($25\,W\,m^{-1}\,K^{-1}$) for a higher thermal conductor AlN ($170\,W\,m^{-1}\,K^{-1}$).

On the other hand, to increase planar trap performance not only material election but on-surface electrode-to-electrode distance are fundamental. Fused silica posses high electrical strengths and if combined with laser induced etching techniques high-aspect ratio structures of up to 5:1 can be used as gaps in between nearest trap electrodes[67].

Our design herein presented is of a hybrid-type in the sense that by combining the capabilities of two different fabrication processes lead to a planar trap. The previous design whit integrating current-carrying as shown in

[a] or around the region where the ion is trapped

Sec. 5.6.2, can be extended if the conducting wires are placed on a second substrate. Placing the conducting wires on a second layer, provides enough degrees of freedom to optimize wire geometry. For instance, wire width can laterally be extend such that magnetic field gradient and Joule heat transfer are maximized.

The on-glass micromachined planar trap covering a surface area of $2\times1\,\mathrm{mm}^2$ is presented in Figure 3.10. It structures on its front side a) up to 9 DC electrode pairs (blue) to hold the ions along the trap axis. The confinement along the radial directions is achieved by a pair of RF assymetric electrodes (red) resulting in a tilt of the radial modes of approximately 8° with respect to normal direction of trapping electrodes.

An ion-to-surface distance of 100 µm and mode frequencies ranging from 3 MHz are expected. On the backside of the ion trap b) deep gaps (about 200 µm) to house thick wires[a] are also etched by laser means. These gaps permit an easy ensemble of both microstructured ion trap and thick film filter board. In the next section the characteristics of the printed thick wires are discussed.

2.2.1 Ion Chip with High Aspect Ratio Structures

The design is optimized using the methods presented in Sec. 1.3.1, respectively. Since there is a non zero relative angle between the RF and DC principal axes a coupling between radial and axial oscillation modes is expected. Nevertheless neither ion stability nor oscillation mode independence are compromised, but underestimation of the coupling is an upper limit compared to a symmetric paul trap[87]. Even if the equations are coupled there are still independent three independent oscillation modes. However, the oscillation directions may not necessary be along the trap principal axes[71].

The geometry is optimize such that the radial modes are rotated with respect to the vertical direction (normal to surface electrode) in order to increase efficient laser cooling. As shown in Figure 3.10, the principal axes for RF and DC potentials are rotated with respect to the vertical direction by 8.2° and 7.1° respectively.

[a] explained later in text

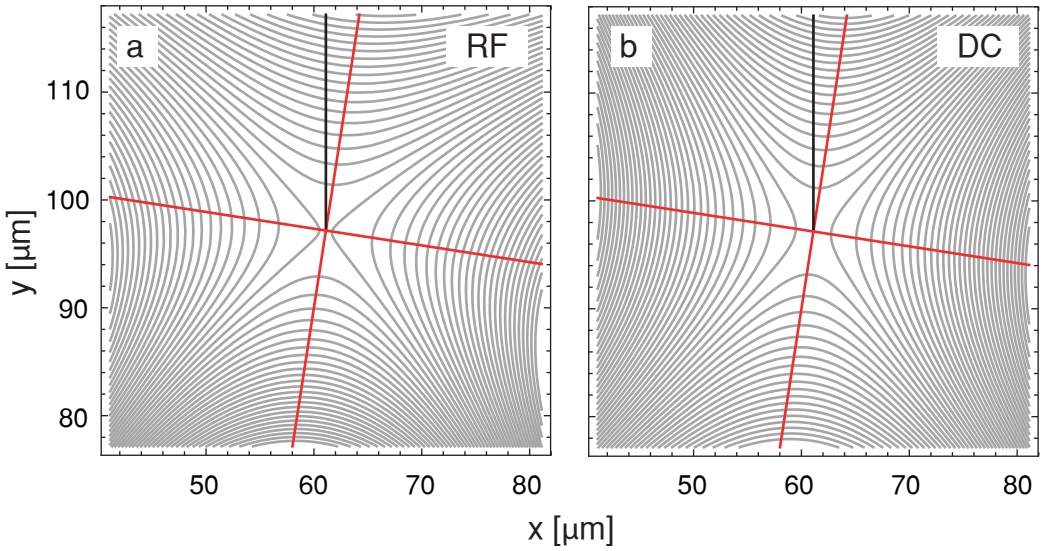


Figure 2.12 Trapping RF and DC potentials on Mainz-Translume chip. A frequency $\Omega = 2\pi \cdot 30.8\,\mathrm{MHz}$ drives the trapped ion at an RF amplitude voltage $V_{RF} = 100\,\mathrm{V}$ leading to radial mode frequencies of $\omega_x = 2\pi{\cdot}4.9\,\mathrm{MHz}$, $\omega_y = 2\pi{\cdot}3.9\,\mathrm{MHz}$ for a stability parameter $A_{zz} = 4{\cdot}10^{-3}$. The direction of principal modes between the a) DC and b) RF potential agrees within 1 %, sufficient to be corrected by the voltage applied to DC segments to avoid mode coupling.

The trap will be installed in a vacuum system together with in-situ trap surface cleaning tools and a water cooling system. This trap will be used for quantum simulation experiments for the investigation of strong (32 kHz) spin-spin interactions in trapped ions with state-dependent forces generated by strong ($10–100\,\mathrm{T\,m^{-1}}$) magnetic field gradients .

2.2.2 High-density Current-Carrying Wires

In order to generate strong magnetic field gradients high density current wires are needed. Recently thick film technology has been incorporated to fabricate UHV compatible interfaces for electrical signals (of large cross-section) printed on Al_2O_3 [88]. In this this technology is extended into a high thermal conductor such as AlN ($170\,\mathrm{W\,m^{-1}\,K^{-1}}$). The discussion regarding the fabrication steps are given in Sec. 3.5.3 and in what follows we will describe the geometry optimization of the wires placed underneath the ion chip.

A filterboard fabricated by thick film technology, including electrical lines for DC and AC voltages supply for ion trapping and pick-up filtering, also has to include current lines which carry several amperes to produce strong

magnetic field gradients. DC and AC lines are straightforward implemented and RF pick up is done by placing SMD elements close to ion trap (20 mm). More challenging is wire geometry election since various constraints have to be fulfilled. These constraints can be classified based physical and technical trap requirements.

Physical constraints.– To nullify the magnetic field, maximize magnetic field gradient and release efficiently Joule heating prior wire damage occurs, there are at least three physical constraints to optimize wires geometry as listed below.

- **magnetic field magnitude:** First, the magnetic field produced at ion's position should vanish. At least a set of three wires are needed to counteract the field in all three Cartesian directions. At the expense of trap mechanical instability –to house a higher number of wires a wider cavity on the back side of ion trap– a higher number of wires is also plausible.

- **magnetic field gradient:** Second, we are interested on quantum simulation of strong spin-spin interactions which occurs in the radial direction. The magnetic field gradient created by a set of three wires is maximized along the radial direction thus the wires should be aligned parallel to trap axis.

- **Joule heating:** Third, since several amperes are supplied through printed wires, Joule heating may lead to irreversible wire damage. Aluminum nitride (AlN) supported on a thick Cu block itself does not suffices to remove Joule heating generated when the wires are operated at maximum current (20 A). We set a wire temperature increase limit, based on a heat transfer model[89],

  $$\Delta T[t] = \frac{hw\rho J^2}{2\pi\kappa}\Gamma[0, \frac{Cw^2}{4\pi^2\kappa t}]$$

  such that the maximal current density (J) supplied during 10 ms should not exceed a temperature increase (ΔT) of about 50 K.

Technical constraints.– Additional constraints to optimize the wire geometry are included based on technical limitations. Basically, three main technical restrictions confering thick film technology resolution (line resolution), ion-to-wire distance and electrical power supply are discussed as follows.

- **line resolution:** In thick film technology, a minimal line width and spacing for two nearest conducting wires is about 120 µm. This line resolution may be scaled down to 40 µm if a tightly focused fs laser additionally ablates previous printed metal and part of the substrate. However, removing printed metal by laser pulses may turn out into rough sidewall wire profiles, and material redepostion, which may lead to inhomogeneous magnetic fields [90].

- **ion-to-wire distance:** this is mainly limited by mechanically instability of fused silica substrate. For shorter ion-to-wire we would require deeper trenches on the back side of glass substrate. Thus a fix ion-to-wire distance of 200 µm will not cause any damage substrate.

- **electrical power:** although a relative low resistivity of Ag/Pt static currents lower than 20 A can be supplied through printed wires (Ag/Pt) due to the limited power source.

The magnetic field and gradients produced by a set of three wires are analytically obtained by summing up the individual contribution of infinitely long rectangular wires of height (h_0) and width (W_c or W_o) when a static current (i_c or i_c) is sent through. Each rectangular electrode is considered to be composed of an infinite number of tiny ideal wires arranged in a rectangular configuration.

The fields at any point in the radial planes (x_0, y_0) constrained to the aforementioned physical and technical requirements lead to width optimization for the set of arbitrary number of wires. In particular, as given in Figure 2.13a), a model based on a three-wire configuration is initially considered. The ion position with respect to the trap ($d_1 = 100\,\mu m$) and to the upper wire surface ($d_2 = 200\,\mu m$) are also illustrated.

A contour plot of magnetic field gradient in the radial direction as a function of both central (W_c) and outermost (W_o) wire width is plotted in Figure 2.13b. The maximal magnetic field gradient ($\frac{\partial B}{\partial y} \approx 65\,T\,m^{-1}$) is obtained when the wires (arranged parallel to trap axis in a three-wire configuration) have width of $W_c = 150\,\mu m$ and $W_o = 250\,\mu m$ for the central and outermost wires. The abrupt change on the megnetic field gradient for width values of the outermost (W_o) wires higher than 250 µm appear as a result of the limiting current 20 A.

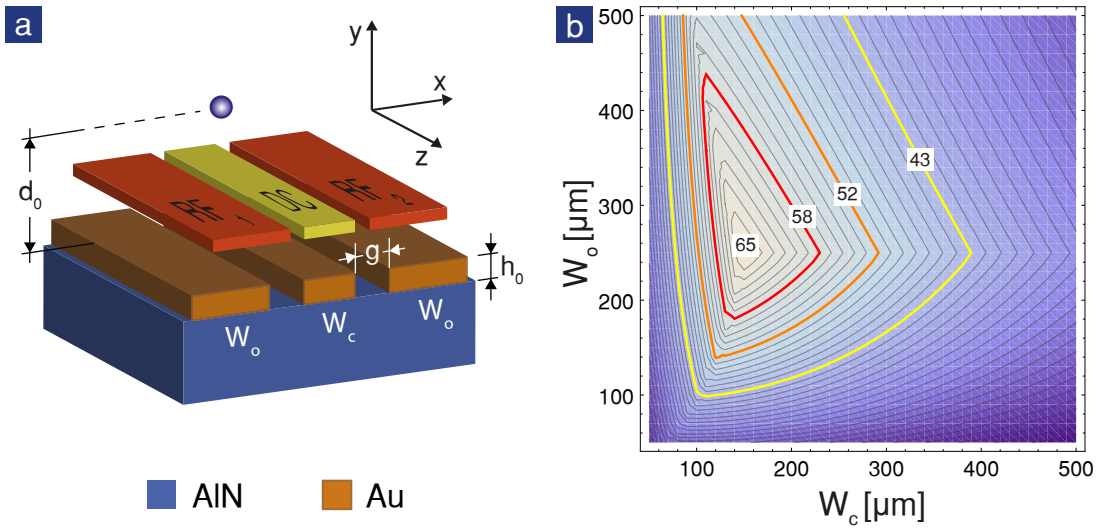


Figure 2.13 Ion-trap chip on thick film wires. a) inner section of the hybrid trap (trap substrate is omitted for illustration purposes). The ion is held at a distance (d_0) with respect to upper surface from two outermost wires of width (W_o) and a third central wire of width (W_c). All three Ag/Pt wires ($\rho = 6\,\mathrm{m\,\Omega/sq}$) of thickness ($h_0 = 40\,\mu\mathrm{m}$) which are separated by a gap distance ($g = 120\,\mu\mathrm{m}$) are printed on a high thermal conductor (AlN). b) maximal magnetic field gradient produced by metals wires arranged in a three-wire configuration. At the ion's position ($d_0 = 200\,\mu\mathrm{m}$) a maximal radial gradient ($\frac{\partial B}{\partial y} \approx 65\,\mathrm{T\,m^{-1}}$) is produced by supplying opposite currents through wires of width $W_c = 150\,\mu\mathrm{m}$ and $W_o = 250\,\mu\mathrm{m}$.

To corroborate the analytical results a numerical simulation of the fields produced by the set of wires is based on RADIA package. In addition, heat transfer simulations indicate that in order to fulfill maximal temperature increase limit ($\Delta T = 50\,\mathrm{K}$), the central wire ($W_c$) should be supplied with a current lower than 10 A. For the case of the outermost wires (W_o), the maximal supplied current should be below 20 A. This reflects on a linear dependence of the magnetic gradient for W_o larger than 250 μm as plotted in Figure 2.13b.

. . . . . .

2.3 Trap IV: Tapered RF rails

A planar ion trap with tapered RF rails offers the possibility to study systematically ion heating rates as a function of ion-to-surface distance d. In contrast to previous ion heating rates studies[62], which directly test ion heating rate as a function of the separation between two needle tips held at DC voltages, our approach relies on fast ion transport to bring the ion close to trap surfaces.

2.3.1 Design for measuring ion-to-surface dependence for ion heating rates

The trapping fields and, as consequence, the trapping parameters are numerically calculated in a similar way as explained in Sec. 2.1.2. The analytical model discussed in Sec. 1.3.1 can in principle be applied for obtaining the trapping conditions of non rectangular shapes. However that will require to discrete the complex geometry on a "enough" number of tiny rectangular electrodes. This might result in a more tedious calculation than the numerical approach which already provides accuracies as high as 99 %.

Thus we use the numerical methods explained in Sec. 2.1.2 to obtain the RF minimum and DC potential configuration for ion trapping and transport from segment 4 (S4) to segment 14 (S14). This results in a ion-height decrement from 160 to 45 µm along 4 mm. The RF amplitude voltages are required to vary from 160 to 40 V in order to place the ion from the zone 3 to zone1 at the same trapping depth. This turns out to increase the stability parameter (q) from 0.09 to 0.3, which is still within the adiabatic approximation.

A variable RF attenuator may allow to change the RF amplitude power to fall within the stability condition while transporting an ion along the RF minimum. If the RF amplitude voltage attenuation is combined together with regularized potentials plotted in Figure 2.15, the ion may be transported from Z1 to Z3 without loss. During the transport an increment on the secular frequencies are expected due to a near-field effect from the electric field produced by the trapping electrodes. From one side while reducing the ion-surface distance the radial frequencies increase from 3 to 5 MHz from zone 1 to zone 3 respectively, as shown in Figure A.3. The axial frequency can instead be kept constant along the transport operation. Moreover, the heating rate is not affected by a change on the radial frequencies but inversely proportional to the axial frequency, $S(w_x) \sim \frac{1}{w_x^{1.8}}$ [56]. We will then measure the ion heating rate for different sequences of ion-surface transports and compare their dependence to different axial frequency settings. With the help of the regularization method and the 20 segments we can create robust potentials to keep constant axial frequencies along RF minimum path from Zone 1 to Zone 3.

In a more elaborated manner, this trap is also suitable for the experimental realization of a recently proposed ion heat engine based on engineering squeezed states [91].

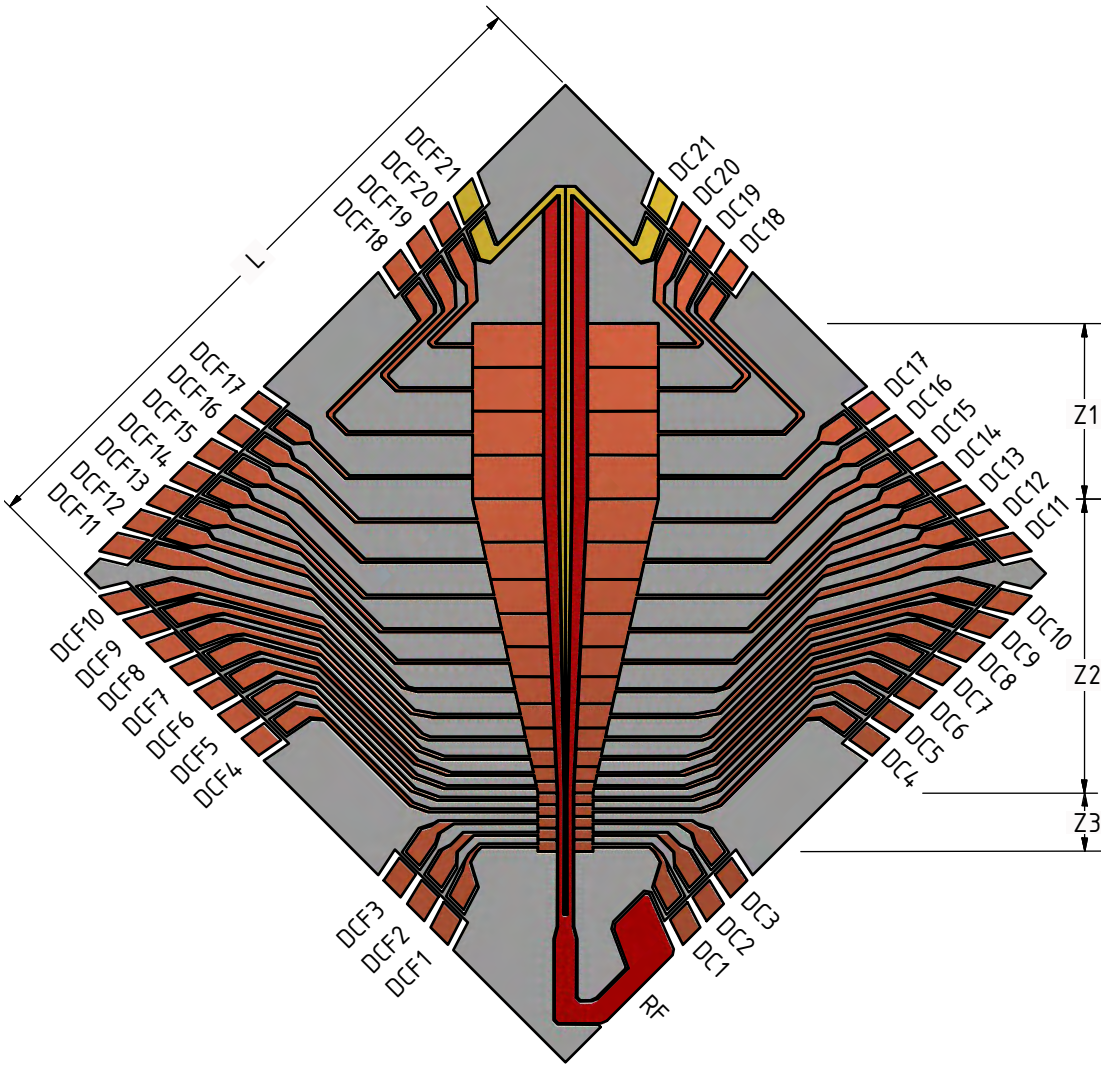


Figure 2.14 (Design layout of planar trap of tapered geometry. An ion will be trapped at zone one (Z1), transported through zone two (Z2) and bring it to zone three (Z3) by more than twenty DC control electrodes. Important dimensions of the trap: L = 9.45 mm, Z1 = 2.40 mm, Z2 = 4.02 mm, Z3 = 0.08 mm.

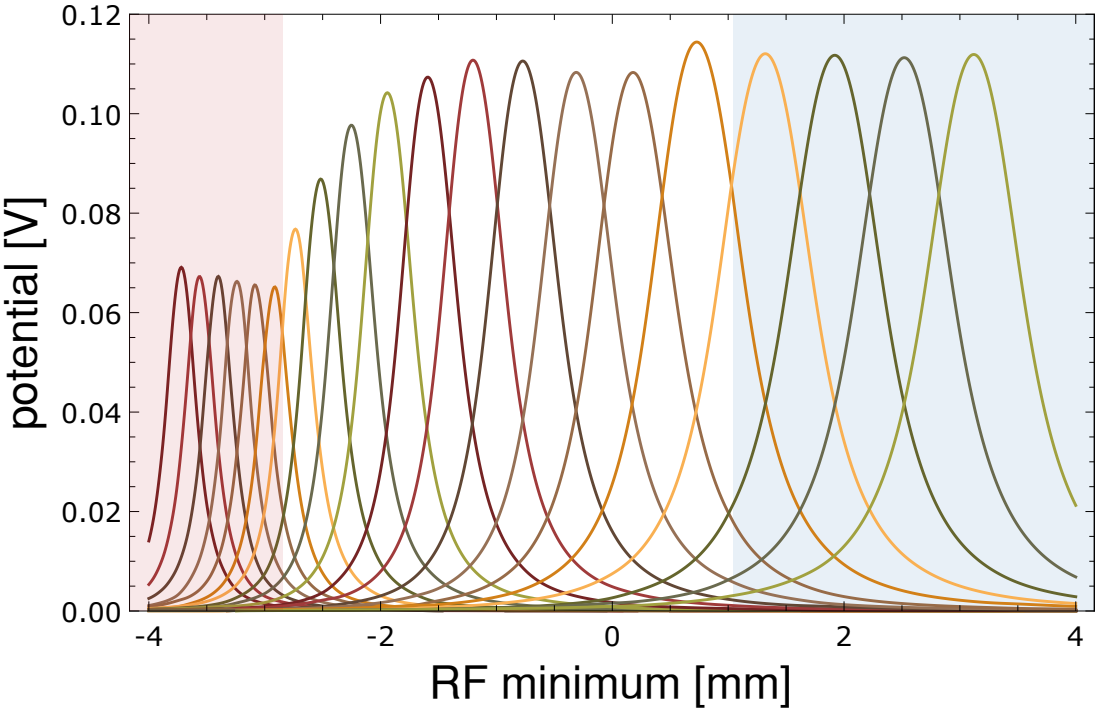


Figure 2.15 Axial potentials of planar trap with tapered RF rails. Individual axial DC potential along the RF minimum of the trap given by twenty segments set at an unitary voltage (1 V). An ion will be trapped in Zone 1 (red) transported through Zone 2 (white) and brought into Zone 3 (green) to measure the excessive motional heating along the trap from an initial ion-trap distance $d = 165\,\mu\text{m}$ to $d = 45\,\mu\text{m}$. Note that the axial potential strength is reduced when the ion approaches the trap surface and it is not critical since the potential exert on an ion close to the surface requires less potential strength to generate the desired frequency.

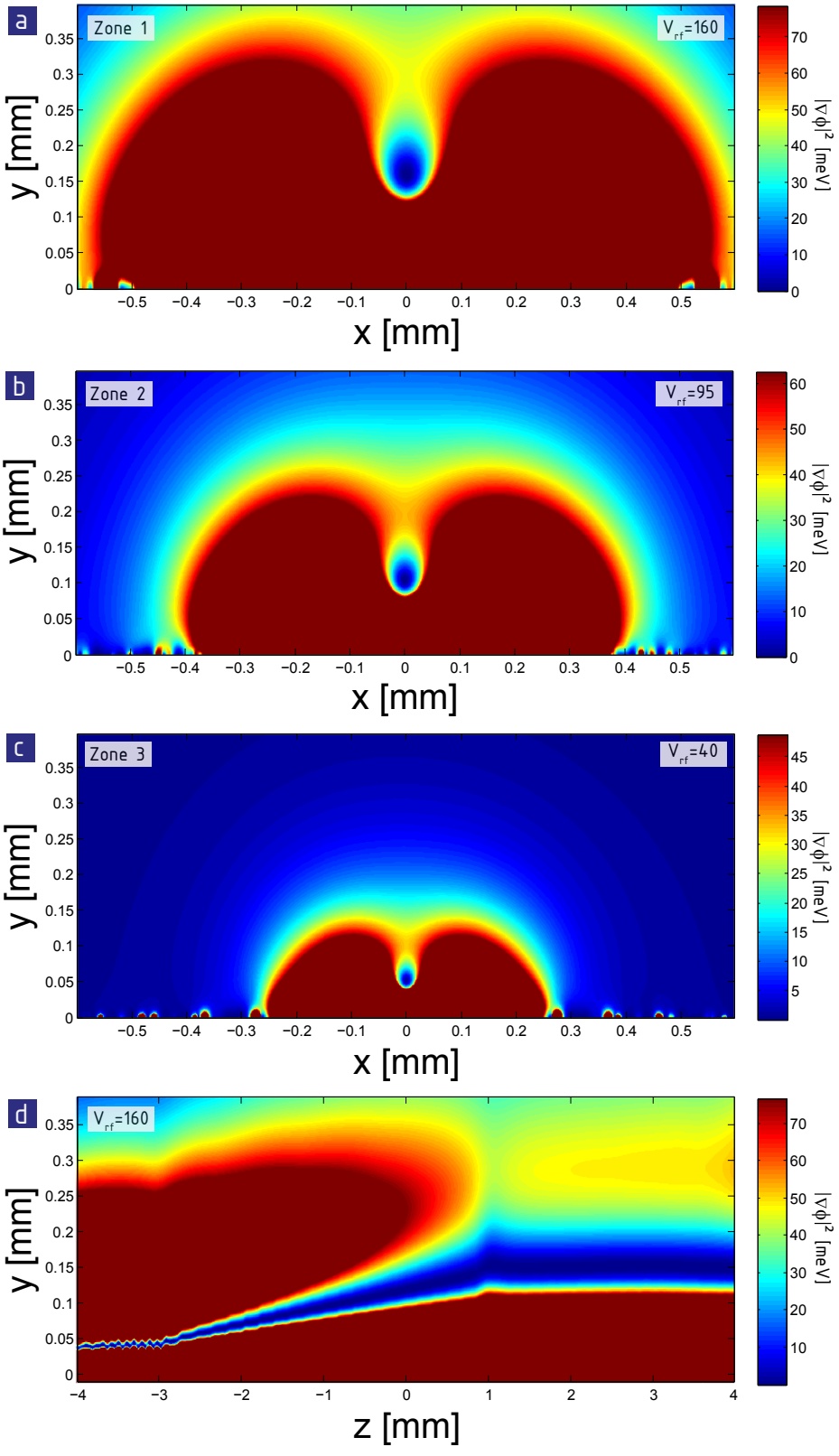


Figure 2.16 Contour plots of the pseudopotential in the radial direction in (a) Zone 1, (b) Zone 2, (c) Zone 3 and along the (d) axial direction of Trap IV

3 Trap Microfabrication

In this chapter I will detail the fabrication methods employed in this work. Along this chapter I will review microfabrication techniques and detail their role for optimizing our fabrication processes. The chapter starts with wafer preprocessing i.e. cleaning and thin layer evaporation. The optical lithography as printing tool will be covered. I will detailed two fabrication methods based basically on electroplating and thermal evaporation as electrode growth methods. These two additive processes will determine the quality of trapping electrodes. For the case of electrodes grown by electroplating, subtractive methods such as wet etching are additionally required, whereas for electrodes grown by evaporation a lift-off processes will be employed to electrically isolate all trapping electrodes.

I will conclude this chapter giving the description of laser-micromachining and thick film technology required for developing high aspect ratio structures (5:1) and high density current wires.

. . . . . .

3.1 Optical Lithography

In modern semiconductor technology the most required type of lithography is photolithography or optical lithography. In a typical photolithography process a light-sensitive polymer, called *photoresist* or solely *resist*, is exposed through a photomask to visible or ultraviolet (UV) light and developed to obtain a relief structure onto the substrate. Regularly, in a resist –an organic polymer–, under UV radiation either breaks (positive tone) or cross-links (negative tone) its chains. As consequence, in a positive resist, the areas exposed to UV radiation can be dissolved when the resist is soaked in a development solution (developer). On the other hand, in a negative resist the areas exposed to UV radiation can not be dissolved. The process of projecting the mask image onto the resist or wafer surface using a light source and a photomask is refered as printing. The equipment used for printing is called mask aligner. In general, there exist three modes of printing [92] –contact, proximity, and projection– and they are explained as follows:

- **Contact mode**: In this mode, wafer and mask are pressed against each other through a mask aligner, resist literally makes contact with the mask surface thus minimizing possible diffraction effects. Although a drawback may be mechanically mask damage or deposition of resist residues onto mask surface, a way to surpass this requires a carefully mask cleaning after exposure in order to prevent mask contamination and future detriment of mask. Since there is no gap between mask and resist by carefully controlling exposure step a resolution down to 0.25 µm is feasible.

- **Proximity mode**: As may be inferred from its name, resist is brought closed to mask surface about 20-50 μm. Due to this gap a near-field diffraction or Fresnel diffraction limits feature resolution. The closer the resist to mask surface the better the resolution is. As consequence the achievable resolution is not as good as in contact printing. Contrary, since mask and resist do not come into contact masks have longer lifetimes than in contact printing.

- **Projection mode**: Even placing a longer gap leads to far-field diffraction or Fraunhoffer diffraction effects. Most modern lithographic equipment employs the projection printing technique. It has the advantage of achieving higher resolution when compared to afore-mentioned methods. Projecting printers use a lens system to project the mask image onto the surface. So that resolution limit is defined as $\mathrm{P_{min}} = \lambda/\mathrm{NA}$ where $\mathrm{NA} = n \cdot \sin\alpha$. From this equation is clear that shorter wavelengths (λ) and/or larger numerical aperture (NA) give rise to higher resolutions (P_{min}). In modern times even higher resolutions are affordable by placing between lens system and wafer a medium with high refractive index (n), so performing what is called immersion optical lithography.

Photomask.– For printting on any type of resist a photomask is needed. The conventions to define the type of mask design vary from manufacturer. Here we adopt the following distinction. In a dark field or positive mask, its background consisting of Cr islands shadows or blocks UV light during resist exposure. In a negative resist, the exposed areas will remain after development. Transparent regions, instead, give rises to developed lines which serves as mold for structuring gold during electroplating. The technical drawings of the positive masks for Trap I and Trap II are depicted in Figure 3.1. Light areas

(gaps) are transparent to UV light, whereas dark areas (Cr) block UV light thus resulting in polymer crosslinking in a negative photoresist.

We have used both electroplating and evaporation as growth methods for gold structures as explained in more detail in Sec. 3.2.

The mask designs are shown in Figure 3.1. The first design was made for building wire structures for electrical current tests. A positive mask is also compatible when evaporation is used for growing the trap electrodes. In this situation, deposition occurs not only the open areas of a structured negative resist but also on top of it. Thus a final lift-off process or resist removal by lifting both developed resist and metal is needed.

3.1.1 Wafer Preparation

This section describes different preprocessing steps before patterning structures onto a wafer. We initially describe the wafer cleaning procedure. On a effective clean wafer surface an adhesion promoter and seed layer depositions are followed. We described then the resist deposition using the spin coating method. The wafer preparation ends with a sof-baking treatment of the prepatterned resist. Thus letting the discussion of exposure dose and post exposure wafer processing for a next section.

Cleaning.– As initial step, wafers require a cleaning process to remove possible contaminates. This step, if effective, provides contaminant-free resist film and permits subsequent processing. On the other hand, if cleaning is not carefully handled, remained chemical stains[a] or solid particulates[b] may produce undesirable effects during photolithography and material deposition. Whereas particulates may produce counterbalance masking effects during lithography, chemical stains may lead to undesirable processes during oxidation or material deposition.

There are various types of wafer cleaning techniques regarding the sort of contaminant intended to be removed. Strictly, to completely remove any slurry particulates we must first determine the contaminant source. In general, it is challenging to establish accurately this source[c]. Thus, we basically classify those into their organic or inorganic nature. A common method to remove

[a] i.e. oil gas, acetone, isopropyl alcohol
[b] i.e. solid pieces of metals or clay
[c] i.e. machine oils, hair dust, sweat, metals, chemicals waste

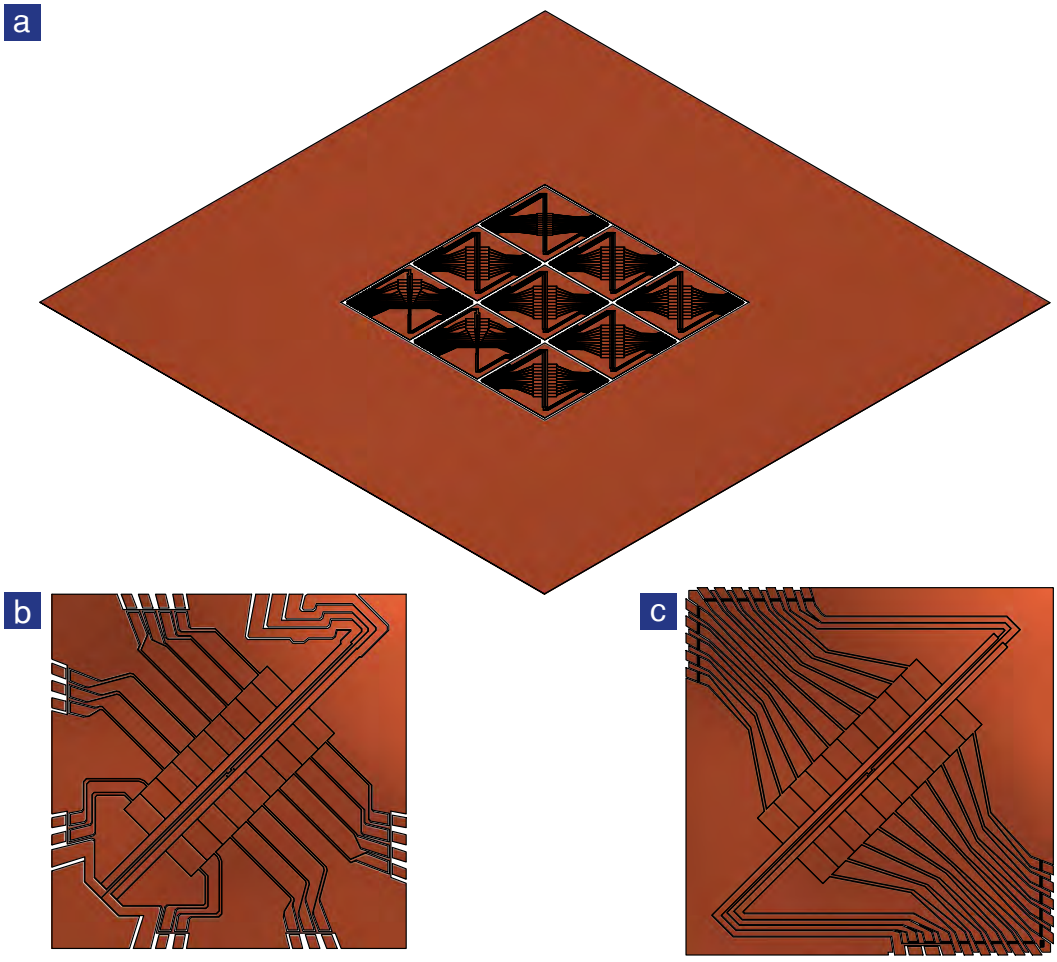


Figure 3.1 Photomask of Microfabricated Traps. a) Example of a 76.2 mm or 3″ mask containing up to nine chips of $1010\,\mathrm{mm}^2$ area. b) this design is used to fabricate the electrode by evaporation (Sec. 3.5.1). c) for this design the electrodes are grown by electroplating (Sec. 3.5.2).

organic dirt relies on the application of piranha solution[a]. In a similar manner, for their inorganic counterparts an RCA[b] solution may be required [93]. Although these methods work to some extent, they are less effective when both types of contaminates lied onto the surface.

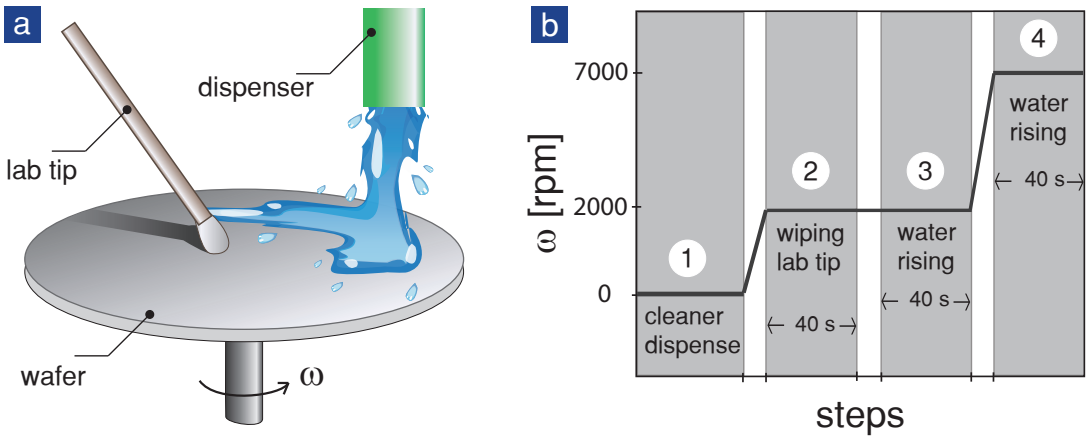


Figure 3.2 Chemical-mechanical wafer cleaning to reduced slurry particulates below 0.5 µm. (a) cleaning solution (AJAX®) is dispensed on a wafer held by a rotating block and lab swaps sweeps the wafer surface to remove particulates. (b) typical step sequence during a wafer using chemical-mechanical means.

After optical inspection of our wafers we have found dirt particulates of around 30 µm. Trying the aforementioned cleaning methods no significant improvement was observed. Additionally after employing acetone (5 min) and isopropanol (5 min), as suggested by the two-stage method, and wafer inspection under AFM in phase mode, we detect alcohol chains residues adhered to the wafer surface.

These results point out the need of an alternative cleaning method which puts aside common solvents such as acetone or isopropanol. Therefore, we have developed a cleaning method which removes both inorganic and organic dirt combining mechanical and chemical means [94]. With an easy handling and effective cleaning, it reduces contaminates' size down to ~0.5 µm. This permits to achieve narrow lines which releases after photo-lithography reliable electrode gaps below 1 µm.

[a] a mixture 4:1 of sulfuric acid (H_2SO_4) and hydrogen peroxide (H_2O_2)
[b] a mixture of hydrochloridic acid (HCl) and hydrogen peroxide (H_2O_2)

The method consists on gently applying a commercial chemical mean[a] on the wafer surface, then a lab swap wipes the surface whereas the wafer is vacuum held and rotated on a metal spindle as shown in Figure 3.2a. The wafer surface is then rinse with abundant deionized water (DI) whereas the wafer is rotated at an initial angular speed of 2000 rpm.

The step sequence can be broken down into as many as four main steps as shown in Figure 3.2b. (1) We start by dispensing the cleaning solution whereas the wafer is still. (2) We then ramp the spindle to 2000 rpm and wipe the surface with a lab tip. We slice the tip always outwards wafer geometric center. We repeat the process during 40 s. (3) At the same speed, and during 40 s, we rinse the wafer surface with plenty of DI water. (4) Right after we ramp the spindle to 7000 rpm and rinse the surface again with abundant DI water. At last the samples are dried with a N_2 gun and placed in direct contact with a hot plate at 120 °C for 5 min. Once the surface is dried and free from solvents or water residues we proceed with the deposition of an adhesion promoter (i. e. Cr or Ti) as explained next.

Adhesion Promoter.– Typically in microfabrication, we aim to support metal electrodes onto insulator substrates, to achieve that we need the help of an intermediate layer named adhesion promoter. The use of an adhesion promoter is justified since an adhesion enhancement between two "incompatible" materials is needed. Typically in IC and MEMS manufacturing technologies, either Cr or Ti are extensively used as intermediated layers[93]. The election is also based on the feasibility of later removing this layer with minimal or no damage of electrode structures. Cr and Ti provide a relatively easy wet etching as will be explained in Sec. 3.5.

In this work we have used nanometric layers of Cr and Ti as intermediate layers between gold electrodes and our[b] substrates. After cleaning the wafers employing the method previously described, we placed the wafers under high vacuum at about 2.0×10^{-7} mbar. When a layer of Ti was needed, we covered the wafer thermally evaporating Ti till a thickness of 50 nm. In the case Cr layer with a thickness of 5 nm was deposited. Right after we deposited a 50 nm gold layer since the Cr was used in combination with an electroplating process, and a gold seed layer was fundamental. The details of the evaporation setup are given in Sec. 3.3. The importance of these layers in the fabrication flow

[a] AJAX®
[b] Glass and Sapphire

are illustrated in sections 3.5.2 and 3.5.1, for the case of Cr and Ti thin layers, respectively.

Once the wafer preparation is done, we can continue with the resist patterning by optical lithography.

3.1.2 Patterning

This section describes the methods to produce our resist mask to later grow the gold electrodes by either electroplating or evaporation process. The processes presented here may define the resist profile and as consequence the yield of the fabrication flow. The processes here presented may be taken as tunable parameters to optimize the patterned structure for an electroplating or evaporation environment which is the topic of a following section.

Spin Coating.– After the wafer treatment, and prior to dose exposure we coated the wafer utilizing the spin coating technique. This method takes advantage of centrifugal forces. material viscosity and surface tension to obtain a desire film thickness. In similar manner as was illustrated in Figure 3.2, we placed our wafer on top of a spinner. The wafer is hold on the spinner base by means of a vacuum system and rotated to a proper spin speed. The election of our resist (AZ nLOF 2070), is based on its reliability to both electroplating and lift-off processes. Whereas it is suitable to mild enviroments (pH > 10), which is the case for most common gold precursors, it also presents a pronounced negative profile desirable for a lift-oft process.

We have characterized our resist by utilizing this technique. In combination to PGMEA[a] a change in viscosity of the resist can be achieved and as consequence its thickness can be controlled from 4 to 16 µm. It is important to notice that even using a mass proportion ratio of 5:1 (AZ nLOF 2070 : PGMEA) the nominal resist thickness can not be reduced further than 4 μm. For higher dilution ratios a detrimental behavior on the resist might be observed. Nevertheless, film thicknesses from 4 to 16 µm fit well to our developed lines from 2 to 10 µm leading to electrode gaps with high aspect ratio (2:1).

Due to the the phenomena involved during spin coating, such as centrifugal forces and surface tension, edge protrusions are produced. These protrusions may have a thickness of about 20 µm and consequently reduce the maximal achievable printing resolution for developed lines. Therefore, an extra

[a] Propylenglykolmonomethylethylacetat i.e. 1-Methoxy-2-propyl-acetat

edge removal process is required, which conveniently has to be perform after resist soft-baking to avoid future dark erosion areas prior exposure.

Soft-Bake.– After spin coating and right before UV resist exposure we placed the wafer in direct contact to a hot plate. This process is called soft-bake (SB) and is done for practical reasons as explained below. First heating the coated resist to a proper temperature and certain time we induce solvent diffusion remaining in the resist. As consequence, an enhancement of surface adhesion properties and prevention of resist foaming by N_2 created during UV exposure are achieved. Even more the use of soft-bake reduces high dark erosion[a] during development. High dark erosion reveals after exposure as mouse-bites, hole and thinning of resist. Therefore, dark erosion have to be avoided or minimized, in order to achieve electrode sidewalls with reduced sidewall roughness or even to avoid shortcuts.

Soft-bake has to be performed under stringent temperature conditions. From one hand, insufficient soft-bake (short time and low temperature) might produce sticking of resist residues to photomask and as consequence a detriment of mask and patterning structures is produced. On the other hand, long soft-bake (long time and high temperature) may maximally eliminate resist solvent, thus making the resist extremely brittle. When a brittle resist is used during an electroplating step, adequate growth of isolated electrodes may be rather complicate or impossible. Additionally long soft-bake may lead to complications during development step since decomposition of photoreactive compound produces longer development rates of exposed resist.

Therefore, an optimization of the soft-bake parameters was carried out. The best results are found if we place the samples in direct contact to a hot plate at temperature of 100 to 120°C for about 1 min per micrometer. The appropriate soft-bake temperature and the bake-time depend on the resist thickness as shown in Table 3.1.

The remaining protrusion resist at the wafer edge is removed after spin coating and soft-bake by rinsing an isopropanol stream at the wafer edge whilst it is rotated by the a spinner. The wafer is placed in a similar manner as in Figure 3.2 onto a spinner and rotated at about 2000 rpm. Then the isopropanol stream reduces about 1 mm in radius a potential patterned area.

[a] Dark erosion refers to fast or slow development rates at localized areas as function of solvent concentration

Exposure Dose.– A mask aligner[a] with output intensity of 10,2 mW/cm^2 is employed for resist exposure to UV radiation. The exposure dose is a function of time,$D = I \cdot t$ given in [mJ/cm^2], where I is the output intensity and t the exposure time.

Depending on the film thickness different exposure times and exposure dose are required. For instance, extremely high dose effects negatively the resist sidewall profile and compromises resist lift-off. Whereas low exposure dose pronounces undercut negative resist profiles (favorable for a lift-off process) a longer exposure dose defines vertical-like profiles (desirable for maximal inter-electrode gaps during electroplating).

In an initial stage during optimization of exposure dose we have used Si wafers since its crystalline structure permits a straightforward cleaving with a diamond tip. We have observed both Si and glass wafers, covered with Au/Cr layers, require similar exposure doses. This criteria allows us to optimize quickly and systematically many samples to finally apply the appropriate parameters on a wafer of interest. The corresponding parameters used after optimization are listed in Table 3.1.

Post-Bake.– In our case, the resist AZ nLOF 2070 requires a post-exposure bake (PEB) which enhance UV sensitivity on its exposed areas and adhesion between it and coated wafer. In addition this type of bake catalitycally enhance and complete photoreactions initiated during exposure dose in the chemical amplified resist[95]. We can also use the PEB treatment as a tune parameter to obtain wider inter-electrode gaps and rounded electrode edges. In a similar way as its SB counterpart the adequate temperature and bake time depend on film thickness. Typical values for temperature and time are around 100-120 °C and one minute, respectively. The parameters found after optimization are presented later in Sec. 3.1.2.

Development.– The development step consists on removing non cross-linked polymer chains during dose exposure. We place two beakers on a water bath at 23°C. The first beaker contains about 20 mL of AZ 826 MIF[b] developer and the second one about 20 mL of DI water. The exposed and post-baked samples are soaked in a development solution of AZ 826 MIF for a certain amount

[a] Karl Suss MJB3 (350W), Garching, Germany
[b] metal ion free

of time[a]. After certain development time the sample is removed from the developer and soaked in the second beaker containing DI water for 20 s. After removed from DI water the sample is rinsed with abundant DI water to drain possible resist and developer residues. The samples are dried using a N_2 gun and monitored under optical microscopy. If development time is not enough the process is repeated as needed until we complete the development cycle (DC).

Patterning Parameters.– In this section we detail some important parameters for patterning our wafers. Note that in Table 3.1 are listed values corresponding to different types of substrate and resist film thicknesses prior patterning. The influence of using different types of wafers during exposure does not indicate any clear tendency. On the other hand, significant effects are observed when resist thickness is increased. To achieve optimal results we characterize the patterning process optimizing the exposure dose as well as baking, development and post-exposure times.

Table 3.1 Typical patterning parameters of AZ® nLOF 2070 depending on wafer type and resist film thickness.

Wafer	FT	Linewidth		SB	ED	PEB	DC
		Resist	Mask				
	[μm]	[μm]	[μm]	[°C, s]	[mJ/cm^2]	[°C, s]	[s]
1" BF33	3.3	2.10	1.4	100, 45	41.82	120, 45	110
1" BF33	9.2	4.68	2.6	90, 120	236.64	110, 120	220
2" Sapphire	5.0	4.0	4.0	100, 90	41.82	120, 70	205
2" Sapphire	5.0	4.68	4,0	100, 90	36.72	120, 70	220

. . . . . .

3.2 Metal Depostion

This section encompasses metal deposition techniques employed during the course of this work. A physical vapor deposition (PVD) technique as thermal evaporation to deposit either an adhesion layer, a metal seed layer or metal electrodes in a lift-off process is employed. On the other hand an electrochemical forming technique such as electroplating to grow high aspect ratio structures is used. The first successful microfabrication of planar traps relied on thermal evaporation and electroplating as metal deposition methods[96]. In the

[a] see Table 3.1

next parts of this section a brief review of those techniques as well as our manufacturing parameters are given.

3.2.1 Thermal Evaporation

The main advantage of thermal evaporation, among other PVD techniques, is its relatively simple application and its high surface purity. Recently it has been taken up again as in-situ coating method to improve heating rate of planar ion traps for two orders of magnitude after treatment[66]. The evaporation technique is a heritage from ICs and MEMS manufacturing and represents a versatile coating tool with application in diverse type of substrate materials. The type of raw material is not only limited to metals, which are extensively used, but solid, liquid or vapor sources may be also applied. Typically substrates are plastics, ceramics, glass and semiconductors[93].

In an evaporation reactor we take advantage of low temperature needed, due to vacuum conditions, to vaporize metal materials with high boiling point such as Al, Au, Ag, Cr, Cu and W. The process itself consists of some elementary steps under a vacuum of 10^{-7} mbar as illustrated in Figure 3.3a. (1) We induce the synthesis of the coating vapor by resistively heating a gold nugget placed on a tungsten crucible. (2) The transport of Au vapors to developed resist structures takes place. (3) Au vapors condensate onto resist and/or wafer surfaces.

Controlling the current, typical deposition rates of 1 Å/s are achieved when vacuum conditions are in the 10^{-7} mbar range. The mean free path of vapor evaporant are on the order of evaporation reactor dimensions and evaporated atoms leave the nugget following straight-line paths until they collide with gas molecules or hit the resist structures. The choose of low rate depositions is intended as overheating of tungsten crucible may lead to alloy impurities deposition.

We deposit metal thin films using the system shown in Figure 3.3a. The conic shape of metal vapors limits the region of homogenous coating. Still we are able to place inside the homogenous region (HR) up to eight wafers of 1" diameter (BF33) and six of 2" diamater (Sapphire). The process is illustrated in Figure 3.3b. In the case of the Au/Cr layer the following steps are done. After wafer cleaning, we place either BF33 or sapphire wafer inside HR. The samples are sticked to a wafer holder downside to avoid contaminant deposition. We also allocate metal nuggets of Cr and Au onto separated tungsten

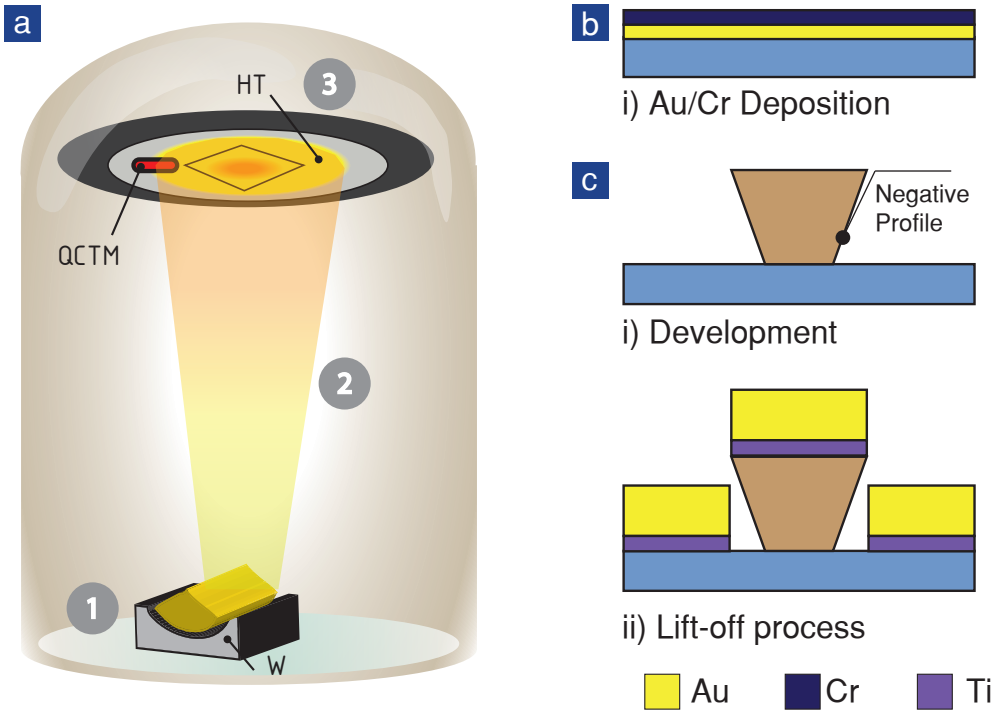


Figure 3.3 (a) Thermal evaporation reactor. (b) Coating of Cr ahesion layer and Au seed layer. (c) Lift-off process. Abbreviations and numbers are explained in text. (Not to scale)

(W) crucibles. We close the reactor and turbopump until a stable pressure of 1×10^{-7} mbar is reached. Next we first deposit a Cr layer of 6 nm with a deposition rate about 1 Å/s. The deposition thickness is controlled using a quartz crystal thickness monitor (QCTM) installed inside the HR. After Cr layer we deposit 50 nm of Au with a rate of 1 Å/s. The final sample Au/Cr/substrate is suitable to an electroplating process as explained in section 3.7 and is illustrated in Figure 3.3b.

3.2.2 Lift-off

The deposition of high quallity gold surface electrodes is also carried out via thermal deposition[a] under a similar setup given in Figure 3.3. The application of thermal evaporation serves as metal deposition method for a lift-oft process as illustrated in Figure 3.3c. The sapphire wafer(450 µm) to be coated is previously cleaned and photolithography patterned resist structures released on top of its surface. The wafers are mechanically clamped and the vacuum chamber is evacuated until a pressure of 2×10^{-6}mbar is reached. At first an adhesion layer (50 nm of Ti) is deposited to enhance adhesion between the wafer surface and deposited electrodes. A second deposition of a thick conductive layer (1.9 µm of Au) defines the trapping electrodes. The pronounce negative profile of developed resist (AZ nLOF 2070) permits a sufficient shadowing to avoid sidewall deposition of Au vaporants. A final step require to rinse the wafer in a constant flow of acetone to take off both resist mask and Au/Ti layers avoiding redeposition onto wafer structure surface.

3.2.3 Electroplating

In planar traps, interelectrode gaps need to have high aspect ratio, if possible, close to (1:1) in order to shield effectively local charges on exposed insulator generated by an impinging laser beam. Electroplating is the most powerful additive process to build very high aspect ratio (HAR) microstructures. Indeed, it offers the possibility of building large aspect ratios, of up to 4:1[94], and of 200:1 for micromechanical systems[93].

In contrast to thermal evaporation, electroplating represents a low-cost alternative when HAR structures are required. Moreover, its chemical and conforming nature permits to transfer with high fidelity fine (nanometric size) re-

[a] Nanofabrication facilities at Ben-Gurion University

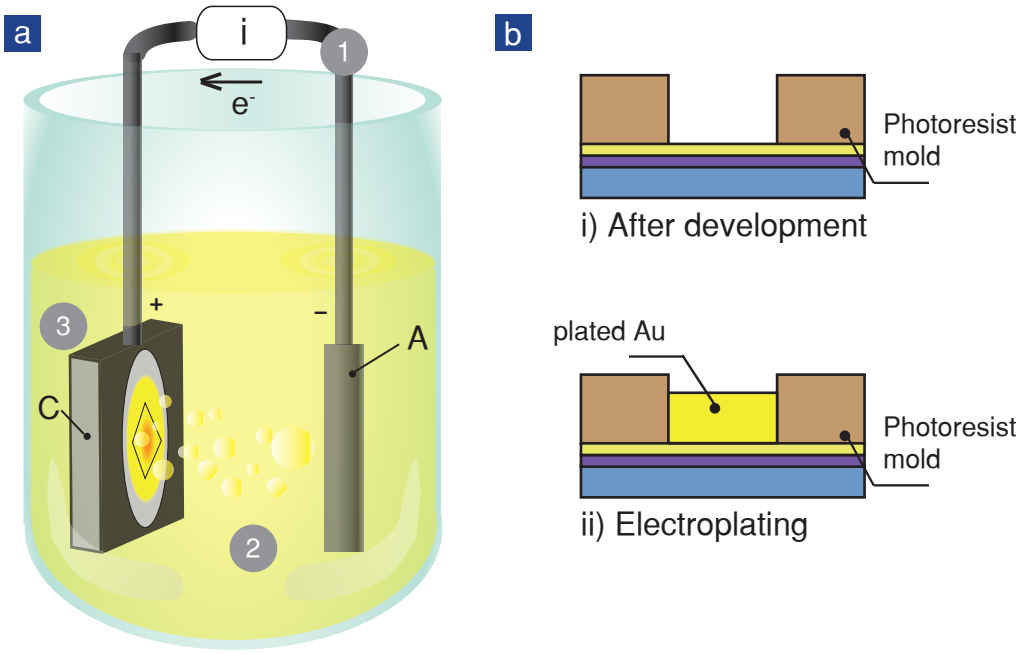


Figure 3.4 Electroplating deposition. a) a typical electroplating cell. b) basic electroplating step in the fabrication flow. Abbreviations and numbers are explained in text. (Not to scale)

sist features. In particular, it yields very smooth electrode sidewalls typically below 1 nm. Thus higher trap operating voltages are possible before electrical breakdown occurs. As a rule of thumb, and to obtaining high quality electrode surfaces one requires high control of deposition parameters –current density, temperature and plating solution. If, in addition, low deposition currents are used smooth surface finishes as good as the ones produced by evaporation can be obtained [97].

The setup used for electroplating[a] gold onto a BF33 or shappire wafers is schematically shown in Figure 3.7. It consists basically on two electrodes connected through an external wire immersed in a cyanide-free electrolyte solution (pH = 7.5). The wafer is clamped to a cathode (C) and immersed in a mixed-salt gold complex[b] to close the circuit an anode electrode (A) serves as counter electrode. (1) A constant current is applied between the two electrodes and Faraday processes occur at each electrode/electrolyte interface. (2) The charge transport occurs in the electrolyte via ion motion. (3) A cathodic

[a]The author thanks detailed information provided by U. Heikel from MicroGan GmbH
[b]Microfab 100-B, www.enthone.de

reaction occurs and gold sulfite complex is reduced. At the anode an oxidation of a distinct conducting material closes the redox process. We chose AZ nLOF 2070 due to its high adhesion properties and chemical stability even to mild environments (pH > 8). An effective metal conforming in between the resist mold is attained. After metalization removal of resist mold is basically performed inmersing the wafer in NMP and plasma etching in O_2, as described in detail in Sec. 3.3.

. . . . . .

3.3 Resist Stripping

After metal deposition a resist removal step is required. This may be done either by wet or dry chemical means or a combination of both. Chemically removing a resist mold (after electroplating) or a developed resist (after photolithography) requires the use of any solvent such as acetone or N-Methyl-2-Pyrrolidon (NMP). In an early optimization stage we first immerse the electroplated wafers in 20 mL of NMP for 36 h. After optical inspection traces of resist residues on top of the Au seed layer are found. An additional plasma etching cleaning ($RIEO_2$) for 15 min is performed. After optimizing the process immersing the wafer in NMP for 1 h and under $RIEO_2$ for 20 min no resist residues are observed under optical microscopy inspection.

. . . . . .

3.4 Etching

A subtractive method by removing material in an anisotropic or isotropic manner, are termed dry and wet etching respectively. The starting seed layer, grown by pilling an adhesion layer (Cr) and a subsequent (Au) layer, short circuit the trapping electrode.

Each of them have different characteristics which should be taken into account when planning a fabrication flow. Despite Cr starts to diffuse at about 350° its thermal deposition and wet etching is straightforward. Cr etchant does not attack conventional wafers as Si, Borosilicate glass or quartz. Whereas Ti deposition and etching is relatively simple, a special care has to be taken when combining to SiO_2 materials, since Ti etchant (HF) chemically attacks such wafers. It is common that noble (bulk) metals do not interact [a] with their environment following neither an oxidation or corrosion process.

[a] at the nanometric level chemical and physical properties might change dramatically

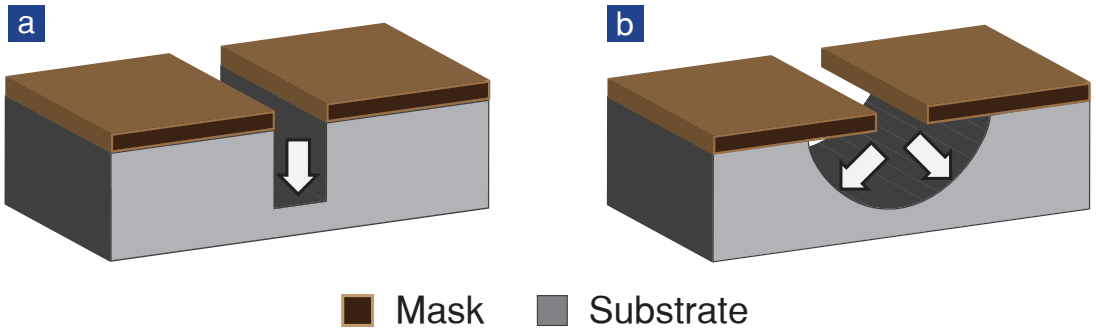


Figure 3.5 Isotropic and anisotropic etching. (a) Anisotropic etching results in vertical profiles. (b) In isotropic etching a material is removed in all directions.

3.4.1 Gold Etching

As it is explained in section 3.1.1 a seed layer (50 nm of Au) is deposited on top of wafer coated with an adhesion layer (5 nm of Cr). A prerequisite to electrically isolate the electroplated structures requires the removal of this layer. After resist stripping the Au seed layer is selectively etched by using a gold etchant solution (KI/I_2) where gold and iodide form gold iodide (AuI) as follows:

$$2\,Au + I_2 \rightarrow 2\,AuI \tag{3.1}$$

We add KI to the solution to increase the solubility of AuI. After optimizing the etching process we find an etch rate about 16 nm/min with a 1:1 solution proportion. Application of this solution removes the Au layer whereas a detriment effect on the final surface roughness of Au is observed. After diluting KI/I_2 in H_2O, with a solution proportion of 1:2 a lower etch rate of 4 nm/min is obtained. The optimized process to successfully removing a 50 nm seed layer of gold without appreciable detrimental on Au surface roughness consists as follows. We immerse the wafer of interest in a puddle containing a diluted 1:2 solution of KI/I_2: H_2O. After a certain time immersing time (typically 1 min), we remove the wafer from the puddle, rinse it with abundandt DI water and inspected under optical microscopy in a polarization mode to detect surface reliefs. We repeat the method until no trace of Au is resolved, which commonly is achieved after cycle time of 12 min.

After the seed layer removal to completely electrically isolate the trapping electrodes has to follow a etching process of the adhesion layer. This step is carried out as follows.

3.4.2 Chromium Etching

During fabrication an intermediate layer to enhance adhesion between wafers and trapping electrodes in order to avoid electrode peel off is required. This thin Cr layer (5 nm) has to be remove in order to to completely achieve isolated islands of electroplated Au structures. After immersing our free-seed layer wafers in a commercial Cr etchant solution[a] an etch rate of 600 nm/s at room temperature is observed.

This rate does not permit a high control of the etching process and excessive under etching produce removing completely the adhesion layer. Thus producing the peel off of electroplated structures. Diluting the commercial Cr etchant into DI water with a 1:2 solution ratio permits to reduce the etch rate to 100 nm/s and have higher control of Cr under etching. The time require to completely remove the adhesion Cr layer and 1 μm Cr under etching about 10 s are required.

[a] Ceric ammonium nitrate : perchloric acid : H_2O (10.9 % : 4.25 % : 84.85 %))

. . . . . .

3.5 Fabrication Layouts

All fabrication steps (or simply fabrication flow) are hierarchical in nature. Each further step requires a well-optimized previous step. For this work, two fabrication flows were developed. One based on evaporation and a second one based on electroplating as growth methods, respectively. The main difference is fundamentally on the type of metal deposition employed in each method.

The first fabrication flow, developed in collaboration with the group of Prof. Folman[a] is based on a lift-off process. This method yields electrodes with a thickness of up to 1.9 µm grown via thermal evaporation as it will be explained in Sec. 3.5.1. A second method is developed in house where electroplating permits to structure high aspect ratio (2:3) trap electrodes given in detail above and summarized in Sec. 3.5.2.

3.5.1 Trap I: Evaporated Gold Electrodes

The fabrication flow to produce high quality electrode surfaces is illustrated in Figure 3.6. On a good heat conductivitor (sapphire substrate), a photolithographic step is carried out on a negative tone resist. The developed resist serves as a mask for the deposition of a 50 nm adhesion layer of titanium and a high quality gold film of about 2 Îijm thickness, both being deposited by a thermal evaporator. The Ti and Au deposited on the resist top are removed in a lift-off process. From an AFM analysis we find an rms surface roughness of less than 5 nm, while an SEM analysis determines the edge roughness to be 40 nm (peak-to-peak) (see Fig. 3). The process has an overall alignment accuracy of better than 1 µm. In our tests, we continuously apply 205 V amplitude without observing any sparking which we attribute to the high quality of the electrodes without sharp edges.

3.5.2 Trap II: Electroplated Electrodes

We first prepared our wafers as described in section 3.1.1. We cleaned either a polished borosilicate glass (BF33) or sapphire wafer. a) Onto a cleaned wafer an adhesion layer (Cr, 5 nm) and seed layer (Au, 50 nm) are deposited via thermal evaporation. The Cr layer ensures good adhesion between Au electrodes

[a]Ben-Gurion University, Tel Aviv, Israel

and glass substrates whereas the Au layer prompts high electrical conductivity during Au electrodeposition. b) The prepared wafer was spin coated with a negative photoresist (AZ nLOF 2070) and printed in direct contact to a dark field (Cr) photomask. c) After UV exposure the wafer was rinsed in a developer (NMP), which removes unexposed parts of photoresist and conforms a resist mold for electroplating. d) The wafer was placed in a plating bath where the cavities of the photoresist mold defined the trapping electrodes. e) The wafer was rinsed in a stripping solution (EBR) and cleaned under dry etching ($RIEO_2$). This latter step assures complete removal of remaining developed resist. f) The seed layer was removed using a gold etchant (KI/I_2) and a final Cr etchant isolated electrically the trapping electrodes. We diced the wafers and ball bonded the chip electrodes to an 84-pin Kyocera chip carrier using Au wires of 25 µm in diameter. Under UHV conditions with 10-7 mbar, we investigated the limit of the applied electric field by raising slowly the applied voltage. We observed an electrical breakdown at approximately 180 V for 1.2 µm to 720 V for 4.0 µm gap width, far above the required trap voltages.

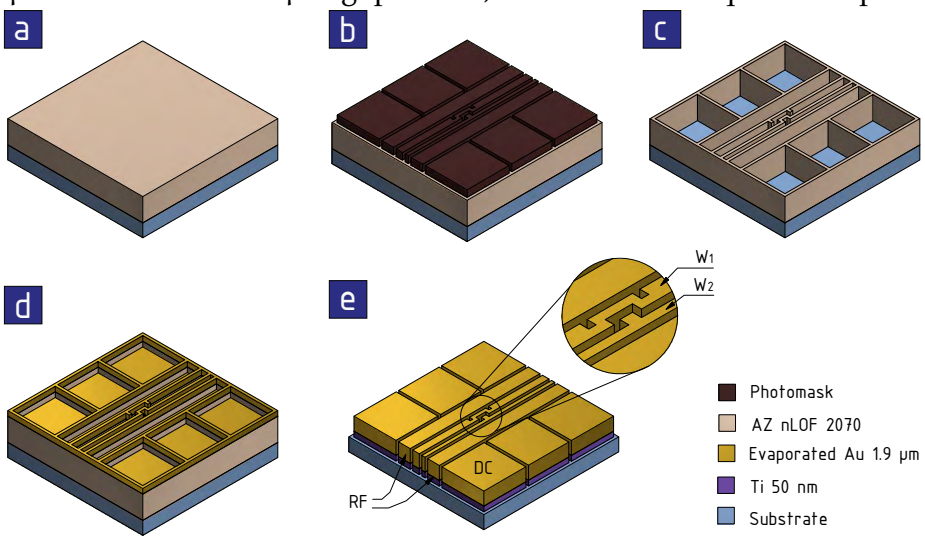


Figure 3.6 Fabrication layout including thermal evaporation and lift-off for Trap I. a) spin-coating of resist on substrate (sapphire or BF33). b) photolithography in contact mode to a bright field mask. c) development of pronounced negative profile resist. d) thermal evaporation of gold on resist cavities and resist top surface. e) resist lines and gold deposited on top of it are removed via a lift-oft.

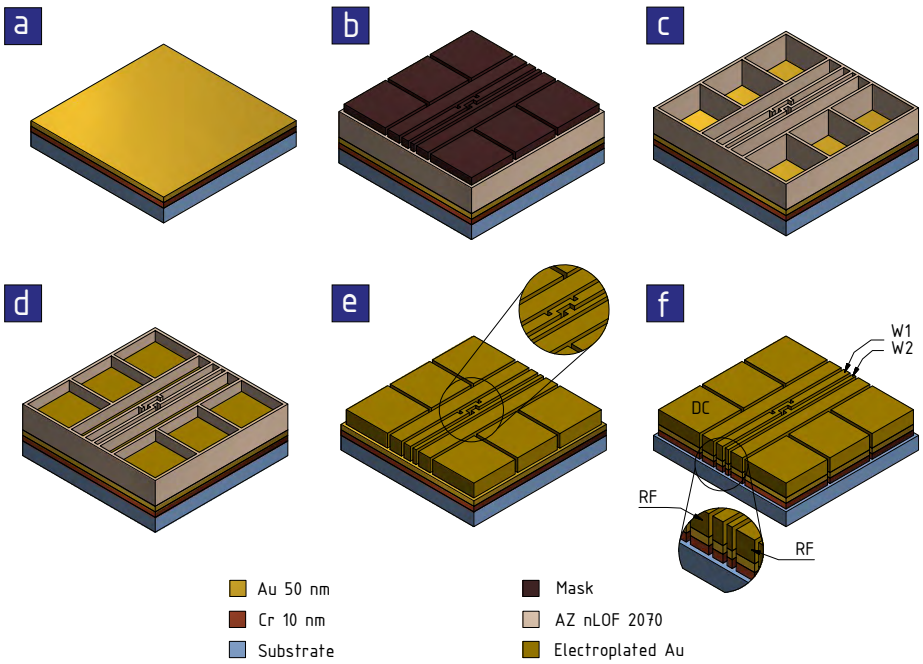


Figure 3.7 Fabrication layout including electroplating for Trap II. a) after wafer cleaning an adhesion layer (Cr, 10 nm) and seed layer (Au, 50 nm) are deposited via thermal evaporation. b) photolithography is carried out in contact mode using a dark field mask on a spin coated resist. c) after development a negative resist (AZ nLOF 2070) serves as mold during d) electroplating. e) the resist mold is stripped and finally f) both adhesion and seed layers are wet etched.

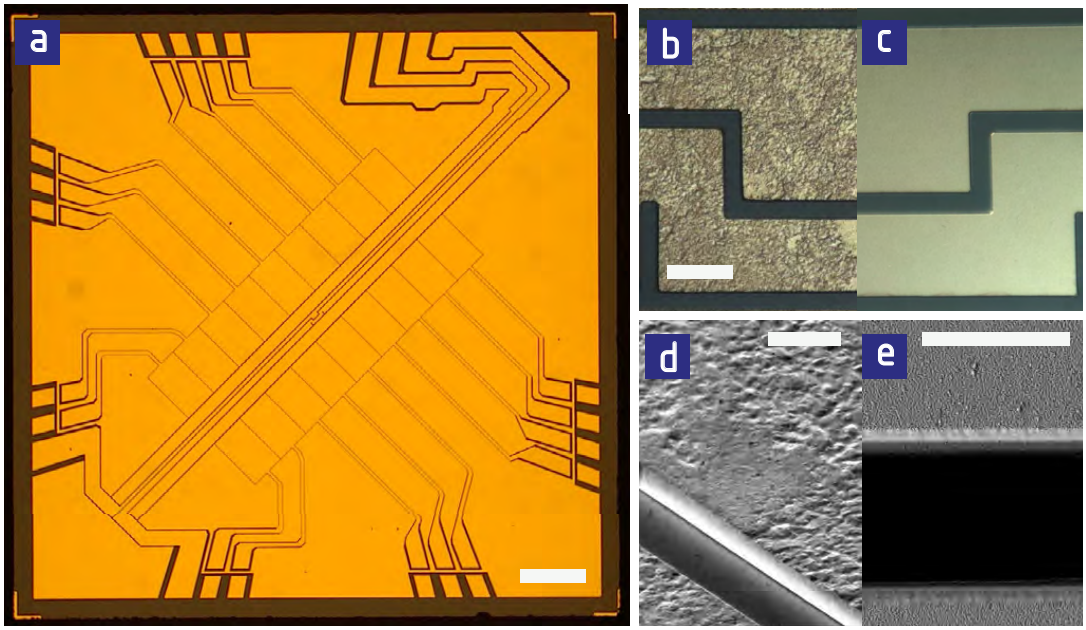


Figure 3.8 Fabrication output from electroplated and evaporated Traps. a) Optical micrograph of (whole chip) Trap I fabricated via gold evaporation as described in Sec. 3.5.1, scale bar equals 1 mm. b) optical micrograph of half section of the innermost part of Trap II fabricated via gold electroplating using the methods described in Sec. 3.5.2, scale bar equals 50 µm. c) optical migrograph of innermost part of Trap I. d) SEM micrograph of innermost part of Trap II and e) SEM micrograph of innermost part of Trap I, scale bars equal 10 µm.

3.5.3 Trap III: Laser-micromachining and thick film technology

The hybrid design here presented combines technologies recently incorporated to ion trap microfabrication such as glass-micromachining and thick film technology. From one hand, thick film technology permits the realization of metal structures(Ag/Pt) printed on AlN substrates. On the other hand, laser-micromachining combined with Al thermal evaporation allows to fabricate ion traps with high aspect ratio structures. The schematic representation of both fabrication processes are given in the following sections.

Metal Wires Printed by Thick-Film Technology.– There are currently various technologies which achieve the fabrication of high current density wires. Among them stand out electroplating, conventional printed circuit board (PCB) and thick film due to their resulting high aspect ratio structures. Electroplating is also backbone of a more elaborated fabrication process termed LIGA[a] from which structures with high height-to-width aspect ratio up to 100:1 are obtained. Although high aspect ratio structures are achieved by the LIGA process its main limitation consists on the elevated production cost since X-ray lithography is required .

Moreover, printed circuit board (PCB) technology relies on poor thermal conductive ($0.23\,\mathrm{W\,m^{-1}\,K^{-1}}$) substrates made for instance of polymide[b]. In this respect, thick film technology represents our best option with additional low cost production and high height-to-width aspect ratio. In the past, Al_2O_3 has been extendedly used as substrate for microelectronics components but recently it has been successfully substituted by AlN [c].

The fabrication of thick wires in our design via thick film technology was carried out at Fraunhofer Institute IKTS[d] at Dresden. It starts, Figure 3.9a), with 1) laser drilling or lasering of the AlN substrate for the integration of vias and cavities to place in there the micromachined ion trap . 2) A conductor paste of AgPt slurry in dispensed on the substrate through screen printing to create soft circuit lines. 3) The slurry paste is hardened via firing at a temperature of 850° and finally 4) the filterboard is cleaved. Additional metal wires are printed on top of AlN to solder SMD components for RF-pickup filtering.

[a] derived from the german definition Lithographie, Galvanik und Abformung, developed in Karlsruhe more about that see Ref. 93

[b] In the case of UHV compatible substrates

[c] www.anceram.de

[d] Keramische Technologien und Systeme, www.ikts.fraunhofer.de

Ion Trap on Micromachined Fused Silica.– The ion trap is structured on fused silica (300 µm) by laser induced wet etching[98]. The fabrication is commercially available by Translume Co [a]. The electrode gaps (10 µm) constituted the removed material with high height-to-width aspect ratio (5:1).

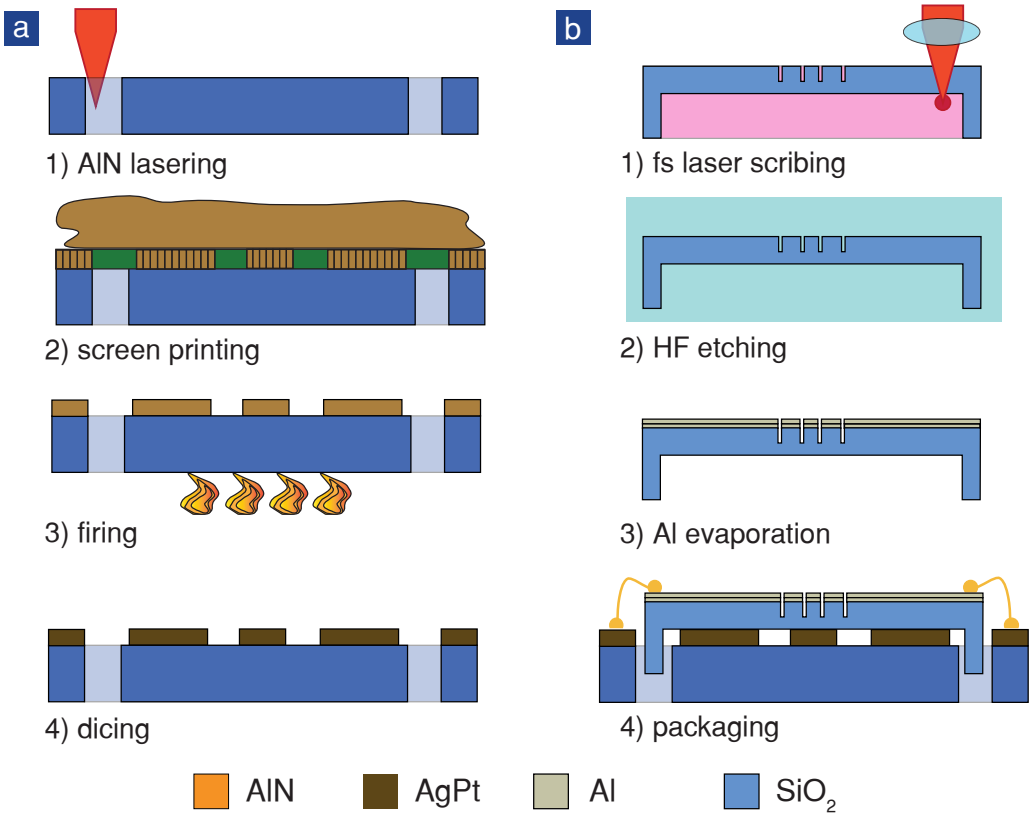


Figure 3.9 Glass-micromachining and thick film technology. a) Thick film technology: 1) AlN substrate is machined using lasering for drilling holes, 2) screen printiing of AgPt slurry, 3) AlN and paste are fired above 850° for paste hardening, 4) substrate is diced. b) Laser assisted glass etching: 1) a femtosecond laser changes locally the reactivity of glass delineating the ion trap structures, 2) previous illuminated glass substrate is rinsed into an etchant HF bath and illuminated parts are selectively removed, 3) microstructured glass upper surface is coated by thermal evaporation of metal layers (Al) up to 400 nm, 4) both printed AgPt and micro-machined fused silica substrates are glued by an UV epoxy. Finally ion trap electrodes are wire bonded onto printed AlN substrate for electrical feeding.

Trap electrodes are grown by evaporation of Al on top of the micro-structured fused silica substrate. Glass micro-structuring basically consists on two steps as illustrated in Figure 3.9b). 1) 3D scribing of a preprogrammed design is

[a] www.translume.com

done by focusing an IR femtosecond (fs) laser which optically damages fused silica substrates. 2) Exposed areas are removed in a etchant bath, 5% aqueous solution of hydrofluoric acid (HF). Microstructured silica substrates (3) are coated with Al thin film (300 nm) at Prof. Häffner's Group.

Finally, both AlN filterboard and microstructured ion trap are assembled and wirebonded. The heat produced by the thick wires when runing at maximal current (20 A) is stimated to be about 2 kW thus an additional water cooling system has been included in the trap setup together with an Ar^+ bombardment. In a next section (Sec. 4.1.5) we will discuss the assembly and setup update for this trap.

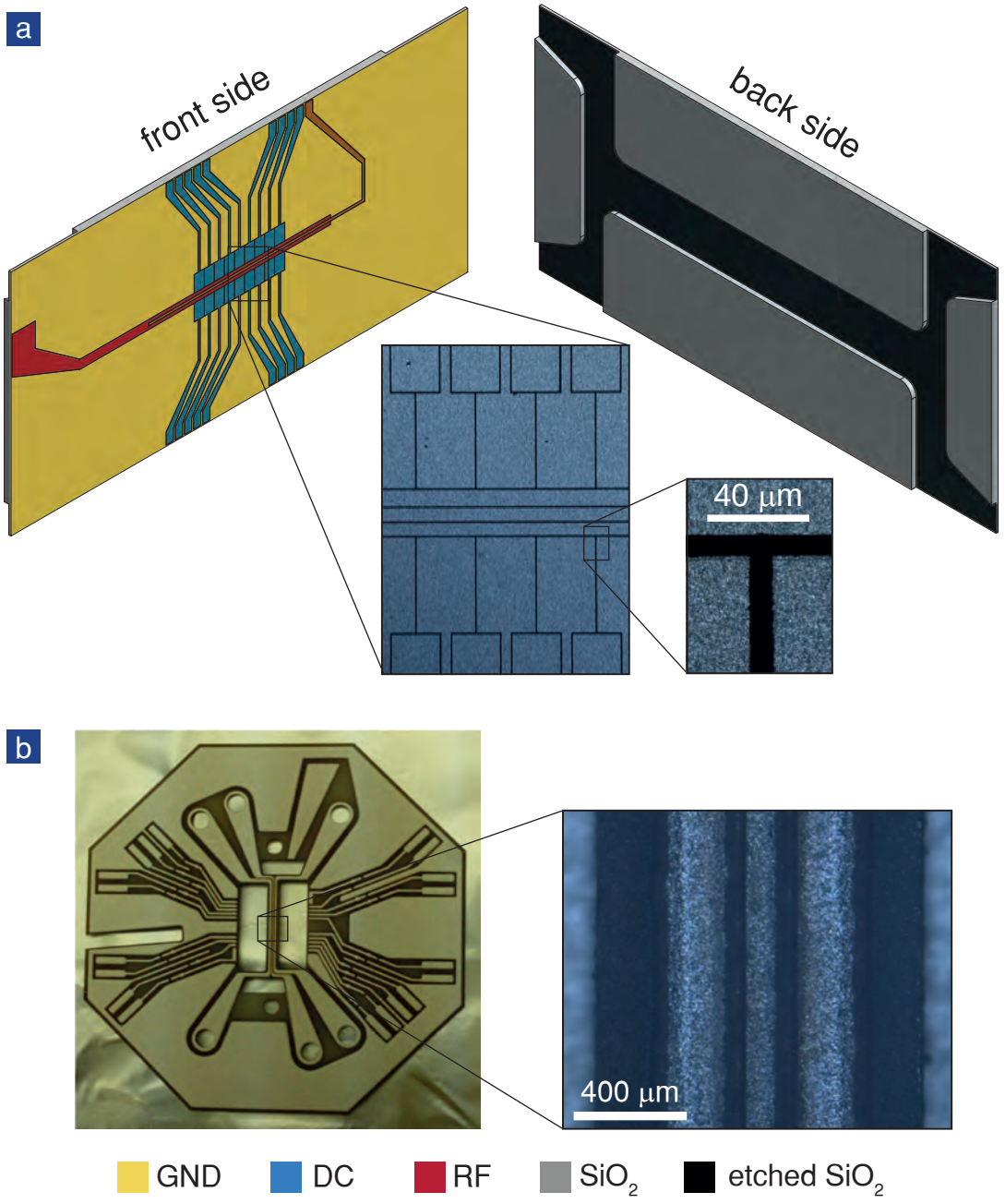


Figure 3.10 Micromachined ion chip and thick printed wires. a) micromachined ion chip: electrode gaps (black lines, inset) of $10\,\mu m$ are done by laser induced glass-etching method of fused silica. On the front side, electrodes are shaped by Al evaporation ($400\,nm$). On the back side, a wide cavity of width~$1\,mm$ and depth ($200\,\mu m$) is also laser microstructured to house three thick wires printed on an additional AlN substrate (not shown). The total area of trap chip covers a surface of $2{\times}1\,mm^2$. b) thick wires and filterboard: Ag/Pt circuits are screen printed on AlN substrate ($75\,mm$). Holes are laser drilled to partially insert back side of ion chip, electrically connect thick wires (W_c and W_o), to mount SMD elements and to feed DC and RF trapping voltages. The inset shows a optical micrograph three thick wires of widths $W_o = 330\,\mu m$ and $W_c = 150\,\mu m$ and gap between wires of $g = 120\,\mu m$

4 Chip Assembly and Apparatus

The chapter starts with description of the vacuum components. Of high relevance is the carefully chip packaging and chip montage as a continuation to the fabrication methods explained in the last chapter. After the chip is assembled and mounted inside an ultra high vacuum system special care has been taken during the bake-out process. The supply of either static or oscillating voltages is treated in a following section. For the manipulation of the dipole and quadrupole transitions of $^{40}Ca^{+}$ ion qubits and for laser cooling, the required laser setup is described. This chapter ends with the description of the hardware used for the experiment control.

. . . . . .

4.1 Vacuum Vessel

An ultrahigh vacuum (UHV) system is used to decrease the probability of ion-molecules collisions prior and after ion trapping. The vacuum system[a] has been adapted for these experiments from a previous modular configuration[99]. The modified system allows the operation of arbitrary trap geometries but principally of complex trap geometries with a high number of control electrodes. Up to 100 DC voltages can be readily fed through the system top flange. The vacuum circuit starts with a main cylindrical chamber which viewports axis and trap center coincide with each other at its geometric center, as shown in Figure 4.1. The pumping stage for low pressures (10^{-11} mbar) is connected through an axes B_8 and consists of a ion getter[b], a Ti sublimation pump[c] and an ionization gauge[d]. The low pressures pumping stage is backed by a turbo molecular and mechanical pump for fore pumping (10^{-7} mbar) through an angle valve[e] with same cross section (NW63CF) as the pumping circuit for high pumping power.

The main chamber has an inner diameter of 199 mm, height of 149 mm and its center is separated by 220 mm from the optical table. The laser beams may

[a] Hositrad, Hoevelaken, Niederlande
[b] VacIon Plus 20, StarCell 20 l/s, Agilent Technologies, Frankfurt, Germany (earlier Varian Inc.)
[c] ST22, Vacuum Generators, St. Leonards-on-Sea, England
[d] UHV-24p, Agilent Technologies, Frankfurt, Germany (earlier Varian Inc.)
[e] UHV all-metal angle valve, VAT, Haag, Switzerland

be focused through three optical axis ($B_1 - B_5$, $B_2 - B_6$, $B_3 - B_7$) at distances of 187.6 mm from normal viewports (B_2, B_3 amd B_6, NW63CF) or 47 mm from inverted viewports (B_1, B_5 and B_7, NW63CF) to the chamber center. All laser are also aligned parallel to the optical table using XYZ-stages[a] with a precision of 10 µm. All viewport windows are made of quartz glass (SiO_2) and coated from both sides[b] with an anti-reflection layer for a wavelength of 397 nm.

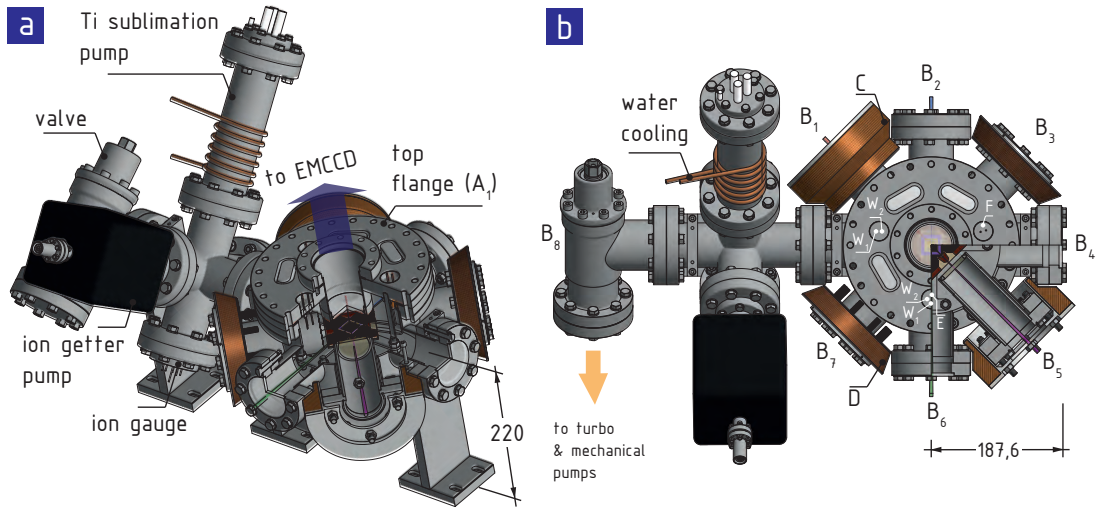


Figure 4.1 Vacuum system setup. a) Isometric projection combining elevation and section of the main cylindrical chamber. b) top view of vacuum system optical axis and principal electrical connections for the current-carrying wires (W_1 and W_2), as well as rf line and dc connectors are shown. (units in mm)

A flange (NW200CF) at the top of the main chamber serves as multitask element, having an inverted viewport (NW75CF) for ion imaging, four dc voltage connectors (Sub-D 25 pins) and high voltage feed throughs (up to 5 kV) as high DC current and RF lines.

4.1.1 Chip Assembly of Trap I

We have fabricated ion traps by two methods differing each other essentially on the type of electrode growth method, Chapter 3. The chips having electroplated electrodes are used for electrical breakdown and current failure tests and the results are explained in Sec. 5.1. On the other hand, a trap chip having

[a] see Sec. 4.3.5
[b] Thin Film Technology Tafelmaier GmbH, Rosenheim

evaporated electrodes is assembled an installed in an UHV system as shown in Figure 4.2.

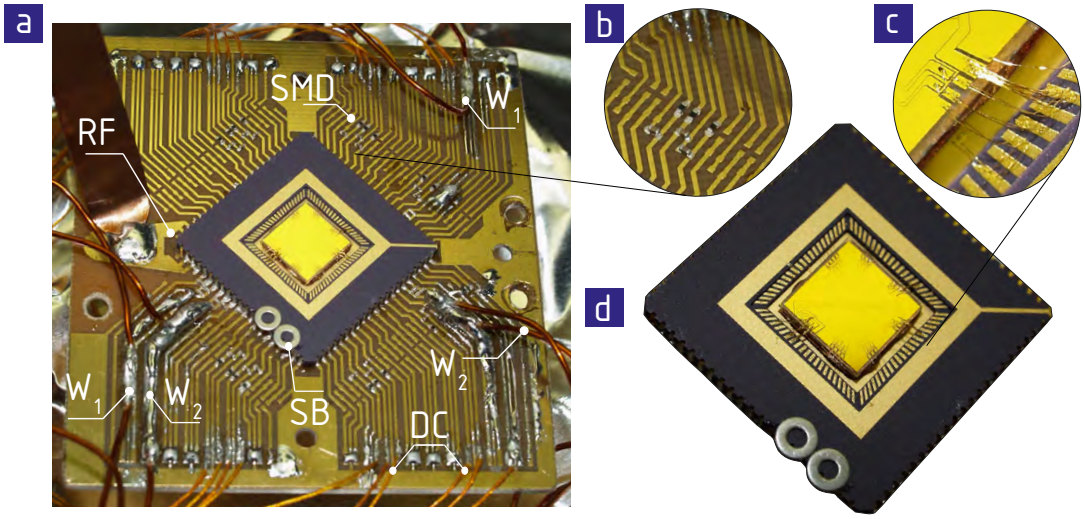


Figure 4.2 Trap packaging and RF filtering. a) Ion chip in a ceramic carrier glued on a filter-board. b) surface mount devices (SMD) for filtering frequencies higher than f_c =74 kHz. c) wirebonding (two bonds) for DC electrodes and (eleven bonds) for current-carrying wires W_1 and W_2. d) ion trap chip mounted on a Cu block and wirebonded to lead less chip carrrier, the washers serve as shielding block for Ca vapors.

The chip assembly consists of some basic but fundamental steps as explained below.

- **Cleaning**: prior chip assembly into the UHV chamber, the carefully use of an effective cleaning method is of essential importance not only to improve UHV compatibility but also to minimize possible traces of adsorbed contaminants on the trap surface. All elements placed under vacuum are cleaned using a two-stage method. This consist on placing the samples under a container with acetone, followed by isopropanol and a final step of deionized water. The time use for each step may vary according to contaminant source but typically 5 min in each steps are taken. At the end of the assembly the trap surface has to be free of contaminants to reduce excess heating rates. Therefore, the only element placed under vacuum without cleaning at this stage is the trap chip.

- **Packaging**: A chip having evaporated electrodes after microfabrication (Trap I), Sec. 3.5.1, and without additional cleaning is glued onto an ox-

igen free Cu base block previously cleaned by a two-step process. The optical epoxy[a] is gently applied at the sides of the chip and Cu block edges, and cured using an UV lamp[b] for 30 s.

After hardening of UV epoxy, a Cu block is glued at the bottom of the inner cavity (12 mm) of a lead less ceramic chip carrier[c] (84LCC) with the UV epoxy. The ceramic chip carrier not only provides excellent vacuum compatibility but also highest thermal contact and the additional advantage of setting the trap exchange process relatively simple.

- **Wirebonding**: All electrical paths from the chip are wire bonded by gold wires with 25 µm in diameter employing a wire bonder[d] set in ball mode, Figure 4.2c and Figure 4.2d. For connecting the rf and dc electrodes four and two wirebonds are respectively done. Previous current failure tests using one wirebond for a current-carrying wire show an electrical failure after sending 1 A for 100 ms. Therefore, for the current-carrying wires up to eleven wirebonds are done to avoid current failure by sending currents up to 10 A for 100 ms. As a precaution to avoid floating electrodes, the inner metal part of the ceramic carrier as well as all remaining pins in it are wirebonded to ground.

- **Noise Filtering**: After chip wirebonding the ceramic chip carrier and low pass filters are mounted to a polyimide laminate printed circuit board (PCB)[e], Figure 4.2a and Figure 4.2b. Low pass filters for each dc electrode are built at about 20 mm apart from the trap edge using surface mount devices (SMD). Each low pass filter is constituted from a capacitor (6.5 nF)[f] and a resistor (330 Ω)[g] with a cut-off frequency of 74 kHz. The capacitors are set closer to the trap than the resistors for filtering noise signal coming from outside into the chamber.

  Both ceramic carrier and SMD elements are connected using a silver conductive epoxy[h]. For a better mechanical stability of the ceramic chip carrier, UV epoxy is applied and cured at each of its corners. The conductive

[a] Epo-Tek OG142-13, Polytec PT GmbH, Waldbronn, Germany
[b] BlueWave 50, Dymax Europe GmbH, Frankfurt, Germany
[c] 84LCC, KYOCERA
[d] HB10, TPT Wire Bonder GmbH & Co KG, Karslfeld, Germany
[e] Isola p97, Isola GmbH, Düren, Germany
[f] C1005, TDK Electronics Europe GmbH, Düsseldorf, Germany
[g] R0402, Yageo GmbH, Hamburg, Germany
[h] Epo-Tek H20E, Polytec PT GmbH, Waldbronn, Germany

epoxy is prepared with a 1:1 weight ratio between Part A and Part B. An effective epoxy hardening is achieved by placing the filterboard in direct contact to a hotplate at 180 °C for 60 s and the temperature is ramped down to 140 °C for 2 h. Longer times and higher temperatures (~180 °C) may be also carry as far as nor SMD or kapton cables have to be heated.

- **Soldering**: The electrical connection for each dc electrode at the filterboard is done through Kapton cables soldered with a lead free wire solder[a] and clamped to D-type connector receptacles[b] at the top flange. After soldering the parts are rinsed with deionized water to remove soldering residues. The filterboard is screwed on a stainless steel holder and mounted faceing the inner side of an inverted viewport for flourescence detection as shown in Figure 4.1.1.

- **Characterization**: The resistance of wires W_1 and W_2 are measured after wirebonding at the outmost ceramic carrier pins, the corresponding values are 1.9 Ω and 2.8 Ω, respectively. The resistances measured after mounting the ceramic carrier to the filterboard are 3.0 Ω and 4.4 Ω, for W_1 and W_2 respectively. The increase of the resistance is clearly affected by the application of the Ag conductive epoxy between the external carrier pins and filterboard paths. In the future the only use of lead free solder wire may guarantee no dramatical increase on the resistance together with a re-flow oven. We have also connected capacitors to wires W_1 and W_2 of 9.8 nF which in combination to the resistance of the wires provide a filtering frequency of 5.4 MHz and 3.7 MHz respectively.

[a] 331 Solder Wire, Kester, Euro Tool GmbH, Hagenburg, Germany
[b] Allectra GmbH, Berlin, Germany

4.1.2 Trap Montage of Trap I

For an easy exchange and/or montage of the trap into the vacuum chamber we make use of a flange (NW200CF) as a multitask element. This top flange, as it is named for simplicity, provides up to 100 sub-D pins for the supply of control voltages. Additionally, up to eight welded feedthrough, operating up to 20 A, are used as rf and dc current lines (oven and two current carrying wires, W_1 and W_2). A technical cross section drawing is shown in Figure 4.3 to illustrate the installation of the trap into vacuum.

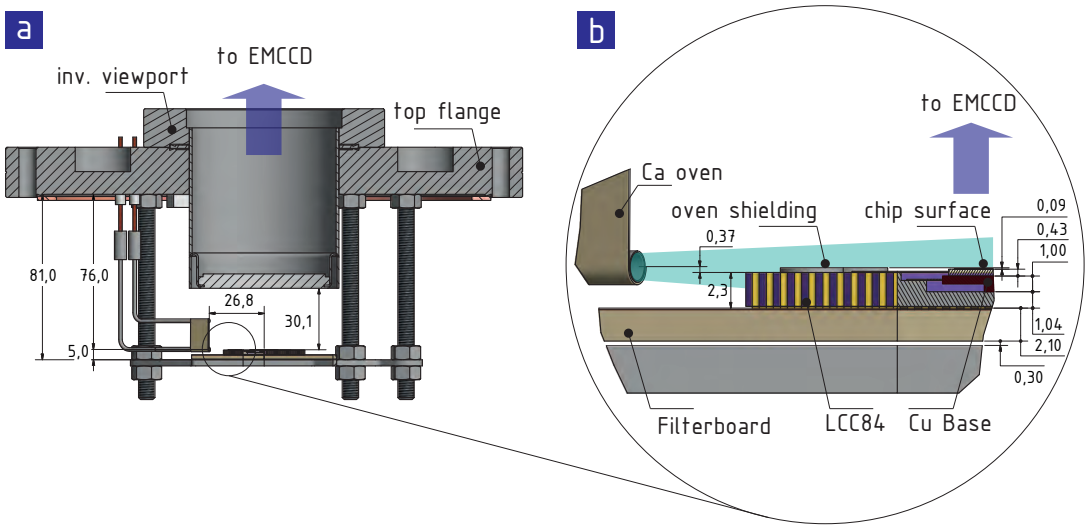


Figure 4.3 Trap montage into the vacuum vessel. a) cross section of the top flange (NW200CF). The surface of the trap faces the inner side of an inverted viewport and is separated by a distance of ~30 mm. b) chip mounted on a ceramic chip carrier and electrically connected to a filterboard. The Ca vapor (light blue) is partially blocked to diminish neutral Ca deposition on trap surface. (units in mm)

After the chip-ceramic carrier is mounted on a filterboard, as explained in Sec. 4.1.1, a stainless steel base is used to held the chip under vacuum as depicted in Figure 4.3a. The ion position coincides with the center of the vacuum chamber and has a distance of 76 mm to the inner side of the top flange. The filterboard is elevated by six stainless steel washers from the holder by 0.3 mm thus avoiding possible outgassing from possible trapped gases between the filterboard and steel block surfaces. The trap surface is separated from the inner side of an inverted viewport by a distance of about 30 mm. Through the inner rod of this port a lens collects the fluorescence light emitted by the trapped

ions for ion detection. An important step before the installation of the Ca oven is done by cross checking all electrical connections from the top flange to the trap electrodes.

The Ca oven design, based in a former development[100], is aligned in such a way that its axes coincides with the ion position and is parallel to the chip surface. The oven tube has a length of 30 mm, an inner diameter of 1.8 mm and a Ta foil closes the circuit for operating currents up to 20 A. The inner part of the oven tube is filled (in less than 5 min) with Ca granules[a] until the later highest temperature point situated in between the tube base and the Ta foil. This guarantees the correct operation of the oven since the temperature at the position of the Ta foil rapidly decreases. The oven is electrically connected by copper in-line connectors to the welded feedthroughs at the inner side of the top flange.

A half cross section of the chip on ceramic carrier and the oven tip are shown in Figure 4.3b. The oven tip is approximately situated of about 30 mm far from the center of the trap. The neutral Ca vapors (light blue) spread about 3° from the concentric oven tube axes, thus a block between oven tip and trap surface is glued[b] at the top surface of the ceramic chip carrier. This shielding block shadows the trap surface from the neutral Ca stream at approximately 0.09 mm over the trap surface, thus minimizing Ca deposition while allowing enough neutral Ca access for the photoionization process at the trapping position.

Right after the installation of the Ca oven, the vacuum chamber is closed and fore-pumped by a mechanical and tumbo molecular pump as preamble for the bake out step.

4.1.3 Bake Test of SMD Elements

All of the components used in our system are bakeable at high temperatures (>200 °C) except for the SMD capacitor and resistors. The optimal operation of the SMD elements installed in our system is compromised at such high temperatures. The maximal operating temperature for both SMD capacitors and resistors indicated by their manufacturer is about 150 °C. For a faster desorption of gases, and specially water molecules trapped at the vacuum chamber walls and Ca granules, higher bake temperatures need to be used. Therefore,

[a] Alfa Aesar GmbH, Karlsruhe, Germany
[b] Using both UV epoxy and Ag conductive epoxy explained in Sec. 4.1.1

before chip assembly we carry out a bake temperature test of SMD elements at temperatures up to 180 °C. The electrical properties of both SMD capacitors and resistors are monitored for a couple of weeks.

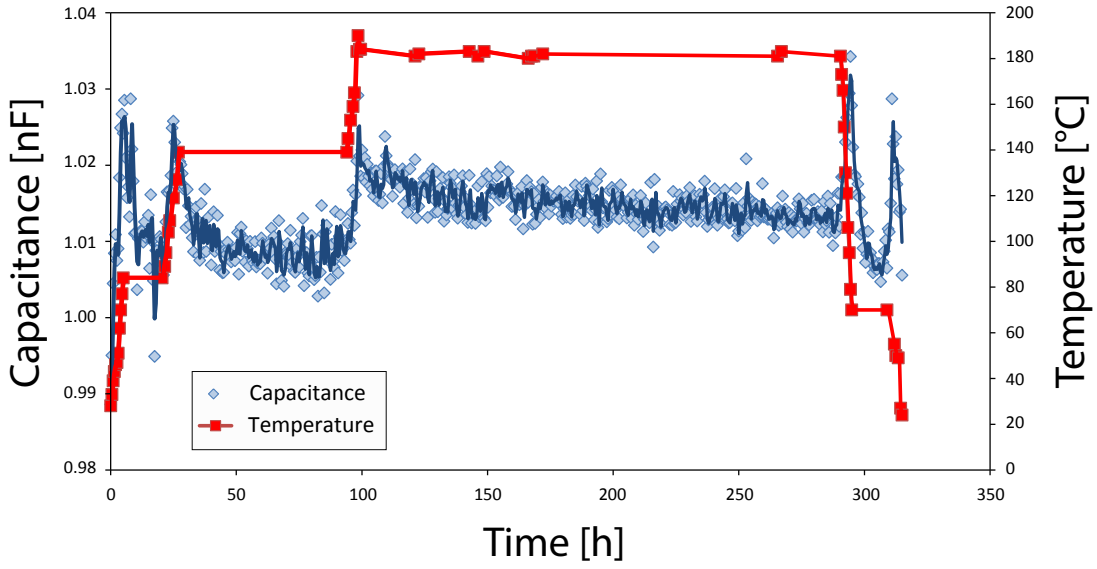


Figure 4.4 Heating test of SMD elements. A capacitor (1 nF) is heated at 180 °C for about a week with minimal capacitance change (< 4%). The capacitance is monitored at different temperatures from room temperature 23 °C to 180 °C for 320 h.

Since the SMD resistors have a slightly higher operating temperature (155 °C) than the SMD capacitors (150 °C), we only show the results from the latter without loss of generality. Both SMD capacitors (1 nF) and resistors (16 Ω) are glued with a Ag conductive epoxy and electrically connected soldering Kapton cables with a lead free solder as explained in Sec. 4.1.1. The capacitance is measured by a multimeter and the temperature by a termocoupler. The chamber is evacuated by a mechanical and turbo molecular pump till a pressure of 10^{-7} mbar. The chamber walls are thermally isolated with several layers of Al foil and resistively heated. The temperature sensor is situated in between the chamber walls and the Al foil layers. The temperature is varied from room temperature up to 180 °C for a total interval of 320 h. As shown in Figure 4.4 the capacitance of our SMD element (0.99(1) nF) varies less than 4% even when the chamber is constantly heated at 180 °C for a long period of time (200 h). The abrupt peaks on the measurement of SMD capacitance are due to mechanical noise during setup handling.

4.1.4 Chamber Bake Out

Together with an effective vacuum hardware cleaning, the bake out process constitutes one of the most important steps to obtain UHV conditions. It is clear that the higher the baking temperatures the shorter the baking times for gas desorption trapped at the chamber walls are needed. For instance, in order to achieve a base pressure of about 10^{-9} mbar[a] a bake time for about a week at a bake temperature of 200 °C is required.

After trap installation and forepump (10^{-4} mbar), the vacuum chamber is enclosed in an insulating bakeout tent[b] and heated using both a heater fan and four glass fibre heating tapes with a preset temperature in the range of 50 °C to 250 °C. In a similar manner as in Sec. 4.1.3 four temperature sensors are placed at the outer side of the chamber walls for monitoring the temperature during bakeout. The vacuum chamber is further covered with multiple layers of Al foil and the temperature is controlled via a termocouple and a LabView code setting a ramp of 10 °C/h. After reaching a stable bake temperature of 180 °C the bakeout is kept for about a week and then ramped down (10 °C/h) to room temperature.

During the bakeout schedule crucial degassing steps have to be done. For instance, being Calcium a high hydrophilic molecule it is necessary several periodic turn on and off runs. Through the time of bakeout schedule, the Ca oven is regularly operated every day with progressively currents from 1 A to 4 A for operating times varying from 1 min to 30 min depending on the amount of water desorption monitored by a mass spectrometer, see a next section.

Moreover, once reached a stable temperature and base pressure of 10^{-8} mbar both ion getter and pressure gauge are periodically turned on and off to release diverse types of trapped gases. Besides all filaments of the Ti sublimation pump are consecutively started by setting a current of 30 A for 1 min once a day. After the ramp down a base pressure of 1.5×10^{-10} mbar is reached.

Rest Gas Analysis.– To get insight into the source of molecules outgassed through the bakeout schedule we perform a rest gas analysis. At the forepump stage, in addition to a turbo molecular and mechanical pump, a mass spectrometer[c] is attached for monitoring the evacuated gases during the bake out process. In the temperature ramp-up phase (after forepump and between room

[a] without low pressure stage
[b] Tectra GmbH, Frankfurt am Main, Germany
[c] Rest Gas Analyser, DYCOR LC-D,Vacom, Jena, Germany

temperature and 180 °C) alcohol chains are detected resulting from the desorption of remaining aceton and isoproponal used for the two-stage cleaning (Isopropanol, Acetone). These alcohol traces are vanished after reaching a stable temperature of 180 °C.

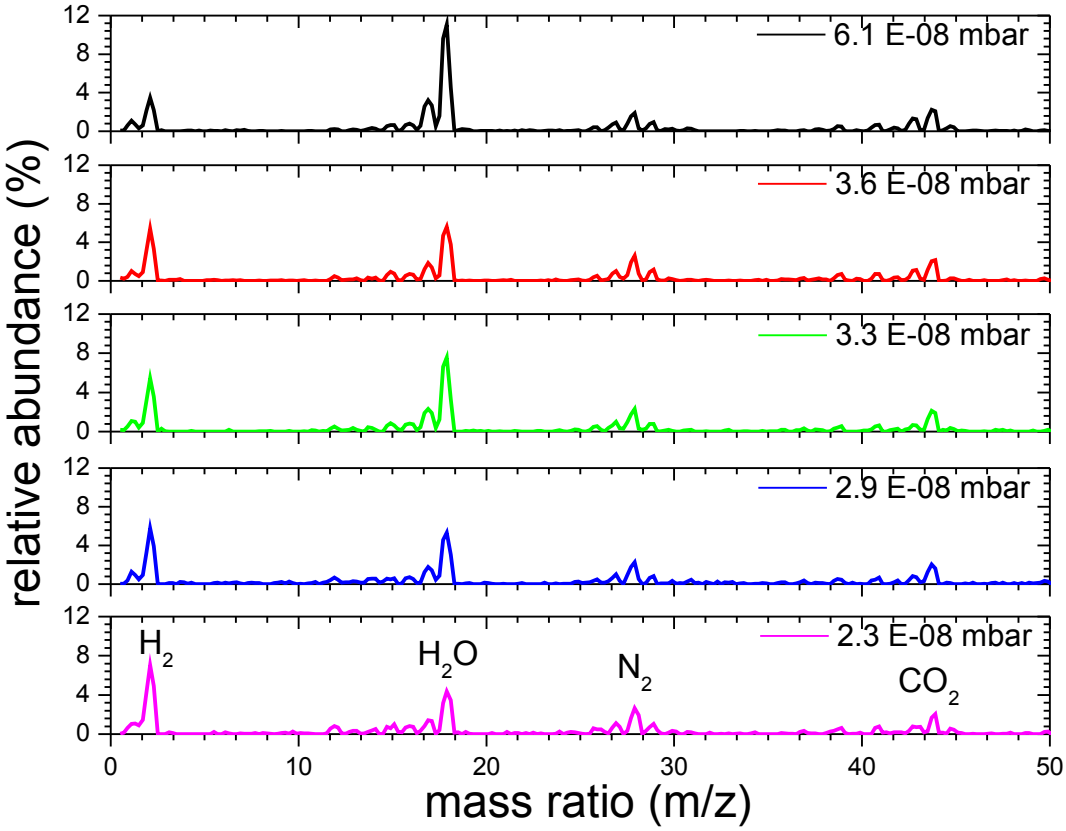


Figure 4.5 Mass spectrometry during chamber bakeout at 180 °C. The original spectra are taken until a mass ratio of 120 (mass ratios larger than 50 contribute minimally and thus in this plot omitted)

The mass spectra are taken periodically every two days in average, at a chamber temperature of 180 °C. The rest gas analysis is presented in Figure 4.5. In order to achieve low pressures (10^{-9} mbar) it is clear that water desorption from chamber walls and Calcium granules have to be minimized. At the last stage of the bakeout, we observe a high concentration of H_2, presumably resulting from uncontrolled processes during stainless steel manufacturing. They limit, at this temperature, the total chamber pressure to about 10^{-8} mbar. The relative abundance of other molecules such as N_2 and CO_2 did not change

significantly throughout the rest of the bakeout. After two weeks of baking time the vacuum chamber reached a stable pressure of 5×10^{-11} mbar.

4.1.5 Trap Assembly and Setup Uptade for Trap III

In addition to Ar^+ ion bombardment to reduce ion heating rates, a water cooling systems will dissipate Joule heating generated by the thick wires operating at maximum power.

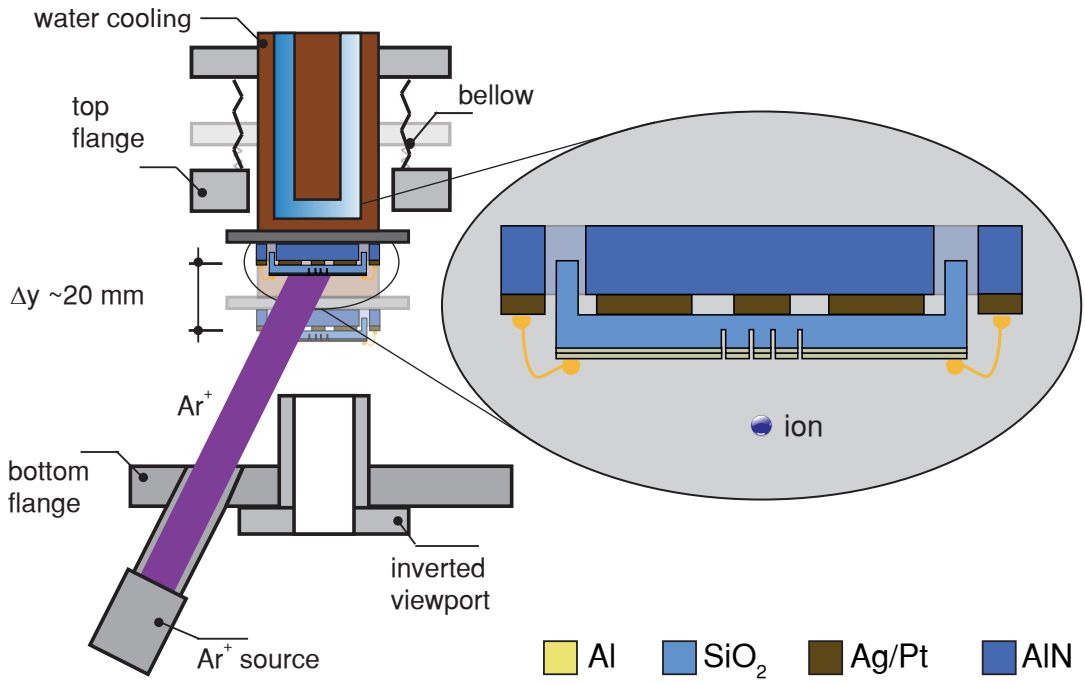


Figure 4.6 Vacuum chamber update to include Ar^+ cleaning and water cooling. A microstructured ion trap is mounted on printed thick wires on AlN. They are glued [a] on top of a copper block which includes a water cooling system. The trap position can be varied on about ($\delta y = 20\,\text{mm}$) for surface cleaning with Ar^+ ion bombardment which is installed on a (bottom) flange.

The basic vacuum setup for the hybrid trap is illustrated in Figure 4.6. It consists on a modification of the system presented in Sec. 4.1 where the pumping system and main chamber (C) are kept. The top and bottom flanges are modified as follows.

First, water cooling system is connected to the chamber through a flange port (NW75CF) mounted on a second flange (NW63CF). The latter is connected though the top flange (NW200CF) using a edge welded bellow which

permits to adjust the trap position for optimizing metal yield sputtering. The trap previously assembled and wirebonded, as described in Sec. 3.5.3, is glued on top on water cooling system.

Second, the Ar^+ ion source is connected through a flange port (NW40CF) at an angle 68° with respect to the optical axes. An inverted viewport (NW75CF) mounted on the center of the bottom flange permits to collect ion florescence.

. . . . . .

4.2 Voltage and Current Supply

Three different types of sources are needed to operate the planar trap with integrated current-carrying wires. First, high voltages amplitudes (100 to 200 V) at a stable frequency in the range of 1 MHz to 50 MHz. Second, a programmable multi-channel voltage supply having a range between −10 V and 10 V for the generation of axial frequencies around 1 MHz. Third, a stable current supply with variable pulse length in the range of 1×10^{-6} s to 1×10^{3} s

4.2.1 Radiofrequency Power Supply

The voltage amplitude supplied at 31 MHz is provided by an Adret signal generator[a] and preamplified by a RF-amplifier[b] providing a 40 dB amplification. The final amplification step is given by a quarter-wave helical resonator[101]. Figure 4.7 shows a typical RF line connection and the layout of a helical resonator. The RF signal is then fed through the top flange and connected to the trap. In between the helical resonator and the trap a (100:1) capacitive divider[99] is connected for monitoring the amplitude voltage in an oscilloscope as shown in Figure 4.7a.

The earlier study done by Macalpine et. al.[101] considers an isolated operation and self resonance frequency of the helical resonator. However when an ion trap is connected to the resonator its resonance frequency is shifted due to a lossy capacitance of the trap. The frequency shift, measured after the helical resonator is loaded, can be modeled by a simple lumped system, where only the capacitance due to the helix and the trap may be considered. When the resonator is loaded the $\lambda/4$ condition imposed for its design is not longer valid since technically an additional cable connects the trap to the end of the resonator.

[a] Adret 6315, 0.4 MHz to 600 MHz, Messtechnik, Köln
[b] ZHL-5W-1, Mini-Circuits, New York, USA

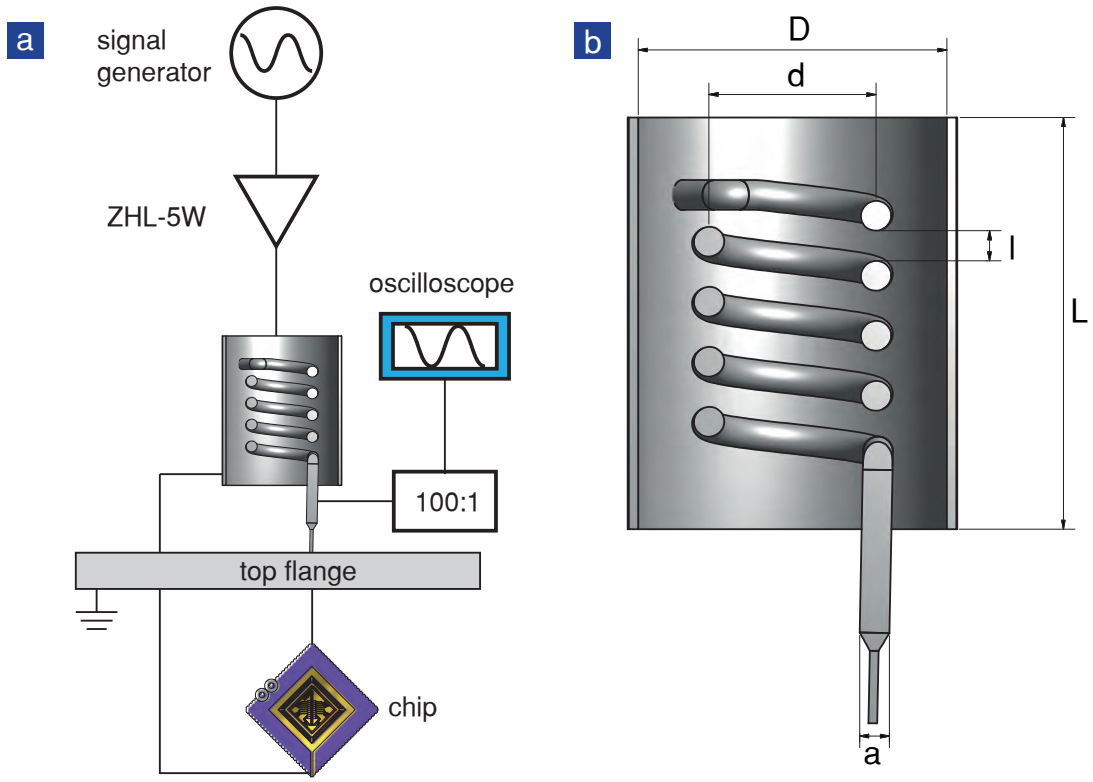


Figure 4.7 Radiofrequency power supply. (a) loaded resonator with a resonant frequency at $2\pi{\cdot}34\,\mathrm{MHz}$. (b) unloaded $\lambda/4$-helical resonator with a resonant frequency at $2\pi{\cdot}84\,\mathrm{MHz}$

In order to describe the total losses along the radiofrequency line, we have determine the total inductance (L) and capacitance (C) of each element have to be considered. Although it is in principle possible to measure the capacitance and resistance of the ion trap, for practical purposes we follow a simplified lumped model[102]. This assumption is valid since each element in the circuit is much smaller than the characteristic wavelength of the radiofrequency input. The model considers the helical resonator as a coaxial cable with the inner coil as the core and the outer cylinder as the shielding core. Therefore the load (ion trap) can be seen as an extension of the line and when solved using the condition of $\lambda/4$ the resonance frequency (f_l) of the loaded resonator is defined as:

$$\frac{1}{f_l} = \frac{1}{f_0} + \frac{1}{f_1} \tag{4.1}$$

where (f_0) is a bare frequency of the unloaded resonator and (f_1) a characteristic frequency of the trap. Equation 4.1 conditions that for high values of f_1 (or low trap capacitance, C_t) the loaded frequency approaches the bare frequency value.

After installation of the trap, the bare frequency of the resonator (f_0 = 84 MHz) is shifted to f_l = 34 MHz thus giving a value for the characteristic frequency of the trap of f_1 = 57 MHz. A further reduction of the loaded resonator frequency f_l = 31 MHz was measured after we connected an external low pass filter at the top flange for filtering frequencies higher than f_c = 59 kHz.

In our setup a helical resonator[103] with a total number of turns $N = 6$ and a helix diameter d = 47 mm is used. The copper helix is enclosed in a cylinder with diameter D = 86 mm and length L = 114 mm. The pitch equals l = 11.9 mm with a wire thickness of a = 6 mm.

4.2.2 Control Voltages

At the first stage of this work DC voltages were supplied by low noise power sources. Although each electrode could be independently controlled to generate complex trapping potentials, extending this method to the whole dc segments available (nine) is unpractical. Instead, a more robust and scalable way to set the control voltage was achieved by the recent development of a fast voltage supplier given in detail in the PhD thesis from Ziesel[79]. In this FPGA-based multichannel supplier, the voltages are generated by a set of 16 digital to analog converter (DAC) connected in parallel. Each of the four independent outputs of one DAC can be programmed to generate a range from −10 V to 10 V. For our setup, one DAC already suffices to control the nine independent dc pairs of our trap. The DC configuration is programmed via the software interface in C++ language. A difference voltage between each dc pair segment defines a lateral compensation voltage.

The static potential produced by this analog converter source agrees within 3 % with the experimental values when they are extracted from the axial frequency measured by either exciting the ion motion with an oscillating electric field or by direct measurement during laser spectroscopy. In contrast, measuring the RF voltages supplied to the trap require an appropriate impedance matching to avoid non linear detection of the RF amplitude.

4.3 Laser Systems

The electronic transitions of $^{40}Ca^{+}$ are manipulated by coherent light from readily available commercial sources[a]. Each of the required beams can be basically classified into two categories: 1) ultraviolet (UV) lasers (wavelengths: 397 nm, 423 nm and 375 nm) and 2) infrared (IR) lasers (wavelengths: 866 nm, 854 nm and 729 nm). Their respective application for the experiments will be explained in the next sections. For the experiments performed in this work both frequency stabilization and intensity beam control are fundamental. The Pound-Drever-Hall (PDH) method is implemented to stabilize the frequency, whereas the intensity is controlled by an acousto-optic modulator (AOM).

4.3.1 Fluorescence excitation, Doppler cooling and optical pumping

Light with a laser wavelength near 397 nm generated by a second harmonic generation (SHG) system[b] is used for fluorescence excitation, Doppler cooling and optical pumping of $^{40}Ca^{+}$ ions. The schematic layout of the SHG system, main optical and driving electronics components are shown in Figure 4.8.

The master oscillator arranged in Littrow configuration[104], consists of a Fabry-Perot (FP) laser diode (wavelength near 793 nm, 50 mW) and a blazed grating (BG) glued on a piezo electric mount to create an extended tunable resonator (ETR)[105]. In the Littrow configuration, the blazed grating feeds back the first-order diffraction into the FP laser diode and the zero-order diffraction is used as output (single longitudinal mode) beam. A Faraday isolator (FI) prevents damage to the FP laser diode from possible reflected light. From the principal beam few mW are extracted and equally (1/2:1/2) guided to a Fabry-Perot resonator (Cavity) and wavelength meter (λ-m)[c]. The principal IR beam is coupled to a tapered amplifier (TA) p-n junction which amplifies the power (up to 190 mW). A second FI protects the TA from reflected beams. The amplified principal IR beam is coupled to a SHG system consisting of four mirrors (ring configuration) and a non-linear crystal (NC) for frequency doubling. Photodiodes (PD) monitor both transmission (T) and error (E) signals. From the SHG system, the resulting blue light (397 nm) is filtered

[a] TOPTICA, Munich, Germany
[b] TA SHG 397 nm, TOPTICA, Munich, Germany
[c] HF-ANGSTROM WSU-30, HighFinesse GmbH, Tübingen, Germany

by a dichroic mirror and its elliptic UV beam profile circularly rendered by an adjustable anamorphic prism pair (AAPP). After a telescope, the collimated beam diameter is reduced to about 1 mm.

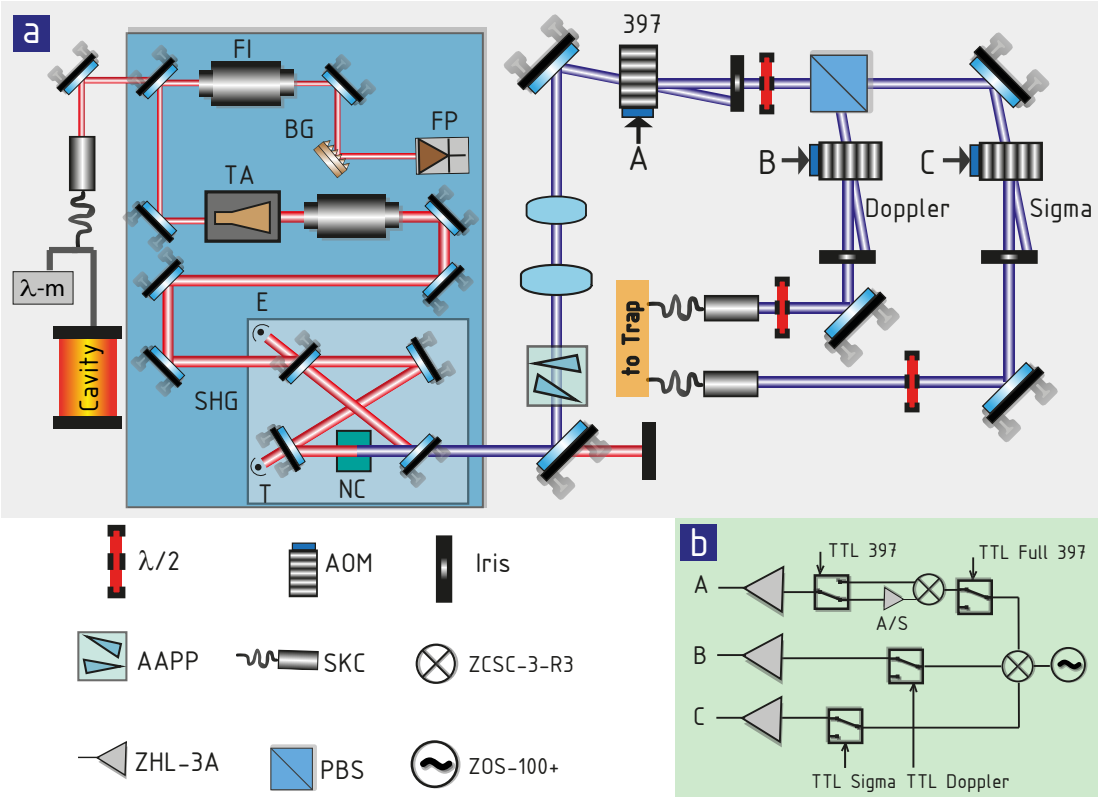


Figure 4.8 Laser system at 397 nm. (a) Schematics of the setup of the SHG 397 nm beam: Doppler cooling, optical pumping (σ) and detection lasers paths are shown. (b) AOM driving circuit: electronic components are mounted underneath the optical table. Acronyms are explained in text.

Underneath the optical table, the driving electronics of the AOM's[a] are mounted on a Cu block. The AOM switching circuit is schematically shown in Figure 4.8b. The Cu block serves as electrical ground and as heat sink for the electronic components which are driven by a voltage-controlled oscillator[b] at the frequency (80 MHz). The signal power is split[c] into three ways, switched

[a] BRI-QZF-80-20, Brimrose, Sparks, USA
[b] ZOS-100+, Mini-Circuits, New York, USA
[c] ZCSC-3-R3+,Mini-Circuits, New York, USA

via TTL by high frequency switches[a] and finally amplified[b] right before each AOM.

For the first AOM (A) an additional attenuator (A/S)[c] is provided, which desaturates the laser power for efficient Doppler cooling. After this AOM the +first-order diffraction of the laser beam is polarized by a half wave plate ($\lambda/2$) and split in two paths by a polarized beam splitter (PBS) for Doppler cooling and optical pumping (σ beam). The -first-order diffraction of the resulting two beam paths are respectively polarized ($\lambda/2$) and coupled to polarization maintaining fibers (SKC)[d]. The two independent Doppler and σ beams are finally guided trough single mode optical fibers to the viewports of the trap chamber, see Sec. 4.3.5 for details about the laser alignment. The transmission through the fiber is about 30% leading to typical powers of 50 µW to 150 µW at the ion's position.

4.3.2 Two-Step Photoionization

For the ionization of the effusive neutral ^{40}Ca stream a two-step photoionization process is carried out[100]. It has the advantage of inducing less surface stray charges, being isotope selective and reducing electrode trap damage compared to a former method by electron impact ionization[102].

The highly efficient and selective two-step photoionization begins with irradiation of neutral ^{40}Ca by light at the wavelength near 423 nm. In this case, the electron is initially excited from the ground state 4^1S_0 into the excited state 4^1P_1. This light at 423 nm is created in a similar SHG system as explained in Sec. 4.3.1 and the setup previously developed[106]. The second laser freely running at near 375 nm re-excites the electron from the excited transition level $P_0^{4^1}$ into the continuum[104]. Both beams are coupled to a single mode optical fiber and guided to the trap viewports, see Sec. 4.3.5 for details about the alignment.

4.3.3 Repumping and Quenching

Two IR lasers at wavelengths near 866 nm and 854 nm are used to empty the $^2D_{3/2}$ and $^2D_{5/2}$ metastable states, herein refered as repumping and quenching

[a] ZYSW-2-50DR, Mini-Circuits, New York, USA
[b] ZHL-3A, Mini-Circuits, New York, USA
[c] TFAS-2+, Mini-Circuits, New York, USA
[d] Schäfter & Kirchhoff GmbH, Hamburg, Germany

respectively. Their optical and electronic setup are shown in Figure 4.9. Both lasers are based on a commercial tunable laser diode system[a] with ultra stable design against acoustic and frequency drifts. The quasi Gaussian beam profile does not need further reshaping and is partially reflected to a wavelength meter (λ-m) . Only the beam at 866 nm is also guided to an external resonator cavity for PDH stabilization. The two principal IR beams are independently arranged in a double pass configuration (Figure 4.9a) where a plano-convex lens and mirror downstream from the AOM are used to form a cat's retroreflector[107] thus increasing the diffraction efficiency and tuning bandwidth. After switching, the two beams are recombined and coupled to polarization maintaining elements (SKC) which guiding the beam to the trap viewports, see Sec. 4.3.5 for laser alignment. In this case, all AOM switching electronics are driven by a single voltage controlled oscillator (VCO) and single mixer. A fast switch and an amplifier control each beam intensity (Figure 4.9b).

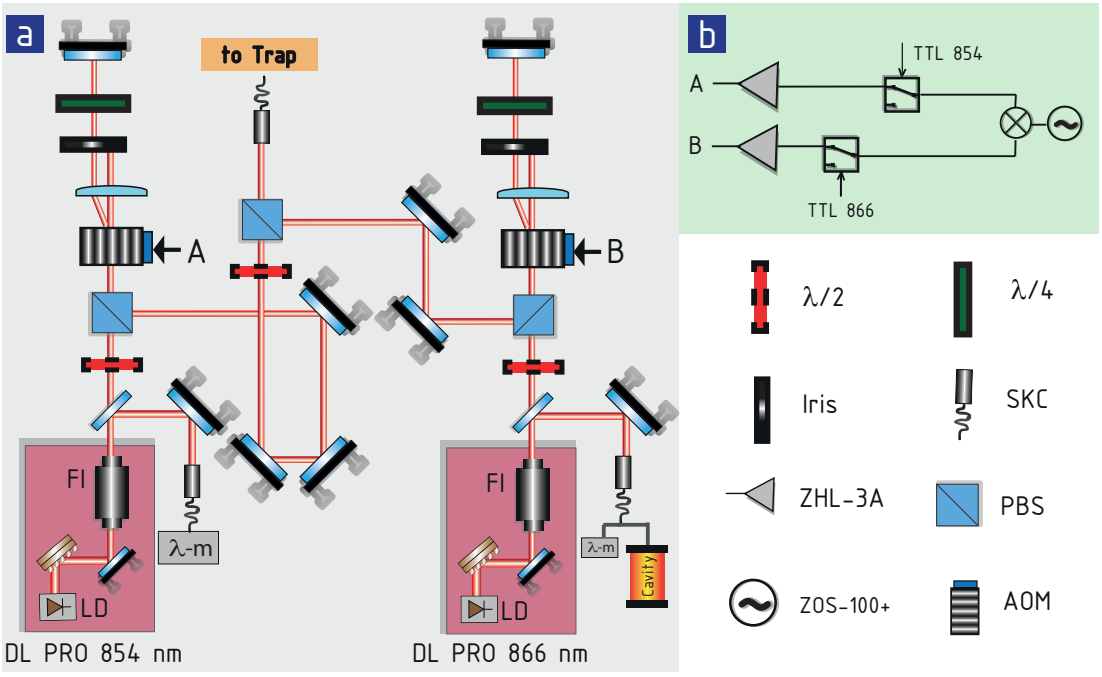


Figure 4.9 Laser systems at 854 nm and 866 nm. (a) Schematics of the optical setup for laser at wavelengths 866 nm and 854 nm. (b) AOM electronics components for beam switching

[a] DL PRO, TOPTICA, Munich, Germany

4.3.4 Electron Shelving

The laser at wavelength 729 nm is also built on an extended tunable resonator configuration as explained in Sec. 4.3.1. However, the frequency stabilization in this case is more stringent since the system is very sensitive to small drifts on the temperature and mechanical noise. Therefore, the components of the external cavity are inside a HV vertical system. Herein, the light at 729 nm is borrowed from the setup built by Poschinger[106], we do refer therein for more details about the setup. After the second FI the beam is split to a high finesse cavity and to a second experiment (μTrap). To this existing setup, an additional path is built in a double-pass configuration and the light is guided to our laboratory through optical fibers.

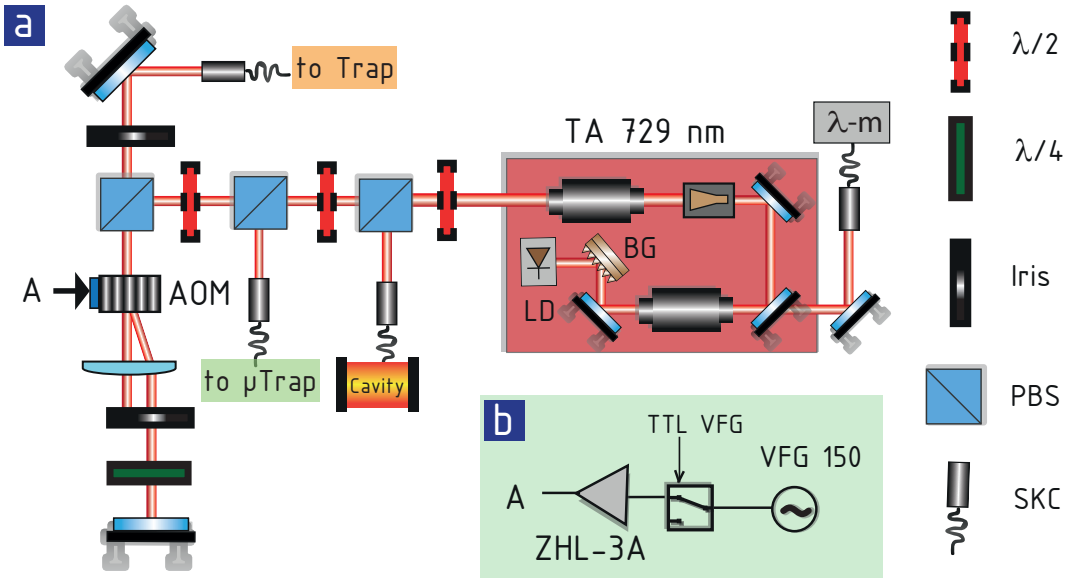


Figure 4.10 Laser system at 729 nm. Schematics of the basic optical and electronics components of the laser at 729 nm for electron shelving. The laser path is set in a double-pass configuration and controlled via an AOM. The driving electronics b) permit to implement laser pulses with specific pulse length, amplitude and phase for spectroscopy experiments.

The basic optical and electronics components are depicted in a scheme in Figure 4.10. In Figure 4.10b) the system is driven by a versatile function generator (VFG)[a] such that spectroscopy pulses to drive the dipole forbidden $^2S_{1/2}$-$^2D_{5/2}$ transition with determined phase, pulse length and amplitude can be

[a] VFG 150, TOPTICA, Munich, Germany

implemented. Note that in the double pass configuration the frequency will be shifted two times by the driving frequency of the AOM. After beam outcoupling in front of the vacuum viewport typical laser powers are about 10-15 mW.

4.3.5 Beams Alignment and Guiding

A total of seven laser beams are focused to the trap center at different wavelengths (397 nm, σ-397 nm, 423 nm, 375 nm, 866 nm, 854 nm and 729 nm). All beams are coupled to polarization maintaining collimators and sent from the optical table to the trap center with single mode optical fibers which facilitate laser alignment and light delivery through challenge-to-reach points.

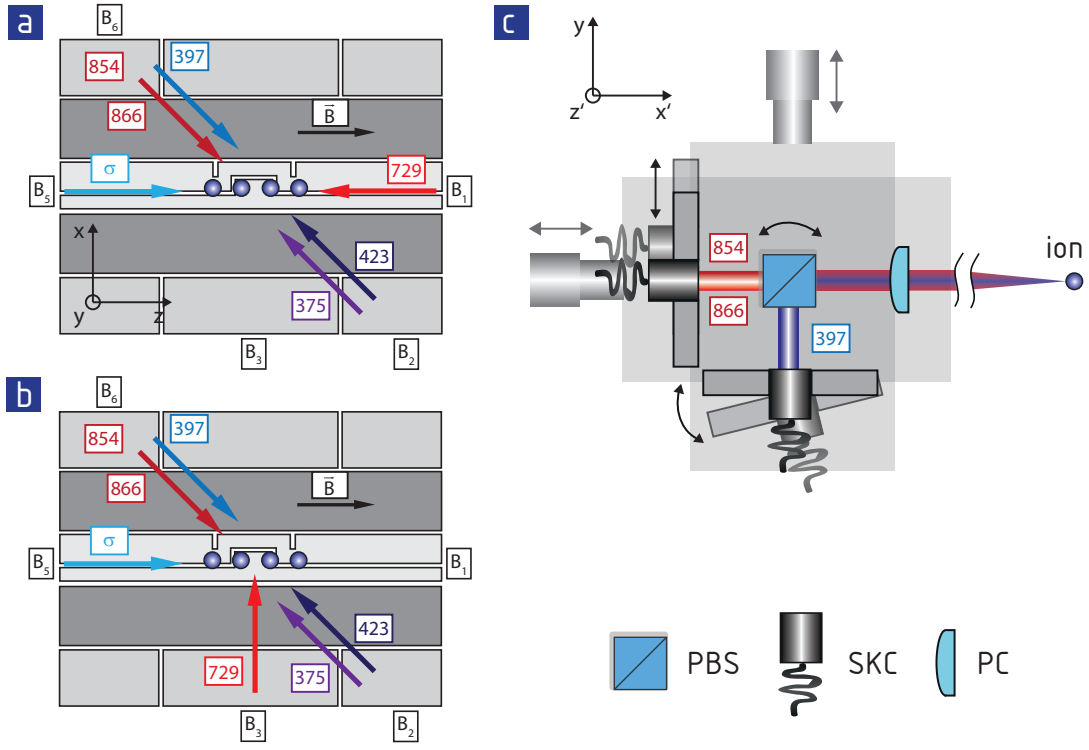


Figure 4.11 Simplified picture of laser alignment and beam guiding. Laser wave vector at 729 nm has a fully projection on the a) axial and b) radial direction of ion motion. Viewport axes labels, as given in Sec. 4.1, are added as reference. c) Beam guiding and positioning: in this case blue (Doppler cooling, 397 nm) and red (repumping, quenching, 866 nm and 854 nm) beams are overlapped through a beam splitter and mounted on a XYZ-stage (in the background). The minimal beam positioning is 10 µm.

To have a projection of the wave vector (729 nm) into either axial (z-axis) or radial ion motion modes (x-axis) basically two laser beam configurations have been used along this work (schematically shown in Figure 4.11). In either cases the position of each beam is controlled by XYZ translational stages[a] with a precision of 10 µm. Four beams, previously couple to polarization maintaining fibers, are superimposed into two pairs of beams: at 866: 854 nm and 423: 375 nm.

For all the beam paths, except for 729 nm, we have used beam collimators[b] and single mode optical fibers optimized at their respective wavelength. For the out-coupling of light at 729 nm, where the focus diameter is more stringent, we have used a different collimator[c] to increase the beam diameter (254 mm) after out-coupling.

The XYZ-translational stage is combined with a commercial[d] cage system (30 mm). As shown in Figure 4.11c) this setup provides enough degrees of freedom to reduce the challenge at superimposing complex paths. In total, four XYZ-stages are used: three to align two single beams (σ-397 nm, 729 nm) and one for a superimposed beam (375-423 nm). A fourth XYZ-stage houses the Doppler cooling (397 nm) and the superimposed pumping-quenching (866-854 nm) beams. In this case, the two paths are recombined by a PBS into a single path and a plano-convex achromatic lens focuses it at the trap center (f_l = 200 mm).

All beams foci can be adjusted by both the collimator lens system and an additional plano-convex (PC) achromatic lens[e] placed at end of the cage system, as shown in Figure 4.11c). After alignment, the FWHM for the beams 397 nm and 854-866 nm at this position are 108 µm and 520 µm respectively. A single beam (729 nm) is more tightly focused with a FWHM of 22 µm.

Laser beams requiring no fast switching (ns-order) are blocked, prior fiber coupling, by low-cost loudspeaker-based shutters[108], with shuttling times on the ms range. With this shutter the photoionization laser beams (423 nm and 375 nm) after ion loading is blocked.

[a] PT3/M, Thorlabs GmbH, Dachau/Munich, Germany
[b] 60FC, Schäfter & Kirchhoff GmbH, Hamburg, Germany
[c] Schäfter & Kirchhoff GmbH, Hamburg, Germany
[d] 30 mm Cage Systems, Thorlabs GmbH, Dachau/Munich, Germany
[e] Lens-Optics GmbH, Allershausen, Germany

. . . . . .

4.4 Imaging and Detection System

The trap imaging optics is mainly made from a custom made lens [a], an Electron Multiplying Charge-Coupled Device (EMCCD) camera from Andor[b] and two xyz-translational stages[c]. The system axis goes along the normal direction of the trap and permits to collect ion flourescence near the trap center over the whole trapping range.

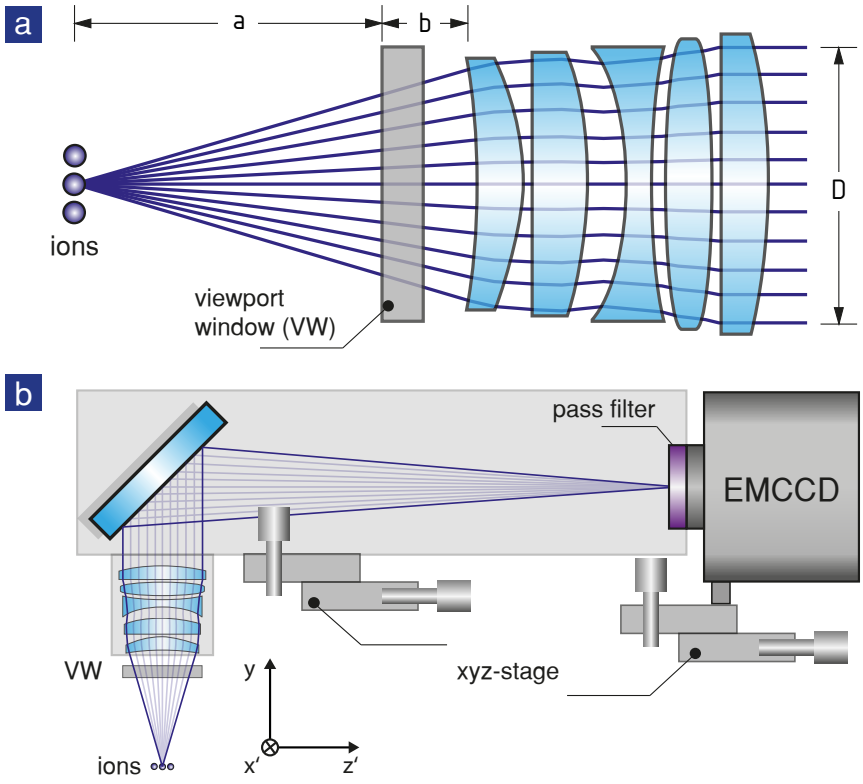


Figure 4.12 Imaging optics for ion fluorescence detection. a) lens system to collect UV light at 397 nm wavelength (modified from Ref. 109) . b) optics system to collect ion fluorescence light at 397 nm mainly consisting on UV lens system, UV high reflecting mirror and a EMCCD camera. The camera focus position is adjusted by a pair of xyz-stage with a precision of 10 µm.

[a] developed by J. Benhelm and F. Schmidt-Kaler, and manufactured by Sill Optics GmbH, Wendelstein, Germany

[b] iXon3 DU897-ECS-BBB, Andor Technology, Belfast, Northern Ireland

[c] RB13M, Thorlabs GmbH, Dachau/Munich, Germany

A custom made objective lens of NA∼0.27 collects the ion fluorescence. Each pixel of the recorded image corresponds typical values around 1 µm[a] pro pixel determined by comparing the inter-ion distance in a two-ion crystal predicted by theory[44]. In order to minimize the influence from other light sources, we equipped the EMCCD camera with an additional bandpass filter[b] around 397 nm. The advantage of using a CCD system, instead of a photo-multiplier (PMT) relies on the fact of spatial resolution whit the pay off less quantum detection efficiency.

4.4.1 State Readout

The camera control relies on a library written in the group by Alex Wiens[110], based on Andors Software Development Kit (SDK), allowing to fully integrate it into our Master Control Program (MCP) for the experiment. The full width of the camera covers about one segment of the trap (around 600 µm). To reduce noise, which typically comes from insulating material in the trap setup which is exposed to our laser at 397 nm, and to speed up the charge readout speed, we carry out spectroscopy measurements in the sub-Image mode already provided on the Andor SDK.

We employ a EMMCD camera to distinguish between the *dark* state, which corresponds to the ion being excited from $S_{1/2(m=-1/2)}$ into the metastable state $D_{5/2}$, and the *bright* state to $S_{1/2(m=+1/2)}$. Prior to each measurement, a photon-counting threshold (σ_{th}) value has to be calculated, distinguishing fluorescence counts from background photons (Figure 4.13).

To obtain a reasonable estimate for this threshold, 100 measurements are taken with the ion prepared in a bright or dark state, respectively. The dark state is mimicked by omitting a repump laser during detection, such that the ion falls into a dark state and does not scatter any photons. We select a region of interest around each ion and sum up the number of photon counts for each measurement. After 100 experiments with bright and dark ions we build a histogram of all occurrences for a exposure time of 3 ms.

Two Poissonian distributions can be seen in Figure 4.13, corresponding to the dark state and the bright state. The threshold value (σ_{th}) is calculated

[a] This value can slightly vary depending on the focus settings
[b] Semrock FF01-377/50-25, Semrock, New York, USA

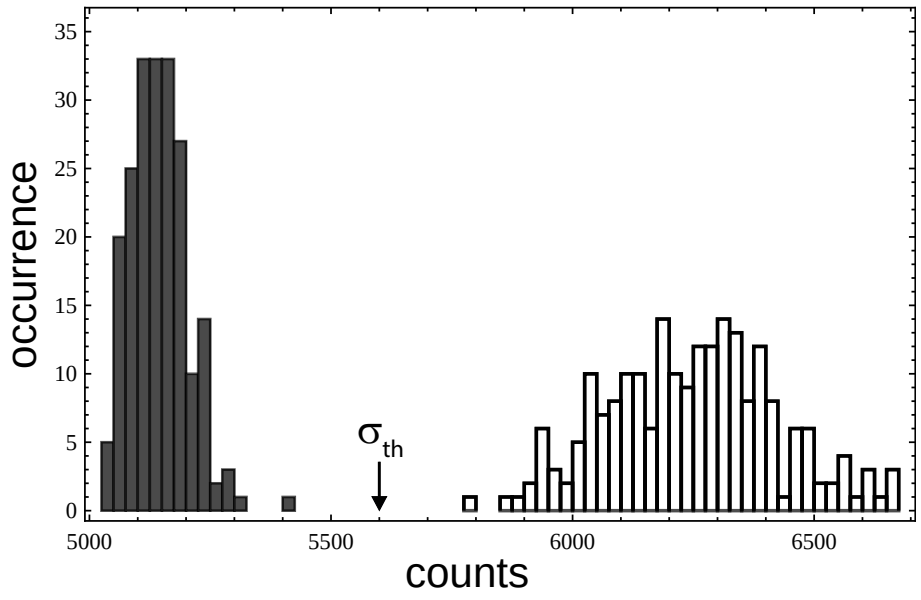


Figure 4.13 Ion flourescence histogram for a dark and bright sate of a trapped ion of a single trapped ion. The threshold value corresponds to $\sigma_{th} = 5600$ counts from an exposure time of 3 ms

from the geometrical mean of the average values of both distributions respectively[83]. The detection time in our measurements is from 3 ms to 4 ms, using an EM gain of 300.

. . . . . .

4.5 Experiment Control

Two personal computers are used to control the whole experimental setup. The control of all experiments sequences is done via a home-made software package[a]. Based on the C/C++ programming language, different modules are custom-made which eases the implementation of new functions or devices according to the needs of the experimenter.

A functional diagram block (Figure 4.14) depicts the main hardware controlled by the main computer. The control software communicates via two data acquisition cards through peripheral component interconnect (PCI) bus. All eight digital channels have a time resolution of 1 MS/s.

[a] developed mainly by K. Singer, G. Huber and D. Maiwald and here termed MCP (Master Control Program)

An additional PCI card[a] is required for data acquisition of ion fluorescence via an EMCCD camera. The camera acquisition sequences are synchronized by an additional TTL signal level and the camera control functions implemented through this additional card. All lasers are switched via TTL signals, except for the lasers with wavelength at 423 nm and 375 nm where loudspeakers-based shutters block the individual path for each beam. An input TTL signal closes the circuit on the pulse generator for the supply of constant current pulses.

One output signal of a fast synthesizer (VFG) drives the AOM of the electron shelving laser (AOM 729). A second output signal, subsequently amplified, provides AC voltages through the inner wires (W_1, W_2). The generated oscillating magnetic field coherently manipulates the qubit state of the $^{40}Ca^{+}$ ions encoded in the $S_{1/2}$ ground state.

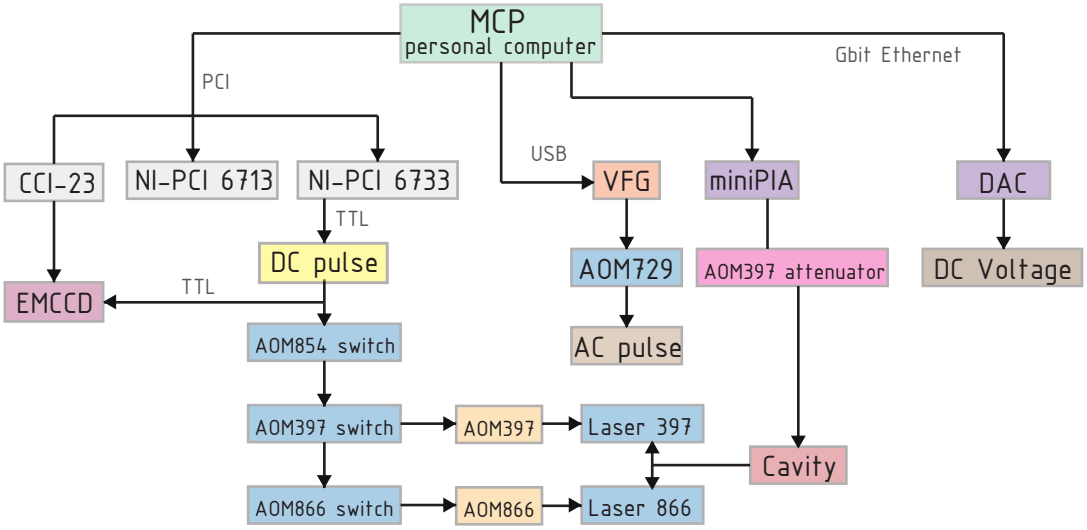


Figure 4.14 Functional diagram block of the main hardware components and personal computer as core unit. Ion florescence experiments are mainly exerted via NI-PCI cards and synchronized to EMCCD image acquisition.

Two analog voltages magnified by a fast three-channel high voltage amplifier[b] are fed to piezo-elements of a locking cavity, enabling the detuning of light at 397 nm and 866 nm. A second amplified analog voltage controls

[a] CCI-23 PCI, Andor Technology, Darmstadt, Germany
[b] miniPIA, TEM Messtechnik GmbH, Hannover, Germany

an AOM attenuator to completely block or maximize the intensity of the laser light at 397 nm.

The control voltages for 19 DC electrodes are supplied by a fast multichannel voltage supplier which communicates with the personal computer via Gigabit Ethernet. A second personal computer accomplish minor tasks i.e. monitoring the wavelength of the lasers, laser alignment and digital laser locking.

5 Trap Characterization

This chapter describes the characterization of Trap I. It starts with electrical current tests performed to the surface-mounted current-carrying wires. Then ion trapping of $^{40}Ca^{+}$ as well as its internal states manipulation by laser fields is covered. Laser cooling techniques such Doppler and resolved sideband cooling are covered. This prepare the scenario for the implementation of rf-spectroscopy on the Zeeman ground level. Then the magnetic field and magnetic field gradients generated by the on-chip current carrying wires are measured using rf- and laser-spectroscopy.

This chapter ends up with ion stability analysis while sending alternating current pulses through one of the current-carrying wires.

. . . . . .

5.1 Current Failure Tests

We showed in Sec. 2.1.3 that high density currents at the surface of the inner wires W_1 and W_2 of the trap, are required to generate high magnetic field gradients at the position of the $^{40}Ca^{+}$ trapped ions. Due to their minute dimensions these microstructured wires are prompt to fuse or melt even when 1 A is supplied for a relatively short period of time (∼1 s). To study the maximal current threshold of the inner wires before any irreversible damage occur, we performed two types of electrical current tests. The first one consisted on sending constant pulse currents for short periods of time from 10 ns to 1000 ms. Then a measurement of the voltage drop for a single pulse was carried out. We send oscillating current pulses of constant duration (500 ms) separated by a cool down time (variable) and measure the average resistance for each pulse. These two types of measruments are shown in the following parts of this sections.

5.1.1 Single pulse

A commercial power source [a] providing +15 V and −15 V is connected to a pulse generator (P), Figure 5.1a). The pulse generator may be switched either analogically or digitally by a TTL signal supplied from the Master Control Program (MCP). A pulse duration is set analogically by appropriate capacitors in

[a] Statron 2225.2 – Not shown in the scheme

the range of 10 ns to 1000 ms. For manipulating the internal states of trapped ions via magnetic field gradients, a static current pulse of few ms is required to avoid overheating of current-carrying wires. For spin state preparation by radiofrequency oscillating magnetic fields, shorter static current pulses of few ns duration may be employed.

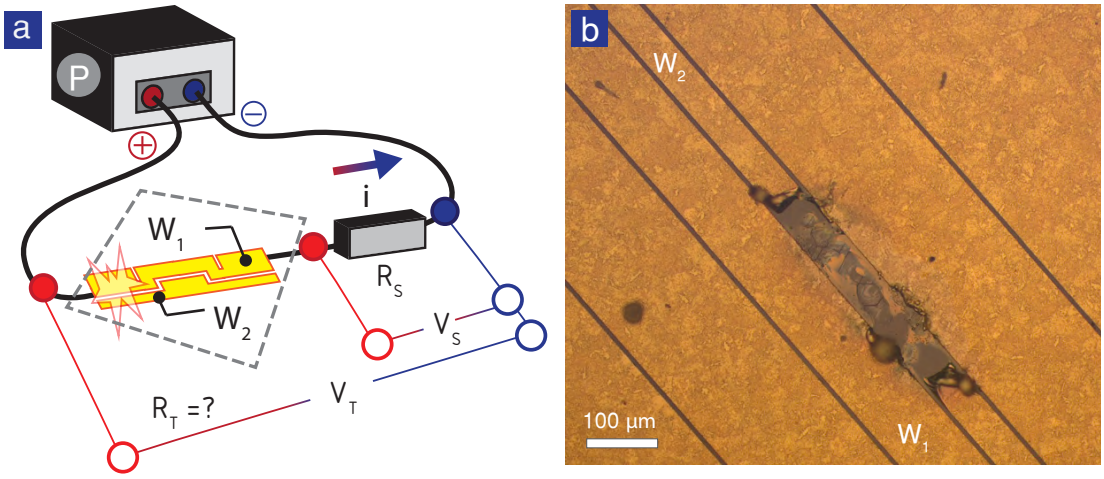


Figure 5.1 Setup schematics for current testing. a) Cartoon of the setup for testing applied maximal currents on surface mounted wires of the trap. b) Optical micrograph of a current failure on wire (W_2) after supplying 6 A for about 100 ms.

Current failure test consists as follows. A chip, schematically shown in Figure 5.1a), is wirebonded to a ceramic chip carrier[a] and placed under vacuum conditions (10^6 mbar). It is additionally connected in series to a shunt resistor (0.39 Ω). In order to diminish the possibility of electrical failure due to lossy or insufficient wirebonding paths, we use up to 11 wirebonds (25 µm in diameter) to electrically connect the inner wires (W_1 and W_2) to a ceramic chip carrier. A shunt resistor placed over a heat sink, to avoid overheating, is connected to a pulse generator to close the circuit. Oscilloscope probes are used to monitor the total voltage of the circuit (V_T) and the shunt voltage (V_S) at the fix resistor. The voltage drop at the trap wire (W_1 or W_2) is determined as the voltage difference of the measured voltages ($V_T - V_S$). The current at the shunt remains constant, due to proper cooling, and we simply divide the shunt voltage over its cold resistance (R_S) to obtain the constant current (i) through

[a] Kyocera PLCC84

the circuit. The voltage drop of the trap wires when supplying different current values for a single pulse is plotted in Figure 5.2a). After applying currents pulses of magnitudes ranging from 1 to 6 A and lengths from 100 to 750 ms, we do not observe damage of the wire. In the range of high currents we take the precaution to set short pulses so that, for example, W_1 when supplying 6 A thorugh wire (W_1) for 0.080 s we do not observe damage of the wire. This current value corresponds to a current density $J = 1.5 \cdot 10^{10} A \cdot m^{-2}$ at the outermost part of the wire and $J = 3 \cdot 10^{10} A \cdot m^{-2}$ at the wiggle just right under the trapped ions.

For these initial current tests, an sapphire block was used to thermally connect the outer side of the trap surface and the chip carrier. This guarantees a good thermal contact, but not as good as in the real experimental setup where we have used a Cu block instead. Even though in these preliminary test the inner wires could stand high current values up to 6 A, as shown here. In addition, the traps used for these tests are constituted from electrodes with electroplating finishes.

The trap for ion trapping, however, is made of electrodes built based on evaporation. Although the electrode thickness of the trap installed for quantum experiments is reduced by a factor 2, it is expected equivalent current values as the ones presented here may be under reach.

5.1.2 Pulse Train

In order to study the current failure of the wires during normal operation times (~30 min) we supply a pulse train as an input TTL signal on the pulse generator. So that, additionally of varying the current magnitude flowing through the wires, we may set a pulse repetition period larger than a certain pulse current duration (550 ms). To the setup shown in Figure 5.1a), additional to the power supplier a signal wave generator to set a TTL pulse is connected. To understand the possible heat transfer process occurring at the interface between the metal wires and the substrate while sending the train pulse we may define a relative cool time as:

$$\Delta P = \frac{|P_T - P_D|}{P_D} = \frac{C_T}{P_D} \tag{5.1}$$

where the difference between the pulse repetition period (P_T) and the pulse duration (P_D) is defined as a cool down time(C_T). This fraction of time allows

that part of the resistive heating generated at the wires (Gold, 2 µm) dissipates through the substrate (sapphire, 330 µm). Depending on the values of either current or cool down time the value of the resistance saturates at critical values or safe values as shown in Figure 5.2b). The dashed line at about 2.05 Ω defines a critical value of the wire resistance, when considering an increase of 50 % on the wire resistance may cause an irreversible damage[89]. Additionally, each data point represents the mean value of the measured resistance (R_T) over a pulse duration of 550 ms. We apply 0.5 A (blue symbols), 0.75 A (red symbols), 1.0 A (black symbols) for relative cool down times from 0.1 to 17.2. A logarithimic fit of the two set of data closed to the critical resistance value, (1.0 A, C_T = 0.8) and (0.75 A, C_T = 0.1), indicates this critical value will be reached after 4.0 h and 4.6 h, respectively.

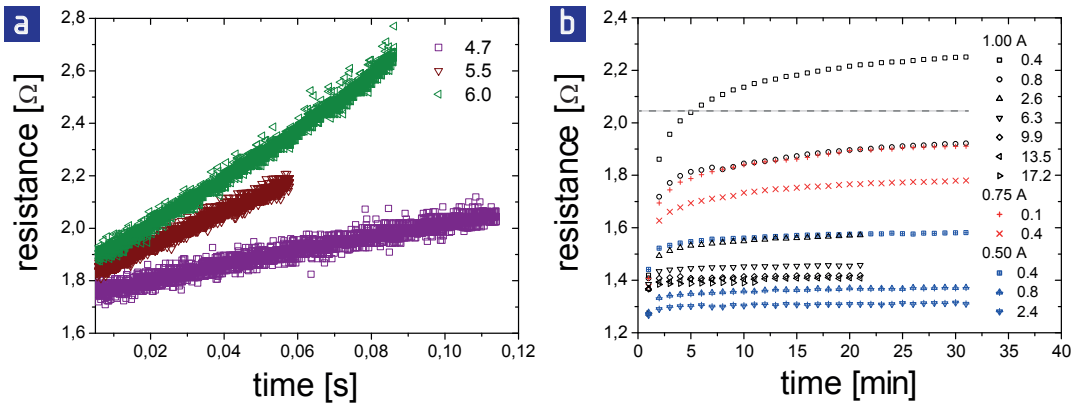


Figure 5.2 Resistance increase while applying pulsed static currents to the inner wires W_1 and W_2. a) Resistance increase over time for current values of 4.7 to 6.0 A during a single pulse experiment. b) Resistance increase over time during a pulse train for different relative cooling times and current values.

The heating process governing the electrical failure can be understood as joule heating. Clearly the use of a substrate with high thermal conductivity such as sapphire (35 $W\,m^{-1}\,K^{-1}$) and the use of relative cooling times higher than 2.5 effects positively in order to send higher density currents through the wires.

5.2 Ion Trapping

Storing ions in planar traps differs slightly from the way it is done in more robust ion traps. From one hand, in a planar trap the ions are trapped near to mirror-like surfaces, thus stray lights from impinging lasers or from the pump filaments may considerable hinder ion fluorescence detection. The laser beams and focusing system have to coincide at the position of the trapped ions right above high reflecting metal surfaces. Another substantial difference is also that in planar traps the minimum of both DC and RF potentials do not coincide with the geometric center. Therefore, more elaborate DC voltage configurations are required in order to held the ions with minimal micromotion. As we have discussed in Sec. 1.3.1 we do require at least a set of four DC electrodes which are sufficient to nullify the electric field and give a desired axial frequency at the ion's position.

5.2.1 Doppler beam positioning

For the laser alignment configuration given in Sec. 4.3.5, a laser with wavelength at 397 nm is carefully aligned parallel to the trap's surface to minimize scattered laser light from electrode gaps. First, we take advantage of high surface quality of the trap electrodes. Scattered light, from small hillocks (100 nm) on top of electrode surface and closed below the ion position, is collected by a EMMCD camera. The photon counts are maximized by adjusting both laser position and imaging focus. Once the signal is maximized, a reference for the laser position and optics focusing along the y-direction is defined. Then the laser beam and imaging focus are positioned at the expected trap distance (y_0 = 167 µm) using XYZ-stages, Sec. 4.3.5, with a precision of 10 µm. This procedure is also suitable for aligning a sigma laser (σ–beam) which wavelength can be also detected by a UV filtered EMCCD camera.

5.2.2 Neutral atom fluorescence

A first step prior ion trapping consists on detecting neutral atom fluorescence. It allows to rapidly prove the correct operation of the neutral Ca oven. Initially, the photoionization lasers are aligned parallel to the trap surface as explained in Sec. 4.3.5. Both the photoionization lasers beam and imaging focus are set at a distance of 400 µm above the expected ion trapping position. In addition,

the hot-filament gauge is turned off, and the view-ports are optically blocked to avoid that any stray light may hinder the detection of atom flourescence when using an EMMCD camera.

Due to the relative high amount of water present inside the vacuum chamber during bake out, see Sec. 4.1.4, a thin oxide layer on the Ca granules is prompt to form. Therefore, the oven was initially operated for few seconds (20 s) at a high current (6 A). After that, the calcium oven was operated at lower values, which are about 4.5 A as a preamble for trapping. Still while operating the Ca oven at this current, the wavelength of the pothoionization laser (423 nm) is modulated by a triangular waveform. Neutral fluorescence is detected once a current dependent signal is observed, being the triangular modulation no longer observed. Atom flourescence signal is maximized by adjusting the EMCCD camera focus, then both photoionization laser beams and imaging focus are positioned back at the expected trapped ion position.

. . . . . .

5.3 Ion Loading and Compensation

In our trap, two types of voltage compensation are set along the lateral (x–axis) and vertical (y-axis) directions. The first voltage compensation is set by applying a voltage difference between two opposite DC electrode corresponding to one segment i.e. the voltage on each electrode is set as $V_i \pm \Delta_l$, where Δ_l is the voltage compensation in the lateral direction. Additionally, due to the force excert by patch potentials on the trap surface, in the planar traps it is also necessary to apply a vertical offset of the trapping potential minimum, named Δ_v voltage compensation along the vertical direction.

The compensation voltage settings have to be adjusted from day to day each time the experiment is run. However, in our setup they variation are around 100 mV. In the case of the Δ_l they change from -0.050 V to 0.050 V. In the vertical direction Δ_v varies from 0.060 V to 0.160 V. The trap has shown high sensitivity to these values i.e. if the voltages are not set inside this range ion trapping is completely hindered. A single ion remains in the trap for about 30 s and 40 min without and with Doppler cooling respectively.

5.3.1 Loading Ions

In our trap, we have loaded single and multiple ion crystals using three or more inner segments. The election of certain DC potential configuration de-

pends on the needs of the experimenter. For tight confining axial potentials (above $2\pi\cdot500\,\mathrm{kHz}$) it is necessary to employ all the (nine) segments available. For low frequencies (below $2\pi\cdot500\,\mathrm{kHz}$), instead, setting the DC potentials on three segments already provide the desired curvature. However, if a long ion chain is of interest, the use of the whole set of available electrodes or at least five segments demonstrated to be effective.

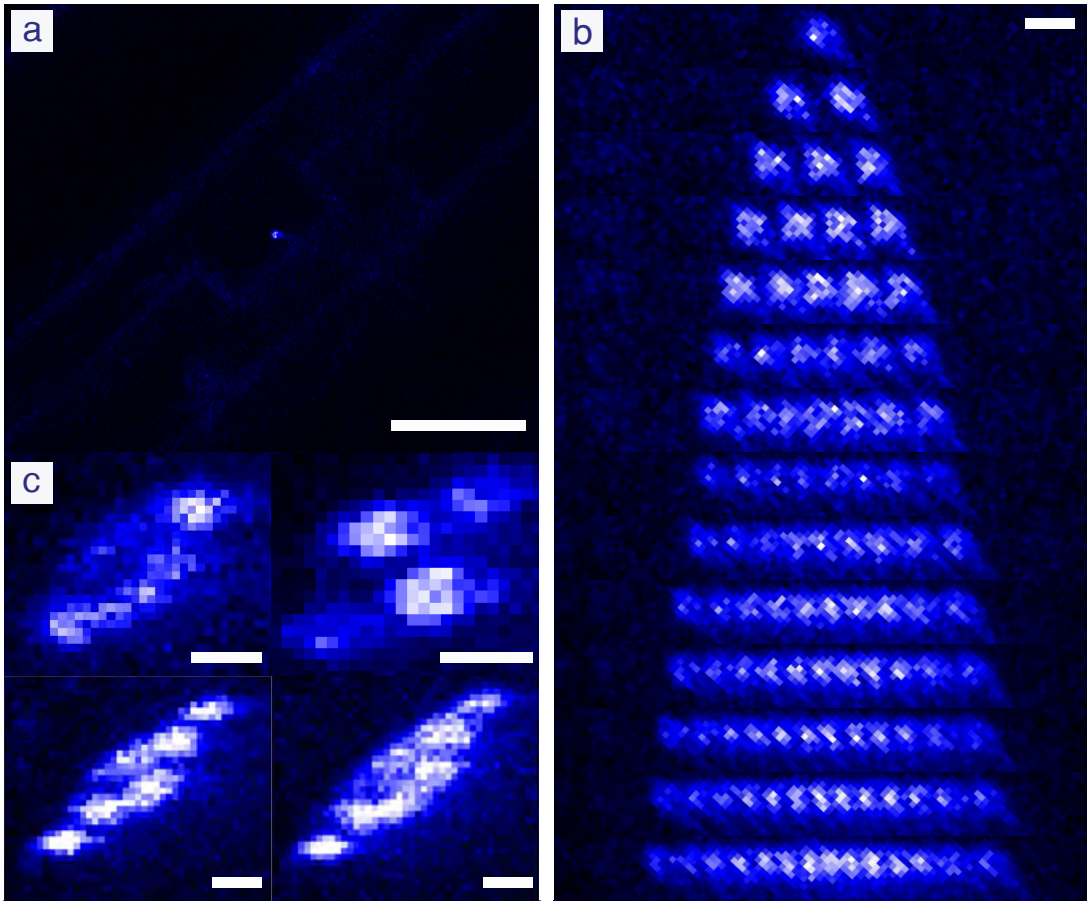


Figure 5.3 Fluorescence signal of trapped $^{40}Ca^{+}$ ion crystals above the central segment (S5) on Trap I. a) A single ion crystal trapped right above wire (W_2). b) ion loading sequence from a single ion and up to 16 ions on the middle of the trap. c) zig-zag configurations when the strength of the axial confinement ($\omega_z = 2\pi\cdot650\,\mathrm{kHz}$) becomes comparable to the radial frequency ($\omega_x = 2\pi\cdot800\,\mathrm{kHz}$). All ion crystals are trapped using the beam configuration shown in Figure 4.11a) at a ion-surface distance of 167 µm. The exposure time on the EMMCD camera was about 5 ms. The scale bar on a) corresponds to 100 µm, whereas on b) and c) it represents 10 µm .

The DC voltage settings differ in a important point from the calculations developed in Sec. 1.3.1. The main difference so far encountered is that the DC configuration required for ion trapping has to be modified such that the axial potential, still having the right curvature A_{zz}, should create a repulsive force against the trap center in the normal direction of the trap surface. The experiments developed, so far, and presented in this chapter fulfill this premise.

For the first ion trapping the following set of DC voltages were applied on each segment Vi=(0,0,0,0,1.3,6.2,-6.2,6.2,1.3) the inner wires W1 and W2 were set at compensation volatges of 0.4 V and -0.4 V respectively. After comparing to numerical simulation shown in Sec. 2.1.2 a remaining electric field (Ex,Ey,Ez)= (360,0,300) V/m may be extracted. After one year of trap operation stray electric fields mainly increased along the z-direction leading to (Ex,Ey,Ez)= (-50,0,1000) V/m. In this case the set of DC voltages Vi=(0, 0, 0, 0, 9.50, -6.54, 8.65, 0) with a lateral compensation voltage of $\Delta_l = 0.079$ V.

Typical axial frequencies used for the experiments range from $2\pi \cdot 100\,\mathrm{kHz}$ to $2\pi \cdot 760\,\mathrm{kHz}$ which correspond to a stiffness parameter (A_{zz}) of 3×10^{-4} and 12×10^{-4}, respectively. The radial frequencies are in the range from $2\pi{\cdot}0.8\,\mathrm{MHz}$ to $2\pi{\cdot}1.2\,\mathrm{MHz}$ and are consistent with a stability parameters $Q_{x,y} \equiv 0.08$ to 0.12. In this range the adiabatic approximation is satisfied and it permits to treat the ion motion along these directions as close as an harmonic oscillator. Out of these (Q_i) parameter range the instability of an ion was compromised and even sometimes no trapping was possible to observe.

In Figure 5.3c, upper right side, both axial ($\omega_z = 2\pi \cdot 600\,\mathrm{kHz}$) and radial ($\omega_x = 2\pi \cdot 650\,\mathrm{kHz}$) frequency become both comparable leading to an anisotropy factor of $\alpha = 0.85$ while the trap is operated with a low stability factor $Q_{zz} = 0.10$. In this situation, the strong axial confinement weakens one of the radial modes perpendicular to the trap axis and parallel to the trap surface in the x-direction.

Different ion crystal arrays arranged into linear or zig-zag configurations, Figure 5.3, depending on the critical ratio $\alpha = (\omega_r/\omega_z)^2$, between radial and axial frequencies set on the trap. In Figure 5.3a) a single ion captured above wire W_2 near segment five (Sg5) is shown. The scattered light coming from the exposed insulator gaps makes evident the wires structure. The scale bar corresponds to 100 µm. The consecutive ion loading from 1 to 14 ions is depicted in Figure 5.3b). After loading, an ion lost of approximately 5 min pro

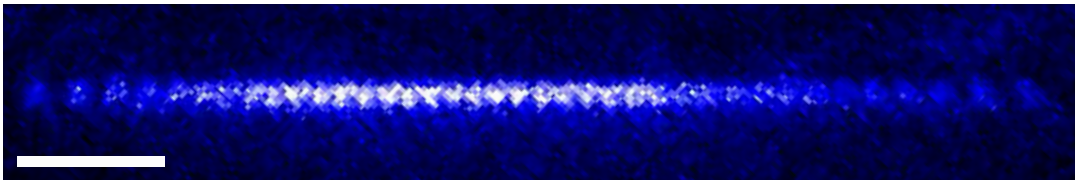


Figure 5.4 Fluorescence detection of an ion chain for thirty eight $^{40}Ca^{+}$ ions trapped along the axial direction with a frequency $\omega_z = 2\pi \cdot 80\,\text{kHz}$ and characteristic length corresponding to $l \approx 4\,\mu\text{m}$ consistent with theory from ref. 44. The laser configuration used in this case is the one depicted in Figure 4.11a) where additionally the σ-beam has been also used for Doppler cooling. Scale bar equals 50 µm

ion is observable. Here, the distance between two trapped ions corresponds to $\Delta z = 10\,\mu\text{m}$ as represented by the scale bar.

A large number of ions, as shown in Figure 5.4, have been also confined. The axial frequency was reduced to 80 kHz generated by large number of DC electrodes (in this case the five innermost segments). Here, up to thirty eight $^{40}Ca^{+}$ ions arranged in a linear configuration along the trap axis. A positive DC potential of 0.3 V is only applied to the outermost segments whereas the three innermost segments are set to 0 V. The resulting axial frequency is about $\omega_z = 2\pi \cdot 80\,\text{kHz}$. The laser for optical pumping, aligned collinear to the trap axis, was used also for Doppler cooling. Whitout this colinear beam a limited chain length for about 14 or 15 ions was observed. The waist (150 µm) of the first Doppler cooling beam is clearly visible on the image, where ion's fluorescence rate is higher whereas the outermost ions are sympathetically cooled by the innermost ions and the optical pumping laser used as cooling beam.

5.3.2 Trapping Frequencies

This section refers to the basic characterization of the trap consisting on the determination of the trapping frequencies. A method widely used to determine the secular modes consists on the electronic excitation of such modes via an oscillating electric field. Albeit it is straightforward to implement it, it provides reasonable accuracies[83] in the order of 10^{-3}.

In our trap, an oscillating voltage is supplied on one of the inner current-carrying electrodes (W_2). The oscillating field strength depends highly on the type of mode to be excited and of course from the ion-to-surface distance. Typical values for electrodes close enough to the trapped ion lye between 100 mV

to 500 mV. Once the excitation frequency is closed to resonance of one of the modes, a decrement on ion flourescence due to a change on the ions velocity distribution can be observed on an EMMCD camera. The resonance condition is, however, not only determined by the strength of the applied field, but also on the amount of the cooling laser power and on the strength of non linearities arising from the confining potentials[72].

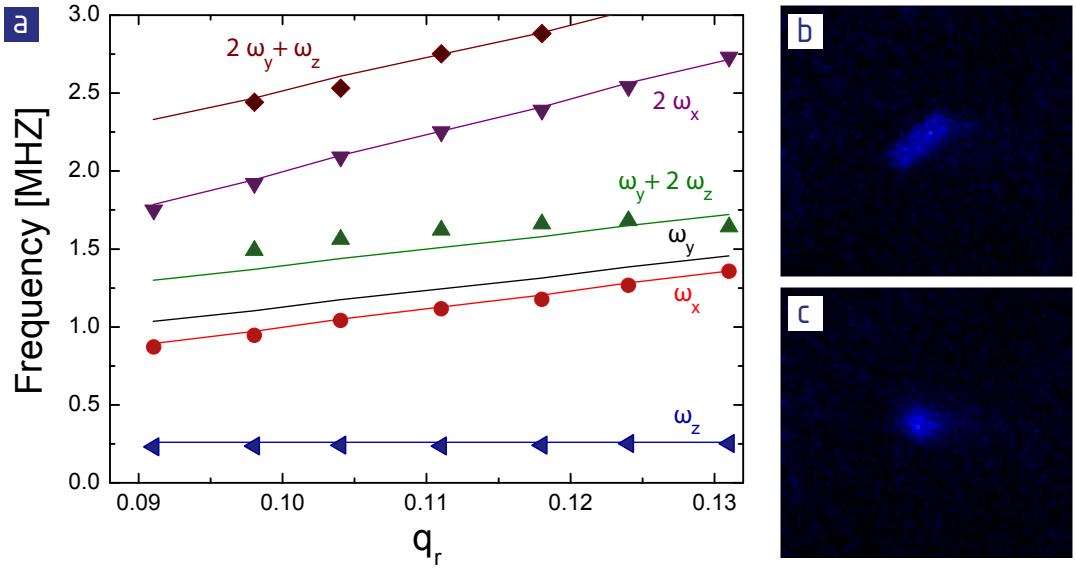


Figure 5.5 Electronic excitation of the secular modes of a single trapped $^{40}Ca^{+}$ ion. a) secular frequencies against stability parameter in the radial direction (q_r). The solid symbol are the measured values when the resonance condition is fulfilled. The solid lines are the expected frequency as a function of the stability parameter calculated numerically. b) axial direction of the trap and c) perpendicular to trap surface. Lines correspond to numerical calculations as explained in Sec. 2.1.2 when the trap is driven by $\Omega = 2\pi \cdot 30.8\,\mathrm{MHz}$

If the confining potentials deviates from an ideal quadrupole, a shift of the secular frequencies and the iso beta (β_i) boundaries on the stability plane (a,q) have to be taken into account[111]. However, as far as the ion is Doppler cooled at the very center of the confining potentials, these contributions can be fairly approximated to the ones present in conventional quadrupole traps.

In our case, the measured frequencies (solid symbols) shown in Figure 5.5a coincides to the numerical values obtained using the methods presented in Sec. 2.1.2. Different linear combinations of the secular modes can be resolved by this method. The vertical mode (ω_y), in the y-direction, was not possible

to be resolved without exciting the more sensitive mode along the x-direction (ω_x).

An adavantage of this method is that the direction of secular modes can be resolved via an EMCCD camera as depicted in Figure 5.5b. In contrast, the secular mode perpendicular along the out-of-plane direction cannot be resolved. Higher oscillation modes correspond to linear combinations of the resolved axial and radial modes ($2\omega_y + \omega_z$), Figure 5.5c.

. . . . . .

5.4 Laser Spectroscopy

In this section we will describe spectroscopic tools implemented to manipulate an optical qubit defined by two internal electronic states on single $^{40}Ca^{+}$ ion. These tools are required for implementing more advanced experiments such as resolved sideband cooling or ion heating rate measurements. In addition they are the backbone for experiments on a spin qubit on the Zeeman sublevels via a static magnetic field gradient generated and radiofrequency radiation generated by the inner electromagnets (Sec. 5.5).

For the experiments presented in this section and in Sec. 5.5, we have used two independent qubit representations. The first one, based on two optical transitions, and herein therefore termed *optical qubit*, is defined between a ground state $S_{1/2}$ and a metastable state $D_{5/2}$ driven by the preparation laser at 729 nm. The second one, is defined between the Zeeman sublevels of the ground state $S_{1/2}$, consequently named *spin qubit*. It is driven by radiofrequency radiation (RF) provided by an oscillating current sent through one inner wire (W_2). On what follows we will concentrate our discussion on the optical qubit, and lead the treatment of the spin qubit for Sec. 5.5.

5.4.1 Pulse Sequence

Part of the spectroscopic tools used in this sections were earlier developed in Ref. 83 and here adapted. The main difference consist on additional oscillating (B′) and static (B) magnetic field pulses which manipulate the Zeeman sublevels instead of the typical Raman laser setup. A example scheme of the pulse sequence is presented in Figure 5.6 consisting on the following steps:

I Preparation: the ion is precooled by Doppler laser to a mean phonon number between 17 and 20. After that it is optically pumped to the state $S_{1/2(m_j=-1/2)}$ by a circularly polarized light (σ-397 nm).

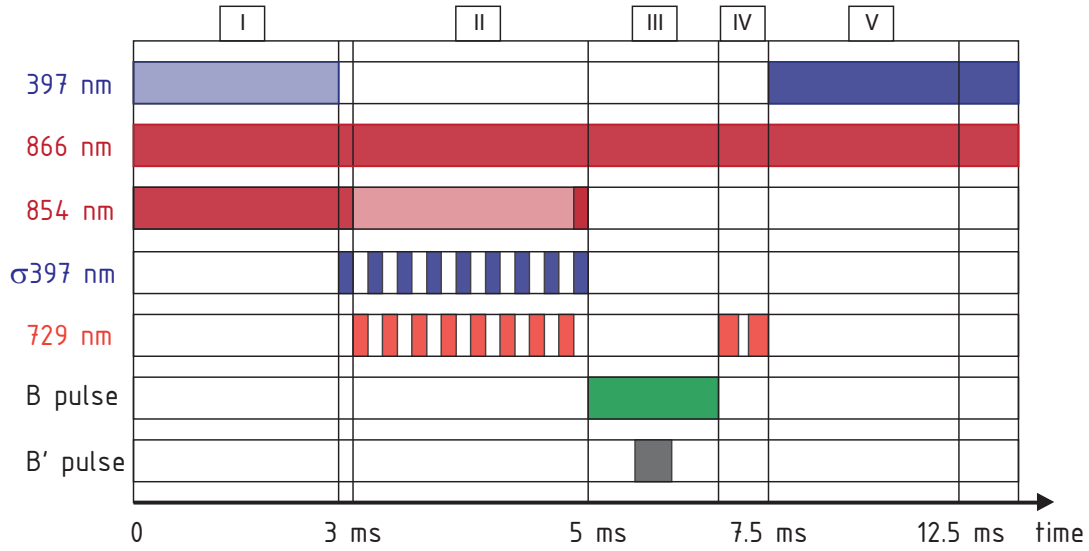


Figure 5.6 Pulsed laser spectroscopy scheme including static (B) and oscillating (B′) magnetic field pulses. The change in contrast indicates a lower radiation power.

II Sideband Cooling: light at 729 nm is brought in resonance to the lower motional sideband (red side band) of the transition whereas the background light at 854 nm assures a rapid decay to the ground state. At each pulse one phonon number is reduced and a successive short pulse from the optical pumping laser prevents spurious transitions into a non-cooled state. A final optical pumping pulse defines the initial state of the ion.

III Manipulation: on the optical qubit the motional state can be manipulated by light at 729 nm either by varying the frequency or the pulse length. In the case of the spin qubit its dynamics, see Sec. 5.5, is determined by both the additional static and oscillating magnetic fields generated by the integrated electromagnets

IV Analysis: at this stage we investigate the occupancy of the state $D_{5/2}$ by rectangular or chirped pulses at the wavelength 729 nm. The addition of chirped pulse to drive the quadrupole transition provide efficient population transfer up to 99.6 %[106], in what follows termed a rapid adiabatic passage (RAP)

V Detection: the resulting state is read out by turning on the Doppler laser. The counts collected by an EMMCD camera are compared to a previous threshold value (σ_{th}) thus given the state probability of the population of being on the state $D_{5/2}$.

All spectroscopic experiments presented here are based on this scheme. Although exact timing depend to the type of investigation the skeleton is conserved.

5.4.2 Resolved Sideband Cooling

The most basic experiment using the scheme described above consist on identifying the carrier transition from $S_{1/2} \leftrightarrow D_{5/2}$. A careful control of noise sources such as oscillating magnetic fields, laser power and laser polarization make this possible As first step the bias magnetic field provided by the external coils is characterized. The magnitude of the external magnetic field does not exceed 5 G since linewidth broadening on the transition $S_{1/2} \leftrightarrow P_{3/2}$ may also increase the Doppler limit[83]. The bias magnetic field is appropiately set at 4.5 G such that no degeneracies between the principal (carrier) and sideband transitions are encountered. Otherwise efficient sideband cooling may be compromised.

On the other hand, the light wavevector ($\mathbf{k}$) at 729 nm should have enough projection on each secular modes. However, if all the modes are resolved by the beam proyection the frequency spectrum becomes more complicated and degeneracies can be also present from combinations of the secular frequencies.

Therefore, for the investigation of the carrier transitions and to resolve their sidebands we use the following configurations:

1 ($\mathbf{k} \parallel \mathbf{B}$) In this configuration only transitions with angular momentum ($\Delta m = \pm 1$) are allowed. This is specially desired is the qubit states is aimed to be manipulated entirely by radiofrequency radiation, Sec. 5.5.

2 ($\mathbf{k} \perp \mathbf{B}$) This configuration allows transition excitation for ($\Delta m = \pm 1, \pm 2$). The sideband necessary for sideband cooling can be prepare in this configuration by appropriate choose of the angle (γ) between beam polarization and bias magnetic field direction.

The transition from $S_{1/2(m=-1/2)} \leftrightarrow D_{5/2(m=-3/2)}$ and its first sidebands (Figure 5.7) is obtained by varying the frequency of the preparation beam together

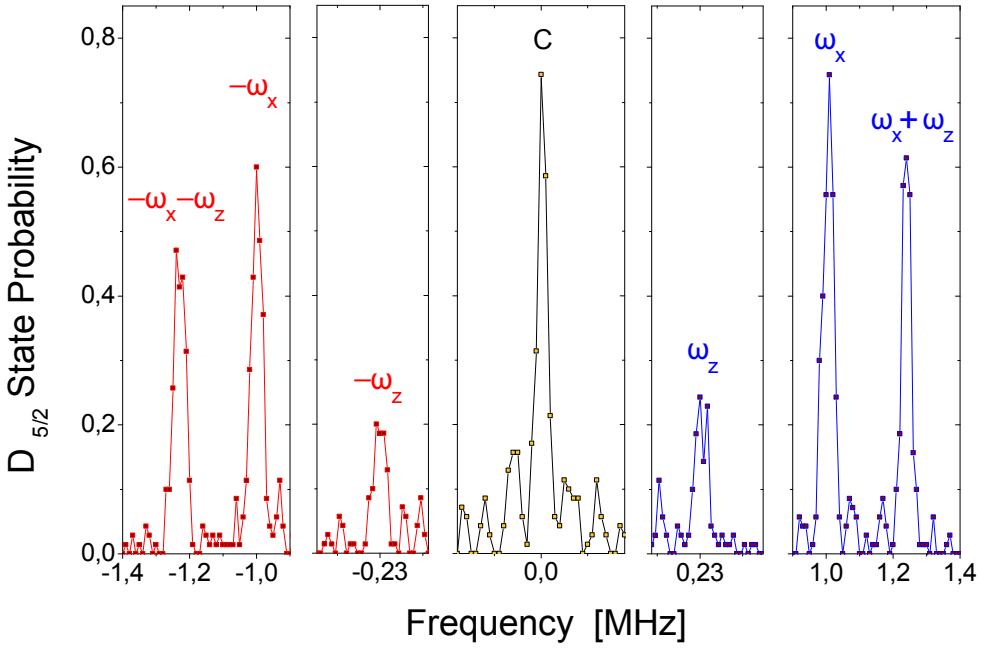


Figure 5.7 The transition from $S_{1/2(m=-1/2)} \leftrightarrow D_{5/2(m=-3/2)}$ and its sidebands are displayed. The corresponding secular frequencies in the z-direction, $\omega_z = 2\pi \cdot 230\,\mathrm{kHz}$, and perpendicular to trap axis in x-direction, $\omega_x = 2\pi \cdot 1.0\,\mathrm{MHz}$, are resolved. The y-oscillation mode does not couple to the laser with a pulse duration of $\tau = 50\,\mu\mathrm{s}$. The configuration explained in (2), Sec. 5.4.2 is used and the polarization beam oriented parallel to the bias magnetic field $\vec{\mathbf{B}}$, ($\gamma = 0°$). Higher order modes are visible such as $(\omega_x + \omega_z)$.

with configuration (2), Sec. 5.4.2. In this case, the lowest motional (red) and higher (blue) sidebands are resolved around the carrier (C) transition using an square pulse shape. The oscillator in the y-direction does not couple to the laser field.

5.4.3 Optical Qubit Coherent Dynamics

Once identifying the carrier and sideband transitions we are able to study the dynamics of the approximated two-level system by varying the pulse length of the preparation beam (at 729 nm). If the laser frequency is set exactly on resonance to one of the transitions, the atom states will undergo Rabi oscillations.

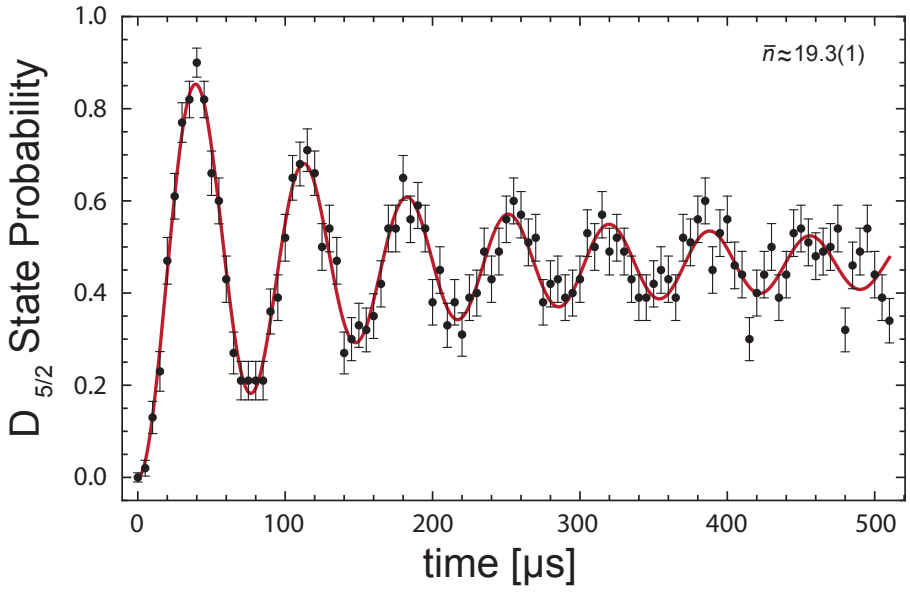


Figure 5.8 Rabi oscillations from the ground state $S_{1/2}$ to the $D_{5/2}$ state. The solid line (red) is a fit from Eq. 1.32 and each point (black) represents 100 experiments. The detuning (δ) of the laser frequency and the phonon distribution $\bar{n}$ have been varied to match the data for π-time = 34 µs and laser power of 12 mW. The resulting Lamb-Dicke parameter is calculated to be ($\eta = 0.01$)

Increasing the pulse time while excitating the ion in resonance drives the population between between the ground and excited state, $S_{-1/2(m_j=-1/2)} \leftrightarrow D_{5/2(m_j=-3/2)}$ as shown in Figure 5.8. The solid line is a fit using Eq. 1.32 and is consistent with a dephasing with a mean phonon distribution of $\bar{n} = 19.3(1)$.

5.4.4 Sideband Cooling

After preparing the ion into the Lamb-Dicke regime we can manipulate its motional states by repetitively exciting in resonance the lower sideband of its carrier transition until the motional ground state is reached with high probability.

We have used the pulsed scheme explained in Sec. 5.4.1 to investigate sideband cooling to the ground state. In Figure 5.9, the Rabi oscillation of the carrier after sideband cooling is displayed. The fit (red line) has been done after setting as variable the phonon number $\bar{n}$. This is consistent with a residual mean phonon number of $\bar{n} = 3(3)$.

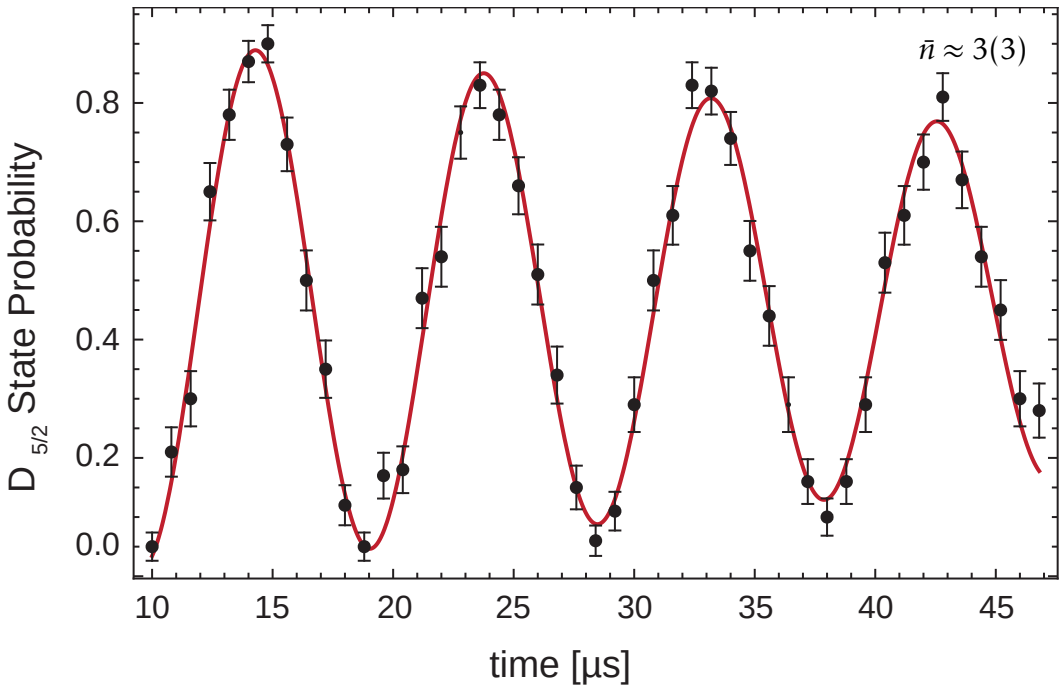


Figure 5.9 Phonon number state after sideband cooling protocol. The carrier transition ($S_{1/2(m_j=+1/2)} \leftrightarrow D_{5/2(mj=+5/2)}$) is driven after successive pulses of the preparation laser in which a radial mode (x-direction) couples to the laser wavevector by an angle ($\gamma = 90°$). The remaining phonon number is associated to an excessive anomalous ion heating rate ($3\,\mathrm{ms}^{-1}$)

The carrier transition which is driven by succesive pulses of the preparation laser corresponds to $S_{1/2(m_j=+1/2)} \leftrightarrow D_{5/2(mj=+5/2)}$. It couples to the laser wavevector at an angle ($\gamma = 90°$) between the polarization beam and the bias magnetic field direction, (see Config. 2, Sec. 5.4.2). The remaining phonon

number is associated to an excessive anomalous ion heating rate ($3\,\mathrm{ms}^{-1}$) which strongly couples to the radial mode at a frequency of $\omega_x = 2\pi{\cdot}1$ MHz. For future experiments an in-situ trap cleaning system will be used to reduce excessive ion heating rates, the discussion of the system is presented in Sec. 4.1.5.

5.4.5 Ion Heating Rate

Trapped ions near to metal surfaces are extremely sensitive to small variations of electric fields. The rate at which their mean phonon number increases per unit time is called *heating rate*. This anomalous heating has been correlated to patch potentials randomly distributed on the trap surface[112] following a four power scaling of the trap size (d^{-4}). However, its main source is still under current active investigation.

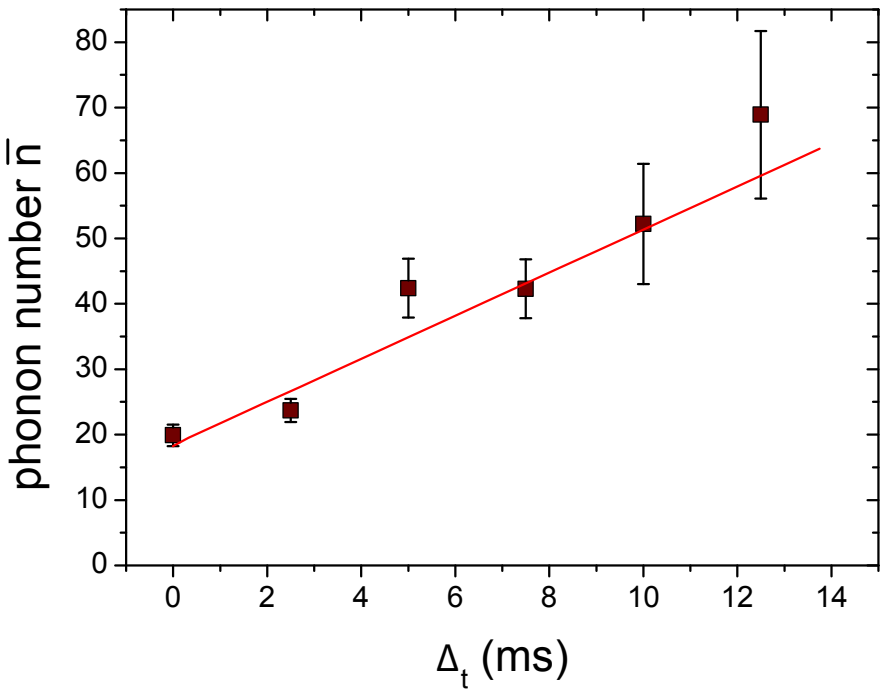


Figure 5.10 Phonon number as a function of delay time of laser light at 397 nm. Each point and their associated statistical errors represent the average of 100 interrogations to the carrier by the manipulation laser at 729 nm assuming a thermal distribution given by Eq. 1.32. A linear fit is consistent with an initial phonon number of 18, given by Doppler cooling a single trapped ion, and results in a ion heating rate of $\dot{\bar{n}} = 3(1)$ phonons/ms.

We have measured the corresponding ion heating on trap I. These are consistent with the four power scaling thus associated to patch potentials of contaminants adsorbed on the trap surface.

In order to measure ion heating rates in Trap I, we have modified the pulse scheme presented in Sec. 5.4.1. In this modifies scheme we have added a delay time (Δ_t) after a Doppler cooling (I) and before state manipulation (III), while omitting (II). After certain delay time (Δ_t) the carrier is excited in resonance by varying the length of manipulation laser at 729 nm. The system undergoes Rabi oscillations and can be defined approximatively to a thermal distribution, where the phonon number is extracted from fitting the resulting data to Eq. 1.32.

The resulting phonon number after 100 interrogations on the carrier transition at certain delay time (Δ_t) of light at 397 nm is plotted in Figure 5.10. The laser configuration used for these experiments is given in Sec. 4.3.5 where the laser wavevector at 729 nm has a maximal projection on the radial mode (x-axis) being investigated. The ion heating rate $\bar{n} = 3(1)$ phonons/ms is extracted from a linear fit of the set of data assuming a thermal state for the ion motion[83]. One limitation of this method is that the distinction of the thermal state of the ion motion for high phonon numbers is less accurate as given by the statistical error bars in Fig. 5.10.

Ion heating rates measured for this trap are consistent to similar traps with characteristic length of $d = 167\,\mu$m. A way to possibly minimize these values, below enough a fault-tolerant threshold (10^{-4}), would be for instance to include in-vacuum cleaning techniques such as Ar^+ bombardment recently reported in Ref. 66 and 67. We will come back to this discussion in Sec. 4.6.

. . . . . .

5.5 Radiofrequency Spectroscopy

In this section, the manipulation by radiofrequency radiation of a spin qubit encoded on the Zeeman sublevels of the ground state $S_{1/2}$ of $^{40}Ca^{+}$ is presented. In contrast to a optical qubit, a magnetic spin qubit presents no spontaneous decay with long coherence times (~30 ms)[113].

From the trap presented in Sec. 2, two independent electrodes (W_1 and W_2), are supplied by either static or oscillating currents. The total static magnetic field ($\vec{B}$) results from the sum of an homogenous field ($\vec{B}_0$) and position dependent field ($\vec{B}_1$) generated by two coils and an integrated electromagnet (W_1) respectively. An oscillating (rf)[a] current sent through wire W_2 generates the oscillating magnetic field ($\vec{B}'$) which flips the spin direction. The total static and oscillatory magnetic fields and their corresponding angular frequencies (ω_0 and ω_1) are sketched in Figure 5.11b.

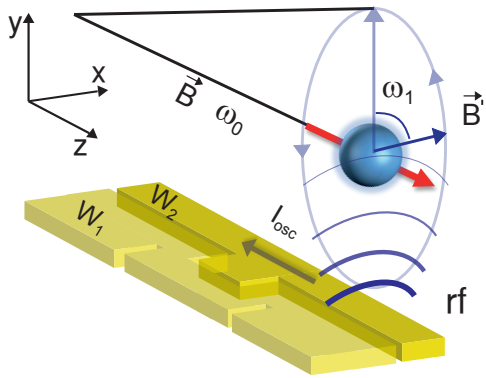


Figure 5.11 Spin qubit implementation on the Zeeman sublevels. A total static magnetic field ($\vec{B} = \vec{B}_0 + \vec{B}_1$) defines the (z-) quantization axis an exerts an angular frequency in the laboratory (ω_0). An oscillating magnetic field ($\vec{B}'$) produced by an integrated current-carrying wire (W_2) place 167 µm far from the trapped $^{40}Ca^{+}$ flips the spin state with an angular frequency (ω_1) in the rotating frame.

After Rabi original work[114], for the particular case when, the oscillating term ($\vec{B}'$) is perpendicular to the total static field ($\vec{B}$) the spin qubit dynamics is defined by,

$$P(\downarrow \rightarrow \uparrow) = |c_{\uparrow}(t)|^2 = \frac{\omega_1^2}{(\omega-\omega_0)^2+\omega_1^2}\sin^2\left(\frac{\sqrt{(\omega-\omega_0)^2+\omega_1^2}}{2}t\right) \tag{5.2}$$

$$\Omega_R(\omega) = \sqrt{(\omega-\omega_0)^2+\omega_1^2} \tag{5.3}$$

[a] note the change in terminology to distnguish between the radiofrequency (rf) current and the RF potentials

In this case, a static magnetic field along the trap axis (z-direction) splits the Zeeman sublevels and an oscillating magnetic field perperdicular to it drives the spin. Additional, if an ion is exerted to interact with a high magnetic field gradient, its spatial position becomes dependent on the applied gradient [34].

5.5.1 Spin Qubit Preparation and Manipulation

The laser-less pulse scheme for manipulating the spin qubit requires two implementations: the electron shelving technique and coupling of the Zeeman sublevels to radiofrequency radiation. A single spin qubit state manipulation including the static and oscillating magnetic current pulse is described in this section.

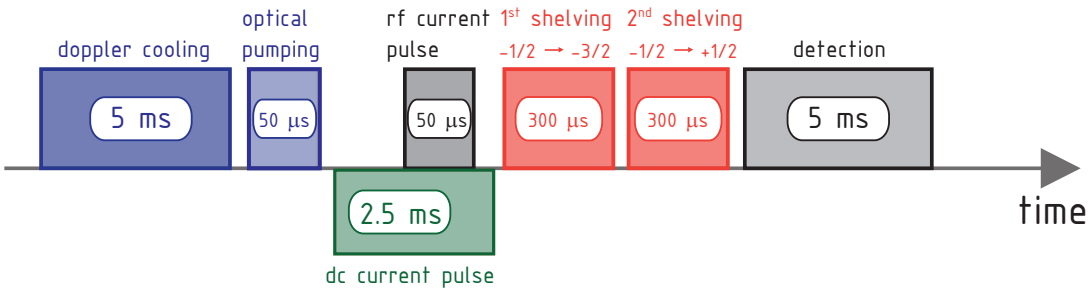


Figure 5.12 Radiofrequency spectroscopy sequence. After state preparation by Doppler cooling and optical pumping, a static current is applied to a inner wire (W_1) close to the trapped ion. Whereas a static magnetic field is switched on, an oscillating magnetic field produced by W_2 permits to drive the state population at the Zeeman's sublevels at 12.7 MHz. Then both static and oscillating currents are turned off and the spin state is shelved to the metastable state $D_{3/2}$. The final ion's state probed by ion's fluorescence detection. A final Doppler cooling step is included until the duration of the whole experiment completes a line trigger of 50 Hz to strobe magnetic field fluctuations caused by the current line supply.

The experimental (rf) pulsed sequence is depicted in Figure 5.12. The spin qubit is initially prepared by Doopler cooling and optical pumping into the down state $|\downarrow\rangle$. After then, a static current pulse is supplied to an inner wire (W_1) and the generated magnetic field gradient along the trap axis serves to lift the degeneracy of the Zeeman sublevels. An oscillating (RF) current pulse, sent through a second inner wire (W_2), generates an oscillating magnetic field –acting as a spin flip operator. The population of being either in $|\downarrow\rangle$ or $|\uparrow\rangle$ state is shelved into the $D_{5/2}$ state via a chirped laser pulse near 729 nm. To increase

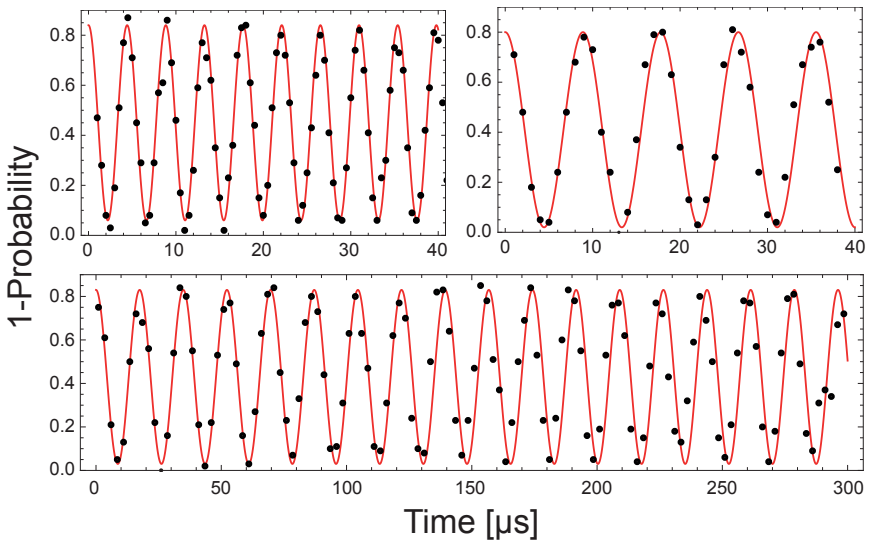


Figure 5.13 Coherent excitations on the Zeeman sublevels of a single $^{40}Ca^{+}$ ion. The spin is prepared by optical pumping in the initial state $|\uparrow\rangle$. An oscillating magnetic field of amplitude B' drives the spin at different Rabi frequencies. a) $\Omega_R = 2\pi \cdot 226(1)\,\text{kHz}$, b) $2\pi{\cdot}112(1)\,\text{kHz}$ and c) $2\pi{\cdot}57(1)\,\text{kHz}$. The contrast is limited by the initial state preparation with an error about 15 %.

electron transfer efficiency the population is shelved simultaneously onto a second different $S_{1/2} \leftrightarrow D_{5/2}$ level. For the final state readout, an EMMCD camera captures with relatively short detecting times (0.5 ms) ion's fluorescence. Once the final state dectection is completed, the Doppler cooling lasers are turned on until the experiment sequence completes a line trigger time (20 ms).

5.5.2 Spin Qubit Resonance

In this section, the state dynamics of the spin qubit via radiofrequency (rf) radiation in Trap I is investigated. The laser configuration (C1) used to manipulate the optical transitions from S↔D levels is sketched in Sec. 4.3.5. The quantum magnetization axis is defined by a static magnetic field ($\mathbf{B}_0$) of magnitude (4.5 G) produced by a pair of coils externally mounted on the vacuum chamber.

The resulting separation in frequency space of the Zeeman sublevels is reachable under radiofrequency radiation (ν =12.7 MHz). Therefore, an oscillating current in resonance to the Zeeman frequency is supplied through W_2 serving as spin flip operator. A static magnetic field gradient along the

trap axis is generated by an inner electromagnet (W1). Each experimental data corresponds to the average of 100 experiments taken via the pulse scheme explained in Sec. 5.5.1.

The population transfer between the down $|\downarrow\rangle$ to the up $|\uparrow\rangle$ state in $^{40}Ca^{+}$ via radiofrequency radiation is plotted in Figure 5.13. The signature of the oscillatory behavior of the two-level system is observed for a rf frequency on resonance to the Zeeman frequency. The system is let evolved in time and a pulse length scan is registered. Then the transition probability from Eq. 5.2 is reduced to

$$|c_{\uparrow}(t)|^2 = \sin^2\left(\frac{\Omega_R t}{2}\right) \tag{5.4}$$

where $\Omega_R = \omega_1 = \mu B'$ for the case of zero detuning ($\delta = \omega - \omega_0$). The Rabi frequency (Figure 5.13) on the Zeeman sub levels is directly proportional to the oscillating magnetic field strength (B').

By varying the frequency detuning δ around the spin drive frequency (ω) the spin angular frequency is described as depicted in Figure 5.14. The spin is flipped at different frequencies, such that the farther the excitation frequency from the spin resonance the faster the spin flipping or Rabi frequency is. On addition, increasing the detuning a decrement on the contrast is observed as described by the left mulplying term from Eq. 5.2.

Using rf radiation to manipulate the spin state reduces the complexity of more robust laser systems. For instance for driving Raman transitions one requires high powers (mWs) in contrast to few (μWs) as discussed in this section.

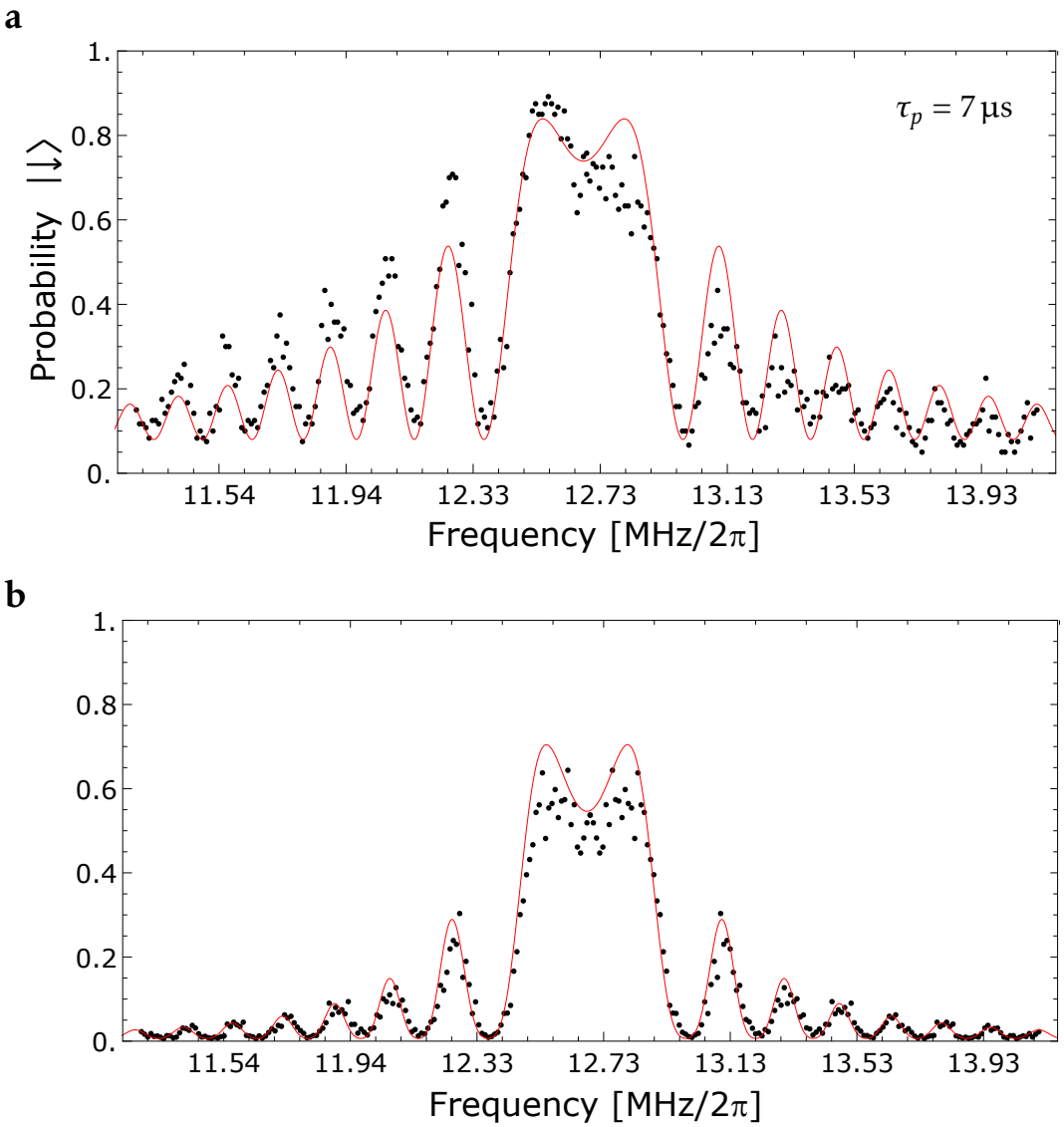


Figure 5.14 Carrier transition between the Zeeman sub niveaus for a rf pulse length of 7 µs. For an rf detuning close to carrier transition (12.7 MHz) the Rabi frequency is consistent with a spin oscillating at angular frequency of $\omega_1 = 2\pi \cdot 479\,\mathrm{kHz}$ produced by an oscillating current of 2 mA sent through wire W_2. a) probability of having the spin in down state $|\downarrow\rangle$ where data points consist on an average over 100 consecutive experiments leading to a maximal error of about 5 % . b) symmetric average of probability of having the spin in down state $|\downarrow\rangle$ around (12.68 MHz) carrier transition.

5.6 Ion as Magnetic Field Probe

We have used a $^{40}Ca^{+}$ ion to sense the magnetic field produced by W_1 from the design explained in Sec. 2.1 and to characterize the magnetic field gradients produced in Trap I. The magnetic field ($\vec{B}_1$) is generated by a static current sent through an on-chip-integrated electromagnet (W_1) and by two external coils which adds an homogenous magnetic field ($\vec{B}_0$) to the total magnetic field $\vec{B}$. The strength of this resulting magnetic field has been determined following two strategies as shown in Figure 5.15:

- Laser spectroscopy: a trapped $^{40}Ca^{+}$ ion above an inner segment (S7) far from the middle of the trap senses the change on the magnetic field strength when the static current amplitude applied to W_1 is varied. The Zeeman splitting is tracked via laser spectroscopy in which the state population is shelved from the ground state $S_{1/2}$ into the state level $D_{5/2}$. This will be treated in more detail in Sec. 5.6.1
- Radiofrequency spectroscopy: Transporting a $^{40}Ca^{+}$ ion along 600 µms in z-direction, between two innermost segment (S4 and S6), the magnetic field produced by the wiggle (in W_1) is spatially resolved. This will be treated in more detail in Sec. 5.6.2

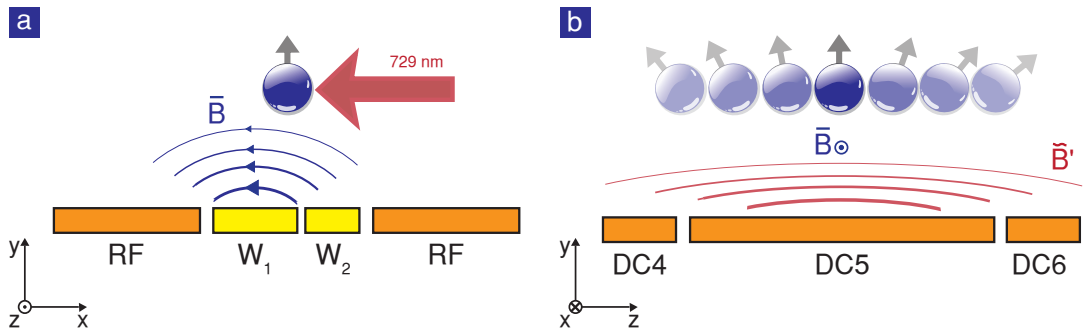


Figure 5.15 a) cross section of segment 7 (Sg7). Different static current amplitudes are applied on W_1 and the magnetic field tracked via laser spectroscopy in which the state population is shelved from the ground state $S_{1/2}$ into the state level $D_{5/2}$. b) an ion is transported from segment 4 and 6 (S4 and S6) such that the change of the magnetic field produced by the wiggle (in W_1) is spatially resolved along a distance of 600 µm in z-direction. An oscillating magnetic field ($\vec{B}'$) generated by applying a rf frequency current flips the population in the Zeeman sublevels depending on the strength of the static magnetic field ($\vec{B}$).

For both cases we monitored the change of the total magnetic field magnitude due to the Zeeman effect. We will first discuss the methods developed in Sec. 5.4.

5.6.1 Measuring the Magnetic Field Strength via Laser Spectroscopy

The total magnetic field sensed by a single $^{40}Ca^{+}$ ion depending on the amplitude of the static current supplied through W_1 is investigated by laser spectroscopy. Two internal optical transitions of a single $^{40}Ca^{+}$ ion trapped above an inner segment (S6) serve to track the total magnetic field magnitude via Zeeman splitting. We generated axial frequencies from $2\pi\cdot 100\,\mathrm{kHz}$ and $2\pi\cdot 750\,\mathrm{kHz}$ by setting appropriate static voltages (as discussed in Sec. 1.3.1) to three DC segments (S5, S6, S7). Additionally, the radial frequencies were set typically from $2\pi\cdot 0.8\,\mathrm{MHz}$ and $2\pi\cdot 1.2\,\mathrm{MHz}$. The laser configuration (C1), as described in Sec. 4.3.5, permits to drive S↔D transitions less sensitive to magnetic field fluctuations.

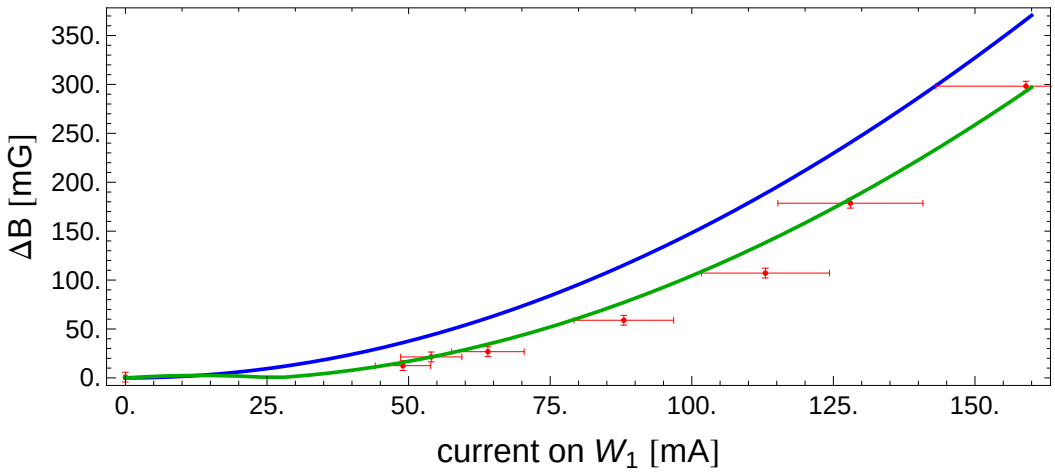


Figure 5.16 Numerical simulations (blue solid line) obtained by RADIA considering an ion is placed at 167 µm above W_1. The measured magnetic field by recording the Zeeman splitting on two optical transitions of the metastable state is shown in green. Assuming a small deviation (about 0.8°) of the homogenous magnetic field (B_0) with respect to the z-axis a correction may be estimated (green solid line).

The magnitude difference of the magnetic field ($\Delta B = B - B_0$) as a function

of the current applied on W_1 is plotted in Figure 5.16. The error bars in the y-direction are associated to a statistical error after 100 measurements. The simulated magnetic field difference (blue solid line) agrees within ten percent from the data points (red). The disagreement (green solid line) may be estimated by assuming the homogeneous field, originally supposed completely parallel to the trap axis, has a small deviation (about 0.8°) with respect to the z-axis. Such a misalignment is indeed possible, considering that both the trap chip and carrier have been mounted by hand, as shown in Sec. 4.1.1.

The numerical simulations agrees within 2 % to the magnetic field analytically obtained when wire W_1 is considered an ideal wire of infinite thickness placed 175 µm far from the ion's position. The numerical simulations obtained by RADIA considers the ion is trapped 167 µm above the trap surface with wire dimensions of 100 µm × 2 µm cross-section.

When the experimental data was routinely taken we observed an additional magnetic field offset produced by the current supplied through the oven. Numerical simulations, using FEM, when a current of 3.45 A is supplied to the oven results in a magnetic field ($\mathbf{B}_{oven} = \{0.03, -0.002, 0\}$ mG).

In addition to the static current supplied on wire (W_1) the measurements given in the last section are demanding in the sense that they dependent strongly on the laser stabilization (729 nm). A simplification of the measurement scheme is obtain applying an rf oscillating current on a second current-carrying wire (W_2) to directly drive the Zeeman sublevels.

5.6.2 Measuring the Magnetic Field Strength via Radiofrequency Spectroscopy

For the characterization of the magnetic field generated by the current applied through wire (W_1) we measured directly the Zeeman splitting frequency when an rf radiation drove in resonance the spin qubit state. The laser pulsed scheme, in this case plays a second role, and serves to discriminate between the Zeeman states of the spin by shelving the population to the metastable state $|D\rangle$.

An example of a typical spin resonance profile used on the experiments to relate the static Zeeman splitting is shown in Figure 5.17. In this case, we have supplied to wire W_2 a low rf power (μW) for a relative long rf pulse time (40 µs). Particularly, an oscillating magnetic field (4 mG) produced a FWHM

of 30 kHz which permits to detect minimal changes of the magnetic field of about 0.5 mG.

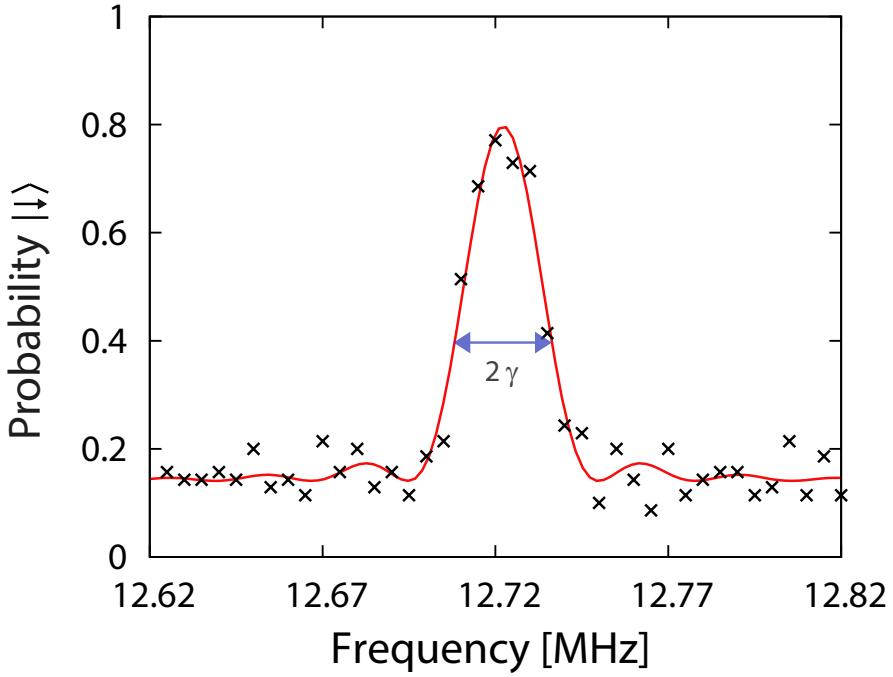


Figure 5.17 Transition probability from $|\uparrow\rangle$ to $|\downarrow\rangle$ spin state on the Zeeman sub levels. Spin resonance at 12.7 MHz of the Zemman splitting produced by a static magnetic field (4.5 G) along the trap axis. No current is supplied through wire W_1. The FWHM of 30 kHz after an rf pulse of 4×10^{-5} s is extracted after fitting the data to Eq. 5.2

The magnetic field strength is directly monitored by the rf resonance condition of the Zeeman sub levels or simply radiofrequency spectroscopy. A static magnetic field (4.5 G), produced by two external coils, gives rise to a bare frequency of the Zeeman splitting (12.7 MHz)

A static current supplied through wire W_1, determined by the voltage drop through a shunt resistor as explained in Sec. 5.1, adds to the total static magnetic field. We have observed additional noise due to RF pickup on the inner wires W_1 and W_2 which broadens the measured voltage across the shunt resist. Therefore, the voltage values taken to calculate the current flowing through wire W_1 consist on averaging the maximal and minimal voltage values measured during the whole pulse duration.

Magnetic Field Gradient.– Using the methods described in the previous section we probed the spatial distribution of the magnetic field along a complete inner segment (S5). Above this segment a wiggle structure (on W_1) provides a maximal gradient along the z-axis. An applying oscillating current on a second wire W_2 permits to drive magnetically the Zeeman sublevels and thus track the strength of the field.

A single $^{40}Ca^+$ ion is moved along a test distance (600 µm) using the methods presented in Sec. 1.3 such that a constant axial frequency ($\omega_z = 2\pi\cdot 266\,\mathrm{kHz}$) is maintained along the RF knot. A static current pulse of ($I_c = 102\,\mathrm{mA}$) was supplied to W_1, using the scheme described in Sec. 5.5.1. An oscillating current pulse ($I_o = 0.15\,\mathrm{mA}$) supplied to W_2 generates an rf magnetic field to drive the Zeeman sublevels.

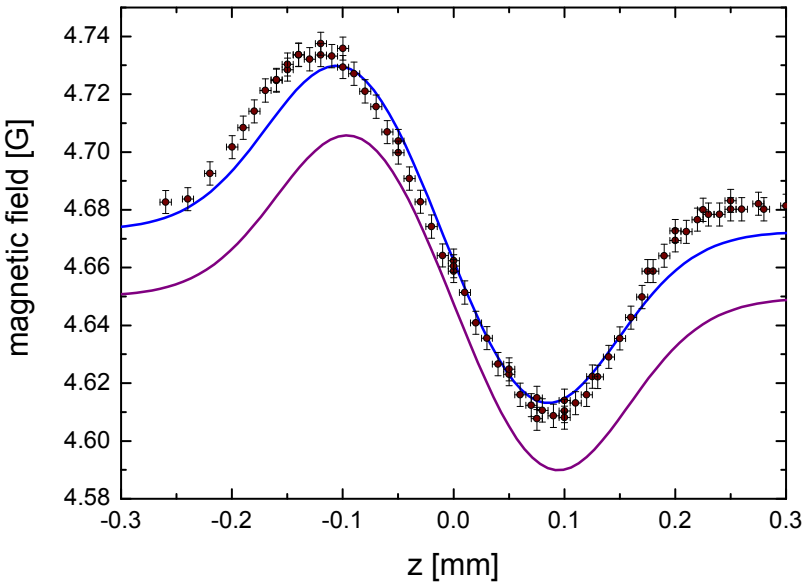


Figure 5.18 For the simulations $I = 102\,\mathrm{mA}$ the ion's position is determined during the experiment via the EMMCD camera to an arbitrary origin (middle of the trap). The discrepancy to the simulated position (BEM) differs on about 10 µm due to a mismatch between applied and measured DC voltages. The magnetic field (lila) results from an applied current of $I = 102\,\mathrm{mA}$ on wire (W_1). A homogeneous magnetic field (4.5 G) is set along the trap axis by two external coils.

The measured magnitude of the static magnetic field as a function of the ion's position along the trap axis is given in Figure 5.18. The zero position

corresponds to the center of a inner voltage segment (S5). The error for the determination of the ion's position along the trap axis is around 10 µm which corresponds to the disagrement between simulated and measured axial potentials. The assymetric ion positioning near segment 5 (negative part in z-axis) is associated to shortcuts on one side of four segments named DC1 to DC4 after neutral Ca deposition on the filter board. The resulting non-ohmic contacts, with resistances between (100 Ω to 300 Ω), act as voltage dividers thus lowering the axial confining the close the ion is moved towards segment four (S4).

The lila solid line correspond to the simulated strength of the field if we take into account the supplied static current of $I_c = 102\,\mathrm{mA}$ on wire W_1. In this situation the homogenous magnetic field (4.5 G) produced by two external coils has been assumed to be aligned completely parallel to trap axis. A possible contribution of the magnetic field produced by running the Ca oven for 4.5 A did not explained the disagreement between simulated and experimental data. However, if we assumed that the homogenous magnetic field is tilt by only about 0.75° the experimental and theoretical values matched within 5 % as shown by the blue solid line. The applied static current on wire (W_1), results on a magnetic field gradient of $1.11 \pm 0.18\ \mathrm{T\,m^{-1}\,A^{-1}}$.

Although, the measurement accuracy here reported $\frac{\Delta B}{B_0} = 10^{-4}$, is lower than an alternative technique $\frac{\Delta B}{B_0} = 10^{-7}$ developed in our group [115], our method substitutes the use of a more complicated Raman laser setup in favor of on-chip-integrated electromagnets and radiofrequency oscillating magnetic fields to resonantly resolve Zeeman frequency shifts. Moreover, by transporting a single $^{40}Ca^{+}$ ion along the trap axis (600 µm) we measured the total static magnetic field which yields a gradient of $1.11 \pm 0.18\ \frac{\mathrm{T}}{\mathrm{m\cdot A}}$ in this direction. Based on these results and the simulations presented in Sec. 2.1.3 we anticipate gradients of $10\ \frac{\mathrm{T}}{\mathrm{m\cdot A}}$ perpendicular to the trap axis when counterpropagating currents $I_1 = 10\,\mathrm{A}$ and $I_2 = -10\,\mathrm{A}$ may be applied to electrodes W_1 and W_2 respectively.

There is however an overhead resulting from supplying oscillating current pulses close to the trap drive frequency (Ω) which together with higher order trapping potentials results into ion instability and/or ion loss as we will explain in a coming section 5.7.

. . . . . .

5.7 Ion Instability under Non-linear Fields and Pulsed Static Currents

To investigate the ion stability when an external electric field may excite the ion's motion we carried out state-dependent ion fluorescence detection as a function of an applied (rf) frequency current. If the ion is excited resonantly at certain frequency (ν) its energy, and as consequence its velocity distribution will increase, therefore decreasing the photon rate emission. After a threshold value[a] the ion cannot be longer contained thus a decrement on ion florescence can be detected.

Initially we define a $s(\nu, a, q)$ parameter, with a being constant we tuned the excitation frequency (ν) from 9 MHz to 16 MHz. We observed that at certain frequencies the ion's fluorescence decreases to values below the threshold defined in Sec. 5.4, thus observing a resonance-like deep. We associate this decrement on the ion fluorescence as an increment on the velocity distribution due to the exciting radiation and from now on called *instability band*. For long pulses and high (rf) power such instability bands broadened. In addition by varying the frequency and increasing the radial confinement (so that a q_r could be associated) we observed a wandering of the instability bands as a function of the exciting (rf) frequency.

5.7.1 Experimental Sequence

A single $^{40}Ca^{+}$ ion is first Doppler cooled (5 ms), and a σ^{+} polarized beam prepares the ion in the state $|\downarrow\rangle$. A sinusoidal (rf) voltage pulse (~10 mA) for different pulse length (300 µs and 2 ms) excites the ion's motion. The ion fluorescence is collected by an EMMCD camera and the experiment repeated 100 times to take the average ion's state.

The presence of instability bands can be explained as follows. After the laser cooling is off, the rf pulse drives the ion out of the trap center. Depending on the amplitude of the ion excursions higher order of the potential may be probed by the ion. The consideration of a quadrupole trapping field is therefore only valid as far as the ion remains at the very center of the trap. At higher rf powers, the ion will be kicked farther from the trap center, it will lead to probe higher order terms resulting on nonlinear resonances near the

[a] when the kinetic energy surpasses the trap depth

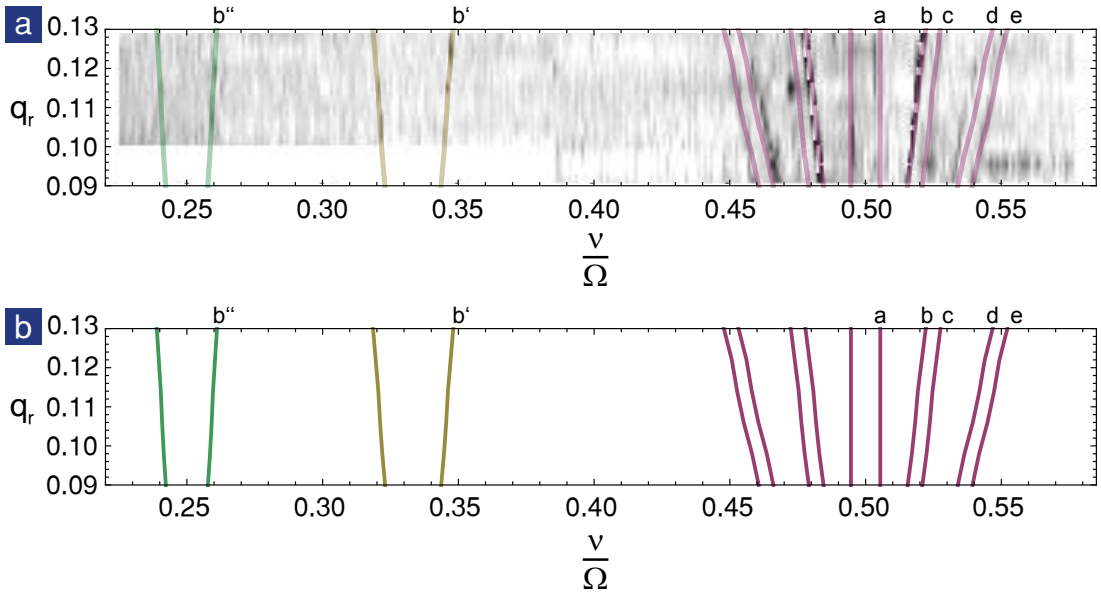


Figure 5.19 Stability diagram and non linear terms of a single $^{40}Ca^{+}$ ion. a) linear superposition of higher order motional frequencies and irradiating (ν) rf frequency convey to drive (in resonance) the micromotion frequency (Ω). b) The instability bands are described by [72] linear combinations of $\frac{1}{m}[\Omega \pm (n\ \omega_x + p\ \omega_z)]$ where m, n, p are integer numbers satisfying $m{+}n{+}p = N$ and x, z indicate the radial and axial directions respectively.

first fractional relative frequencies. At low rf power an instability band prevails around $\nu' = \nu/\Omega = 1/2 = 0.5$.

We observed non-linear resonances close to fractions of the trap drive frequency (Ω) which reflects as a decrease in ion fluorescence. The exact source of this is not well understood, but it is likely the result of higher order contributions to the trapping potential[72]. The observed resonance at fractional frequency (ν') for an ion driven by Ω are reproduced if we consider the following linear combinations.

The resonances near to fractional frequencies of the drive frequency (Ω) might be investigated in terms of nonlinear contributions to the trapping potentials. For instance, by varying the initial conditions of the ion i. e. before the ion is driven by the excitation field, a slightly different compensation voltage can be set. So that we can know, with high probability, the initial position of the ion out of the trap center. Then the stability diagram can be plotted for different compensation voltages. Indeed this method can be used to find the trap center. With this conditions, the stability diagram as presented in Fig-

ure 5.19, will present only weak instability lines around $\nu' = 0.5$, as observed for a quadrupole linear trap perturbed by a quadrupolar field[111].

$$\nu = \frac{1}{m}(\Omega \pm (n\ \omega_x + p\ \omega_z)). \tag{5.5}$$

For instance, the lines labeled in Figure 5.19 are obtained as follows,

$$a \equiv \frac{1}{2}(\Omega \pm \omega_z) \text{ for } m = 2,\ n = 0,\ p = 1$$
$$b \equiv \frac{1}{2}(\Omega \pm \omega_x),\quad b' \equiv \frac{1}{3}(\Omega \pm \omega_x),\quad b'' \equiv \frac{1}{4}(\Omega \pm \omega_x) \text{ for } m = 2,3,4,\ n = 1,\ p = 0$$
$$c \equiv \frac{1}{2}(\Omega \pm (\omega_x + \omega_z)) \text{ for } m = 2,\ n = 1,\ p = 1$$
$$d \equiv \frac{1}{2}(\Omega \pm (2\ \omega_x + \omega_z)) \text{ for } m = 2,\ n = 2,\ p = 1$$
$$e \equiv \frac{1}{2}(\Omega \pm (2\ \omega_x + 2\ \omega_z)) \text{ for } m = 2,\ n = 2,\ p = 2$$

where $\Omega = 2\pi \cdot 30.8\,\text{MHz}, \omega_z = 2\pi \cdot 333\,\text{kHz}$ and $\omega_x(q)$

Conclusions

The design and fabrication of planar traps which generate strong magnetic field gradients at the ion's position with optimized trap geometry for ion transport and maximal trap depth has been described. Special emphasis has been given to develop, in house and within international collaboration, microfabrication processing. Commercial technologies such as thick film and laser induced wet etching were utilized for the fabrication of a novel hybrid ion trap.

Concerning microfabrication processing, two flows were used during the course of this work. One base on photolithography, electroplating and wet-etching. This has led to structures with high height-to-width aspect ratios (3:2) which sustained high current densities $J = 3 \times 10^{-10}\,\mathrm{A\,m^{-2}}$. A second fabrication processing, leads to evaporated gold as trap electrodes with low electrical resistivity ($3.8 \times 10^{-7}\,\mathrm{S\,m^{-1}}$) and high surface quality (rms roughness $R_q = 48\,\text{Å}$ in $1 \times 1\,\mu\mathrm{m}^2$).

A fabricated trap based on this latter method has demonstrated successful loading of a single and up to 38 $^{40}Ca^{+}$ ion crystals for several minutes (40 min) even though the trap was operated at shallow trap depth (35 meV). The reliability of ion trapping permitted to implement laser spectroscopy, sideband cooling, radiofrequency spectroscopy of a single $^{40}Ca^{+}$ ion for the characterization of ion heating rates and magnetic field gradient measurements.

The experimental investigation of ion instability resonances arise from coupling of the irradiated field to ion modes such that the linear superposition of all modes excites in resonance micromotion. We attribute these ion instabilities to additional non-linear terms on the confining potentials. Even though, the use of non-linear resonances excitation is very promising in the fields of quantum chaos and non-linear systems.

A second generation of a planar trap packaged onto an independent AlN substrate was constructed by screen printed and laser induced glass etching. Trap cleaning by Ar^{+} ion bombardment will lead to realization of fault tolerant quantum computing in planar ion traps. In addition, high magnetic field gradients of about $3\,\mathrm{T\,m^{-1}\,A^{-1}}$ will be used to engineer strong (30 kHz) spin-spin interaction.

. . . . . .

Outlook

In the coming years, novel ion traps including more complex on-chip elements such as interconnects or vias will require to develop more elaborate fabrication processes. For instance, an extension to multiple structure layers of our fabrication process based on electroplating can be done as follows. A novel trap microprocessing, shown in Figure 5.20, may be implemented using a Damascene process.

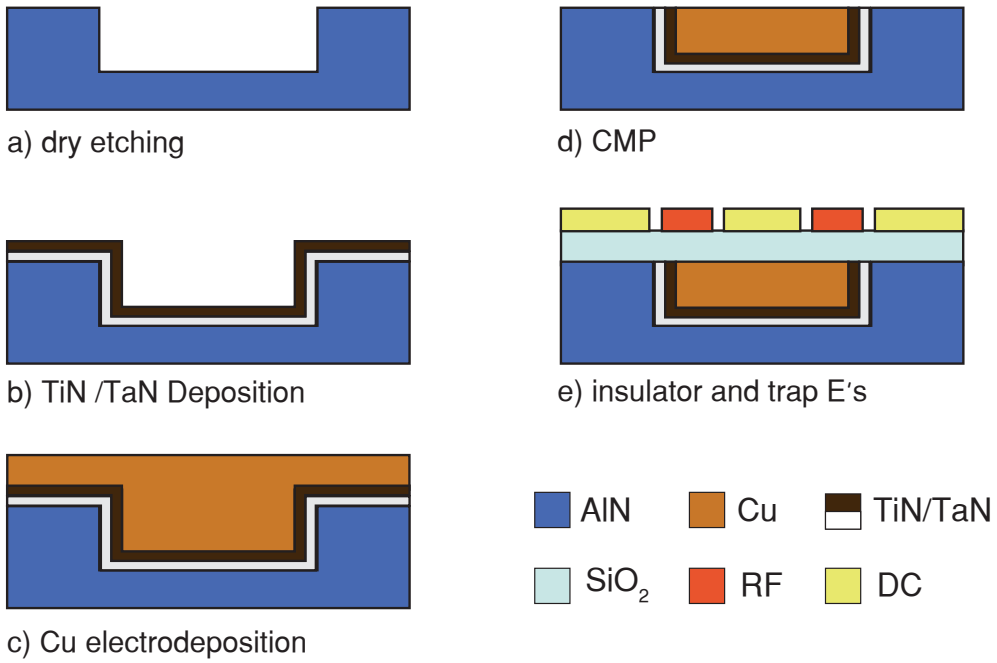


Figure 5.20 Multilayer fabrication based on a Damascene process (b–d). a) dry etching of AlN. b) Cu diffusion barrier (TiN or TaN) deposition by CVD or PVD. c) Cu electroplating. d) selective chemical-mechanical polishing of Cu. e) SiO_2 deposition by CVD. After, conventional photolithography and electroplating will form trap electrodes.

Wafer preparation should start by AlN etching on a mixture of (SF_6/ Ar) gas by reactive ion etching (RIE), where up to 140 nm/min etching rates are within reach[116]. After etching grooves in AlN substrate, a Damascene process consisting of three basic steps (b–d) can be performed in a similar fashion as in conventional Si substrates processing[117]. b) A thin layer of Ta/TaN layer grown by magnetron sputtering[118] will stop Cu-diffusion into AlN substrate thus increasing wire performance. c) a thin Cu-seed layer (10 – 20 nm) will

avoid formation of voids during Cu-plating. d) chemical-mechanical polishing (CMP) will remove excessive Cu-plating structures. Planarization indeed is the key technolgy on the Damascene process for multilayer processing[93]. e) after Damascene process conventional SiO_2 deposition by CVD together with trap structuring via photolithography and electroplating will be finally done.

Another field in which current planar trap will be developed is surface science using a trapped ion as impurity sensor. For instance, the systematic study of controlled contaminates above trap electrode surface and their correlation to ion heating rates is under reach with current technology.

The deposition of either oxides, nitrides, metals or even compounds can currently be done by magnetron sputtering techniques under UHV conditions [a]. As CO molecules constitute one of the most abundant adsorbates into ion trap chambers[67] they will be prompt to react with controlled deposited compounds. Thus a trapped ion brought close to "contaminated" areas (Zone 1) by adsorbates will sense ion heating rates as a function of the adsorbates species. Au NP's supported on thin oxide layers may be used to correlate adsorbate reactivity since they possess CO catalytic properties. Their deposition feasibility onto the trap surface is also under reach of actual thin film technology by magnetron sputtering[119]. An Ar^+ ion bombardment will "reset" Zone 1 from adsorbates and a new layer from a previous and/or different source can be deposited. Finally, to correlate ion heating rates to chemical reactivity it will be required to incorporate into trap vacuum system auxiliary analytical techniques such as Auger Spectroscopy (AES) and/or X-ray Photoelectron Spectroscopy (XPS).

[a] Omicron GmbH, www.omicron.de, Mantis Deposition Ltd. www.mantisdeposition.com

A Surface Quality Characterization

For the characterization of trap surface quality analytical techniques such as optical microscopy (OM), scanning electron microscopy (SEM) and atomic force microscopy (AFM) were during the course of this work.

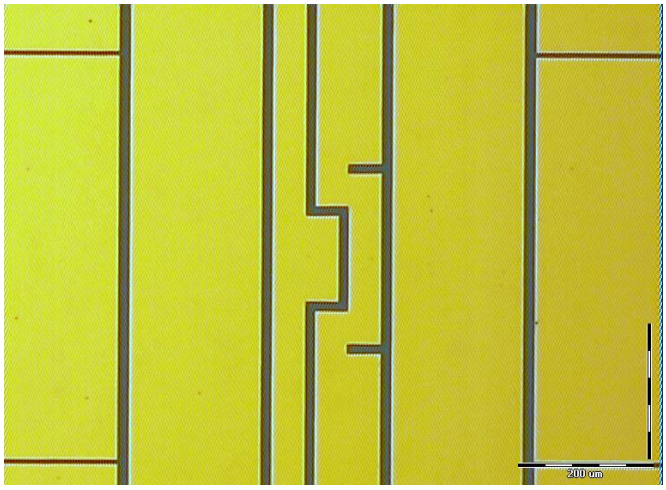
In its simplest form, optical microscopy, provides rapid testing of either prototypes or final products. Increasing in complexity but also in accuracy, scanning electron microscopy resolves small features such as grain size, small defects and cracks on the trap electrodes.

If a detail detailed look of the trap surface is required, atomic force microscope (AFM) provided to detect, either remaining byproducts, or roughness trap electrodes.

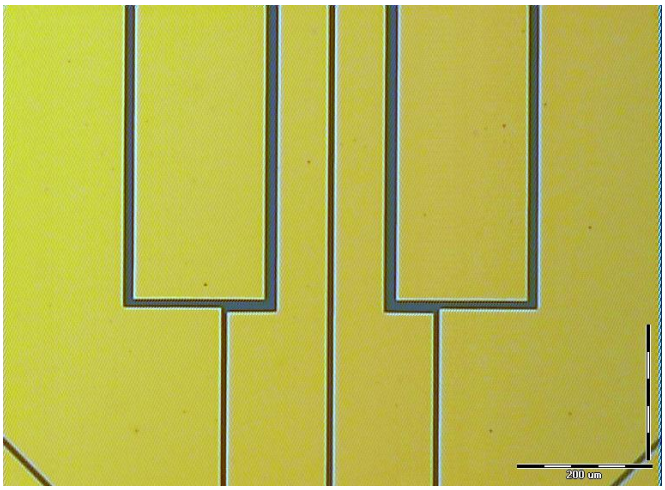
Table A.1 Typical dimensions and properties of gold electrodes fabricated by the lift-off process

Paremeter	Values
Film Thickness	1.88-2.20 µm
Electrical Resistivity	2.63 µΩ cm
Grain Size	120-160 nm
Surface Roughness	4.8 Å

Note that the gold conductivity of the electrodes fabricated via thermal evaporation ($3.8 \times 10^{-7}\,\mathrm{S\,m^{-1}}$) slightly differs from the bulk value ($4.3 \times 10^{-7}\,\mathrm{S\,m^{-1}}$). In contrast for the electrodes fabricated via electroplating a much lower value in the range of $0.6–4.3 \times 10^{-7}\,\mathrm{S\,m^{-1}}$ is reported [120]



(a) Innermost part of Trap I with integrated eletromagnets

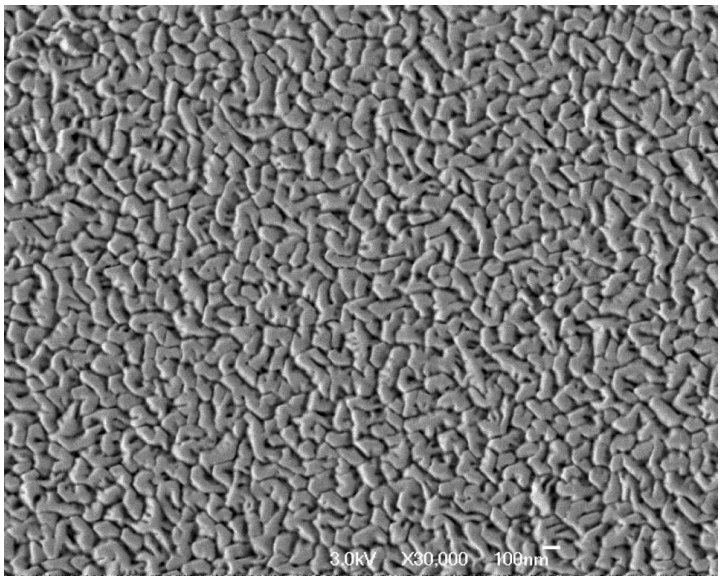


(b) outermost part of rf electrodes an a split of the rf ground electrode

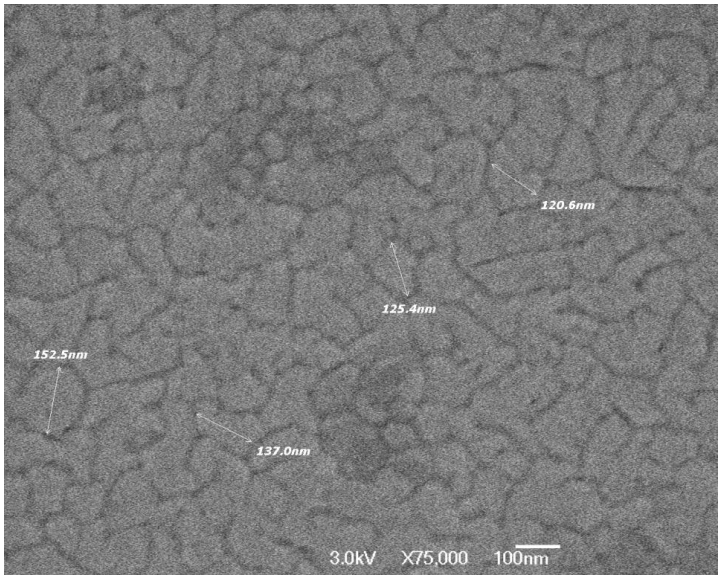


(c) trapping zone (Z3) of Trap IV

Figure A.1 Optical micrographs of different planar traps with electrodes grown by thermal evaporation of 2 µm



(a) Grain size of Au film on Trap I with integrated eletromagnets



(b) Grain size of about 150 nm on film of 1.9 µm thickness

Figure A.2 SEM Micrographs of of Grain Size in Trap I

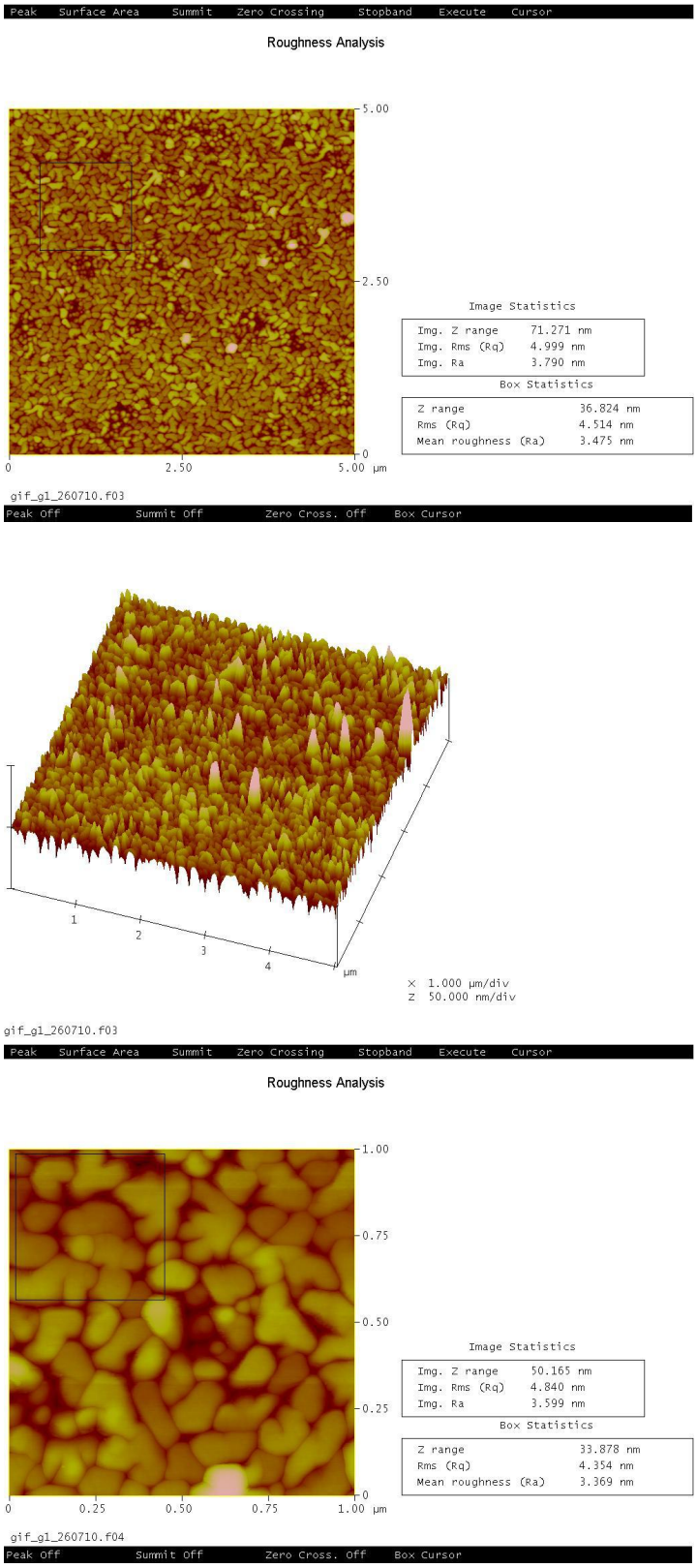


Figure A.3 AFM Micrographs of Trap I on electrodes with 1.9 µm thickness with a mean roughness of $R_a = 3.8\,\mathrm{nm}$ in a surface area of $1{\times}1\ \mu\mathrm{m}^2$

B Fabrication Processes for Planar Traps

In recent times, planar traps geometry have increase in complexity either by implementing multi-layered processes or by integrating on-chip elements. Here, relevant fabrication process to build on-single plane or multi-layered planar trap geometries are shortly reviewed. The methods discussed here can in part be found in Ref. 53 and references in there.

Since the original design and first realization of a surface-electrode or planar trap by Chiaverini et. al.[52] in the group of Dr. Wineland in 2006, the implementation of such a trap has rapidly spread among the ion-based quantum computing community. The advantages of this planar design over their macroscopic counterparts are remarkable. Apart from their relative easy fabrication processing, it is a strong candidate as the hardware unit of a large-scale quantum computer architecture. The easy integration of qubit manipulation tools such as micro optical elements or microwave circuitry makes this design also very attractive.

In the following sections we will briefly review most of the relevant planar trap architectures together with their corresponding fabrication processes.

. . . . . .

B.1 In-plane Electrodes

The first design consists of electrodes structured on top of a dielectric planar substrate. These electrodes can be deposited through conventional additive processes such as thermal evaporation or electroplating.

The typical procedure consists on developing a previously lithographically patterned resist (organic polymer) on top of a dielectric substrate. Then an additive process such as electroplating or thermal evaporation is used to form metal electrodes[39,96,121]. A final wet etching step is done to remove an initial seed layer typically required for electroplating. This method can be also inverted, where silver is first evaporated on the dielectric substrate followed by a mask resist and a final silver wet etching clears the inter-electrode gaps on the trap[65]. A generic trap built by this process is shown in Figure B.1.

In a more elaborated process, but followed the same basic principles, a recent trap with transparent trap electrodes (TiO_2) has been also demonstrated. It promises being an efficient ion-photon coupling system[122].

Due to the simplicity on its fabrication steps, involving less agents or chemicals the planar traps built by these methods poses the highest surface quality compared to more elaborated processes (discussed below). This is spe-

cially true if the additive process consists on thermal evaporation where bulk properties are mostly kept in contrast to electroplated finishes. Indeed it is critical when properties such as thermal conductivity or resistivity are of high interest. For instance, the conductivity of gold electrodes fabricated via thermal evaporation ($3.8 \times 10^{-7}\,\mathrm{S\,m^{-1}}$)[a] slightly differs from the bulk value ($4.3 \times 10^{-7}\,\mathrm{S\,m^{-1}}$). In contrast for gold electrodes fabricated via electroplating much lower values in the range of $0.6–4.3 \times 10^{-7}\,\mathrm{S\,m^{-1}}$ are reported[120].

. . . . . .

B.2 Very Large Scale Integration

An extension of single metal layer traps, multilayered traps offer the possibility for more robust ion traps, which may include integrated elements for filtering (capacitors), qubit detection (integrated optics) or qubit manipulation (current-carrying wires) to generated high magnetic field gradients[123]. In addition, a multi-layered design may offer a route to shield patch charges generated on exposed insulators.

A planar trap consisting of multiple metal-insulator layers is shown in Figure B.1b). This design relies on a very large scale integration (VLSI) process where a commercial silicon-on-insulator (SOI) substrate is coated with a conducting layer to create a ground layer. On top of it, a thin insulating material (0.5 µm) and two pillars of insulator material(SiO2) of about 10 to 20 µm are deposited by a Physical Enhanced Chemical Vapor Deposition (PECVD) process. A subsequent conducting layer on top of the thin insulating layer shields charge paths produced at the insulating surface. A micrometer metal layer on top of the pillars serves as RF electrodes. Overhang of the latter metal layer permits a coating of metals such as Au or Ag, which are not complatible to VLSI process. Additional vias can be fabricated to interconnect two separate conducting layers.

As a remarkable advantage of this design stands the elevation of the rf-electrodes by growing an intermediate insulating layer –decreasing the capacitance of the trap by increasing the RF-DC electrode distance. The integration of interconnection vias makes this design suitable for the fabrication of more elaborated trapping electrode geometries[124]. For instance by implementing or modifying this process the integration of in-surface capacitors[56] for compacting the trapping setup or micro optical elements for manipulation or the col-

[a] values for the trap used in this work

lection of ion fluorescence[54] has been done. The transport through optimized Y-junctions has been also demonstrated using this design[57].

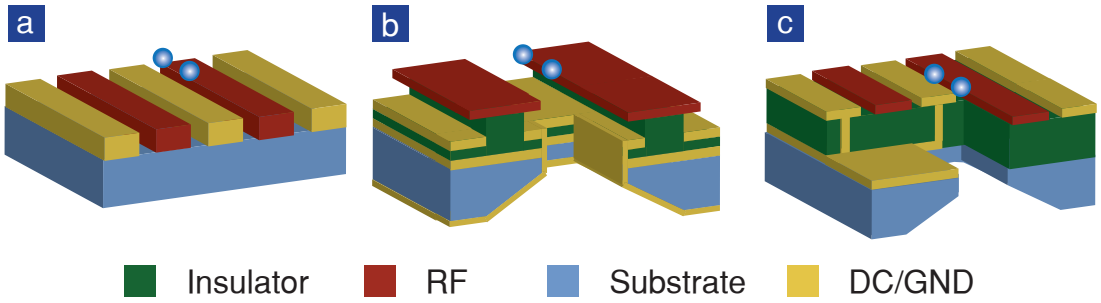


Figure B.1 Half and full cross-sections for different planar ion trap designs. (a) five-wire planar trap on a single metal layer[59,96,121]. (b) five-wire configuration based on VLSI process[123–125]. (c) modified five-wire planar trap with ion loading slot and vias[126]. (not to scale)

. . . . . .

B.3 Buried Multilayered Electrodes

Another method to construct multilayer planar traps, and a direct extension of the original proposal consists of a Metal Buried Multilayer (MBM). It requires less processing steps as the previous (ML) design and also incorporates a loading slot and metal vias as interconnectors[126] as shown in Figure B.1c. The fabrication starts with the thermal evaporation deposition of an adhesion promoter layer (20 nm of Ti) followed by conductive layer (300nm of Au). An additional adhesion promoter layer (20 nm of Ti) is evaporated on top of the conductive layer to bond a successive insulating layer (SiO_2). This insulating layer is grown by a Chemical Vapor Deposition (CVD) process. Exposed areas of the insulating layer are plasma etched to connect the two conducting layers. After a photolithography patterned resist the second conducting layer is evaporatively deposited onto intermediate insulating layer. A lift-off process is carried to removed the resist mask and metal deposited on top. A primary slot via mechanical milling is drilled on the backside of the substrate, and a final Focus Ion Milling (FIM) defines further the ion loading slot shape. This design process was used to build a hexagonal planar ion network showing the flexibility of planar traps to realize storing and processing zones for the manipulation of many ions[126].

B. FABRICATION PROCESSES FOR PLANAR TRAPS

We have shortly reviewed some fabrication layouts based on, modified or extended versions of a single layer planar trap. The use of any of these layouts depends entirely on any intended application. If it is required to send high current densities through metal wires, an stringent conditions is its reliability to electrical failure. Among the fabrication design discussed previously the single layer trapping electrode configuration offers the highest electrode cross section, reliable electric contacts, and good thermal contact to substrate.

Since we have N ions and in general three spatial degrees of freedom the Hessian of Eq. 1.34 can be written formally as

$$\begin{aligned} M_{jN+o,kN+p} &= m\omega_z^2\Bigg(\frac{\delta_{jk}\delta_{op}}{\alpha_j} + \frac{l^3}{2}\sum_{n\neq m}(\delta_{on}-\delta_{om})(\delta_{np}-\delta_{mp})\cdot \\ &\quad \cdot\left[\frac{3(x_{n,k}-x_{m,k})(x_{n,j}-x_{m,j})}{|\mathbf{x}_n-\mathbf{x}_m|^5} - \frac{\delta_{kj}}{|\mathbf{x}_n-\mathbf{x}_m|^3}\right]_{\bar{\mathbf{x}}_n,\bar{\mathbf{x}}_m}\Bigg), \end{aligned}$$

with o and p denoting the ion's number, j and k the spatial direction and δ_{jk} the Kronecker delta. For a single string and as long as one stays below the critical value of α, ions align linearly and thus M reduces to a block diagonal matrix[44,127] with entries $m\omega_z^2(B^x, B^y, A)$ where

$$\begin{aligned} A_{n,m} &= \begin{cases} 1 + 2\sum_{\substack{p=1\\p\neq m}}^{N} \frac{l^3}{|\bar{z}_m-\bar{z}_p|^3} & \text{if } n = m \\ \frac{-2l^3}{|\bar{z}_m-\bar{z}_n|^3} & \text{if } n \neq m \end{cases} \\ B^i_{n,m} &= \left(\frac{1}{\alpha_i}+\frac{1}{2}\right)\delta_{nm} - \frac{1}{2}A_{nm}. \end{aligned}$$

In the case of two strings with each holding N ions, the two sums in M can be split apart in intra string and inter string components:

$$\sum_{n=1}^{2N}\sum_{\substack{m=1\\m\neq n}}^{2N} = \sum_{\substack{n,m=1\\m\neq n}}^{N} + \sum_{\substack{n,m=N+1\\m\neq n}}^{2N} + 2\sum_{n=1}^{N}\sum_{m=N+1}^{2N} = (a)+(b)+(c).$$

Sum (a) will yield to the matrices A and B for one chain, (b) to that of the other chain, such that one has a matrix $(B^{x1}, B^{x2}, B^{y1}, B^{y2}, A^1, A^2)$.

Part (c) however leads to new entries in M, which reads with $\delta^{op}_{nm} = (\delta_{no} -$

$\delta_{mo})(\delta_{np} - \delta_{mp})$:

$$
\begin{aligned}
C_{op}^{xx} &= l^3 \sum_{n,m} \delta_{nm}^{op} \frac{2(x_n - x_m)^2 - (z_n - z_m)^2}{|\mathbf{x}_n - \mathbf{x}_m|^5} \\
C_{op}^{zz} &= l^3 \sum_{n,m} \delta_{nm}^{op} \frac{2(z_n - z_m)^2 - (x_n - x_m)^2}{|\mathbf{x}_n - \mathbf{x}_m|^5} \\
C_{op}^{xz} &= l^3 \sum_{n,m} \delta_{nm}^{op} \frac{3(x_m - x_n)(z_n - z_m)}{|\mathbf{x}_n - \mathbf{x}_m|^5} = C_{op}^{zx} \\
C_{op}^{yy} &= l^3 \sum_{n,m} \delta_{nm}^{op} \frac{-1}{|\mathbf{x}_n - \mathbf{x}_m|^3} \\
C_{op}^{xy} &= C_{op}^{yx} = C_{op}^{zy} = C_{op}^{yz} = 0
\end{aligned}
$$

D.1 Related to this work

- J. Welzel, **A. Bautista-Salvador**, C. Abarbanel, V. Wineman-Fisher, C. Wunderlich, R. Folman and F. Schmidt-Kaler. Eur. Phys. J. D, **65** 285-297 (2011).
- M. Hellwig, **A. Bautista-Salvador**, K. Singer, G. Werth and F. Schmidt-Kaler. New J. Phys., **12**, 065019 (2010).

D.2 Previous work

- J.-A. Reyes-Esqueda, **A. Bautista-Salvador** and R. Zanella-Specia. J. Nanosci. Nanotechnol., **8**, 3843-3850 (2008)

D.3 Posters

2012	Magnetfeldgradienten in planare Ionenfallen zur Simulation von Spinmodellen, Universität Stuttgart
2011	Spin-Spin interaction in impurity doped ion crystal, Universität Dresden
2010	Simulation und Herstellung verschiedener zweidimensionaler Ionenfallen für die Quanteninformationsverarbeitung, Universität Hannover
2009	A planar segmented Ion Trap with a Y-Junction, Universität Hamburg

Acknowledgements

This work would not have been possible without the support of uncountable talented people.

Zuerst bedane ich mich an Herrn Prof. Dr. Ferdinand Schmidt-Kaler, für Deine bedingungslos Unterstützung und das grosses Vertrauen den Du mir immer angegeben hast.

My sincere gratitude to Prof. Fedor Jelezko who kindly accepted to be my second referee. Thanks to Prof. Ron Folman and his team for fabricating Trap I at Nanofabrication facilities at Ben-Gurion University.

With his perpetual accurate observations, Jens Welzel, deserves a notable mention. I have always been impressed of your pragmatism combined with that inexhaustible willingness to listening even the most apparent non-sense idea. Great part of my admiration goes to Niels Kurz, who kept alive the scientific spirit combined with the ability of going beyond simple plans. Without your careful programming schedules most of the experimental data reported here would not have been possible.

To my former colleagues from University of Ulm and University of Mainz, whose dedicated scientific attitude provided me a daily source of motivation and inspiration. I am specially in debt to Dr. René Gerritsma who guided part of this work and reviewed the manuscript.

I thank all my Professors of the "Advanced Materials" program at the University of Ulm. Specially mention deserve Dr. Alfred Plettl, Prof. Paul Ziemann and Prof. Peter Unger who provided me a solid knowledge on semiconductor fabrication technologies.

Meine ewige Dankbarkeit an meine liebe Frau Zaneta und liebenswert Nachwuchs Jan Flavio. Danke für so unbeschreiblichen Unterstützung und bedingungslose Quelle der Inspiration. A mi pequeñita Flavia Krystyna que pronto estarás con nosotros. Los amo en demasía.

Gracias hermano Oswaldo por esos incontables momentos idílicos que hemos vivido. A mi hermanita Emmaluz, de corazón cálido y vívido. A mi Padre Amado por su entereza y mi adorable Abuelita Emma por sus valiosos consejos. A mis tíos Elisa y Alejandro Salvador por su enorme y siempre incondicional amor.

En especial agradezco a mi maravillosa Madre Flavia Salvador, el ser más noble e inteligente que he conocido a lo largo de mi vida. En tus manos encontré siempre esa destreza única y en tu mente esa agudeza para sobrepasar cualquier obstáculo.

ACKNOWLEDGEMENTS

Im Allgemein bedanke ich mich an Deutschland, eine wunderbare Himmelstück. Das Land nicht nur der beste Brezel oder das geschmakvolles Bier sonder auch der hervorragende wissenschaftliche Umgebung.

The author acknowledges support by CONACyT in an early stage of the work. Funding within the research program framework from SFB/TRR21, DFG and GIF is gratefully acknowledged.

References

1. Feynman, R. P. *Engineering and Science* **23**, 22–36 (1960).
2. Intel. *www.intel.com* (2012).
3. Schirhagl, R., Chang, K., Loretz, M., and Degen, C. L. *Annu. Rev. Phys. Chem.* **65**, 83–105 (2014).
4. Benioff, P. *J. Stat. Phys.* **22**, 563–591 (1980).
5. Feynman, R. P. *Int. J. Theor. Phys.* **21**, 467–488 (1982).
6. Lloyd, S. *Science* **273**, 1073–1078 (1996).
7. Shor, P. W. *SIAM J. Sci. Statist. Comput.* **26**, 1484 (1997).
8. Leibfried, D., Blatt, R., Monroe, C., and Wineland, D. *Rev. Mod. Phys.* **75**, 281–324 (2003).
9. Häffner, H., Hänsel, W., Roos, C., Benhelm, J., D, C., Chwalla, M., Körber, T., Rapol, U., Riebe, M., Schmidt, P., Becher, C., Gühne, O., Dür, W., and Blatt, R. *Nature* **438**, 643–646 (2005).
10. Cirac, J. I. and Zoller, P. *Phys. Rev. Lett.* **74**, 4091–4094 (1995).
11. DiVincenzo, D. P. *Fortschr. Phys.* **48**, 771–783 (2000).
12. Monroe, C., Meekhof, D. M., King, B. E., Itano, W. M., and Wineland, D. J. *Phys. Rev. Lett.* **75**, 4714–4717 (1995).
13. King, B. E., Wood, C. S., Myatt, C. J., Turchette, Q. A., Leibfried, D., Itano, W. M., Monroe, C., and Wineland, D. J. *Phys. Rev. Lett.* **81**, 1525–1528 (1998).
14. Roos, C., Zeiger, T., Rohde, H., Nägerl, H. C., Eschner, J., Leibfried, D., Schmidt-Kaler, F., and Blatt, R. *Phys. Rev. Lett.* **83**, 4713–4716 (1999).
15. Monroe, C., Meekhof, D. M., King, B. E., Jefferts, S. R., Itano, W. M., Wineland, D. J., and Gould, P. *Phys. Rev. Lett.* **75**, 4011–4014 (1995).
16. Sackett, C. A., Kielpinski, D., King, B. E., Langer, C., Meyer, V., Myatt, C. J., Rowe, M., Turchette, Q. A., Itano, W. M., Wineland, D. J., and Monroe, C. *Nature* **404**, 256–259 (2000).

17. Nägerl, H. C., Leibfried, D., Rohde, H., Thalhammer, G., Eschner, J., Schmidt-Kaler, F., and Blatt, R. *Phys. Rev. A* **60**, 145–148 (1999).

18. Blatt, R. and Zoller, P. *Eur. J. Phys.* **9**, 250–256 (1988).

19. Rowe, M. A., Kielpinski, D., Meyer, V., Sackett, C. A., Itano, W. M., Monroe, C., and Wineland, D. J. *Nature* **409**, 791–794 (2001).

20. Cirac and Zoller. *Nature* **404**, 579–581 (2000).

21. Kielpinski, D., Monroe, C., and Wineland, D. J. *Nature* **417**, 709–711 (2002).

22. Johanning, M., Braun, A., Timoney, N., Elman, V., Neuhauser, W., and Wunderlich, C. *Phys. Rev. Lett.* **102**, 073004 (2009).

23. Warring, U., Ospelkaus, C., Colombe, Y., Brown, K. R., Amini, J. M., Carsjens, M., Leibfried, D., and Wineland, D. J. *Phys. Rev. A* **87** (2013).

24. Porras, D. and Cirac, J. *Phys. Rev. Lett.* **92**, 207901 (2004).

25. Blatt, R. and Roos, C. F. *Nature Phys.* **8**, 277–284 (2012).

26. Johanning, M., Varón, A. F., and Wunderlich, C. *Journal of Physics B: Atomic, Molecular and Optical Physics* **42** (2009).

27. Schneider, C., Porras, D., and Schaetz, T. *Rep. Prog. Phys.* **75**, 024401 (2012).

28. Friedenauer, A., Schmitz, H., Glueckert, J. T., Porras, D., and Schaetz, T. *Nature Phys.* **4**, 757–761.

29. Kim, K., Chang, M., Korenblit, S., Islam, R., Edwards, E., Freericks, J., Lin, G., Duan, L., and Monroe, C. *Nature* **465**(7298), 590–593 (2010).

30. Islam, R., Edwards, E., Kim, K., Korenblit, S., Noh, C., Carmichael, H., Lin, G., Duan, L., Wang, C. J., Freericks, J., and Monroe, C. *Nature Comm.* **2**, 377 (2011).

31. Islam, R., Senko, C., Campbell, W. C., Korenblit, S., Smith, J., Lee, A., Edwards, E. E., Wang, C.-C. J., Freericks, J. K., and Monroe, C. *Science* **340**, 583–587 (2013).

32. Jurcevic, P., Lanyon, B. P., Hauke, P., Hempel, C., Zoller, P., Blatt, R., and Roos, C. F. *Nature* **511**, 202–205 (2014).

33. Richerme, P., Gong, Z.-X., Lee, A., Senko, C., Smith, J., M. Foss-Feig, S. M., and A. V. Gorshkov, C. M. *arXiv:1401.5088* (2014).

34. Wunderlich, C. In *Laser Physics at the Limits*, Figger, H., Zimmermann, C., and Meschede, D., editors, 261–273. Springer, Berlin (2002).

35. Mintert, F. and Wunderlich, C. *Phys. Rev. Lett.* **87**, 257904 (2001).

36. Schmidt-Kaler, F., Häffner, H., Riebe, M., Gulde, S., Lancaster, G., Deuschle, T., Becher, C., Roos, C., Eschner, J., and Blatt, R. *Nature* **422**, 408–411 (2003).

37. Wang, S. X., Labaziewicz, J., Ge, Y., Shewmon, R., and Chuang, I. L. *Appl. Phys. Lett.* **94**, 094103 (2009).

38. Kunert, P. J., Georgen, D., Bogunia, L., Baig, M. T., Baggash, M. A., Johanning, M., and Wunderlich, C. *Appl. Phys. B* **114** (2013).

39. Ospelkaus, C., Warring, U., Colombe, Y., Brown, K., Amini, J., Leibfried, D., and Wineland, D. *Nature* **476**, 181–184 (2011).

40. Khromova, A., Piltz, C., Scharfenberger, B., Gloger, T., Johanning, M., Varón, A., and Wunderlich, C. *Phys. Rev. Lett.* **108**, 220502 (2012).

41. Wilson, A. C., Colombe, Y., Brown, K. R., Knill, E., Leibfried, D., and Wineland, D. J. *Nature* **512**, 57–60 (2014).

42. Wunderlich, H., Wunderlich, C., Singer, K., and Ferdinand, S. *Phys. Rev. A* **79**, 052324 (2009).

43. Chiaverini, J. and Lybarger, W. *Phys. Rev. A* **77**, 022324 (2008).

44. James, D. *Appl. Phys. B* **66**, 181–190 (1998).

45. Lin, G., Zhu, S., Islam, R., Kim, K., Chang, M., Korenblit, S., Monroe, C., and Duan, L. *Europhys. Lett.* **86**, 60004 (2009).

46. Walther, A., Ziesel, F., Ruster, T., Dawkins, S., Ott, K., Hettrich, M., Singer, K., F, S., and Poschinger, U. *Phys. Rev. Lett.* **109**, 080501 (2012).

47. Bowler, R., Gaebler, J., Lin, Y., Tan, T., Hanneke, D., Jost, J., Home, J., Leibfried, D., and Wineland, D. *Phys. Rev. Lett.* **109**, 080502 (2012).

48. Raizen, M. G., Gilligan, M., Bergquist, J., Itano, W. M., and Wineland, D. J. *Phys. Rev. A* **45**, 6493–6501 (1992).

49. Wineland, D. and Leibfried, D. *Laser Phys. Lett.* **8**, 175 (2011).

50. Schulz, S. A., Poschinger, U., Ziesel, F., and Schmidt-Kaler, F. *New J. Phys.* **10**, 045007 (2008).

51. Wilpers, G., See, P., Gill, P., and Sinclair, A. *Nature Nanotech.* **7**, 572–576 (2012).

52. Chiaverini, J., Blakestad, R. B., Britton, J., Jost, J. D., Langer, C., Leibfried, D., Ozeri, R., and Wineland, D. J. *Quant. Inf. Comput.* **5**, 419–439 (2005).

53. Hughes, M. D., Lekitsch, B., Broersma, J. A., and Hensinger, W. K. *Contemp. Phys.* **52** (2011).

54. Merrill, J. T., Volin, C., Landgren, D., Amini, J. M., Wright, K., Doret, S. C., Pai, C., Hayden, H., Killian, T., Faircloth, D., Brown, K. R., Harter, A. W., and Slusher, R. E. *New J. Phys.* **13**, 103005 (2011).

55. Herskind, P., Wang, S., Shi, M., Ge, Y., Cetina, M., and Chuang, I. *Opt. Lett.* **36**, 3045–3047 (2011).

56. Allcock, D. T. C., Harty, T. P., Janacek, H. A., Linke, N. M., Ballance, C. J., Steane, A. M., Lucas, D. M., Jarecki, R. L., Habermehl, S. D., Blain, M. G., Stick, D., and Moehring, D. L. *Appl. Phys. B* **107**, 913–919 (2011).

57. Moehring, D. L., Highstrete, C., Stick, D., Fortier, K. M., Haltli, R., Tigges, C., and Blain, M. G. *New J. Phys.* **13**, 075018 (2011).

58. Ospelkaus, C., Langer, C., Amini, J., Brown, K., Leibfried, D., and Wineland, D. *Phys. Rev. Lett.* **101**, 090502 (2008).

59. Welzel, J., Bautista-Salvador, A., Abarbanel, C., Wineman-Fisher, V., Wunderlich, C., Folman, R., and Schmidt-Kaler, F. *Eur. Phys. J. D* **65**, 285–297 (2011).

60. Blakestad, R. B. *Transport of Trapped-Ion Qubits within a Scalable Quantum Processor*. PhD thesis, University of Colorado, (2010).

61. Turchette, Q. A., Kielpinski, D., King, B. E., Liebfried, D., Meekhof, D. M., Myatt, C. J., Rowe, M. A., Sackett, C. A., Wood, C. S., Itano, W. M., and Wineland, D. J. *Phys Rev. A* **61**, 063418 (2000).

62. Deslauriers, L., Olmschenk, S., Stick, D., Hensinger, W. K., Sterk, J., and Monroe, C. *Phys. Rev. Lett.* **97**, 103007 (2006).

63. Brownnutt, M., Kumph, M., Rabl, P., and Blatt, R. *arXiv:1409.6572* (2014).

64. Labaziewicz, J., Ge, Y., Antohi, P., Leibrandt, D., Brown, K. R., and Chuang, I. L. *Phys. Rev. Lett.* **100**, 013001 (2008).

65. Labaziewicz, J., Ge, Y., Leibrandt, D., Wang, S., Shewmon, R., and Chuang, I. *Phys. Rev. Lett.* **101**, 180602 (2008).

66. Hite, D., Colombe, Y., Wilson, A., Brown, K., Warring, U., Jördens, R., Jost, J., McKay, K., Pappas, D., Leibfried, D., and Wineland, D. *Phys. Rev. Lett.* **109**, 103001 (2012).

67. Daniilidis, N., Gerber, S., Bolloten, G., Ransford, M. R. A., Ulin-Avila, E., Talukdar, I., and Häffner, H. *arXiv:1307.7194* (2013).

68. Blatt, R. and Wineland, D. *Nature* **453**, 1008–1015 (2008).

69. Earnshaw, S. *Trans. Camb. Phil. Soc.* **6-8**, 1837–1846 (1842).

70. Paul, W. *Rev. Mod. Phys.* **62**, 531–540 (1990).

71. House, M. G. *Phys. Rev. A* **78**, 033402 (2008).

72. Major, F. G., Gheorghe, V. N., and Werth, G. *Charged Particles Traps: Physics and Techniques of Charged Particles Field Confinement*, volume 37. Springer Series: Atomic, Optical, and Plasma Physics, Heildelberg, (2005).

73. Oliveira, M. H. and Miranda, J. A. *Eur. J. Phys.* **22**, 063410 (2001).

74. Wesenberg, J. *Phys. Rev. A* **78**, 063410 (2008).

75. Schmied, R. *New J. Phys.* **12**, 023038 (2010).

76. Singer, K., Poschinger, U., Murphy, M., Ivanov, P., Ziesel, F., Calarco, T., and Schmidt-Kaler, F. *Rev. Mod. Phys.* **82**, 2609 (2010).

77. Jackson, J. D. *Classical Electrodynamics*. Wiley, Hoboken, 3rd edition, (1999).

78. Huber, G., Ziesel, F., Poschinger, U., Singer, K., and Ferdinand, S. *Appl. Phys. B* **100**, 725–730 (2010).

79. Ziesel, F. *Quantum State Manipulation and Dynamics in Micro Ion Traps*. PhD thesis, Universität Ulm, (2012).

80. Hänsch, T. and Schawlow, A. *Opt. Comm.* **13**, 68 (1975).

81. Wineland, D. J., Drullinger, R. E., and Walls, F. L. *Phys. Rev. Lett.* **40**, 1639–1642 (1978).

82. Fox, M. *Quantum Optics*. Oxford University Press, Oxford, (2006).

83. Roos, C. F. *Controlling the Quantum State of Trapped Ions*. PhD thesis, Universität Innsbruck, (2000).

84. Ziesel, F. *Spektroskopie und Transport von Ionen in einer Mikrofalle*. Diplomarbeit, Universität Ulm. (2008).

85. Welzel, J. *Planare Spin-Spin Simulatoren*. Diplomarbeit, Universität Ulm. (2011).

86. Pearson, C., Leibrandt, D., Bakr, W., Mallard, W., Brown, K., and Chuang, I. *Phys. Rev. A* **73**, 032307 (2006).

87. Shaikh, F. A. and Ozakin, A. *J. Appl. Phys.* **112**, 074904 (2012).

88. Kaufmann, D., Collath, T., Baig, M., Kaufmann, P., Asenwar, E., Johanning, M., and Wunderlich, C. *Appl. Phys. B* **107**, 935–943 (2012).

89. Groth, S., Krüger, P., Wildermuth, S., Folman, R., Fernholz, T., Schmiedmayer, J., Mahalu, D., and Bar-Joseph, I. *Appl. Phys. Lett.* **85**, 2980 (2004).

90. Moktadir, Z., Darquié, B., Kraft, M., and Hinds, E. A. *J. Mod. Optic.* **54** (2007).

91. Roßnagel, J., Abah, O., Schmidt-Kaler, F., Singer, K., and Lutz, E. *Phys. Rev. Lett.* **112**, 030602 (2014).

92. Mack, C. A. *Fundamental Principles of Optical Lithography: The Science of Microfabrication*. John Wiley & Sons, London, 1st edition, (2007).

93. Madou, M. J. *Fundamentals of Microfabrication and Nanotechnology.* CRC Press, Boca Raton, Florida, 3rd edition, (2012).

94. Bautista-Salvador, A. *Microfabrication of a Planar Paul Trap.* Master's thesis, University of Ulm. (2008).

95. Koch, C. and Rinke, T. J. *Lithography: Theory and Application of Photoresists, Developers, Solvents and Etchants*. Microchemicals, Washington, D. C., (2008/2009).

96. Seidelin, S., Chiaverini, J., Reichle, R., Bollinger, J. J., Leibfried, D., Britton, J., Wesenberg, J. H., Blakestad, R. B., Epstein, R., Hume, D. B., Itano, W. M., Jost, J. D., Langer, C., Ozeri, R., Shiga, N., and Wineland, D. J. *Phys. Rev. Lett.* **96**, 253003 (2006).

97. Koukharenko, E., Moktadir, Z., Kraft, M., Abdelsalam, M., Bagnall, D., Vale, C., Jones, M., and Hinds, E. *Sensor. Actuat. A-Phys.* **115**, 600–607 (2004).

98. Marcinkevicius, A., Juodkazis, S., Watanabe, M., Miwa, M., Matsuo, S., Misawa, H., and Nishii, J. *Opt. Lett.* **26**, 277–279 (2001).

99. Deutschle, T. *Kalte Ionenkristalle in einer segmentierten Paul-Falle*. PhD thesis, Universität Ulm, (2006).

100. Rotter, D. *Photoionisation von Kalzium*. Diplomarbeit, Universität Innsbruck. (2003).

101. Macalpine, W. W. and Schildknecht, R. O. *Proc. of the IEEE* **47** (1959).

102. Gulde, S. T. *Experimental Realization of Quantum Gates and the Deutsch-Jozsa Algorith with* $^{40}Ca^{+}$ *Trapped Ions*. PhD thesis, Universität Innsbruck, (2003).

103. Petrich, M. *Kryogenische Mikro-Ionenfallen.* Diplomarbeit, Universität Ulm. (2010).

104. Eble, J. *Versatile Operations with Calcium and Multi-Species Ion Crystals*. PhD thesis, Universität Ulm, (2011).

105. Ricci, L., Weidemüller, M., Esslinger, T., Hemmerich, A., Zimmermann, C., Vuletic, V., König, W., and Hänsch, T. *Opt. Commun.* **117**, 541–549 (1995).

106. Poschinger, U. G. *Quantum Optics Experiments in a Microstructured Ion Trap*. PhD thesis, Universität Ulm, (2010).

107. Donley, E., Heavner, T., Levi, F., Tataw, M., and Jefferts, S. *Rev. Sci. Instrum.* **76**, 063112 (2005).

108. Singer, K., Jochim, S., Mudrich, M., Mosk, A., and Weidemüller, M. *Rev. Sci. Instrum.* **73**, 4402 (2002).

109. Schulz, S. *Scalable Microchip Ion Traps for Quantum Computationp*. PhD thesis, Universität Ulm, (2009).

110. Wiens, A. *Detection of Qubit Registers in a Micro Trap*. Diplomarbeit, Johannes Gutenberg-Universität Mainz. (2011).

111. Konenkov, N., Sudakov, M., and Douglas, D. *J. Am. Soc. Mass. Spectr.* **13**, 597–613 (2002).

112. Deslauriers, L., Haljan, P. C., Lee, P. J., Brickman, K.-A., Blinov, B. B., Madsen, M. J., and Monroe, C. *Phys. Rev. A* **70**, 043408 (2004).

113. Haze, S., Ohno, T., Toyoda, K., and Urabe, S. *Appl. Phys. B* **105**, 761–765 (2011).

114. Rabi, I. I. *Phys. Rev.* **51**, 652–654 (1937).

115. Walther, A., Poschinger, U., Ziesel, F., Hettrich, M., Wiens, A., Welzel, J., and F., S. *Phys. Rev. A* **83**, 062329 (2011).

116. Chen, D., Xu, D., Wang, J., Zhao, B., and Zhang, Y. *Vacuum* **83**, 282–285 (2008).

117. Pratt, A. *Advanced Energy Industries Inc., Fort Collins, CO* (2004).

118. Gupta, T. *Copper Interconnect Technology*. Springer, Massachusetts, (2009).

119. Louis, C. and Pluchery, O. *Gold Nanoparticles For Physics, Chemistry and Biology*. Imperial College Press, London, (2012).

120. Fowler, M. *Proc. IREE Australia* , 148–164 (1970).

121. Hellwig, M., Bautista-Salvador, A., Singer, K., Werth, G., and Schmidt-Kaler, F. *New J. Phys.* **12**, 065019 (2010).

122. Eltony, A. M., Wang, S. X., Akselrod, G. M., Herskind, P. F., and Chuang, I. L. *Appl. Phys. Lett.* **102**, 054106 (2013).

123. Stick, D., Fortier, K. M., Haltl, R., Highstrete, C., Moehring, D. L., Tigges, C., and Blain, M. G. *arXiv:1008.0990v2* (2010).

124. Leibrandt, D. R., Labaziewicz, J., Clarck, R. J., Chuang, I. L., Epstein, R. J., Ospelkaus, C., Wesenberg, J. H., Bollinger, J. J., Leibfried, D., Wineland, D. J., Stick, D., Sterk, J., Monroe, C., Pai, C.-S., Low, Y., Frahm, R., and Slusher, R. E. *Quant. Inf. Comput.* **9**, 0901–0919 (2009).

125. Britton, J., Leibfried, D., Beall, J. A., Blakestad, R. B., Wesenberg, J. H., and Wineland, D. J. *Appl. Phys. Lett.* **95**, 173102 (2009).

126. Amini, J. M., Uys, H., Wesenberg, J. H., Seidelin, S., Britton, J., Bollinger, J. J., Leibfried, D., Ospelkaus, C., VanDevender, A. P., and Wineland, D. J. *New J. Phys.* **12**, 033031 (2010).

127. Enzer, D. G., Schauer, M. M., Gomez, J. J., Gulley, M. S., Holzscheiter, M. H., Kwiat, P. G., Lamoreaux, S. K., Peterson, C. G., Sandberg, V. D., Tupa, D., White, A. G., Hughes, R. J., and James, D. F. V. *Phys. Rev. Lett.* **85**, 2466 (2000).

Amado Bautista-Salvador

Curriculum Vitæ

Ausbildung

Promotion in Physik

03.2009– Universität Ulm, Ulm

Master of Science in Nanomaterialien

10.2006–12.2008 Universität Ulm, Ulm

Physik

02.2000–08.2006 Nationale Autonome Universität von Mexiko (UNAM), Mexiko-Stadt, Mexiko

Beruflicher Werdegang

seit 01.06.2014	Leibniz Universität Hannover, Hannover Wissenschaftlicher Mitarbeiter (PostDoc)
09.2010-01.2013	Johannes Gutenberg-Universität Mainz, Institut für Physik, Mainz Wissenschaftlicher Mitarbeiter (Doktorand)
03.2009–08.2010	Universität Ulm, Institut für Quanten-Informationsverarbeitung, Ulm Akademischer Mitarbeiter (Doktorand)

Publikationen

[1] M. Hellwig, A. Bautista-Salvador, K. Singer, G. Werth, and F. Schmidt-Kaler. Fabrication of a planar micro Penning trap and numerical investigations of versatile ion positioning protocols. *New Journal of Physics*, 12, 2010.

[2] J.-A. Reyes-Esqueda, A Bautista-Salvador, and R. Zanella-Specia. Size control of Au Nanoparticles on TiO_2 and Al_2O_3 by DP Urea: Optical Absorption and Electron Microscopy as Control Probes. *Journal of Nanoscience and Nanotechnology*, 8, 2008.

[3] J. Welzel, A. Bautista-Salvador, C. Abarbanel, V. Wineman-Fisher, C. Wunderlich, R. Folman, and F. Schmidt-Kaler. Designing spin-spin interactions with one and two dimensional ion crystals in planar micro traps. *The European Physical Journal D*, 65, 2011.

Posters

2012	Magnetfeldgradienten in planare Ionenfallen zur Simulation von Spinmodellen, Universität Stuttgart
2011	Spin-Spin interaction in impurity doped ion crystal, Universität Dresden
2010	Simulation und Herstellung verschiedener zweidimensionaler Ionenfallen für die Quanteninformationsverarbeitung, Universität Hannover
2009	A planar segmented Ion Trap with a Y-Junction, Universität Hamburg

Gustavsburg, 17. Januar, 2015